

Julius-Maximilians-Universität Würzburg
Université de Montréal

LIGAND DESIGN FOR Ru(II) PHOTSENSITIZERS IN PHOTOCATALYTIC HYDROGEN EVOLUTION

by

Mira Theresa Rupp

from Langen (Hessen), Germany

Thesis for the attainment of the doctoral degree in natural sciences
Dissertation zur Erlangung des naturwissenschaftlichen Doktorgrades
Thèse présentée en vue de l'obtention du grade de Philosophae Doctor (Ph.D.) en
Chimie

Würzburg, July 2021

© Mira Theresa Rupp, 2021



Eingereicht bei der Fakultät für Chemie und Pharmazie am

Gutachter der schriftlichen Arbeit:

1. Gutachter: _____

2. Gutachter: _____

Prüfer des öffentlichen Promotionskolloquiums:

1. Prüfer: _____

2. Prüfer: _____

3. Prüfer: _____

4. Prüfer: _____

5. Prüfer: _____

Datum des öffentlichen Promotionskolloquiums

Doktorurkunde ausgehändigt am

Julius-Maximilians-Universität Würzburg – Fakultät für Chemie und Pharmazie
Université de Montréal – Faculté des Arts et Sciences, Département de Chimie

Cette thèse intitulée

LIGAND DESIGN FOR Ru(II) PHOTOCATALYTIC HYDROGEN EVOLUTION

Présentée par

Mira Theresa Rupp

A été évaluée par un jury composé des personnes suivantes

Summary

This thesis investigates different ligand designs for Ru(II) complexes and the activity of the complexes as photosensitizer (PS) in photocatalytic hydrogen evolution. The catalytic system typically contains a catalyst, a sacrificial electron donor (SED) and a PS, which needs to exhibit strong absorption and luminescence, as well as reversible redox behavior. Electron-withdrawing pyridine substituents on the terpyridine metal ion receptor result in an increase of excited-state lifetime and quantum yield ($\Phi = 74 \cdot 10^{-5}$; $\tau = 3.8$ ns) and lead to complex **III-C1** exhibiting activity as PS. While the turn-over frequency (TOF_{max}) and turn-over number (TON) are relatively low ($\text{TOF}_{\text{max}} = 57 \text{ mmol}_{\text{H}_2} \text{ mol}_{\text{PS}}^{-1} \text{ min}^{-1}$; $\text{TON}(44 \text{ h}) = 134 \text{ mmol}_{\text{H}_2} \text{ mol}_{\text{PS}}^{-1}$), the catalytic system is long-lived, losing only 20% of its activity over the course of 12 days. Interestingly, the heteroleptic design in **III-C1** proves to be beneficial for the performance as PS, despite **III-C1** having comparable photophysical and electrochemical properties as the homoleptic complex **IV-C2** ($\text{TOF}_{\text{max}} = 35 \text{ mmol}_{\text{H}_2} \text{ mol}_{\text{PS}}^{-1} \text{ min}^{-1}$; $\text{TON}(24 \text{ h}) = 14 \text{ mmol}_{\text{H}_2} \text{ mol}_{\text{PS}}^{-1}$). Reductive quenching of the excited PS by the SED is identified as rate-limiting step in both cases.

Hence, the ligands are designed to be more electron-accepting either *via* *N*-methylation of the peripheral pyridine substituents or introduction of a pyrimidine ring in the metal ion receptor, leading to increased excited-state lifetimes ($\tau = 9\text{--}40$ ns) and luminescence quantum yields ($\Phi = 40\text{--}400 \cdot 10^{-5}$). However, the more electron-accepting character of the ligands also results in anodically shifted reduction potentials, leading to a lack of driving force for the electron transfer from the reduced PS to the catalyst. Hence, this electron transfer step is found to be a limiting factor to the overall performance of the PS. While higher TOF_{max} in hydrogen evolution experiments are observed for pyrimidine-containing PS ($\text{TOF}_{\text{max}} = 300\text{--}715 \text{ mmol}_{\text{H}_2} \text{ mol}_{\text{PS}}^{-1} \text{ min}^{-1}$), the longevity for these systems is reduced with half-life times of 2–6 h.

Expansion of the pyrimidine-containing ligands to dinuclear complexes yields a stronger absorptivity ($\epsilon = 100\text{--}135 \cdot 10^3 \text{ L mol}^{-1} \text{ cm}^{-1}$), increased luminescence ($\tau = 90\text{--}125$ ns, $\Phi = 210\text{--}350 \cdot 10^{-5}$) and can also result in higher TOF_{max} given sufficient driving force for electron transfer to the catalyst ($\text{TOF}_{\text{max}} = 1500 \text{ mmol}_{\text{H}_2} \text{ mol}_{\text{PS}}^{-1} \text{ min}^{-1}$). When comparing complexes with similar driving forces, stronger luminescence is reflected in a higher TOF_{max} . Besides thermodynamic considerations, kinetic effects and electron

transfer efficiency are assumed to impact the observed activity in hydrogen evolution. In summary, this work shows that targeted ligand design can make the previously disregarded group of Ru(II) complexes with tridentate ligands attractive candidates for use as PS in photocatalytic hydrogen evolution.

Zusammenfassung

In dieser Arbeit werden verschiedene Liganden für Ru(II)-Komplexe und die Aktivität der Komplexe als Photosensibilisatoren (PS) in der photokatalytischen Wasserstoffentwicklung untersucht. Das katalytische System besteht typischerweise aus einem Katalysator, einem Opferelektronendonator (SED) und einem PS, welcher eine starke Absorption und Lumineszenz sowie ein reversibles Redoxverhalten aufweisen sollte. Elektronenziehende Pyridin-Substituenten am Terpyridin-Metallionenrezeptor resultieren in einer Erhöhung der Lebensdauer des angeregten Zustands sowie der Quantenausbeute ($\Phi = 74 \cdot 10^{-5}$; $\tau = 3.8$ ns), was dazu führt, dass Komplex **III-C1** als PS aktiv ist. Während die Wechselzahl (TOF_{max}) und der Umsatz (TON) relativ niedrig sind ($\text{TOF}_{\text{max}} = 57 \text{ mmol}_{\text{H}_2} \text{ mol}_{\text{PS}}^{-1} \text{ min}^{-1}$; $\text{TON}(44 \text{ h}) = 134 \text{ mmol}_{\text{H}_2} \text{ mol}_{\text{PS}}^{-1}$), ist das katalytische System langlebig und verliert im Laufe von 12 Tagen nur 20% seiner Aktivität. Das heteroleptische Design in **III-C1** erweist sich als vorteilhaft für die Leistung als PS, obwohl **III-C1** vergleichbare photophysikalische und elektrochemische Eigenschaften besitzt wie der homoleptische Komplex **IV-C2** ($\text{TOF}_{\text{max}} = 35 \text{ mmol}_{\text{H}_2} \text{ mol}_{\text{PS}}^{-1} \text{ min}^{-1}$; $\text{TON}(24 \text{ h}) = 14 \text{ mmol}_{\text{H}_2} \text{ mol}_{\text{PS}}^{-1}$). In beiden Fällen erweist sich das reduktive Lumineszenzlöschen des angeregten PS durch den SED als geschwindigkeitsbestimmender Schritt.

Daher werden die Liganden entweder durch *N*-Methylierung der peripheren Pyridin-Substituenten oder durch Einführung eines Pyrimidinrings in den Metallionenrezeptor elektronenziehender gestaltet, was zu erhöhten Lebensdauern des angeregten Zustands ($\tau = 9\text{--}40$ ns) und Lumineszenzquantenausbeuten ($\Phi = 40\text{--}400 \cdot 10^{-5}$) führt. Der stärker elektronenziehende Charakter der Liganden führt allerdings auch zu anodisch verschobenen Reduktionspotentialen, wodurch die treibende Kraft für den Elektronentransfer vom reduzierten PS zum Katalysator reduziert wird. Daher erweist sich dieser Elektronentransferschritt als ein limitierender Faktor für die Gesamtleistung des PS. Während höhere TOF_{max} in Wasserstoffproduktionsexperimenten für Pyrimidin-haltige PS beobachtet werden ($\text{TOF}_{\text{max}} = 300\text{--}715 \text{ mmol}_{\text{H}_2} \text{ mol}_{\text{PS}}^{-1} \text{ min}^{-1}$), ist die Langlebigkeit für diese Systeme mit Halbwertszeiten von 2–6 h deutlich reduziert.

Die Erweiterung der Pyrimidin-haltigen Liganden zu zweikernigen Komplexen führt zu einem stärkeren Absorptionsvermögen ($\epsilon = 100\text{--}135 \cdot 10^3 \text{ L mol}^{-1} \text{ cm}^{-1}$), erhöhter Lumineszenz ($\tau = 90\text{--}125 \text{ ns}$, $\Phi = 210\text{--}350 \cdot 10^{-5}$) und kann bei ausreichender treibender Kraft für den Elektronentransfer zum Katalysator auch zu einer höheren TOF_{max} führen ($\text{TOF}_{\text{max}} = 1500 \text{ mmol}_{\text{H}_2} \text{ mol}_{\text{PS}}^{-1} \text{ min}^{-1}$). Beim Vergleich von Komplexen mit ähnlichen treibenden Kräften spiegelt sich die stärkere Lumineszenz in einem höheren TOF_{max} wider. Es wird angenommen, dass neben thermodynamischen Faktoren auch kinetische Effekte und die Effizienz des Elektronentransfers die beobachtete Aktivität bei der Wasserstoffentwicklung beeinflussen. Zusammenfassend zeigt diese Arbeit, dass gezieltes Ligandendesign die bisher vernachlässigte Gruppe der Ru(II)-Komplexe mit tridentaten Liganden zu attraktiven Kandidaten für den Einsatz als PS in der photokatalytischen Wasserstoffentwicklung machen kann.

Résumé

Cette thèse étudie la conception de différents ligands pour les complexes de Ru(II) et leur activité comme photosensibilisateur (PS) dans l'évolution photocatalytique de l'hydrogène. Le système catalytique contient généralement un catalyseur, un donneur d'électron sacrificiel (SED) et un PS, qui doit présenter une forte absorption et luminescence et un comportement redox réversible. Les substituants pyridine attracteurs d'électrons sur le récepteur d'ions métalliques terpyridine entraînent une augmentation de la durée de vie de l'état excité et du rendement quantique ($\Phi = 74 \cdot 10^{-5}$; $\tau = 3.8$ ns) et permettent au complexe **III-C1** de présenter une activité en tant que PS. Bien que la fréquence (TOF_{max}) et le nombre de cycle catalytique (TON) soient relativement faibles ($\text{TOF}_{\text{max}} = 57 \text{ mmol}_{\text{H}_2} \text{ mol}_{\text{PS}}^{-1} \text{ min}^{-1}$; $\text{TON}(44 \text{ h}) = 134 \text{ mmol}_{\text{H}_2} \text{ mol}_{\text{PS}}^{-1}$), le système catalytique a une longue durée de vie, ne perdant que 20% de son activité au cours de 12 jours. De manière intéressante, la conception hétérolytique dans **III-C1** s'avère être bénéfique pour la performance en tant que PS, malgré des propriétés photophysiques et électrochimiques comparables à celles du complexe homoleptique **IV-C2** ($\text{TOF}_{\text{max}} = 35 \text{ mmol}_{\text{H}_2} \text{ mol}_{\text{PS}}^{-1} \text{ min}^{-1}$; $\text{TON}(24 \text{ h}) = 14 \text{ mmol}_{\text{H}_2} \text{ mol}_{\text{PS}}^{-1}$). L'extinction réductive de la PS excitée par le SED est identifiée comme l'étape limitant la vitesse dans les deux cas.

Par conséquent, les ligands sont modifiés pour être plus accepteurs d'électrons, soit par *N*-méthylation des substituants pyridine périphériques, soit par introduction d'un cycle pyrimidine dans le récepteur d'ion métallique, ce qui conduit à une augmentation des durées de vie des états excités ($\tau = 9\text{--}40$ ns) et des rendements quantiques de luminescence ($\Phi = 40\text{--}400 \cdot 10^{-5}$). Cependant, le caractère plus accepteur d'électrons des ligands entraîne également des potentiels de réduction décalés anodiquement, ce qui conduit à un manque de force motrice pour le transfert d'électrons du PS réduit au catalyseur. Ainsi, cette étape de transfert d'électrons s'avère être un facteur limitant de la performance globale du PS. Alors que des TOF_{max} plus élevés dans les expériences d'évolution de l'hydrogène sont observés pour les PS contenant le motif pyrimidine ($\text{TOF}_{\text{max}} = 300\text{--}715 \text{ mmol}_{\text{H}_2} \text{ mol}_{\text{PS}}^{-1} \text{ min}^{-1}$), la longévité de ces systèmes est réduite avec des temps de demi-vie de 2–6 h.

L'expansion des ligands contenant le motif pyrimidine en complexes dinucléaires conduit à une absorptivité plus forte ($\epsilon = 100\text{--}135 \cdot 10^3 \text{ L mol}^{-1} \text{ cm}^{-1}$), une

luminescence accrue ($\tau = 90\text{--}125\text{ ns}$, $\Phi = 210\text{--}350 \times 10^{-5}$) et peut également entraîner un TOF_{max} plus élevé si la force motrice est suffisante pour le transfert d'électrons vers le catalyseur ($1500\text{ mmol}_{\text{H}_2}\text{ mol}_{\text{PS}}^{-1}\text{ min}^{-1}$). En comparant des complexes avec des forces motrices similaires, une luminescence plus forte se traduit par un TOF_{max} plus élevé. Outre les considérations thermodynamiques, les effets cinétiques et l'efficacité du transfert d'électrons sont supposés avoir un impact sur l'activité observée dans l'évolution de l'hydrogène. En résumé, ce travail montre que la conception ciblée de ligands peut faire du groupe précédemment négligé des complexes de Ru(II) avec des ligands tridentés des candidats attrayants pour une utilisation comme PS dans l'évolution photocatalytique de l'hydrogène.

List of Publications

Parts of this thesis were published/submitted previously in the following journal articles:

1. M. Rupp, T. Auvray, E. Rousset, G. M. Mercier, V. Marvaud, D. G. Kurth, G. S. Hanan, Photocatalytic Hydrogen evolution driven by a heteroleptic Ru(II) bis-terpyridine complex. *Inorganic Chemistry* **2019**, *58*, 9127-9134.
2. M. Rupp, T. Auvray, N. Shevchenko, L. Swoboda, G. S. Hanan, D. G. Kurth, Substituted 2,4-di(pyridin-2-yl)-pyrimidine based ruthenium photosensitizers for hydrogen photo-evolution under red light. *Inorganic Chemistry* **2021**, *60*, 292-302.
3. M. T. Rupp, T. Auvray, G. S. Hanan, D. G. Kurth, Electrochemical and photophysical study of homoleptic and heteroleptic methylated ruthenium(II) bis-terpyridine complexes. *European Journal of Inorganic Chemistry* **2021**, *2021* (28), 2822-2829.
4. Mira T. Rupp; Daniel Chartrand, Garry S. Hanan, Dirk G. Kurth, CCDC 2090569: Experimental Crystal Structure Determination, *CSD Communication*, **2021**.
5. M. T. Rupp, N. Shevchenko, G. S. Hanan, D. G. Kurth, Enhancing the photophysical properties of Ru(II) complexes by specific design of tridentate ligands. *Coordination Chemistry Reviews* **2021**, *446*, 214127.
6. M. T. Rupp, T. Auvray, D. G. Kurth, G. S. Hanan, Dinuclear 2,4-di(pyridin-2-yl)-pyrimidine based ruthenium photosensitizers for hydrogen photo-evolution under red light. (revised and submitted to *Dalton Transactions*)

A detailed description of the contributions to each publication are given at the end of this thesis.

Acknowledgements

I would like to thank all those who supported, helped, and encouraged me during my PhD studies. First, I would like to express my gratitude towards my PhD supervisors Prof. Dirk G. Kurth and Prof. Garry S. Hanan. Thank you for giving me the opportunity to conduct my studies both in Germany and in Canada, and to work on such an interesting research topic. I really appreciated your feedback, the scientific discussions, and your trust in me, which allowed me to pursue my own ideas. Thank you for your support when it came to writing proposals and other administrative hurdles, of which there were plenty due to the binational nature of the project. Additionally, I would like to thank my thesis committee, Prof. Christian Reber and Prof. Frank Schaper, for their kind support and scientific input.

Furthermore, I am very grateful for both my research groups in Würzburg and Montréal. A special thanks goes to Thomas Auvray who is both a friend and mentor to me. Thank you for teaching me the ropes in the lab and always being there to help others. In addition, I would like to thank Robin for being the friend he is and for putting up with half of the group disappearing to Canada for half of the time. I would further like to thank the current and former members of the Luxenhofer group at the Universität Würzburg and the Schaper group at the Université de Montréal for enriching lunch breaks and after-work activities.

I would also like to express my thanks to the students, who supported me during their research internships, Lukas Swoboda and Pallavi Barman, or their bachelor thesis, Benjamin Gehring. I want to particularly thank Natali Shevchenko for her hard work, her trust in me as a supervisor, and also for being a friend.

In addition, I highly appreciated all the help from Daniel Chartrand when it came to crystallography or photophysical measurements. Plus, I am very grateful for the university employees that kept everything around us running. Special thanks go to Pedro at UdeM, Anna, Sandra, Christian and Steffi in Würzburg, and Diana for helping me with all my administrative hassles.

I would further like to thank the DAAD and the BayFor for the financial support during my time in Montréal and particularly Ms. Gauzy for her kind support.

Finally, I also want to thank my friends who accompanied me through all my studies and were always there to welcome me back home after spending time abroad.

Special thanks go to my family, for their love, and patience throughout my studies, for standing behind me in all my decisions, for always believing in me and for being an empowering support.

Last but not least, I want to thank my partner, Laurent, for always being there – even when we were oceans apart. Thank you for your support, trust, and love. Thanks for always believing in me and making me dream bigger.

Table of contents

Summary	I
Zusammenfassung	III
Résumé	V
List of Publications	VII
Acknowledgements	IX
Table of contents	XI
List of Acronyms and Abbreviations	XV
List of Figures	XXI
List of Charts	XXXV
List of Schemes	XXXVI
List of Tables	XXXVII
I. Introduction	1
I.1. Motivation	3
I.2. Natural Photosynthesis	7
I.3. Artificial Photosynthesis	11
I.4. Photosensitizer	15
I.4.1. Theoretical Background	15
I.4.2. State of the Art	23
I.5. Sacrificial Electron Donor and Acceptor	25
I.6. Catalyst	26
I.6.1. Water Oxidation Catalyst	26
I.6.2. Water Reduction Catalyst	27
I.6.3. Supramolecular Systems	28
I.7. Photophysical and Electrochemical Properties of Ru(II) Complexes with Tridentate Ligands – State of the Art	29
I.7.1. Ligand Design	31
I.7.2. Supramolecular Systems	45
I.8. Conclusion	54
II. Objective and Scope of this Thesis	55
III. Effect of Electron-Donating and Electron-Withdrawing Groups on Ru(II) bis- Terpyridine Complexes	57
III.1. Introduction	59

III.2.	Results and Discussion	60
III.2.1.	Synthesis	60
III.2.2.	Structural Analysis	62
III.2.3.	Photophysical Properties	63
III.2.1.	Electrochemical Properties	65
III.2.2.	Spectroelectrochemistry	67
III.2.1.	DFT Calculations	69
III.2.2.	Hydrogen Evolution Experiments.....	71
III.3.	Conclusion	76
III.4.	Experimental	77
IV.	Effect of Homoleptic vs. Heteroleptic Design of Ru(II) bis-Terpyridine Complexes.....	83
IV.1.	Introduction	85
IV.2.	Results and Discussion	86
IV.2.1.	Synthesis and Structural Analysis.....	86
IV.2.2.	Photophysical Properties	87
IV.2.3.	Electrochemical Properties	89
IV.2.4.	DFT Calculations	91
IV.2.5.	Hydrogen Evolution Experiments.....	93
IV.3.	Conclusion	96
IV.4.	Experimental	97
V.	Effect of <i>N</i> -Methylation of Ru(II) bis-Terpyridine Complexes	99
V.1.	Introduction.....	101
V.2.	Results and Discussion	101
V.2.1.	Synthesis and Structural Analysis.....	101
V.2.2.	Photophysical Properties	103
V.2.3.	Electrochemical Properties	106
V.2.4.	DFT Calculations	108
V.2.5.	Hydrogen Evolution Experiments.....	111
V.3.	Conclusion.....	116
V.4.	Experimental	116
VI.	Effect of other Heterocycles in Ru(II) Complexes of Tridentate Ligands.....	119
VI.1.	Introduction	121
VI.2.	Results and Discussion	122

VI.2.1.	Synthesis and Structural Analysis.....	122
VI.2.2.	Photophysical Properties	124
VI.2.3.	Electrochemical Properties	127
VI.2.4.	DFT Calculations	129
VI.2.5.	Hydrogen Evolution Experiments.....	133
VI.3.	Conclusion	140
VI.4.	Experimental	141
VII.	Effect of Multiple Metal Centers in Ru(II) Complexes of Tridentate Ligands .	149
VII.1.	Introduction	151
VII.2.	Results and Discussion	152
VII.2.1.	Synthesis	152
VII.2.2.	Photophysical Properties	153
VII.2.3.	Electrochemical Properties	159
VII.2.4.	DFT Calculations	162
VII.2.5.	Hydrogen Evolution Experiments.....	163
VII.3.	Conclusion	171
VII.4.	Experimental	173
VIII.	Conclusion.....	177
IX.	Appendix.....	181
IX.1.	Material	183
IX.2.	Instrumentation Details.....	183
IX.3.	NMR Spectra.....	185
IX.4.	Crystallography	213
IX.4.1.	III-C1	213
IX.4.2.	III-C2.....	215
IX.4.3.	IV-C2	217
IX.4.4.	V-C1	219
IX.4.5.	VI-C1	221
IX.4.6.	VI-C4	223
IX.5.	Computational Details	225
IX.5.1.	Natural Transition Analysis	225
IX.5.2.	Contributions to Molecular Orbitals.....	229
IX.6.	Hydrogen Production Experiments.....	230

X. Literature.....	233
Author Contributions.....	243

List of Acronyms and Abbreviations

%	percent
%w	weight percent
[Fe]	hydrogenases with iron active site
[FeFe]	hydrogenases with diiron active site
[NiFe]	hydrogenases with nickel-iron active site
°C	degree Celsius
μ	absorption coefficient
μM	micromolar
μs	microsecond
A	absorption
<i>a</i>	distance between charged species after electron transfer
<i>a</i>	length of cell edge <i>a</i>
Å	Angström
a.u.	arbitrary units
A_1	absorbance of compound under investigation at excitation wavelength
A_e	electron acceptor
Anal.	analytically
Aqu.	aqueous
A_{ref}	absorbance of reference compound at excitation wavelength
ATP	adenosine triphosphate
<i>b</i>	length of cell edge <i>b</i>
BIH	1,3-dimethyl-2-phenylbenzimidazoline
Bipytpy	4'-(4-bromophenyl)-4,4''':4'',4''''-di-pyridinyl-2,2':6',2''-terpyridine
BNAH	1-benzyl-1,4-dihydronicotinamide
bpy	2,2'-bipyridine
<i>c</i>	length of cell edge <i>c</i>
Calc.	calculated
CE	counter electrode
CER	Canada Energy Regulator
cm	centimeter
COSY	correlation spectroscopy
Covid-19	infectious disease with the virus SARS-CoV-2
CPS	photosensitizer concentration
CV	cyclic voltammetry
<i>d</i>	doublet
D^+A^-	charge separated donor-acceptor complex
D_3	dihedral symmetry group of degree 3
DA	donor-acceptor complex
dd	doublet of doublets
ddd	doublet of doublets of doublets
D_e	electron donor
DFIX	ShelX compatible restraint on atom-to-atom distances
DFT	density functional theory
DMF	<i>N,N</i> -dimethylformamide

dmgH	dimethylglyoxime
DMSO	dimethyl sulfoxide
DMT	dimethyl para toluidine
DSSC	dye sensitized solar cell
E	energy
e	electron charge
e.g.	<i>exempli gratia</i> (for example)
E^0	standard potential
$E_{1/2}$	half-wave redox potential
E_a	activation energy
EADP	ShelX compatible restraint to equate U_{ij}
ECCE	catalytic cycle following electron transfer-protonation-protonation-electron transfer cycle
ECEC	catalytic cycle following electron transfer-protonation-electron transfer-protonation cycle
EDG	electron-donating group
EDTA	ethylenediaminetetraacetic acid
EECC	catalytic cycle following electron transfer-electron transfer-protonation-protonation cycle
E_{ox}	oxidation potential
E_{ox}^*	oxidation potential in the excited state
eq	equivalent
E_{red}	reduction potential
E_{red}^*	reduction potential in the excited state
esd	estimated standard deviation
ESI-MS	electrospray ionization mass spectrometry
ET	electron transfer
et al.	<i>et alii</i> (and others)
etc.	<i>et cetera</i> (and the rest)
eV	electron volt
EWG	electron-withdrawing group
exp	exponential function with Euler's number as base
EXYZ	ShelX compatible restraint to equate xyz parameters
F	fluorescence
F(000)	structure factor at $h=0, k=0, l=0$
F^2	structure factor squared
Fc	ferrocene
FEY	fractional energy yield
FLAT	ShelX compatible restraint to restrain atoms to a common plane
FRET	Förster resonance energy transfer
fs	femtosecond
ft	foot
FTO	fluorine doped tin oxide layer
g	gram
Ga K α	X-ray source with Gallium rich alloy and K α emission
GC	gas chromatograph
GISS	Goddard Institute for Space Studies
GISTEMP	GISS Surface Temperature Analysis

GS	ground state
h	hour(s)
h	Planck constant
h	Miller index h (crystallography)
H ⁺	hydrogen cation/ proton
H _{DA}	Hamiltonian for coupling of D _e and A _e
HEC	hydrogen evolution catalyst
HMBC	heteronuclear multiple-bond correlation spectroscopy
HOMO	highest occupied molecular orbital
HPLC	high pressure liquid chromatograph
HR-MS	high-resolution mass spectrometry
HSQC	heteronuclear single quantum correlation spectroscopy
Hz	Hertz
h ν	photon radiation
I	electric current
i.e.	<i>id est</i> (that is)
IC	internal conversion
IEA	International Energy Agency
ILCT	inter-ligand charge transfer
irr	irreversible
ISC	intersystem crossing
ISOR	ShelX compatible restraint on thermal ellipsoids
J	coupling constant
K	Kelvin
k	Miller index k (crystallography)
k^0	sum of radiative and non-radiative decay constants
k^0	pre-factor
k_{ET}	rate constant for electron transfer
k_{nr}	non-radiative decay constant
k_{obs}	observed rate constant
k_r	radiative decay constant
L	liter
L	solvent molecule
l	Miller index l (crystallography)
LC	ligand centered
LED	light-emitting diode
LHE	light-harvesting efficiency
LMCT	ligand-to-metal charge transfer
ln	natural logarithm
lowess	locally weighted scatterplot smoothing
LSAT+SST	land surface air temperature + sea surface temperature
LUMO	lowest unoccupied molecular orbital
m	multiplet
M	molar
m/z	mass-to-charge ratio
MC	metal centered
mCPBA	<i>meta</i> -chloroperoxybenzoic acid
MeCN	acetonitrile

MeOH	methanol
meV	millielectronvolt
mg	milligram
MHz	megahertz
min	minute(s)
mL	milliliter
MLCT	metal-to-ligand charge transfer
mm	millimeter
mM	millimolar
Mtoe	millions of tonnes of oil equivalent
mV	millivolt
mW	milliwatt
MW	microwave
n.d.	not determined
N _A	Avogadro constant
NADP ⁺	reduced form of nicotinamide adenine dinucleotide phosphate
NADPH	nicotinamide adenine dinucleotide phosphate
NaOMe	sodium methanolate
NASA	National Aeronautics and Space Administration
n-e	non-emissive
NHC	<i>N</i> -heterocyclic carbene
NHE	normal hydrogen electrode
NIR	near-infrared
nm	nanometer
NMR	nuclear magnetic resonance
NOAA	National Oceanic and Atmospheric Administration
NR	non-radiative decay
ns	nanosecond
OEC	oxygen evolution center
OTf	triflate group
ox	oxidation
P	phosphorescence
PC	personal computer
pH	<i>potential hydrogenii</i> (potential of hydrogen)
POM	polyoxometalate
ppm	parts per million
PS	photosensitizer
ps	picosecond
PSI	photosystem I
PSII	photosystem II
PWh	Petawatt hours
Py	pyridine
q	displacement
q [*]	displacement of parabola intersection
q ₀ ^P	displacement of product
q ₀ ^R	displacement of reactant
R	rest
R	gas constant

R ₁	confidence factor based on F
RC	reaction center
RE	reference electrode
red	reduction
Ref	reference number
RIGU	Shelx compatible restraint to rigidify bonds
R _{int}	merging error
R _{sigma}	signal-to-noise ratio
s	second
s	singlet (in NMR spectroscopy)
S	singlet state
S ⁰	ground state
S ₁	area of emission peak of compound under investigation
SADI	Shelx compatible restraint on atom-to-atom distances
SCE	saturated calomel electrode
SEA	sacrificial electron acceptor
SED	sacrificial electron donator
SIMU	Shelx compatible restraint on thermal ellipsoids
SQUEEZE	Platon procedure to treat disordered solvent in crystal structures
S _{ref}	area of emission peak of reference compound
SUMP	ShelX compatible restraint linking together free variables
t	triplet
T	triplet state
T	temperature
TBAPF ₆	tetrabutylammonium hexafluorophosphate
tButpy	4'-(4-bromophenyl)-4,4''-di-tert-butyl-2,2':6',2''-terpyridine
td	triplet of doublets
TD-DFT	time-dependent density functional theory
TEA	triethyl amine
TEOA	triethanolamine
t _f	time length of experiment
t _i	begin of time interval
t _j	end of time interval
TMSCN	trimethylsilyl cyanide
TOF	turn-over frequency
TOF _{max}	maximum turn-over frequency
Tolyltpy	<i>p</i> -tolyl-2,2':6',2''-terpyridine
TON	turn-over number
tpy	2,2':6',2''-terpyridine
T _λ	transmission
U _{ij}	anisotropic displacement parameters
USA	United States of America
UV	ultraviolet
UV-vis	ultraviolet-visible
V	Volt
vs.	<i>versus</i> (against)
W	work term

w.r.t.	with respect to
WE	working electrode
WOC	water oxidation catalyst
wR ₂	confidence factor based on F ²
X	substituent X
Y	substituent Y
Z	number of molecules in the unit cell
z(A)	charge of acceptor
z(D)	charge of donor
α	cell angle
β	cell angle
γ	cell angle
δ	chemical shift
Δ [‡] G	Gibbs activation energy
ΔE _p	difference between anodic and cathodic peak potentials
ΔG ⁰ _{ET}	free Gibbs energy for photoinduced electron transfer
Δ _r G ^o	Gibbs standard reaction energy
ε	extinction coefficient
ε ₀	vacuum permittivity
ε _r	relative medium static permittivity
Θ	reflection angle
Λ	reorganization energy
λ	wavelength
λ _{abs}	absorption wavelength
λ _{em}	emission wavelength
λ _{max abs}	maximum absorption wavelength
λ _{max em}	maximum emission wavelength
μA	microampere
μL	microliter
μmol	micromole
π* _L a ₂	anti-bonding ligand-centered π orbital with a ₂ symmetry
π* _L e	anti-bonding ligand-centered π orbital with e symmetry
π* _M	anti-bonding metal-centered π orbital
π _L	bonding ligand-centered π orbital
π _M	bonding metal-centered π orbital
π _{Ma1}	bonding Metal-centered π orbital with a ₁ symmetry
π _{Me}	bonding Metal-centered π orbital with e symmetry
ρ _{calc}	density values calculated from the crystal cell and contents
σ _L	bonding ligand-centered σ orbital
σ _M *	anti-bonding metal-centered σ orbital
τ	excited-state lifetime
Φ	luminescence quantum yield
Φ ₁	quantum yield of compound under investigation
Φ _{ref}	quantum yield of reference compound
ΔE _{em}	emission energy

List of Figures

- Figure I-1. a) Atmospheric carbon dioxide measured at the Mauna Loa Observatory, Hawaii; b) global atmospheric methane. Images provided by NOAA Global Monitoring Laboratory, Boulder, Colorado, USA (<https://esrl.noaa.gov/>).^[2]..... 3
- Figure I-2. Global annual mean surface air temperature change since the year 1880 to present; solid black line: global annual mean; solid red line: five-year lowess smooth; gray shading: total annual uncertainty at 95% confidence interval; graph reproduced from GISTEMP Team, 2021: *GISS Surface Temperature Analysis (GISTEMP), version 4*. NASA Goddard Institute for Space Studies. Dataset accessed 2021-05-31 at <https://data.giss.nasa.gov/gistemp/>.^[6-7]..... 4
- Figure I-3. (a) Net public electricity generation in Germany in 2020, reproduced from Energy-Charts: <https://energy-charts.info/index.html?l=de&c=DE>, last accessed 2021-05-31;^[12] (b) Electricity generation by fuel type in Canada in 2018, reproduced from CER – Canada’s Energy Future 2019: Energy Supply and Demand Projections to 2040.^[13]..... 5
- Figure I-4. Volumetric and gravimetric energy density of different fuels and batteries; reproduced with permission from Proceedings of the Combustion Institute, 37, 109-133, Copyright 2019 Elsevier.^[18]..... 7
- Figure I-5. Z-scheme for photosynthesis in plants and cyanobacteria with oxygen-evolving center (OEC), photosystem I (PSI) and photosystem II (PSII). 9
- Figure I-6. Schematic overview of a dye sensitized solar cell or Grätzel cell. 13
- Figure I-7. Schematic representation of artificial photosynthesis with photosensitizer (PS), water oxidation catalyst (WOC), sacrificial electron donor (SED), hydrogen evolution catalyst (HEC), and sacrificial electron acceptor (SEA). 14
- Figure I-8. (a) Qualitative molecular orbital diagram for Ru(II) polypyridine complexes in octahedral symmetry showing the electronic transitions occurring in the UV-vis region: ligand centered (LC), metal centered (MC), metal-to-ligand

-
- charge transfer (MLCT); (b) detailed molecular orbital diagram of the MLCT transition in D_3 symmetry. 16
- Figure I-9. Simplified Jablonski diagram illustrating the electronic states of Ru(II) polypyridyl complexes and the possible transitions^[52]; hv: photon radiation; A: absorption of photon; F: fluorescence; P: phosphorescence; NR: non-radiative decay; S: singlet state; T: triplet state; MLCT: metal-to-ligand charge transfer; MC: metal-centered; IC: internal conversion; ISC: inter-system crossing; k_r : radiative decay constant; k_{nr} : non-radiative decay constant. 17
 - Figure I-10. Energy transfer scheme *via* the Förster resonance energy transfer (FRET) mechanism and the Dexter energy transfer mechanism. 18
 - Figure I-11. Representation of the important values during an outer-sphere electron transfer; parabolas characteristic for harmonic oscillators represent the Gibbs energy surfaces of the complexes DA and D^+A^- ; q_0^R = displacement of reactant, q_0^P = displacement of product, q^* = displacement of parabola intersection, $\Delta^\ddagger G$ = Gibbs activation energy, $\Delta_r G^\ominus$ = Gibbs standard reaction energy, Λ = reorganization energy. 19
 - Figure I-12. Scheme for photoinduced electron transfer (ET) following a photoinduced reduction or oxidation pathway. 21
 - Figure I-13. Latimer diagram of $[\text{Ru}(\text{bpy})_3]^{2+}$ 22
 - Figure I-14. Schematic representation of the photosensitized electron transfer reaction following different pathways, D_e = electron donor, A_e = electron acceptor, PS = photosensitizer. 23
 - Figure I-15. Different catalytic reaction mechanisms for catalytic hydrogen evolution using cobalt catalysts suggested in the literature; E = electron transfer step, C = protonation step. 28
 - Figure I-16. Qualitative electronic state diagrams presenting the excitation with light in the visible region and the relevant processes influencing the emission properties of a) $[\text{Ru}(\text{bpy})_3]^{2+}$ and b) $[\text{Ru}(\text{tpy})_2]^{2+}$; GS = ground state, MLCT = metal-to-ligand charge transfer, MC = metal-centered, ISC = inter-system crossing, IC = internal conversion, k_r = radiative decay rate, k_{nr} = non-radiative decay rate; upon excitation with light, the Ru(II) polypyridine complexes are excited into the $^1\text{MLCT}$ state, followed by fast ISC to the $^3\text{MLCT}$ state, which
-

-
- either radiatively decays *via* phosphorescence or undergoes IC to the ^3MC state, followed by non-radiative decay. 30
- Figure I-17. Structures of complexes **S01** to **S12** bearing electron-donating and/or electron-withdrawing substituents. 33
 - Figure I-18. Photoisomerization of the trans-trans complex **S08** to its cis-trans form upon irradiation with UV light.^[157] 35
 - Figure I-19. Structures of complexes **N01** to **N07** involving different nitrogen containing heterocycles. 37
 - Figure I-20. Structures of complexes **B01** to **B08** with ligands with expanded bite-angles. 40
 - Figure I-21. Structures of homoleptic and heteroleptic complexes **H01** to **H06**. 42
 - Figure I-22. Structures of terpyridine complexes incorporating an organic chromophore **C01** to **C04**. 45
 - Figure I-23. Structures of polynuclear terpyridine complexes incorporating only ruthenium metal centers **P01** to **P05**. 48
 - Figure I-24. Structures of polynuclear terpyridine complexes incorporating different metal ions **P06** to **P16**. 53
 - Figure III-1. Ellipsoid representation of complexes **III-C1** (left) and **III-C2** (right) at 50% probability. Hydrogen atoms, PF_6^- counter ions and co-crystallized solvent molecules are omitted for clarity. 63
 - Figure III-2. UV-vis absorption (solid lines) and emission spectra (dashed lines) of complexes **III-C1** (blue) and **III-C2** (red); spectra measured in acetonitrile; emission experiments are conducted under inert gas atmosphere at 20 °C and emission spectra are rescaled so that the intensity at $\lambda_{\text{max em}}$ is 1. 64
 - Figure III-3. Cyclic voltammograms of complexes **III-C1** (1.0 mM, blue) and **III-C2** (1.0 mM, red) in dry acetonitrile under inert gas atmosphere, with 0.1 M TBAPF_6 ; scan rate 100 mV/s; scans start at 0°V vs. reference in anodic direction. 66
 - Figure III-4. UV-vis absorption spectra of **III-C1** (left) and **III-C2** (right) in argon-purged acetonitrile (0.1 M TBAPF_6) at oxidation potentials from +0.0 V to +1.5 V vs. Ag/Ag^+ ; arrows indicate change of absorption bands upon oxidation. 68
-

-
- Figure III-5. UV-vis absorption spectra of **III-C1** (left) and **III-C2** (right) in argon-purged acetonitrile (0.1 M TBAPF₆) at reduction potentials from +0.0 V to -2.0 V vs. Ag/Ag⁺; arrows indicate change of absorption bands upon reduction. 69
 - Figure III-6. Hydrogen photoproduction with complex **III-C1** as PS (0.1 mM) under blue light irradiation (LED centered at 445 nm); with TEOA as sacrificial electron donor (1 M) and HBF₄ as proton source (0.1 M), [Co(dmgh)(dmgh₂)Cl₂] as catalyst (1 mM), with dmgh₂ (6 mM) in DMF; TOF: solid line; TON: dashed line; adapted from *Inorganic Chemistry*, **2019**, *58*, 9127-9134. Reproduced with permission of American Chemical Society.^[162]..... 72
 - Figure III-7. Hydrogen photoproduction with complex [Ru(bpy)₃]²⁺ as PS (0.1 mM) under blue light irradiation (LED centered at 445 nm); with TEOA as sacrificial electron donor (1 M) and HBF₄ as proton source (0.1 M), [Co(dmgh)(dmgh₂)Cl₂] as catalyst (1 mM), with dmgh₂ (6 mM) in DMF; addition of same amount of [Ru(bpy)₃]²⁺ in 0.25 mL DMF after 9 hours (highlighted by red arrow); adapted from *Inorganic Chemistry*, **2019**, *58*, 9127-9134. Reproduced with permission of American Chemical Society.^[162]..... 73
 - Figure III-8. Hydrogen photoproduction with complex **III-C1** as PS (0.1 mM) under blue light irradiation (LED centered at 445 nm); with TEOA as sacrificial electron donor (1 M) and HBF₄ as proton source (0.1 M) in DMF; different catalysts are used: [Co(dmgh)(dmgh₂)Cl₂] (1 mM) with dmgh₂ (6 mM) (blue, dashed/dotted line), K₂PtCl₄ (50 μM) as pre-catalyst to form *in-situ* colloidal Pt (black, dotted line), [Co(H₂O)₆](BF₄)₂ as pre-catalyst (1 mM), with dmgh₂ (6 mM) (green, solid line), [Co(dmgh)(dmgh₂)Cl₂] (0.5 mM) with dmgh₂ (3 mM) (red, dashed line); adapted from *Inorganic Chemistry*, **2019**, *58*, 9127-9134. Reproduced with permission of American Chemical Society.^[162]..... 74
 - Figure IV-1. Ellipsoid representation of complex **IV-C2** at 50% probability. Hydrogen atoms, PF₆⁻ counter ions and co-crystallized solvent molecules are omitted for clarity..... 87
 - Figure IV-2. UV-vis absorption (solid lines) and emission spectra (dashed lines) of complexes **IV-C1** (red) and **IV-C2** (green) alongside complex **III-C1** (blue); spectra recorded in acetonitrile; emission experiments are conducted under
-

-
- inert gas atmosphere at 20 °C and emission spectra are rescaled so that the intensity at $\lambda_{\text{max em}}$ is 1..... 88
- Figure IV-3. Cyclic voltammograms of complexes **IV-C1** (0.5 mM, red) and **IV-C2** (0.5 mM, green) alongside complex **III-C1** (0.5 mM, blue) in dry acetonitrile under inert gas atmosphere, with 0.1 M TBAPF₆; scan rate 100 mV/s; scans start at 0°V vs. reference in cathodic direction..... 90
 - Figure IV-4. Hydrogen photoproduction with complexes **III-C1** and **IV-C2** as PS (0.1 mM) under blue light irradiation (LED centered at 445 nm); with TEOA as sacrificial electron donor (1 M) and HBF₄ as proton source (0.1 M) in DMF; left: [Co(H₂O)₆](BF₄)₂ as pre-catalyst (1 mM), with dmgH₂ (6 mM); right: K₂(PtCl₄) as pre-catalyst to form *in-situ* colloidal Pt (0.05 mM); TOF: solid lines; TON: dashed lines; adapted from *Electrochemical and photophysical study of homoleptic and heteroleptic methylated ruthenium(II) bis-terpyridine complexes*, Mira T. Rupp, Thomas Auvray, Garry S. Hanan, Dirk G. Kurth, *European Journal of Inorganic Chemistry* **2021**, 2021 (28), 2822-2829. Reproduced with permission of Wiley-VCH.^[169]..... 94
 - Figure IV-5. UV-vis absorption spectra of DMF solutions containing **IV-C2** (0.1 mM); TEOA (1 M) and HBF₄ (0.1 M) before light irradiation (solid line) alongside reaction mixtures additionally containing (a) [Co(H₂O)₆](BF₄)₂ (1 mM) and dmgH₂ (6 mM) (dashed line) or (b) K₂PtCl₄ (dotted line) after blue light irradiation (LED centered at 445 nm); absorptions are normalized to the MLCT absorption peak; adapted from *Electrochemical and photophysical study of homoleptic and heteroleptic methylated ruthenium(II) bis-terpyridine complexes*, Mira T. Rupp, Thomas Auvray, Garry S. Hanan, Dirk G. Kurth, *European Journal of Inorganic Chemistry* **2021**, 2021 (28), 2822-2829. Reproduced with permission of Wiley-VCH.^[169]..... 96
 - Figure V-1. Ellipsoid representation of complex **V-C1** at 50% probability. Hydrogen atoms, PF₆⁻ counterions and co-crystallized solvent molecules are omitted for clarity..... 103
 - Figure V-2. UV-vis absorption (solid lines) and emission spectra (dashed lines) of methylated complexes **V-C1** (green) and **V-C2** (orange) alongside non-methylated complexes **III-C1** (blue) and **IV-C2** (red); spectra recorded in
-

-
- acetonitrile; adapted from *Electrochemical and photophysical study of homoleptic and heteroleptic methylated ruthenium(II) bis-terpyridine complexes*, Mira T. Rupp, Thomas Auvray, Garry S. Hanan, Dirk G. Kurth, *European Journal of Inorganic Chemistry* **2021**, 2021 (28), 2822-2829. Reproduced with permission of Wiley-VCH.^[169] 104
- Figure V-3. Cyclic voltammograms of complexes **V-C1** (0.5 mM, green) and **V-C2** (0.5 mM, orange) alongside complexes **III-C1** (0.5 mM, blue) and **IV-C2** (0.5 mM, red) in dry acetonitrile under inert gas atmosphere, with 0.1 M TBAPF₆; scan rate 100 mV/s; scans start at 0°V vs. reference in cathodic direction. 106
 - Figure V-4. Square wave voltammetry of complex **V-C1** (left) and **V-C2** (right) in dry acetonitrile under inert gas atmosphere, with 0.1 M TBAPF₆; scan rate 100 mV/s; scans start at 0 V vs. reference electrode; adapted from *Electrochemical and photophysical study of homoleptic and heteroleptic methylated ruthenium(II) bis-terpyridine complexes*, Mira T. Rupp, Thomas Auvray, Garry S. Hanan, Dirk G. Kurth, *European Journal of Inorganic Chemistry* **2021**, 2021 (28), 2822-2829. Reproduced with permission of Wiley-VCH.^[169] 107
 - Figure V-5. Energy diagram of the calculated frontier orbitals of the methylated complexes **V-C1** and **V-C2** alongside the non-methylated complexes **III-C1** and **IV-C2** with energy gaps highlighted (degeneracy threshold of 15 meV); adapted from *Electrochemical and photophysical study of homoleptic and heteroleptic methylated ruthenium(II) bis-terpyridine complexes*, Mira T. Rupp, Thomas Auvray, Garry S. Hanan, Dirk G. Kurth, *European Journal of Inorganic Chemistry* **2021**, 2021 (28), 2822-2829. Reproduced with permission of Wiley-VCH.^[169] 109
 - Figure V-6. Hydrogen photoproduction with complexes **III-C1**, **IV-C2** and **V-C1** as PS (0.1 mM) under blue light irradiation (LED centered at 445 nm); with [Co(H₂O)₆](BF₄)₂ as pre-catalyst (1 mM), with dmgH₂ (6 mM), TEOA as sacrificial electron donor (1 M) and HBF₄ as proton source (0.1 M) in DMF; TOF: solid lines; TON: dashed lines; adapted from *Electrochemical and photophysical study of homoleptic and heteroleptic methylated ruthenium(II) bis-terpyridine*
-

-
- complexes*, Mira T. Rupp, Thomas Auvray, Garry S. Hanan, Dirk G. Kurth, *European Journal of Inorganic Chemistry* **2021**, 2021 (28), 2822-2829. Reproduced with permission of Wiley-VCH.^[169] 112
- Figure V-7. Hydrogen photoproduction of complexes **III-C1**, **IV-C2** and **V-C1** (0.1 mM) under blue light irradiation (LED centered at 445 nm); using $K_2(PtCl_4)$ as pre-catalyst to form *in-situ* colloidal Pt (0.05 mM), TEOA as sacrificial electron donor (1 M) and HBF_4 as proton source (0.1 M) in DMF; TOF: solid lines; TON: dashed lines; adapted from *Electrochemical and photophysical study of homoleptic and heteroleptic methylated ruthenium(II) bis-terpyridine complexes*, Mira T. Rupp, Thomas Auvray, Garry S. Hanan, Dirk G. Kurth, *European Journal of Inorganic Chemistry* **2021**, 2021 (28), 2822-2829. Reproduced with permission of Wiley-VCH.^[169] 113
 - Figure V-8. UV-vis absorption spectra of DMF solutions containing **V-C1** (0.1 mM); TEOA (1 M) and HBF_4 (0.1 M) before light irradiation (green solid line) alongside reaction mixture additionally containing (a) $[Co(H_2O)_6](BF_4)_2$ (1 mM) and $dmgH_2$ (6 mM) (dashed line) or (b) K_2PtCl_4 (dotted line) after blue light irradiation (LED centered at 445 nm); the absorption spectrum of **III-C1** (blue line) is given for comparison; absorptions are normalized to the MLCT absorption peak; adapted from *Electrochemical and photophysical study of homoleptic and heteroleptic methylated ruthenium(II) bis-terpyridine complexes*, Mira T. Rupp, Thomas Auvray, Garry S. Hanan, Dirk G. Kurth, *European Journal of Inorganic Chemistry* **2021**, 2021 (28), 2822-2829. Reproduced with permission of Wiley-VCH.^[169] 114
 - Figure V-9. UV-vis absorption spectra of DMF solutions containing **V-C2** (0.1 mM); TEOA (1 M) and HBF_4 (0.1 M) before light irradiation (orange solid line) alongside reaction mixture additionally containing (a) $[Co(H_2O)_6](BF_4)_2$ (1 mM) and $dmgH_2$ (6 mM) (dashed line) or (b) K_2PtCl_4 (dash-dotted line) after blue light irradiation (LED centered at 445 nm); the absorption spectrum of **IV-C2** (red line) is given for comparison; absorptions are normalized to the MLCT absorption peak; adapted from *Electrochemical and photophysical study of homoleptic and heteroleptic methylated ruthenium(II) bis-terpyridine complexes*, Mira T. Rupp, Thomas Auvray, Garry S. Hanan, Dirk G. Kurth,
-

-
- European Journal of Inorganic Chemistry* **2021**, 2021 (28), 2822-2829. Reproduced with permission of Wiley-VCH.^[169] 115
- Figure VI-1. Ellipsoid representation of complexes **VI-C1** (top) and **VI-C4** (bottom) at 50% probability. Hydrogen atoms, PF₆⁻ counter ions and co-crystallized solvent molecules are omitted for clarity; adapted from *Inorganic Chemistry*, **2021**, 60, 292-302. Reproduced with permission of American Chemical Society.^[168] 124
 - Figure VI-2. UV-vis absorption (solid lines) and emission spectra (dashed lines) of complexes **VI-C1** to **VI-C2** alongside complex **III-C1**; spectra measured in acetonitrile; emission experiments are conducted under inert gas atmosphere at 20 °C and emission spectra are rescaled so that the intensity at $\lambda_{\text{max em}}$ is 1. 125
 - Figure VI-3. Cyclic voltammograms of complexes **VI-C1** (1 mM, blue), **VI-C2** (1 mM, red), **VI-C3** (0.5 mM, green) and **VI-C4** (0.5 mM, orange) alongside complex **III-C1** (0.5 mM, black) in dry acetonitrile under inert gas atmosphere, with 0.1 M TBAPF₆; scan rate 100 mV/s; scans start at 0 V vs. reference in anodic or cathodic direction as indicated by arrows..... 128
 - Figure VI-4. Energy diagram of the calculated frontier orbitals of complexes **VI-C1** to **VI-C4** with energy gaps highlighted (degeneracy threshold of 15 meV) ; adapted from *Inorganic Chemistry*, **2021**, 60, 292-302. Reproduced with permission of American Chemical Society.^[168]..... 130
 - Figure VI-5. Natural transition analysis of the lowest singlet (left) to triplet (right) transition for complex **VI-C1**; adapted from *Inorganic Chemistry*, **2021**, 60, 292-302. Reproduced with permission of American Chemical Society.^[168]..... 132
 - Figure VI-6. Hydrogen photoproduction with complexes **IV-C1** to **IV-C4** as PS (0.1 mM) under blue light irradiation (LED centered at 445 nm); with [Co(H₂O)₆](BF₄)₂ as pre-catalyst (1 mM), with dmgH₂ (6 mM), TEOA as sacrificial electron donor (1 M) and HBF₄ as proton source (0.1 M) in DMF; TOF: solid lines; TON: dashed lines; adapted from *Inorganic Chemistry*, **2021**, 60, 292-302. Reproduced with permission of American Chemical Society.^[168].. 134
 - Figure VI-7. Hydrogen photoproduction with complexes **IV-C1** to **IV-C4** as PS (0.1 mM) under red light irradiation (LED centered at 630 nm); with
-

-
- [Co(H₂O)₆](BF₄)₂ as pre-catalyst (1 mM), with dmgH₂ (6 mM), TEOA as sacrificial electron donor (1 M) and HBF₄ as proton source (0.1 M) in DMF; TOF: solid lines; TON: dashed lines; adapted from *Inorganic Chemistry*, **2021**, *60*, 292-302. Reproduced with permission of American Chemical Society.^[168]. 136
- Figure VI-8. Hydrogen photoproduction with complex **VI-C1** as PS (0.1 mM) under blue light irradiation (LED centered at 445 nm); with TEOA as sacrificial electron donor (1 M) and HBF₄ as proton source (0.1 M), Co(H₂O)₆](BF₄)₂ (1 mM), with dmgH₂ (6 mM) in DMF; left: addition of same amount of **VI-C1** in 0.25 mL DMF after 22 hours (highlighted by red arrow); right: addition of same amount of [Co(H₂O)₆](BF₄)₂ and dmgH₂ in 0.25 ml DMF after 22 hours (highlighted by red arrow); adapted from *Inorganic Chemistry*, **2021**, *60*, 292-302. Reproduced with permission of American Chemical Society.^[168]..... 137
 - Figure VI-9. Hydrogen photoproduction with complex **IV-C1** as PS (0.1 mM) under blue light irradiation (LED centered at 445 nm); with TEOA as sacrificial electron donor (1 M) and HBF₄ as proton source (0.1 M) and different catalysts in DMF; blue: [Co(H₂O)₆](BF₄)₂ as pre-catalyst (1 mM), with dmgH₂ (6 mM); pink: [Co(dmgBF₂)₂(H₂O)] (1 mM), with dmgH₂ (6 mM); K₂(PtCl₄) as pre-catalyst to form *in-situ* colloidal Pt (0.05 mM); TOF: solid lines; TON: dashed lines. 138
 - Figure VI-10. UV-vis absorption spectra of DMF solutions containing **VI-C1** (0.1 mM); TEOA (1 M) and HBF₄ (0.1 M) before light irradiation (solid line) alongside reaction mixtures additionally containing (a) [Co(H₂O)₆](BF₄)₂ (1 mM) and dmgH₂ (6 mM) (dashed line) or (b) K₂PtCl₄ (dotted line) after blue light irradiation (LED centered at 445 nm); absorptions are normalized to the MLCT absorption peak. 139
 - Figure VII-1. Optimized geometries of **VII-C1** (left) and **VII-C2** (right) with torsion angles between the pyrimidine rings and the phenyl spacer..... 153
 - Figure VII-2. UV-vis absorption (solid lines) and emission spectra (dashed lines) of dinuclear complexes **VII-C1** (blue) and **VII-C2** (red), alongside the mononuclear complexes **VI-C1** (green) and **VIC-2** (orange); spectra measured in acetonitrile..... 154
 - Figure VII-3. UV-vis absorption (solid lines) and emission spectra (dashed lines) of complex **VII-C1** in different inert gas-purged solvents; emission spectra are
-

-
- normalized with regard to the absorptivity of the sample solution at the excitation wavelength and the refractive index of the solvent. 156
- Figure VII-4. Emission spectra of the dinuclear complexes **VII-C1** and **VII-C2** as well as the mononuclear complexes **VI-C1** and **VI-C2** in inert gas-purged acetonitrile at different temperatures; temperatures vary between +40 °C and -10 °C. 157
 - Figure VII-5. Temperature-dependence of the emission quantum yield of the dinuclear complexes **VII-C1** and **VII-C2** as well as the mononuclear complexes **VI-C1** and **VI-C2** in inert gas-purged acetonitrile. 158
 - Figure VII-6. Plot of $k_{\text{obs}} (1/T)$ vs. $1000/T$ for **VII-C1**. Curve fit according to Equation I-1 of the manuscript. Excited-state lifetimes are measured in nitrogen-purged acetonitrile solutions. 159
 - Figure VII-7. Cyclic voltammograms of complexes **VII-C1** (0.25 mM, blue), **VII-C2** (0.5 mM, red), **VI-C1** (1 mM, green) and **VI-C2** (1 mM, orange) in dry acetonitrile under inert gas atmosphere, with 0.1 M TBAPF₆; scan rate 100 mV/s; current flow is not to scale, altered for clarity; scans start at 0 V vs. reference in anodic direction. 160
 - Figure VII-8. Square wave voltammetry of complex **VII-C1** (left) and **VII-C2** (right) in dry acetonitrile under inert gas atmosphere, with 0.1 M TBAPF₆; scan rate 100 mV/s; scans start at 0 V vs. reference electrode. 161
 - Figure VII-9. Energy diagram of the calculated frontier orbitals of dinuclear complexes **VII-C1** and **VII-C2** alongside the mononuclear analogues **VI-C1** and **VI-C2** with energy gaps highlighted (degeneracy threshold of 15 meV). 163
 - Figure VII-10. Hydrogen photoproduction with dinuclear complexes **VII-C1**, **VII-C2**, **VI-C1** and **VI-C2** as PS (0.1 mM) under blue light irradiation (LED centered at 445 nm); with [Co(H₂O)₆](BF₄)₂ as pre-catalyst (1 mM), with dmgH₂ (6 mM), TEOA as sacrificial electron donor (1 M) and HBF₄ as proton source (0.1 M) in DMF; TOF: solid lines; TON: dashed lines. 165
 - Figure VII-11. Hydrogen photoproduction with dinuclear complexes **VII-C1**, **VII-C2**, **VI-C1** and **VI-C2** as PS (0.1 mM) under red light irradiation (LED centered at 630 nm); with [Co(H₂O)₆](BF₄)₂ as pre-catalyst (1 mM), with dmgH₂ (6 mM),
-

-
- TEOA as sacrificial electron donor (1 M) and HBF₄ as proton source (0.1 M) in DMF; TOF: solid lines; TON: dashed lines..... 166
- Figure VII-12. UV-vis absorption spectra of DMF solutions containing **VII-C1**, **VII-C2** or **VI-C1** (0.1 mM); [Co(H₂O)₆](BF₄)₂ (1 mM), dmgH₂ (6 mM), TEOA (1 M) and HBF₄ (0.1 M) before (upper graph) and after (lower graph) 23 h under blue light irradiation (LED centered at 445 nm); absorptions are normalized to the MLCT absorption peak..... 167
 - Figure VII-13. UV-vis absorption spectra of DMF solutions containing **VII-C1** (0.1 mM) (a) after 18 h blue light irradiation (LED centered at 445 nm) (dark red dashed line) alongside spectra of reaction mixtures additionally containing (b) TEOA (1 M) and HBF₄ (0.1 M) before light irradiation (dark blue solid line); (c) TEOA (1 M) and HBF₄ (0.1 M) after light irradiation (light blue solid line); (d) [Co(H₂O)₆](BF₄)₂ (1 mM), dmgH₂ (6 mM), TEOA (1 M) and HBF₄ (0.1 M) after light irradiation (orange dashed line); absorptions are normalized to the MLCT absorption peak. 168
 - Figure VII-14. Hydrogen photoproduction with dinuclear complexes **VII-C1** and **VII-C2** as PS (0.1 mM) under blue light irradiation (LED centered at 445 nm); using [Co(dmgH)₂(py)Cl] as catalyst (1 mM), dmgH₂ (6 mM), TEOA as sacrificial electron donor (1 M) and HBF₄ as proton source (0.1 M) in DMF; TOF: solid lines; TON: dashed lines..... 169
 - Figure VII-15. Maximum hydrogen production rate of dinuclear complex **VII-C1** (blue) in comparison with [Ru(bpy)₃]²⁺ (black) for different concentrations of PS in a DMF solution with [Co(H₂O)₆](BF₄)₂ as pre-catalyst (1 mM), dmgH₂ (6 mM), TEOA as sacrificial electron donor (1 M) and HBF₄ as proton source (0.1 M) under blue light irradiation (LED centered at 445 nm)..... 170
 - Figure IX-1. ¹H-NMR spectrum (400 MHz, CDCl₃) of **III-I1**..... 185
 - Figure IX-2. ¹H-NMR spectrum (300 MHz, CDCl₃) of **III-I2**..... 186
 - Figure IX-3. ¹³C-NMR spectrum (75 MHz, CDCl₃) of **III-I2**. 186
 - Figure IX-4. ¹H-NMR spectrum (400 MHz, CDCl₃) of **III-L1**. 187
 - Figure IX-5. ¹³C-NMR spectrum (101 MHz, CDCl₃) of **III-L1**..... 187
 - Figure IX-6. ¹H-NMR spectrum (300 MHz, CDCl₃) of **III-L2**. 188
 - Figure IX-7. ¹³C-NMR spectrum (75 MHz, CDCl₃) of **III-L2**..... 188
-

• Figure IX-8. ^1H -NMR spectrum (300 MHz, CDCl_3) of III-L3	189
• Figure IX-9. ^1H -NMR spectrum (600 MHz, CD_3CN) of III-C1	189
• Figure IX-10. ^{13}C -NMR spectrum (150 MHz, CD_3CN) of III-C1	190
• Figure IX-11. ^1H -NMR spectrum (300 MHz, CD_3CN) of III-C2	190
• Figure IX-12. ^{13}C -NMR spectrum (75 MHz, CD_3CN) of III-C2	191
• Figure IX-13. ^1H -NMR spectrum (300 MHz, CD_3CN) of IV-C1	191
• Figure IX-14. ^{13}C -NMR spectrum (75 MHz, CD_3CN) of IV-C1	192
• Figure IX-15. ^1H -NMR spectrum (400 MHz, CD_3CN) of IV-C2	192
• Figure IX-16. ^{13}C -NMR spectrum (125 MHz, CD_3CN) of IV-C2	193
• Figure IX-17. ^1H -NMR spectrum (300 MHz, CD_3CN) of V-C1	193
• Figure IX-18. ^{13}C -NMR spectrum (75 MHz, CD_3CN) of V-C1	194
• Figure IX-19. ^1H -NMR spectrum (500 MHz, CD_3CN) of V-C2	194
• Figure IX-20. ^{13}C -NMR spectrum (125 MHz, CD_3CN) of V-C2	195
• Figure IX-21. ^1H -NMR spectrum (300 MHz, CDCl_3) of VI-I1	195
• Figure IX-22. ^1H -NMR spectrum (400 MHz, CDCl_3) of VI-I2	196
• Figure IX-23. ^{13}C -NMR spectrum (100 MHz, CDCl_3) of VI-I2	196
• Figure IX-24. ^1H -NMR spectrum (300 MHz, DMSO-d_6) of VI-I3	197
• Figure IX-25. ^1H -NMR spectrum (300 MHz, CDCl_3) of VI-I4	197
• Figure IX-26. ^1H -NMR spectrum (300 MHz, DMSO-d_6) of VI-I5	198
• Figure IX-27. ^1H -NMR spectrum (300 MHz, DMSO-d_6) of VI-I6	198
• Figure IX-28. ^{13}C -NMR spectrum (75 MHz, DMSO-d_6) of VI-I6	199
• Figure IX-29. ^1H -NMR spectrum (500 MHz, CDCl_3) of VI-L1	199
• Figure IX-30. ^{13}C -NMR spectrum (125 MHz, CDCl_3) of VI-L1	200
• Figure IX-31. ^1H -NMR spectrum (500 MHz, CDCl_3) of VI-L2	200
• Figure IX-32. ^{13}C -NMR spectrum (125 MHz, CDCl_3) of VI-L2	201
• Figure IX-33. ^1H -NMR spectrum (300 MHz, CDCl_3) of VI-L3	201
• Figure IX-34. ^{13}C -NMR spectrum (100 MHz, CDCl_3) of VI-L3	202
• Figure IX-35. ^1H -NMR spectrum (500 MHz, CDCl_3) of VI-L4	202
• Figure IX-36. ^{13}C -NMR spectrum (125 MHz, CDCl_3) of VI-L4	203
• Figure IX-37. ^1H -NMR spectrum (500 MHz, CD_3CN) of VI-C1	203
• Figure IX-38. ^{13}C -NMR spectrum (125 MHz, CD_3CN) of VI-C1	204
• Figure IX-39. ^1H -NMR spectrum (700 MHz, CD_3CN) of VI-C2	204

-
- Figure IX-40. ^{13}C -NMR spectrum (176 MHz, CD_3CN) of **VI-C2**. 205
 - Figure IX-41. ^1H -NMR spectrum (500 MHz, CD_3CN) of **VI-C3**. 205
 - Figure IX-42. ^{13}C -NMR spectrum (125 MHz, CD_3CN) of **VI-C3**. 206
 - Figure IX-43. ^1H -NMR spectrum (400 MHz, CD_3CN) of **VI-C4**. 206
 - Figure IX-44. ^{13}C -NMR spectrum (100 MHz, CD_3CN) of **VI-C4**. 207
 - Figure IX-45. ^1H -NMR spectrum (400 MHz, CDCl_3) of **VII-I1**. 207
 - Figure IX-46. ^1H -NMR spectrum (300 MHz, CDCl_3) of **VII-I2**. 208
 - Figure IX-47. ^1H -NMR spectrum (300 MHz, CDCl_3) of **VII-L1**. 208
 - Figure IX-48. ^{13}C -NMR spectrum (75 MHz, CDCl_3) of **VII-L1**. 209
 - Figure IX-49. ^1H -NMR spectrum (300 MHz, CDCl_3) of **VII-L2**. 209
 - Figure IX-50. ^{13}C -NMR spectrum (75 MHz, CDCl_3) of **VII-L2**. 210
 - Figure IX-51. ^1H -NMR spectrum (700 MHz, CD_3CN) of **VII-C1**. 210
 - Figure IX-52. ^{13}C -NMR spectrum (176 MHz, CD_3CN) of **VII-C1**. 211
 - Figure IX-53. ^1H -NMR spectrum (400 MHz, CD_3CN) of **VII-C2**. 211
 - Figure IX-54. ^{13}C -NMR spectrum (100 MHz, CD_3CN) of **VII-C2**. 212
 - Figure IX-55. Natural transition analysis of the lowest singlet (left of arrow) to triplet (right of arrow) transition for complex **III-C1**; contributions of left transition 90%, contributions of right transition 6%. 225
 - Figure IX-56. Natural transition analysis of the lowest singlet (left of arrow) to triplet (right of arrow) transition for complex **IV-C2**; contributions of left transition 48%, contributions of right transition 47%. 226
 - Figure IX-57. Natural transition analysis of the lowest singlet (left of arrow) to triplet (right of arrow) transition for complex **V-C1**. 226
 - Figure IX-58. Natural transition analysis of the lowest singlet (left of arrow) to triplet (right of arrow) transition for complex **V-C2**; contributions of left transition 48%, contributions of right transition 48%. 226
 - Figure IX-59. Natural transition analysis of the lowest singlet (left of arrow) to triplet (right of arrow) transition for complex **VI-C2**. 227
 - Figure IX-60. Natural transition analysis of the lowest singlet (left of arrow) to triplet (right of arrow) transition for complex **VI-C3**. 227
 - Figure IX-61. Natural transition analysis of the lowest singlet (left of arrow) to triplet (right of arrow) transition for complex **VI-C4**. 227
-

-
- Figure IX-62. Natural transition analysis of the lowest singlet (left of arrow) to triplet (right of arrow) transition for complex **VII-C1**; contributions of left transition 76%, contributions of right transition 20%..... 228
 - Figure IX-63. Natural transition analysis of the lowest singlet (left of arrow) to triplet (right of arrow) transition for complex **VII-C2**; contributions of left transition 77%, contributions of right transition 20%..... 228

List of Charts

- Chart I-1. Chemical structures of ATP, NADP⁺ and chlorophyll *a*. 8
- Chart I-2. Chemical structures of the active sites of different types of hydrogenase enzymes..... 11
- Chart III-1. Structures of the heteroleptic Ru(II) complexes **III-C1** and **III-C2** discussed in this chapter; the PF₆⁻ counterions are omitted for clarity. 60
- Chart IV-1. Structures of the homoleptic Ru(II) complexes **IV-C1** and **IV-C2** discussed in this chapter alongside **III-C1**; the PF₆⁻ counterions are omitted for clarity. 85
- Chart VI-1. Structures of the pyrimidine containing complexes **VI-C1** to **VI-C4**; the PF₆⁻ counterions are omitted for clarity. 122
- Chart VII-1. Structures of dinuclear complexes **VII-C1** and **VII-C2**; the PF₆⁻ counterions are omitted for clarity. 151

List of Schemes

- Scheme III-1. Synthesis of 2-acetylpyridine derivatives **III-I1** and **III-I2**..... 61
- Scheme III-2. Synthesis of terpyridine derivatives **III-L1**, **III-L2** and **III-L3**. 61
- Scheme III-3. Microwave assisted (MW) synthesis of the heteroleptic Ru(II) complexes **III-C1** and **III-C2**. 62
- Scheme III-4. Proposed photocatalytic cycles for different catalysts used: a) heterogeneous catalyst such as colloidal Pt; b) Co(III) catalyst such as [Co(dmgh)(dmgh₂)Cl₂]; c) Co(II) catalyst such as [Co(dmgh)₂(H₂O)₂](BF₄)₂. 75
- Scheme IV-1. Microwave assisted (MW) synthesis of homoleptic complex **IV-C2** starting from **III-L1**..... 86
- Scheme V-1. Synthesis of methylated complexes **V-C1** and **V-C1**..... 102
- Scheme VI-1. Synthesis of the precursors **VI-I1** to **VI-I6** as well as the ligands **VI-L1** to **VI-L4**; adapted from *Inorganic Chemistry*, **2021**, *60*, 292-302. Reproduced with permission of American Chemical Society.^[168]..... 123
- Scheme VII-1. Synthesis of bis-enones **VII-I1** and **VII-I2**, ditopic ligands **VII-L1** and **VII-L2**, and dinuclear complexes **VII-C1** and **VII-C2**. 152

List of Tables

- Table I-1. Electrochemical reaction equations for oxidation of H₂O and H⁺ reduction.^[19] 12
- Table I-2. Photophysical and electrochemical properties of [Ru(tpy)₂]²⁺ based complexes **S01** to **S12** depending on their substituents. 34
- Table I-3. Photophysical and electrochemical properties of [Ru(tpy)₂]²⁺ based complexes **N01** to **N07** with different nitrogen containing heterocycles. 36
- Table I-4. Photophysical and electrochemical properties of [Ru(tpy)₂]²⁺ based complexes **B01** to **B08** with expanded bite-angle ligands..... 39
- Table I-5. Photophysical and electrochemical properties of [Ru(tpy)₂]²⁺ based homoleptic and heteroleptic complexes **H01** to **H06**. 43
- Table I-6. Photophysical and electrochemical properties of [Ru(tpy)₂]²⁺ complexes **C01** to **C04**, incorporating an organic chromophore. 44
- Table I-7. Photophysical and electrochemical properties of [Ru(tpy)₂]²⁺ based polynuclear complexes **P01** to **P05**, incorporating only ruthenium metal centers. 49
- Table I-8. Photophysical and electrochemical properties of [Ru(tpy)₂]²⁺ based polynuclear complexes **P06** to **P16**, incorporating different metal ions. 52
- Table III-1. UV-vis absorption and emission data of complexes **III-C1** and **III-C2** (spectra are measured in acetonitrile at 20 °C).^a 65
- Table III-2. Electrochemical half-wave redox potentials E_{1/2} in V vs. Fc/Fc⁺ (ΔE_p / mV) for complexes **III-C1** and **III-C2** in nitrogen-purged acetonitrile.^a 67
- Table III-3. Contributions to molecular orbitals for complexes **III-C1** and **III-C2**. 70
- Table III-4. Excited-state redox potentials and estimated free Gibbs energy ΔG⁰_{ET} for photoinduced electron transfer from TEOA to the excited complexes **III-C1** and **III-C2**. 71
- Table III-5. Hydrogen production results of complexes discussed in this chapter.^a..... 76
- Table IV-1. UV-vis absorption and emission data of complexes **IV-C1** and **IV-C2** alongside complex **III-C1** (spectra measured in acetonitrile at 20 °C).^a.... 89

-
- Table IV-2. Electrochemical half-wave redox potentials $E_{1/2}$ in V vs. Fc/Fc⁺ (ΔE_p / mV) for complexes **IV-C1** and **IV-C2** alongside complex **III-C1** in nitrogen-purged acetonitrile.^a 91
 - Table IV-3. Contributions to molecular orbitals for complexes **III-C1**, **IV-C1** and **IV-C2**..... 92
 - Table IV-4. Excited-state redox potentials and estimated free Gibbs energy ΔG^0_{ET} for photoinduced electron transfer from TEOA to the complexes **III-C1**, **IV-C1** and **IV-C2**..... 93
 - Table V-1. UV-vis absorption and emission data of methylated complexes **V-C1** and **V-C2** alongside non-methylated complexes **III-C1** and **IV-C2** (spectra measured in acetonitrile at 20 °C).^a 105
 - Table V-2. Table III-6. Electrochemical half-wave redox potentials $E_{1/2}$ in V vs. Fc/Fc⁺ (ΔE_p / mV) for methylated complexes **V-C1** and **V-C2** alongside non-methylated complexes **III-C1** and **IV-C2** in nitrogen-purged acetonitrile.^a.... 108
 - Table V-3. Contributions to molecular orbitals for complexes **V-C1** and **V-C2**. 110
 - Table V-4. Excited-state redox potentials and estimated free Gibbs energy ΔG^0_{ET} for photoinduced electron transfer from TEOA to the complexes **III-C1**, **IV-C2**, **V-C1** and **V-C2**. 111
 - Table VI-1. UV-vis absorption and emission data of complexes **VI-C1** to **VI-C4** alongside complex **III-C1** (spectra are measured in acetonitrile at 20 °C).^a. 127
 - Table VI-2. Electrochemical half-wave redox potentials $E_{1/2}$ in V vs. Fc/Fc⁺ (ΔE_p / mV) for complexes **VI-C1** to **VI-C4** alongside complex **III-C1** in nitrogen-purged acetonitrile.^a 129
 - Table VI-3. Contributions to molecular orbitals for complexes **VI-C1** to **VI-C4**; adapted from *Inorganic Chemistry*, **2021**, *60*, 292-302. Reproduced with permission of American Chemical Society.^[168]..... 131
 - Table VI-4. Excited-state redox potentials and estimated free Gibbs energy ΔG^0_{ET} for photoinduced electron transfer from TEOA to the complexes **VI-C1** to **VI-C4** and **III-C1**..... 133
 - Table VI-5. Hydrogen production results of complexes discussed in this chapter.^a..... 140
-

-
- Table VII-1. UV-vis absorption and emission data of dinuclear complexes **VII-C1** and **VII-C2**, alongside the mononuclear complexes **VI-C1** and **VI-C2** (spectra measured in acetonitrile at 20 °C).^a 155
 - Table VII-2. Electrochemical half-wave redox potentials $E_{1/2}$ in V vs. Fc/Fc⁺ (ΔE_p / mV) for dinuclear complexes **VII-C1** and **VII-C2** alongside mononuclear complexes **VI-C1** and **VI-C2** in nitrogen-purged acetonitrile.^a 162
 - Table VII-3. Excited-state redox potentials and estimated free Gibbs energy ΔG^0_{ET} for photoinduced electron transfer from TEOA to the dinuclear complexes **VII-C1** and **VII-C2**, alongside the mononuclear analogues **VI-C1** and **VI-C2**.
..... 164
 - Table VII-4. Hydrogen production results of complexes discussed in this chapter.^a 171
 - Table IX-1. Refinement parameters for complex **III-C1** (CCDC 1872343). ... 214
 - Table IX-2. Refinement parameters for complex **III-C2** (CCDC 2090569). ... 216
 - Table IX-3. Refinement parameters for complex **IV-C2** (CCDC 2034792)... 218
 - Table IX-4. Refinement parameters for complex **V-C1** (CCDC 2034795)... 220
 - Table IX-5. Refinement parameters for complex **VI-C1** (CCDC 1997105)... 222
 - Table IX-6. Refinement parameters for complex **VI-4** (CCDC 1997099). 224
 - Table IX-7. Contributions to molecular orbitals for complexes **VII-C1** and **VII-C2**.
..... 229

I. Introduction

Parts of the presented literature review were previously published under the title “Enhancing the photophysical properties of Ru(II) complexes by specific design of tridentate ligands” in *Coordination Chemistry Reviews*.

Reproduced with permission of Elsevier B.V. from *Coordination Chemistry Reviews* **2021**, 446, 214127.

Contributions:

Mira T. Rupp: Project design, literature research, article writing.

Natali Shevchenko: Literature research, article writing.

Garry S. Hanan: Supervision, project design, revision of the article.

Dirk G. Kurth: Supervision, project design, revision of the article.

I.1. Motivation

The still ongoing Covid-19 pandemic has affected nearly every aspect of everyday life for more than a year by now. With strongly decreased global mobility due to worldwide lockdowns and travel restrictions to limit the spread of the virus the global primary energy demand dropped by almost 4% in 2020.^[1] A drop in demand for coal and oil, particularly due to less demand from the road and aviation transport sector, led to the largest decline in global emissions in human history, i.e., a decrease of 5.8% in CO₂ emissions.^[1] However, this decreased emission is unlikely to have an observable global effect due to the still relatively small decrease and the short time span. In addition, the National Oceanic and Atmospheric Administration (NOAA) Global Monitoring Laboratory estimates that the CO₂ emission from worldwide wildfires in, e.g., Australia, California, Indonesia, Brazil, and Russia, probably counterbalances the reduced emissions due to the pandemic. Hence, the trend of raising CO₂ (Figure I-1 a) is expected to continue despite a decreased energy demand.^[2]

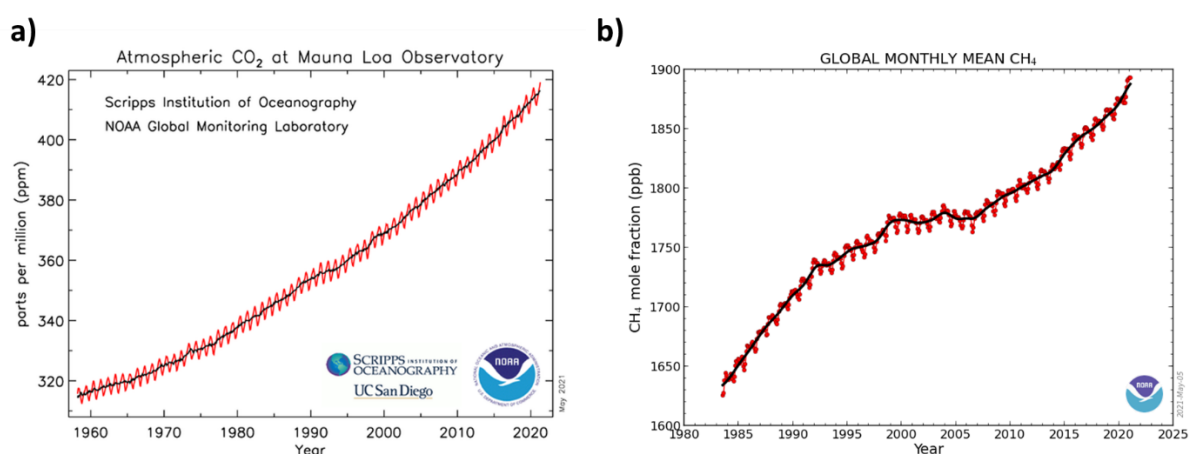


Figure I-1. a) Atmospheric carbon dioxide measured at the Mauna Loa Observatory, Hawaii; b) global atmospheric methane. Images provided by NOAA Global Monitoring Laboratory, Boulder, Colorado, USA (<https://esrl.noaa.gov/>).^[2]

Carbon dioxide, alongside other molecules such as methane, is known to play a key role in global warming. While it only makes up about 0.04% of the earth's atmosphere, its capability to convert infrared radiation into heat leads to the so-called greenhouse effect. The sun emits electromagnetic energy ranging from the ultraviolet (UV) region all the way into the far infrared (IR) region. The solar spectrum is close to a radiating black-body with a peak emission around 500 nm.^[3] When the radiation

reaches the atmosphere, clouds and the surface of the earth reflect approximately 30% of the energy back into space while almost 20% of the energy is absorbed by the atmosphere. Most of the remaining energy is absorbed by the earth's surface, thus heating the surface. As a result, the surface emits IR radiation, which is then absorbed by the IR-active constituent of the atmosphere, the so-called greenhouse gases (water vapor, carbon dioxide, methane, nitrous oxide, and ozone). This naturally occurring process leads to an increased temperature with small fluctuations on the Earth's surface, which makes it inhabitable for microorganisms, plants and animals.^[2] As a comparison, on the moon, which has approximately the same distance to the sun as the earth but lacks a protective atmosphere and hence has no greenhouse effect, during daytime, when sun light hits the surface, temperatures up 130 °C are reached, while after sunset, the temperature decreases to around -170 °C.^[4]

The greenhouse effect is a requirement to life on earth. However, Earth's temperature reacts very sensitive to concentration changes of greenhouse gases in the atmosphere. Thus, a raise of the concentration of greenhouse gases, as seen in Figure I-1 for carbon dioxide and methane, leads to a raise of the global average temperature (Figure I-2).^[5-6]

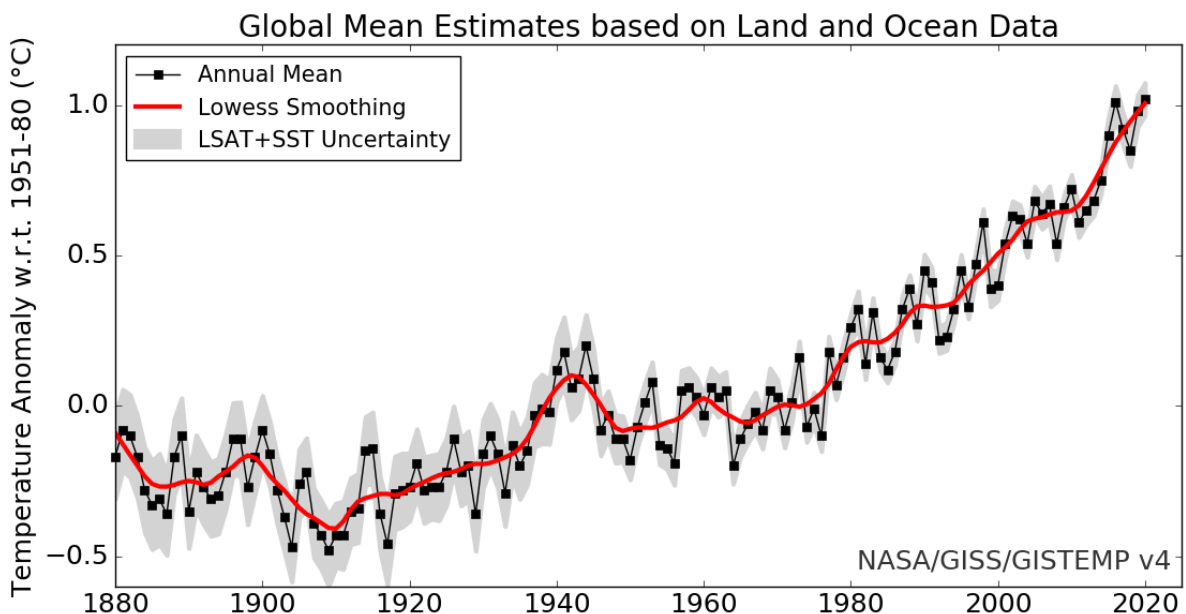


Figure I-2. Global annual mean surface air temperature change since the year 1880 to present; solid black line: global annual mean; solid red line: five-year lowess smooth; gray shading: total annual uncertainty at 95% confidence interval; graph reproduced from GISTEMP Team, 2021: *GISS Surface Temperature Analysis (GISTEMP), version 4*. NASA Goddard Institute for Space Studies. Dataset accessed 2021-05-31 at <https://data.giss.nasa.gov/gistemp/>.^[6-7]

The increase in the global average temperature has widespread effects on the environment such as shrinking glaciers and shifted ecological niches. If the trend of global warming cannot be stopped, scientists predict that sea ice as well as the Greenland ice sheet will be lost, sea levels will rise, and extreme weather phenomena such as heat waves and hurricanes could become more frequent and intense. This change in the global climate is, according to the Intergovernmental Panel on Climate Change, due to human activity. Since the industrial revolution, the burning of fossil fuels such as coal, oil, and natural gas have led to the before-mentioned increase of greenhouse gases, which in return enhance the greenhouse effect.^[8-9]

The International Energy Agency (IEA) estimated the global energy demand in the year 2018 to be more than 14 300 Mtoe (millions of tonnes of oil equivalent), which equals more than 166 PWh.^[10] While the annual energy demand did decrease by almost 6% in 2020 due to the Covid-19 pandemic, it is unlikely that this trend continues in the future, and energy consumption is assumed to increase again.^[1, 11]

Most of the energy is produced by fossil fuels, e.g., coal and gas. In 2020, only half of the electricity (50.9%) in Germany was produced by renewable energies (Figure I-3 (a)). In Canada, on the other hand, more than two thirds of the electricity produced in 2018 came from renewable energy sources, especially hydro and tidal energy (Figure I-3 (b)).^[12-13]

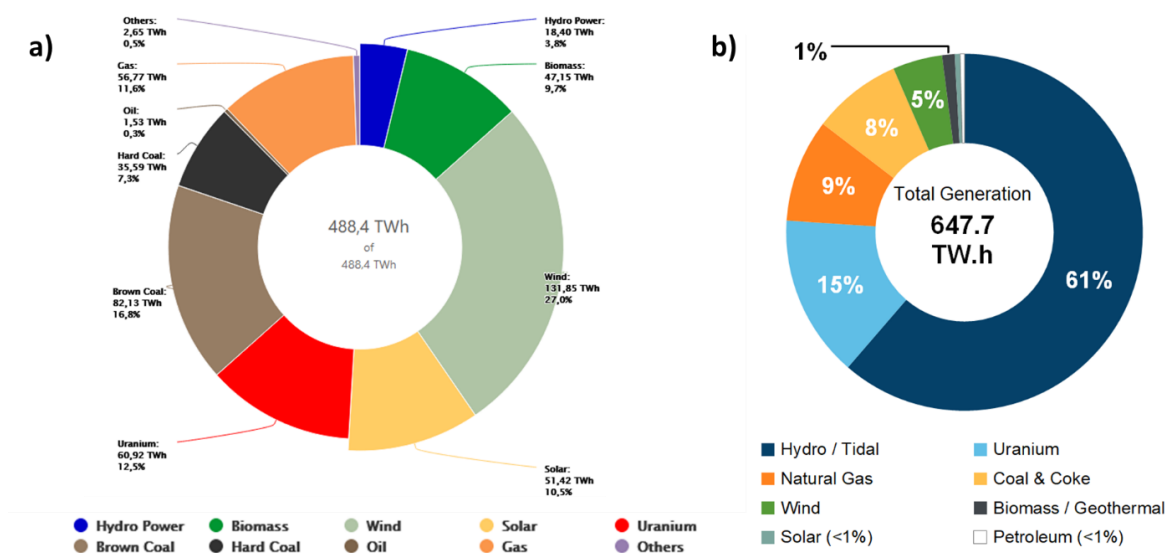


Figure I-3. (a) Net public electricity generation in Germany in 2020, reproduced from Energy-Charts: <https://energy-charts.info/index.html?l=de&c=DE>, last accessed 2021-05-31;^[12] (b) Electricity generation by fuel type in Canada in 2018, reproduced from CER – Canada’s Energy Future 2019: Energy Supply and Demand Projections to 2040.^[13]

To fight climate-change, a variety of different measures need to be taken, both to cut the emission of greenhouse gasses and to reduce the amount of greenhouse gasses already in the atmosphere. The European Green Deal hence supports different strategies with the objective to reach a climate-neutral European Union by 2050, e.g., the development of environmentally friendly technology, protection of natural ecosystems, more energy efficient buildings, etc. Another important goal is the decarbonization of the energy sector. While it is desirable to reduce the energy consumption, a further increase in renewable energy production is also needed to retain the standard of living we have in our modern societies.^[14] The most abundant energy source is by far solar energy with more than 885 000 PWh per year, which is more than three orders of magnitude larger than the yearly global energy use, meaning that within one hour and 40 minutes the yearly amount of energy that is consumed is covered by solar energy reaching the surface of the earth. Even at a conversion efficiency of only 1%, solar energy exceeds the world energy demand.^[15]

In contrast to fossil fuels, the solar energy availability is geographically relatively equally distributed. Yet, only 10.5% of the electricity produced in Germany in 2020 and less than 1% in Canada in 2018 came from solar energy (Figure I-3).^[12-13] One of the main problems when it comes to using solar energy is that the availability does oftentimes not match the demand. While more solar energy can be collected during long and sunny days, i.e., in the summer, in typical households, the main demand is during the winter for heating and lighting. Thus, it is crucial not only to collect solar energy, but also to convert and to store it. Current technologies, like photovoltaic panels, usually convert solar energy into electricity or heat. Both are not ideal for long-term storage or long-distance transportation. Electrical power can be stored in batteries, which is usually considered only a short-term storage device. Furthermore, batteries tend to have a low energy density (Figure I-4), making them unattractive as portable energy supply, e.g., in cars or planes. Another approach is the use of solar energy to produce fuel, e.g., hydrogen gas. The advantage of this method is the high energy density of hydrogen gas compared to that of batteries (see Figure I-4) and the easier transportation and storage as well as the wide variety of other applications, such as fuel cells, oil refining, chemical synthesis or power generation.^[16-17]

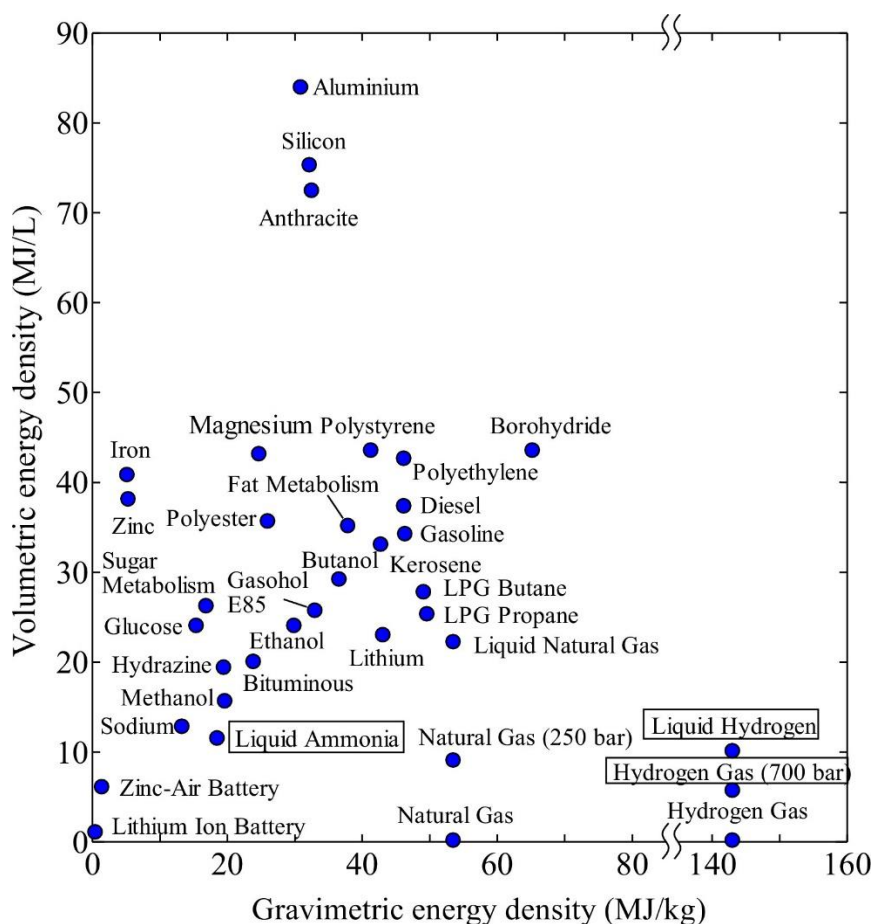


Figure I-4. Volumetric and gravimetric energy density of different fuels and batteries; reproduced with permission from Proceedings of the Combustion Institute, 37, 109-133, Copyright 2019 Elsevier.^[18]

Processes used to convert solar energy into usable fuels, i.e., storing the energy in chemical bonds, are typically inspired by natural photosynthesis. The following sections will go into more detail on the mechanisms of natural photosynthesis taking place in plants and algae as well as artificial photosynthetic systems for the collection and storage of solar energy.

I.2. Natural Photosynthesis

Nature has established a sophisticated mechanism to store solar energy in highly energetic molecules using natural photosynthesis of higher organisms such as plants, algae, and cyanobacteria.^[19] In fact, most of our modern industry relies on the energy stored by photosynthesis as fossil fuels such as oil, gas, and coal are the

remains of ancient organisms. During natural photosynthesis, light is used to reduce carbon dioxide and oxidize water to form oxygen and carbohydrates. The solar energy is thus converted into chemical energy.^[20]

The processes taking place during photosynthesis can be separated in two different phases: The light reactions occur under light irradiation and use the absorbed energy to generate nicotinamide adenine dinucleotide phosphate (NADPH, reduced form of NADP⁺, Chart I-1) and adenosine triphosphate (ATP, Chart I-1). The dark reactions on the other hand are light-independent but they use the products generated during the light reactions to drive the reaction from CO₂ and water to carbohydrates.

Light reactions. The main light absorbing species in natural photosynthesis is chlorophyll. The chemical structure of chlorophyll *a* is shown in Chart I-1. However, different chlorophyll molecules with slight structural variations exist, leading to absorptions in different regions of the visible spectrum.

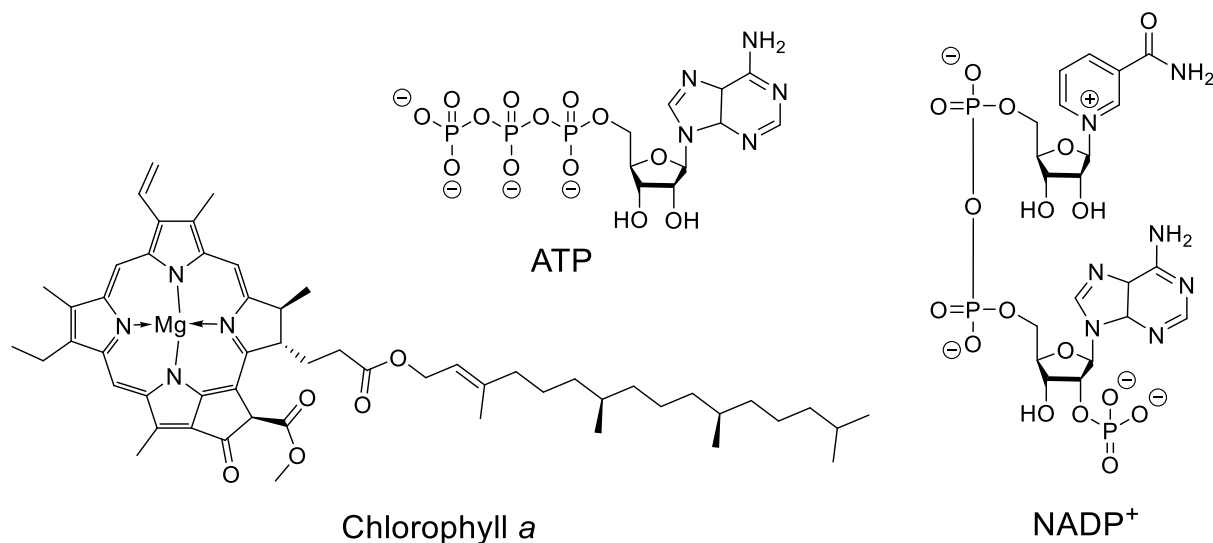


Chart I-1. Chemical structures of ATP, NADP⁺ and chlorophyll *a*.

The chlorophyll molecules act as antenna, funneling the absorbed energy towards photosynthetic reaction centers (RCs). In plants and cyanobacteria, two RCs are connected in a so-called Z-scheme (Figure I-5). Together, those two photosystems drive the photosynthetic reduction of water to form oxygen. In photosystem I (PSI), a weak oxidant and a strong reductant, which can reduce NADP⁺, are generated. In

photosystem II (PSII), a weak reductant and a strong oxidant, which can oxidize water molecules, are generated.

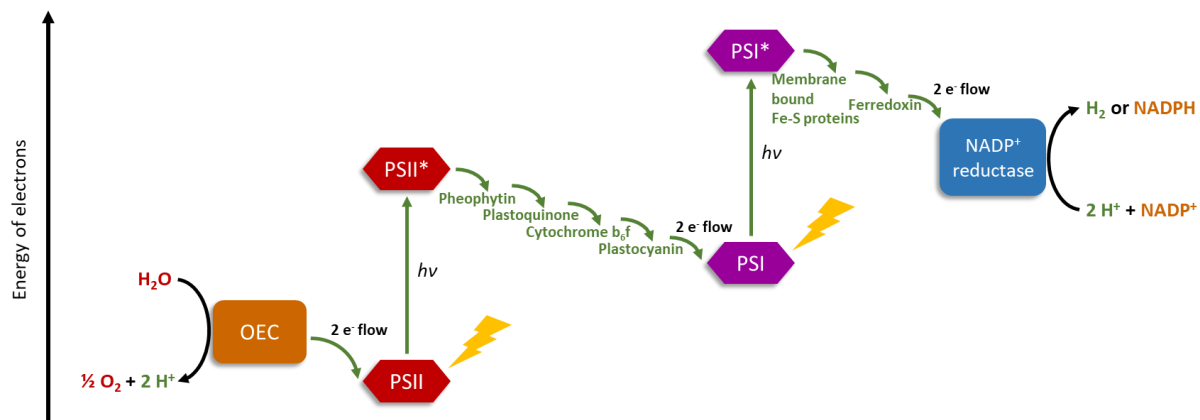


Figure I-5. Z-scheme for photosynthesis in plants and cyanobacteria with oxygen-evolving center (OEC), photosystem I (PSI) and photosystem II (PSII).

The electron transport from the water molecules to the NADP^+ is mediated by three thylakoid membrane-bound particles: PSII, the cytochrome b_6/f complex and PSI. Those complexes are connected by an electron transport chain consisting of mobile electron carriers. The absorption of two photons is necessary to funnel one electron from a water molecule to a NADP^+ molecule, as both photosystems are involved in the process.^[19-20]

In PSII, the oxygen-evolving center (OEC) reduces two water molecules to form one molecule of oxygen in a five-stage, four-electron process. This leads to a minimum of eight photons necessary to produce one molecule of oxygen. It is furthermore important to note, that each O_2 molecule must be produced by a single photosystem.

The electrons, which are released during the oxidation of water, are then funneled *via* cytochrome b_6/f to the PSI. Here, those electrons either participate in the reduction of NADP^+ molecules to form NADPH or are transferred back towards PSII. This mechanism presumably helps to regulate the amount of NADPH. It also explains the observation that the chloroplasts (site of photosynthesis in algae and plants) absorb more than eight photons per oxygen molecule produced. Besides the production of NADPH, the chloroplasts also generate ATP in a similar process.

Dark reactions. While the light reactions generate NADPH and ATP, the dark reactions use these products to transform CO₂ into carbohydrates and other substances. This metabolic pathway is called the Calvin cycle, producing glucose, which can further be converted into starch, sucrose, or cellulose. These final products are where the plant thus eventually stores the absorbed energy in chemical bonds.^[20]

Despite this very complex and sophisticated process, which has been developed and improved by nature for a long time, the efficiency of the process is still relatively low. The overall efficiency of solar energy conversion, i.e., the ratio between the amount of solar energy that irradiates a system and the amount of energy stored in the final chemical product, depends on three factors. The light-harvesting efficiency (LHE) describes the percentage of the incident energy that is absorbed by PSII. The fractional energy yield (FEY) is used to describe the fraction of the excited state energy that is stored in a specific chemical product while the quantum yield gives the probability for this chemical product to be formed after absorption and excited-state formation. Even with different pigments, absorbing light of different wavelengths and a strong absorbance in the region of 300 nm to 700 nm, the overall LHE in PSII is estimated to be only 34%.^[3] The FEY for the redox products in PSII in plants is usually 1-5%. The quantum yield on the other hand can reach values above 90%. However, it is greatly pH dependent. In total, the efficiency of solar energy conversion in PSII is estimated to be around 20%, which is comparable to silicon solar cells currently available. The main energy loss in the processes in PSII is due to mechanisms to avoid back reactions, which would decrease the quantum yield. Additionally, this does not consider other factors such as light saturation or photoinhibition.^[3, 21] Furthermore, the half-life times of PSI are found to be only 35-70 h and even shorter for PSII (1-11 h). This instability, particularly of PSII, is due to photodamage caused by oxidizing species.^[22]

While living organisms can handle instable photosystems by constantly replacing degraded components, such a short-lived photosystem is not suited for a technical application. Furthermore, other limitations such as the low energy yield and the limited absorption range are further reasons why the system of natural photosynthesis is not easily used for commercial applications.^[21]

Another widespread mechanism in nature to provide energy to organisms such as bacteria, archaea and some eukaryotes is the oxidation of molecular hydrogen. To do this, hydrogenases are used. These are metalloenzymes, which catalyze the oxidation of molecular hydrogen to form protons and electrons but also the reverse reaction, the reduction of protons to form dihydrogen molecules. This can help the organism to control the redox potential of the cell. Hydrogenases are classified with regard to the metal ions present in their active sites, [NiFe], [FeFe] or [Fe] (Chart I-2).^[23-24]

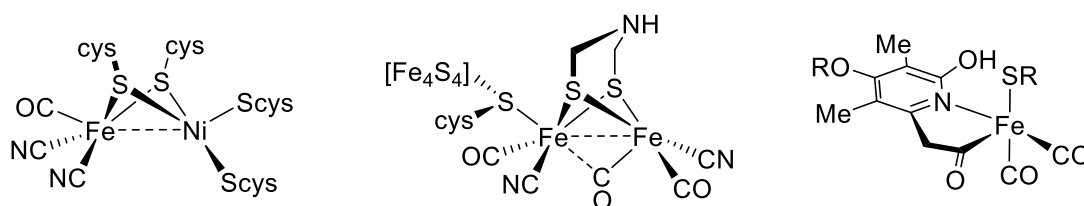


Chart I-2. Chemical structures of the active sites of different types of hydrogenase enzymes.

Many isolated hydrogenases are active to catalyze both proton reduction and dihydrogen oxidation. [NiFe] hydrogenases are often found to be more active as an oxidant while the [FeFe] hydrogenases are more reductive. The active sites are bound to highly specialized proteins, which function as ligand for the metals as well as providing a catalytic reaction pocket and funnel reactants and products to the protein surface. The exact mechanisms employed by hydrogenase enzymes are still under intensive study.^[24]

I.3. Artificial Photosynthesis

The processes taking place in natural photosynthesis have inspired numerous studies on artificial photosynthetic systems, which collect and transform solar energy into chemical energy.^[25] The photocatalytic reduction of CO₂ to form other carbohydrates such as methane or methanol, similar to the Calvin cycle in plants, is one approach to transform solar energy into chemical energy.^[19, 26-27] Furthermore, water splitting, similar to the processes taking place in PSII, has especially gained attention.^[28] While water reduction to form hydrogen gas and water oxidation to form oxygen gas are usually carried out in separate systems^[29], Lehn and Ziessel reported

in 1982 a system, which could simultaneously reduce water and carbon dioxide upon visible light irradiation, producing carbon monoxide as well as hydrogen gas.^[30] Despite the numerous applications of artificial photosynthetic systems to drive photocatalytic reactions^[25, 31] or to generate different solar fuels^[32], for the remainder of this thesis, the focus will be on photocatalytic splitting of water.

In 1972, Fujishima and Honda discovered that titanium dioxide (TiO₂) can catalyze the electrochemical photolysis of water. By using a semiconducting TiO₂ cathode and irradiation of light with a wavelength shorter than 415 nm, they observed the oxidation of water at a more negative potential than the standard potential (Table I-1).^[33] Since then, many researchers have investigated the potential of semiconductors for photocatalytic water splitting and other applications such as photocatalytic degradation of pollutants.^[34] However, the relatively large energy gap of TiO₂ requires high energy light in the UV region, which only makes up a small part of the solar spectrum.^[19]

Table I-1. Electrochemical reaction equations for oxidation of H₂O and H⁺ reduction.^[19]

Reaction	E ⁰ / V vs. NHE
H ₂ O → HO• + 1H ⁺ + 1e ⁻	+2.39
2H ₂ O → HOOH + 2H ⁺ + 2e ⁻	+1.37
2H ₂ O → HOO• + 3H ⁺ + 3e ⁻	+1.26
2H ₂ O → O ₂ + 4H ⁺ + 4e ⁻	+0.81
2H ⁺ + 2e ⁻ → H ₂	-0.41

Lehn and Sauvage first introduced another approach to photocatalytic water splitting in 1977. They showed that hydrogen could be produced from a photocatalytic system containing a photosensitizer (PS), an electron mediator, a sacrificial electron donor and colloidal platinum as catalyst. This study was the first example of molecular artificial synthesis.^[35-36] Grätzel and coworkers investigated similar systems^[37-39] and later combined strategies from molecular photocatalytic water splitting with semiconductor technology to design the first dye sensitized solar cell (DSSC).^[40] The electrodes are made of conducting glass, typically glass coated with a fluorine doped tin oxide layer (FTO). The anode is furthermore covered by a mesoporous oxide layer,

acting as a semiconductor. Typically, TiO_2 is used, however other materials such as ZnO , SnO_2 , Nb_2O_5 or CdSe have also been investigated. Attached to the surface is a monolayer of a charge transfer dye, which injects an electron into the conduction band of the nanocrystalline oxide upon photoexcitation (Figure I-6). The electrolyte, usually based on an organic solvent, contains a mediator, such as the iodide/triiodide couple, which restores the original state of the dye by electron donation. The cathode completes the electric circuit.^[41-42] The most commonly used dyes are ruthenium polypyridyl complexes, resulting in DSSCs with conversion rates of more than 10%.^[43] Many groups are aiming at improving those DSSCs by broadening the absorption region of the dyes^[44], but there have also been numerous studies on the use of natural dyes aiming at decreasing the cost of DSSCs.^[45]

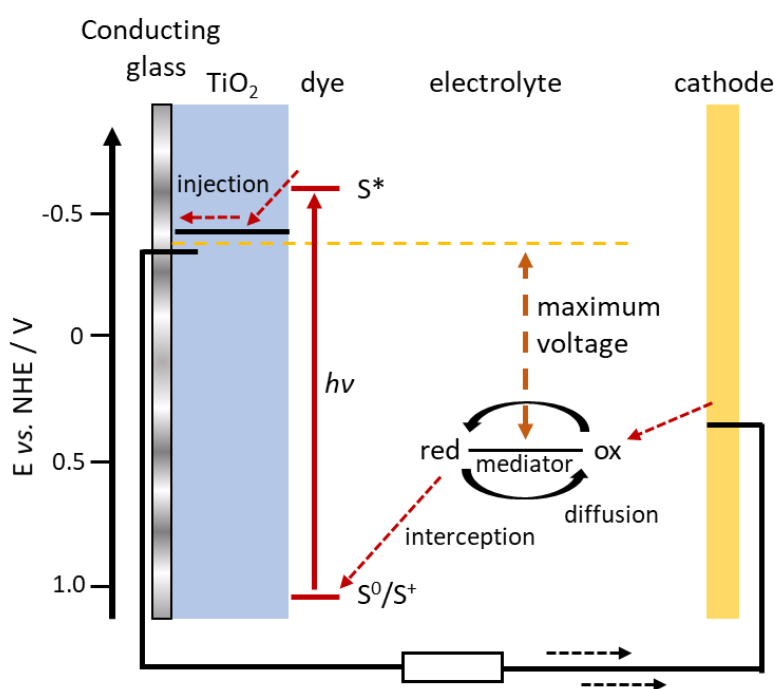


Figure I-6. Schematic overview of a dye sensitized solar cell or Grätzel cell.

While DCCSs transform solar energy into electrical energy, there are multiple other approaches to store energy from absorbed light in chemical bonds. Besides photoelectrochemical systems employing semiconductors and photoelectrodes^[46], there are numerous homogeneous and heterogeneous photocatalytic systems, which are investigated^[47-48]. However, keeping in mind the scope of this project, the focus will

be on molecular photocatalytic water splitting, following the before mentioned example by Lehn and Sauvage.

Similar to natural photosynthesis, molecular artificial systems are composed of an antenna or photosensitizer, which absorbs light and transfers the energy, and a reaction center or catalyst. Water oxidation and reduction can either be coupled together, or one half-reaction can be substituted by a sacrificial electron donor (SED) or sacrificial electron acceptor (SEA). A general, schematic overview of the processes in photocatalytic water splitting can be seen in Figure I-7. The PS is excited by absorbing light, thus populating the lowest unoccupied molecular orbital (LUMO). This generates an electron hole in the highest occupied molecular orbital (HOMO). Depending on the system used, this hole can be filled with an electron either from a SED or by oxidizing the WOC, i.e., reductively quenching the excited PS, or the excited PS can be oxidatively quenched by transferring the electron in the excited state to a hydrogen evolution catalyst (HEC) or a SEA. In case of reductive quenching, the PS is restored by transferring an electron from the reduced PS to either a SEA or HEC. If oxidative quenching takes place, the oxidized PS returns to the ground state *via* an electron transfer from a SED or WOC.^[19, 31]

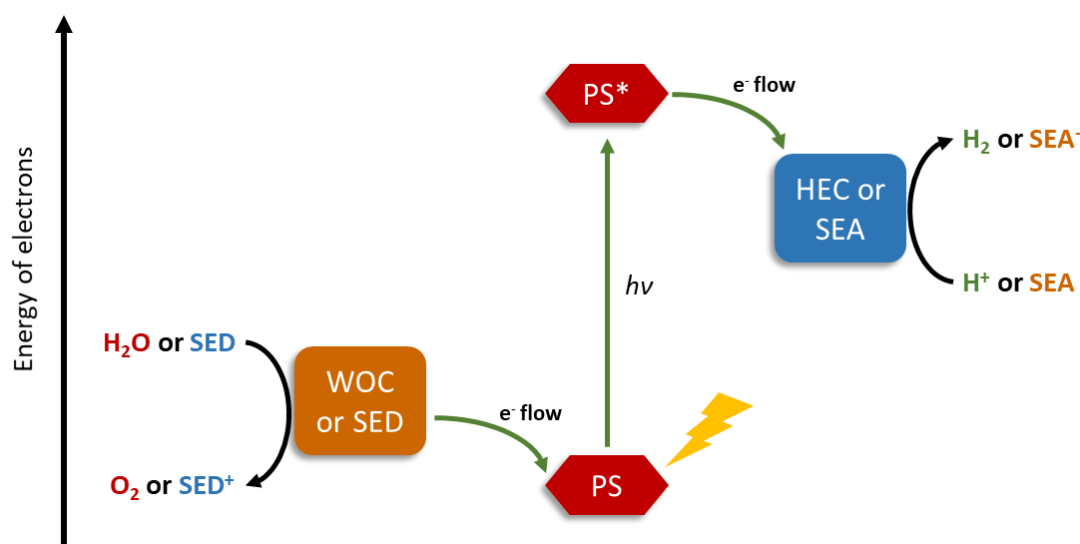


Figure I-7. Schematic representation of artificial photosynthesis with photosensitizer (PS), water oxidation catalyst (WOC), sacrificial electron donor (SED), hydrogen evolution catalyst (HEC), and sacrificial electron acceptor (SEA).

In the following sections, the different components of a photocatalytic water splitting system and the processes taking place will be discussed in more detail, giving the relevant theoretical background as well as examples from the literature.

I.4. Photosensitizer

In order for a compound to be capable to act as a photosensitizer, it needs to meet a number of criteria: (1) It needs to exhibit reversible redox behavior; (2) it needs suitable ground-state and excited-state potentials with regard to the catalyst and the electron donor/acceptor; (3) it should be thermally and photochemically stable; (4) it needs a strong absorption of the exciting light, ideally covering wide regions of the solar spectrum; (5) it should have a high luminescence quantum yield, a long excited-state lifetime and a high energy content of the reactive excited state; (6) it should also have a small energy gap between the relevant excited states.^[49]

Since the first report by Lehn and Sauvage, Ru(II) tris-bipyridine ($[\text{Ru}(\text{bpy})_3]^{2+}$) complexes have been widely studied for the application as PS. The variety of different systems studied as PS will be discussed later in more detail. However, to explore the general properties of an organometallic PS, Ru(II) polypyridine complexes and especially $[\text{Ru}(\text{bpy})_3]^{2+}$ are used as model compounds in the following discussion.

I.4.1. Theoretical Background

Ru(II) polypyridine complexes are d^6 systems with pseudo-octahedral geometry, which absorb strongly in the visible region. This is due to the metal-to-ligand charge transfer transition (MLCT), which can be seen in Figure I-8 (a) alongside the ligand centered (LC) and metal centered (MC) transitions. $[\text{Ru}(\text{bpy})_3]^{2+}$ exhibits D_3 geometry. A more detailed depiction of the MLCT transitions in this geometry is shown in Figure I-8 (b). The HOMOs $\pi_{\text{MA}1}$ and π_{ME} are mainly localized on the metal while the LUMOs $\pi^*_{\text{LA}2}$ and π^*_{LE} are mainly localized on the ligands. Thus, upon excitation of the HOMO-LUMO transition, charge is shifted from metal-localized orbitals to ligand-localized orbitals, resulting in the metal-to-ligand charge transfer.^[50]

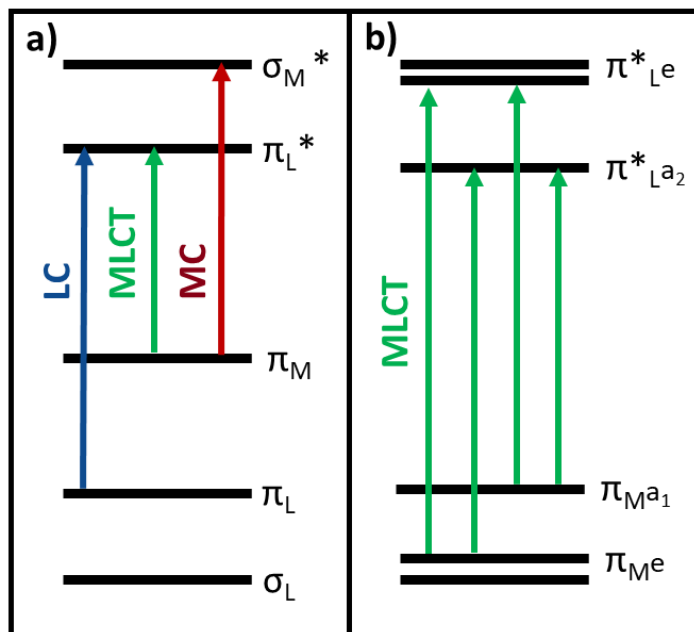


Figure I-8. (a) Qualitative molecular orbital diagram for Ru(II) polypyridine complexes in octahedral symmetry showing the electronic transitions occurring in the UV-vis region: ligand centered (LC), metal centered (MC), metal-to-ligand charge transfer (MLCT); (b) detailed molecular orbital diagram of the MLCT transition in D_3 symmetry.

This excited state can be deactivated following multiple pathways. The excited electron can return to the ground state *via* radiative or non-radiative decay, either directly or following internal conversion processes. The different electronic states and the transitions between them can be seen in the Jablonski diagram in Figure I-9. Upon absorption of light, the Ru(II) polypyridyl complex gets excited in the singlet excited state S_1 , which corresponds to a singlet MLCT state ($^1\text{MLCT}$), from where it undergoes, usually very fast and with very high efficiency, inter system crossing (ISC) to a triplet excited state T_1 , which corresponds to a triplet MLCT state ($^3\text{MLCT}$).^[51] From here, the electron can relax to the ground state S_0 , either *via* radiative (phosphorescence) or non-radiative decay. However, it is also possible that a thermally activated transition to the triplet MC T_2 state by internal conversion (IC) takes place, which is followed by non-radiative decay to the ground state. The activation barrier for the internal conversion to the ^3MC state depends on the relative energy of the molecular orbitals and greatly depends on the ligand design. The excited-state lifetime τ of the complexes is thus temperature dependent, following the following rate law:

$$k_{obs} = \left(\frac{1}{\tau}\right) = k^0 + k^{0'} \exp\left(-\frac{E_a}{RT}\right) \quad \text{Equation I-1}$$

$$k^0 = k_r + k_{nr} \quad \text{Equation I-2}$$

with the radiative decay rate k_r , non-radiative decay rate k_{nr} , prefactor k^0 , gas constant R and activation barrier E_a .^[49, 51]

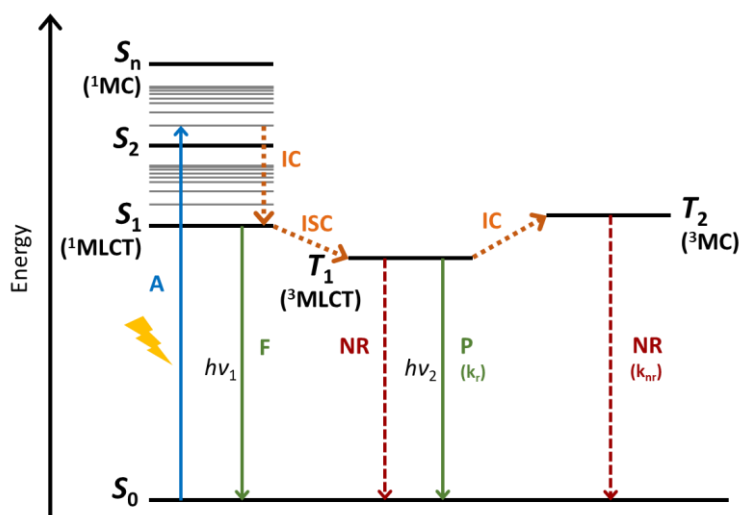


Figure I-9. Simplified Jablonski diagram illustrating the electronic states of Ru(II) polypyridyl complexes and the possible transitions^[52]; $h\nu$: photon radiation; A: absorption of photon; F: fluorescence; P: phosphorescence; NR: non-radiative decay; S: singlet state; T: triplet state; MLCT: metal-to-ligand charge transfer; MC: metal-centered; IC: internal conversion; ISC: inter-system crossing; k_r : radiative decay constant; k_{nr} : non-radiative decay constant.

Apart from relaxation back to the ground state, the excited compound can furthermore transfer the energy to another molecule in the ground state, i.e., quenching its own luminescence. This energy transfer can follow two different mechanisms. The Förster resonance energy transfer (FRET) is an energy transfer from an excited chromophore to an acceptor chromophore in the ground state *via* dipole-dipole interactions. For this energy transfer to be efficient, both chromophores need to be close together (distance in the order of nm) and the emission spectrum of the donor chromophore needs to overlap with the absorption spectrum of the acceptor chromophore. Thus, if the two chromophores come into close reach, the excited chromophore emits a virtual photon, which is instantly absorbed by the acceptor chromophore (Figure I-10). The virtual photon is undetectable. FRET commonly leads to a singlet-singlet energy transfer.^[53-55]

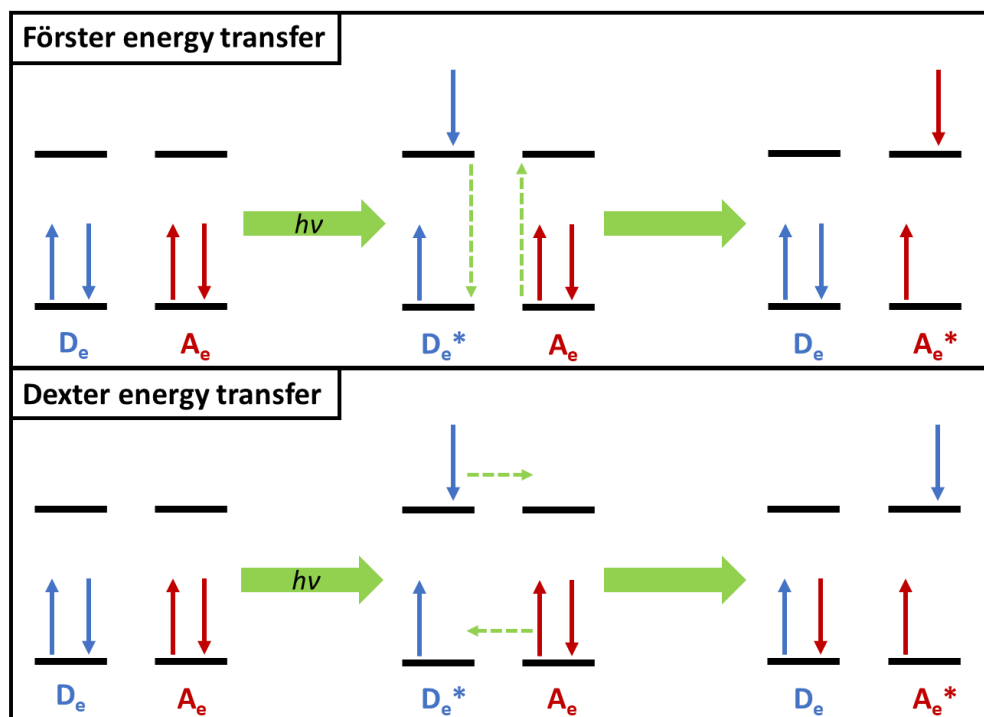


Figure I-10. Energy transfer scheme via the Förster resonance energy transfer (FRET) mechanism and the Dexter energy transfer mechanism.

While the FRET allows energy transfer through space, the Dexter energy transfer takes place at much shorter distances, typically less than 1 nm, i.e., along bonds or in solids. An important requirement for this kind of energy transfer is that the wavefunctions of the donor and acceptor molecule overlap. The energy from the excited donor to the ground state acceptor is transferred by simultaneous or step wise electron exchange. The spin must be conserved during Dexter energy transfer, but it allows for otherwise forbidden transitions and is the dominant mechanism in triplet-triplet energy transfers. Both mechanisms play important roles in light-harvesting complexes in natural photosynthesis.^[56-57]

Another mechanism of quenching an excited compound, which is exploited in artificial photosynthesis, is electron transfer. Such an electron transfer, particularly between two coordination compounds, can follow one of two mechanisms: If the two complexes share the same ligand, this ligand can act as a bridge between the two metal centers and electrons can be transferred *via* an inner-sphere mechanism. This bridge can either be permanent or be formed and broken again in the cause of the electron transfer.^[58-59] The discovery of this electron transfer mechanism, which relies

on strong electronic coupling between the two metal centers *via* a covalent linkage was awarded with the Nobel prize in 1983 for Henry Taube.^[60]

If the two compounds involved in the electron transfer are not linked together but rather are components of a homogeneous solution, the electron transfer follows an outer-sphere mechanism described by the Marcus theory. For an electron transfer to be able to take place the two molecules, an electron donor D_e , and an electron acceptor A_e , need to collide to form a complex DA . This complex can either separate again or an electron transfer can occur to form the complex D^+A^- . This charge separated complex can either break apart or the electron can be transferred back to yield again DA . The electron transfer happens *via* electron tunneling through a potential energy barrier. The height of this barrier depends, partly, on the ionization energies of the complexes DA and D^+A^- . Prior to the electron transfer, the complex DA as well as the surrounding solvent molecules undergo structural rearrangements. The Gibbs activation energy $\Delta^\ddagger G$ depends on the energy needed for this rearrangement as well as on the Gibbs standard reaction energy $\Delta_r G^\ominus$ (Figure I-11).^[53]

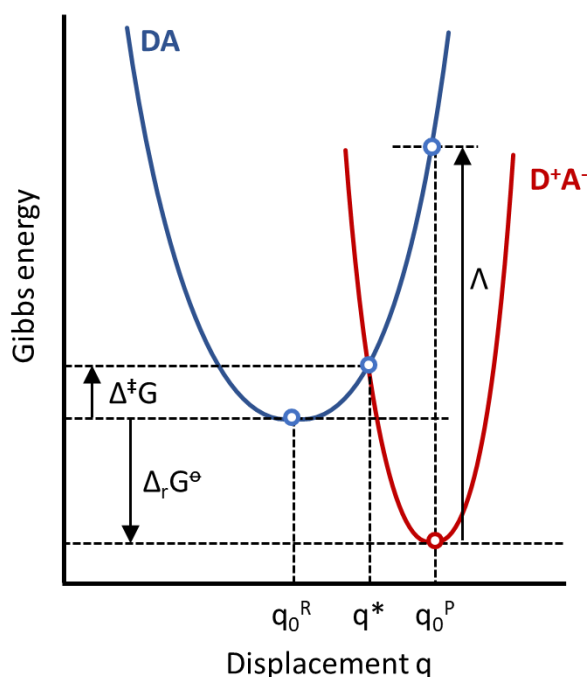


Figure I-11. Representation of the important values during an outer-sphere electron transfer; parabolas characteristic for harmonic oscillators represent the Gibbs energy surfaces of the complexes DA and D^+A^- ; q_0^R = displacement of reactant, q_0^P = displacement of product, q^* = displacement of parabola intersection, $\Delta^\ddagger G$ = Gibbs activation energy, $\Delta_r G^\ominus$ = Gibbs standard reaction energy, Λ = reorganization energy.

The rate constant for the electron transfer k_{ET} in the complex DA is expressed by the following equation:

$$k_{ET} = \frac{2H_{DA}^2}{h} \sqrt{\frac{\pi^3}{\lambda RT}} \exp\left(-\frac{(\lambda + \Delta_r G^\ominus)^2}{4\lambda RT}\right) \quad \text{Equation I-3}$$

with Planck constant h , gas constant R , temperature T and H_{DA} being the Hamiltonian, which describes the coupling of the electronic wavefunctions of D_e and A_e . This electronic coupling term H_{DA} usually decreases exponentially with increasing distance between D_e and A_e in the complex DA, thus decreasing the rate of electron transfer. However, besides this intuitive trend, the Marcus theory further predicts an inverted region where longer D_e - A_e distances actually lead to an increase of the electron transfer rate. This inverted behavior is a result of an interdependence of reorganization energy and electronic coupling. However, there are only very few experimental studies, which manage to unambiguously demonstrate the effect.^[61-62]

In the case of an excited molecule being quenched by electron transfer, the process is called photoinduced electron transfer. Figure I-12 shows the different possible electron transfer processes. If the excited species acts as an electron donor, a photoinduced reduction or oxidative quenching is taking place. If the excited species accepts an electron, it is called a photoinduced oxidation or reductive quenching.

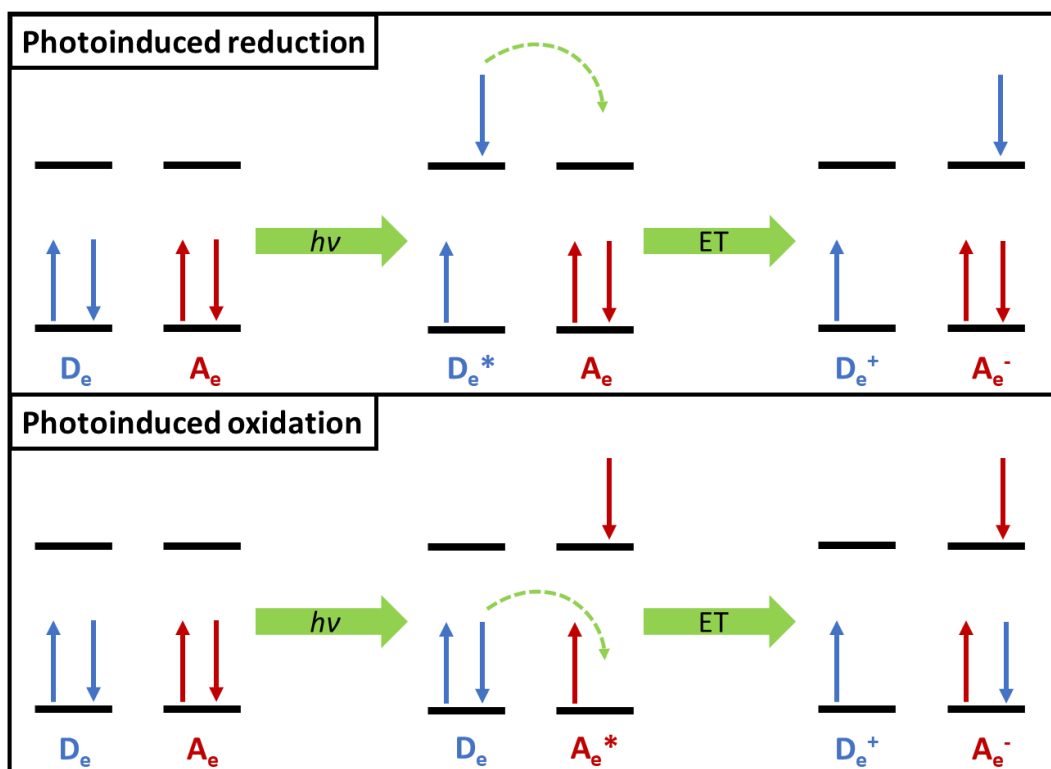


Figure I-12. Scheme for photoinduced electron transfer (ET) following a photoinduced reduction or oxidation pathway.

When Ru(II) polypyridine complexes get excited, they become both easier to reduce and easier to oxidize. The redox potentials in the excited state can be estimated using the following equations:^[63]

$$E_{ox}^* = E_{ox} - \Delta E_{em} \quad \text{Equation I-4}$$

$$E_{red}^* = E_{red} + \Delta E_{em} \quad \text{Equation I-5}$$

with ΔE_{em} (eV) $\approx 1240/\lambda_{em}$ and λ_{em} being the emission wavelength in nm. These redox potentials of the excited state can subsequently be used to calculate the driving force or Gibbs reaction energy for the photoinduced electron transfer $\Delta_r G^\ominus$ using the following equation:^[64]

$$\Delta_r G^\ominus = N_A \{ e (E_{ox} - E_{red}) + W \} - \Delta E_{em} \quad \text{Equation I-6}$$

where N_A is the Avogadro constant, e is the electron charge and W is the work term, i.e., the difference between the Coulombic attraction in the reactants and products. The work term is described by Equation I-7 with $z(A)$ and $z(D)$ being the charge of the acceptor and the donor respectively, ϵ_0 being the vacuum permittivity, ϵ_r being the relative medium static permittivity and a being the distance between the charged species after the electron transfer. This work term reduces the driving force. However, it is often neglected as a first approximation.^[65-66]

$$W = \frac{[z(A) - z(D) - 1]e^2}{4\pi\epsilon_0\epsilon_r a} \quad \text{Equation I-7}$$

The redox potentials in the ground state as well as in the excited state, calculated using Equation I-4 and Equation I-5, of $[\text{Ru}(\text{bpy})_3]^{2+}$ are shown in the Latimer diagram in Figure I-13.^[50, 67]

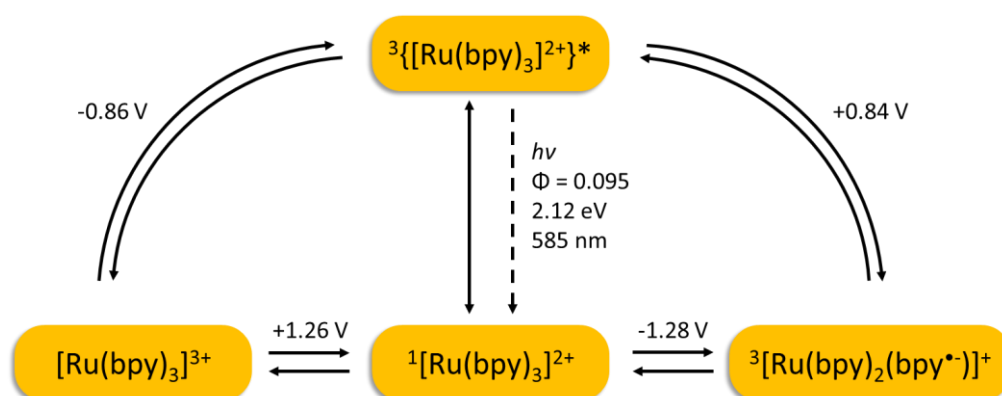


Figure I-13. Latimer diagram of $[\text{Ru}(\text{bpy})_3]^{2+}$.

While $[\text{Ru}(\text{bpy})_3]^{2+}$ has been widely used as photosensitizer in both water oxidation and water reduction, there are numerous other compounds, which are investigated for the same application. As described before, a photosensitizer needs to have certain properties, many of which can be investigated individually such as the photophysical and electrochemical properties. While the overall requirements for a PS in water oxidation and in water reduction are the same, the reactions the PS undergoes can differ from system to system. The excited PS can either be oxidized or reduced first following the reaction pathways shown in Figure I-14. In a catalytic system, the

donor D_e and the acceptor A_e are either a sacrificial electron donor/acceptor or the catalyst.^[49]

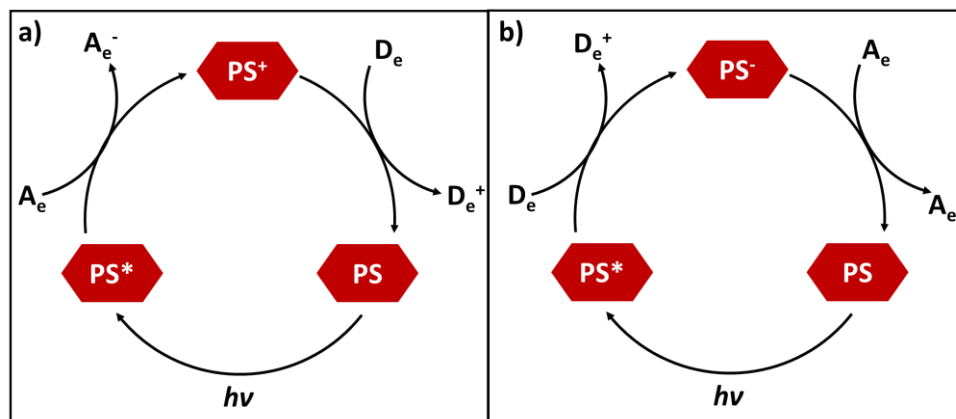


Figure I-14. Schematic representation of the photosensitized electron transfer reaction following different pathways, D_e = electron donor, A_e = electron acceptor, PS = photosensitizer.

An example on how to assess the efficiency of the quenching process is given by Potvin *et al.* They developed a method to screen photosensitizers *via* UV-vis spectroscopy by looking at a solution of a PS, triethanolamine (TEOA) as sacrificial electron donor and methyl viologen under continuous light irradiation. The viologen gets reduced by the excited PS and the resulting methyl viologen cation radical has a blue color, which can be observed intensifying over time.^[68] Time-resolved spectroscopy has been further used to investigate the first steps taking place in homogeneous catalysis, helping to understand the photocatalytic processes as well as the efficiencies of each step. The use of ultrafast pump-probe spectroscopy is particularly useful for the analysis of new PSs and allows to discriminate between oxidative and reductive pathways.^[69]

1.4.2. State of the Art

One of the great drawbacks of $[Ru(bpy)_3]^{2+}$ as PS is its instability under photocatalytic conditions as the complex undergoes photo-induced ligand substitution.^[49, 70-71] While fully organic photosensitizers^[72] as well as inorganic compounds such as CdS nanorods^[73] are being investigated for photocatalytic water splitting, the main focus of PS research is on organometallic compounds.

By varying the substituents on the bipyridine ligands, the electronic properties of Ru(II) tris-bipyridine complexes can be tuned.^[74] By doing so, more active and/or stable PS can be synthesized. Furthermore, the absorption spectra of the PSs can be changed, leading to photosensitizers active even under red light irradiation.^[75-76] Additionally, polytopic ligands can be used to form polynuclear complexes, which outperform $[\text{Ru}(\text{bpy})_3]^{2+}$ both in water oxidation and reduction.^[77-78] Polytopic terpyridine (2,2':6',2''-terpyridine) ligands have also gained some attention as the use of the tridentate terpyridine (tpy) metal ion receptor allows for linear ditopic ligands and thus linear rod-like structures without forming stereoisomers as tris-bipyridine complexes do.^[79] $[\text{Ru}(\text{tpy})_2]^{2+}$ complexes exhibit similar electrochemical and absorption properties to the bipyridine analogue. However, their excited-state lifetime as well as quantum yield are very low, which is the reason why they have been used less for the application as PS. Yet, similar to the bipyridine complexes, terpyridine complexes can be tuned by using different substituents, e.g., additional chromophoric sites^[80-81], or forming polynuclear Ru(II) bis-terpyridine oligomers.^[82-84] Ruthenium complexes with terpyridine metal ion receptors have been employed as PS in DSSC^[85] and water oxidation experiments.^[86-87] The strategies used to improve the photophysical properties of Ru(II) bis-terpyridine complexes are discussed in more detail in section I.7.

Closely related to the Ru(II) tris-bipyridine complex are Ir(III) complexes with bidentate and tridentate polypyridine metal ion receptors^[88-91], which were found to be able to be more active and long-lived than $[\text{Ru}(\text{bpy})_3]^{2+}$ in hydrogen evolution experiments.^[92-94] Re(I) and Pt(II) polypyridine complexes as well as gold complexes have been further investigated as PS.^[90, 95] All these PS have in common that they contain a noble metal center, hence making these complexes relatively expensive regardless of the ligand design. However, there are also attempts on developing photosensitizers based on first row metals such as copper, iron and chromium.^[25] However, polypyridine complexes of these metals often suffer from very short excited-state lifetimes and low luminescence quantum yields, especially with iron as metal center, making them not suitable as PS in homogeneous photocatalysis.^[69, 96-97]

Apart from polypyridine complexes, a commonly studied motif are porphyrin PSs, employing zinc, aluminum, indium, palladium, or platinum metal centers. Those

complexes, which are based on the natural PS chlorophyll have strong absorption in the visible region and excited-state lifetimes in the μs region. They have been found to be active as PS in DSSCs as well as in homogeneous hydrogen production.^[90, 98]

1.5. Sacrificial Electron Donor and Acceptor

The ultimate goal in artificial photosynthesis is simultaneous water oxidation and reduction, producing both oxygen and hydrogen gas. However, the water splitting reaction as a whole is very challenging and thermodynamically highly unfavorable.^[99] Hence, in molecular photocatalytic water splitting, most approaches focus on one of these half reactions. As a result, the other half reaction needs to be replaced, by either an electron donor or acceptor. This species is sacrificed during the photochemical reaction and is thus usually used in great excess.^[100]

In photocatalytic hydrogen production, a variety of SEDs are used. Most commonly, tertiary aliphatic amines such as triethyl amine (TEA), TEOA or ethylenediaminetetraacetic acid (EDTA) act as efficient electron supply. The formation of a carbon centered radical with significant reductive power can lead to reduce the PS or protons, boosting the overall efficiency of the system but the oxidized species can also perform back electron transfer or interact otherwise with PS and catalyst. Furthermore, the redox potentials of amine SEDs depend on the pH of the catalytic solution.^[101-104] Dimethyl para toluidine (DMT) on the other hand, an aromatic amine, is known to dimerize after oxidation, thus yielding less counterproductive interactions with the rest of the catalytic system.^[105]

Another approach to SEDs is found in nature, where NADH is used as electron donor for the reduction of CO_2 . Inspired by this natural electron donor, 1-benzyl-1,4-dihydronicotinamide (BNAH)^[106-108] and 1,3-dimethyl-2-phenylbenzimidazoline (BIH)^[109] have been used, acting as a two-electron donor and one hydride donor. Other commonly studied SEDs include ascorbic acid, carboxylic acids, thiols, and thiolates as well as inorganic molecules such as sulfide and sulfite.^[100, 110]

In systems for photocatalytic water oxidation, SEAs are used. The most widely used SEAs are silver cations, forming elemental silver nanoparticles upon reduction. Those nanoparticles lead to optical changes and could also show catalytic activity of their own, even though rarely discussed. Other SEAs, which have been used are ferric

ions and peroxodisulfate. Other SEA like tetranitromethane or other nitroaromatic compounds did not lead to oxygen production when employed in photocatalytic systems, even though their reduction can be observed. This leads to questions whether the SEAs, which have been found to lead to oxygen production, do not take on a greater role in the overall water oxidation reaction.^[110]

I.6. Catalyst

While PS and SEA/SED supply the energy needed and supply or accept electrons needed for the water splitting reaction, a catalyst is needed to drive the oxidation of water or reduction of protons.

I.6.1. Water Oxidation Catalyst

The photocatalytic splitting of water to form oxygen gas requires a four-electron oxidation. As the PS only transfers one electron at a time, a stepwise oxidation of the water oxidation catalyst is needed. Thus, the potentials of the different intermediate redox couples WOC^{n+1}/WOC^{n+} need to match the potential of the PS^+/PS redox couple. The WOC should be capable of oxidizing water at a minimal overpotential. This process should be fast. Furthermore, the WOC needs to exhibit oxidative, hydrolytic, and thermal stability.^[98, 111]

A common WOC are iridium oxide nanoparticles. However, the electron transfer from a typical ruthenium PS to the catalyst is slow, leading to a decreased stability and longevity of the photocatalytic system. Similar slow electron transfer rates were found for other metal oxides.^[78, 98] When the molecular analog to metal-oxides, polyoxometalates (POMs), were used however, this electron transfer was observed to be much faster. POMs were furthermore found to exhibit a very fast accumulation of electron holes upon electron transfer to the PS.^[86, 111-112]

Other studies aim at mimicking the WOC of natural photosynthesis using a manganese complex^[113], relying on earth abundant elements such as iron in polynuclear oxo-iron complexes^[114] or cobalt and nitrogen co-doped graphene as WOC^[115]. Furthermore, WOCs similar in design to previously discussed PSs are used, such as Ru(III) and Ir(III) polypyridyl complexes and oxo-bridged dimers.^[116-122]

I.6.2. Water Reduction Catalyst

An obvious approach to hydrogen production is mimicking hydrogenases containing iron and/or nickel ions.^[123-124] Mononuclear nickel complexes have also been studied as hydrogen evolution catalyst, typically bearing two diphosphine ligands in a square planar geometry.^[125] Other nickel HECs use pyridyl thiolate ligands, polypyridines or dimethylglyoxime ligands.^[126] While most employed nickel catalysts are Ni(II) complexes, mechanistic studies suggest a Ni⁰ complex as active species. Thus, the active species is formed by two-electron reduction and ligand dissociation leading to a free coordination site for catalysis.^[127]

In 1983, Hawecker *et al.* replaced the commonly used colloidal platinum by a cobalt complex with dimethylglyoxime ligands, also called a cobaloxime.^[128] Yet, it took more than 20 years for this kind of complex to be more frequently employed as HEC.^[129] Since then, cobaloxime HECs have evolved as a standard in photocatalytic hydrogen evolution even though they are prone to hydrolysis under acidic conditions, leading to decomposition and ligand dissociation.^[130] There are different catalytic pathways, which are suggested in the literature (Figure I-15). In the heterolytic mechanisms, an intermediate metal hydride is formed, which then decomposes by attack of a proton, resulting in hydrogen evolution. There are two electrons transferred during the catalytic cycle, either from an electrode (electrocatalysis) or the PS (photocatalysis). The order of electron and proton transfer can either be consecutive or alternating. In the homolytic pathway, dihydrogen is formed by a reductive elimination reaction of two metal hydride complexes *via* a homolytic splitting of the Co-H bonds. Studies have shown that the homolytic pathway is thermodynamically favored. However, no studies regarding the kinetics have been undertaken so far. It is also possible for different pathways to co-exist.^[131-132]

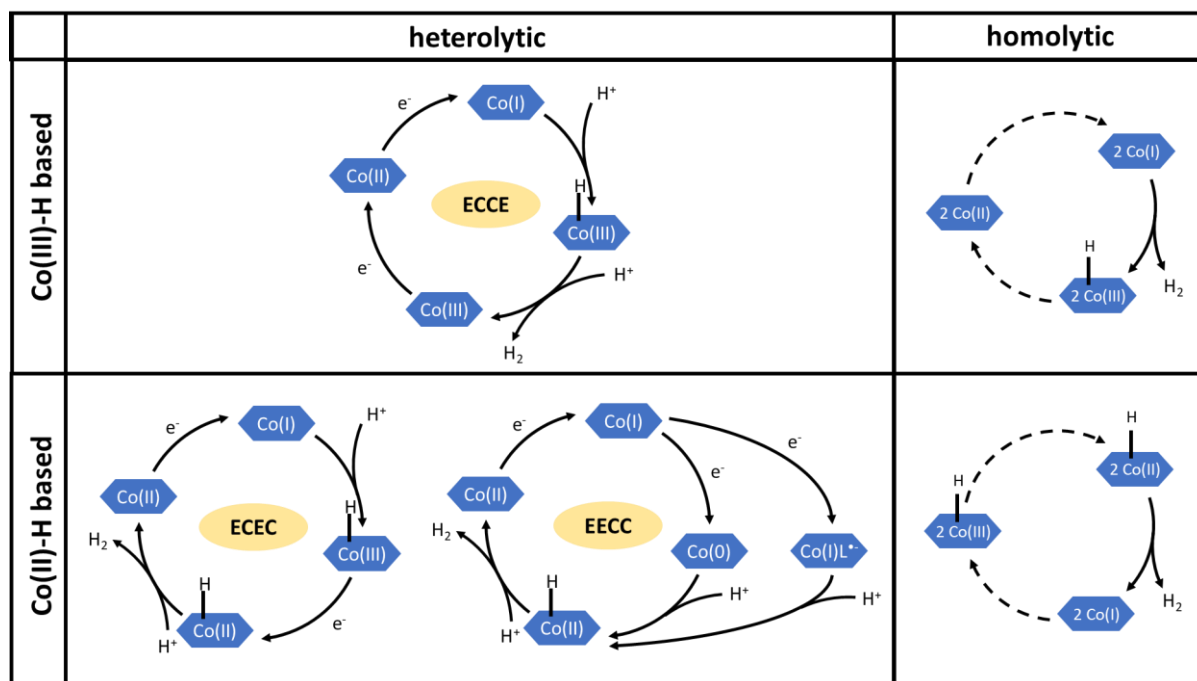


Figure I-15. Different catalytic reaction mechanisms for catalytic hydrogen evolution using cobalt catalysts suggested in the literature; E = electron transfer step, C = protonation step.

While different cobaloxime complexes are widely used for photocatalytic hydrogen evolution^[133-134], other cobalt containing HECs are also under investigation, e.g. using pyridine containing ligands.^[73, 88, 130-131, 135] Furthermore, other metals such as copper, rhenium, manganese or molybdenum^[95, 124, 126, 136] as well as porphyrin complexes with different metal centers^[137] are studied as HEC..

I.6.3. Supramolecular Systems

In molecular artificial photosynthesis, most systems studied consist of three components: The photosensitizer, the catalyst and a sacrificial electron donor or acceptor. However, it is also possible to couple the PS and the catalyst covalently. There are different examples of employing natural compounds, e.g., the use of an electron transfer protein to link PS and catalyst together^[138], a PS coupled to a hydrogenase enzyme^[139], or a photosystem I protein used as PS coupled to a cobaloxime catalyst^[140-141]. A motif studied by several groups is the combination of a Ru(II) polypyridine PS and a cobaloxime catalyst^[142-144] or a platinum catalyst.^[145-147] Another supramolecular motif, which has gained attention, are diiron complexes

mimicking the hydrogenase active site coupled to different PS, such as Ru(II) polypyridyl complexes but also porphyrin and rhenium-based PSs.^[126, 148]

While the idea behind those supramolecular systems, aiming at overcoming diffusional constraints present in bimolecular systems, is simple many of those systems were found to not outperform systems with separate components and some examples lack activity completely. This could be due to insufficient charge separation and back electron transfer processes.^[126]

I.7. Photophysical and Electrochemical Properties of Ru(II) Complexes with Tridentate Ligands – State of the Art

Ru(II) bis-terpyridine complexes are mostly disregarded as PS for many applications due to their poor photophysical properties, i.e., low luminescence quantum yield ($0.5 \cdot 10^{-5}$) and short excited-state lifetime (0.25 ns) compared to Ru(II) tris-bipyridine complexes ($\Phi = 9.5 \cdot 10^{-2}$ and $\tau = 1 \mu\text{s}$).^[52] The observed poor photophysical properties of the terpyridine complexes stem from the rigid nature and geometry of the tridentate metal ion receptor, which leads to a restrained bite angle. In $[\text{Ru}(\text{bpy})_3]^{2+}$, the N-Ru-N *trans* angle is 173.0° while in $[\text{Ru}(\text{tpy})_2]^{2+}$ it is only 158.6° .^[149] This distorted octahedral coordination symmetry leads to a weaker ligand field strength of the terpyridine metal ion receptor.^[150] Therefore, the metal-centered transition is lower in energy and internal conversion, followed by non-radiative decay, is much more efficient at room temperature than it is in bipyridine complexes (Figure I-16).^[151-153]

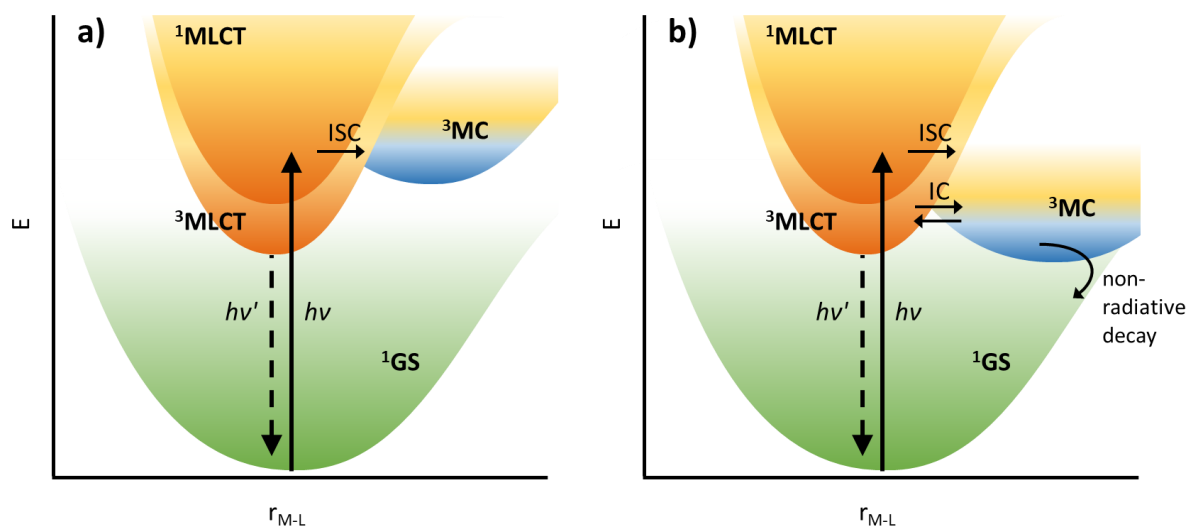


Figure I-16. Qualitative electronic state diagrams presenting the excitation with light in the visible region and the relevant processes influencing the emission properties of a) $[\text{Ru}(\text{bpy})_3]^{2+}$ and b) $[\text{Ru}(\text{tpy})_2]^{2+}$; GS = ground state, MLCT = metal-to-ligand charge transfer, MC = metal-centered, ISC = inter-system crossing, IC = internal conversion, k_r = radiative decay rate, k_{nr} = non-radiative decay rate; upon excitation with light, the Ru(II) polypyridine complexes are excited into the $^1\text{MLCT}$ state, followed by fast ISC to the $^3\text{MLCT}$ state, which either radiatively decays *via* phosphorescence or undergoes IC to the ^3MC state, followed by non-radiative decay.

As has been previously described in Equation I-1 and Equation I-2, the excited-state lifetime τ depends on the radiative decay rate constant k_r and the non-radiative decay rate constant k_{nr} as well as the rate constant related to the internal conversion to the ^3MC state k^0 and the activation energy barrier for this transition E_a .^[51, 154] The non-radiative decay rate k_{nr} has two contributions: From the ^3MC state and directly from the $^3\text{MLCT}$ state to the ground state. To reduce this term, it is important to decrease the accessibility of the ^3MC state. To do so, the energy gap between the $^3\text{MLCT}$ state and the ^3MC state needs to be increased either by destabilizing the ^3MC state or by stabilizing the $^3\text{MLCT}$ state. However, if the $^3\text{MLCT}$ energy gets too low, the non-radiative decay rate will increase due to the energy gap law.^[49, 154-155]

As mentioned above, the rate law is temperature dependent and, therefore, the temperature has a great effect on the photophysical properties. Furthermore, other external factors such as solvent polarity or the pH value can affect absorption and emission properties. Polar solvents can enhance the charge displacement in the $^3\text{MLCT}$ state and thus increase the excited-state lifetime.^[156-157] By using different pH

environments, certain groups such as NH imidazole groups can be protonated or deprotonated, completely altering the emission behavior.^[156, 158]

This chapter gives a review of recent developments in the design of Ru(II) complexes with tridentate metal ion receptors and discusses their photophysical and electrochemical properties. The impact of external factors, such as pH value, solvent polarity, and temperature, will not be considered here. Instead, different designs of Ru(II) complexes with tridentate metal ion receptors and their photophysical and electrochemical properties are discussed, analyzing the effects of substitution on the terpyridine ligands, non-symmetrical complexes, different bite-angles as well as the incorporation of multiple metal centers.

I.7.1. Ligand Design

Substitution of the Terpyridine Backbone. The addition of electron-withdrawing (EWGs) and electron-donating groups (EDGs) on the terpyridine ligands allows to tune the energy of the molecular orbitals and thus vary the photophysical and electrochemical properties of the corresponding Ru(II) complexes. EWGs stabilize the LUMO and, therefore, induce extended electronic delocalization towards the ligand.^[157] The result is a stabilization of the emitting ³MLCT, while the ³MC state is hardly changed in energy, which leads to an increase of the surface crossing barrier.^[159] EDGs on the other hand destabilize the HOMO.^[157] Both EWGs and EDGs result in a red shift of the ¹MLCT absorption maxima and the ³MLCT emission band. Yet only EWGs increase the ³MLCT to ³MC energy gap, leading to increased excited-state lifetimes and emission quantum yields, particularly for complexes with electron-withdrawing substituents or both electron-withdrawing and electron donating substituents.^[159-160]

With regard to the electrochemical properties, complexes with EWGs are expected to display a shift to more positive potentials of their oxidation couple Ru(II)/ Ru(III) as well as the ligand-centered reductions due to electron deficiency resulting in a reduced ligand field.^[161-162] Complexes with strong EDGs are expected to have a less positive shift in their oxidation potential compared to [Ru(tpy)₂]²⁺.^[163]

The use of both electron-donating and electron-withdrawing ligands can lead to molecular dyads, which exhibit charge separation within the molecule. Barthelmes *et*

al. found that in such a donor-acceptor design (see **S01**, **S02** and **S03** in Figure I-17 and Table I-2), the emission decreases with the electron-donating character of the substituent due to reductive emission quenching leading to a charge-separated species.^[164] The introduction of more electron-accepting groups on the other hand increases the emission quantum yield by increasing the ³MLCT-³MC gap (see **S04** vs. **S05**).^[159] The introduction of POM units (see **S06**) could be expected to quench the emission by oxidative quenching. However, it mainly acts as an electron-accepting substituent, increasing the emission of the complexes. This observation can be ascribed to the increased π -conjugation of the POM-substituted ligand, which stabilizes the excited ³MLCT state.^[164] The addition of dirhodium dimers as EWG by Cooke *et al.* on the other hand is found to quench the emission due to efficient energy transfer from the ruthenium metal center to the dirhodium units (see **S07**).^[161]

A study by Pal *et al.* on Ru(II) bis-terpyridine complexes with styrylbenzene units carrying different electron-donating and withdrawing substituents (see **S08** to **S12**) showed a correlation of the excited-state lifetimes of the complexes and the Hammett parameters σ_p , i.e., the excited-state lifetimes increase with increasing electron-donating character of the substituent.^[157] This observation contrasts with the previously described effect and the authors suggest that an inter-ligand charge transfer (ILCT) state coexists with the ³MLCT state. The ³ILCT state leads to the observed biexponential decay and has a greater contribution for more electron-donating substituents. Furthermore, the styrylbenzene units are photoactive for trans-cis isomerization. Conversion from the trans-trans-isomer to the trans-cis-isomer occurring during photolysis, shown in Figure I-18, considerably decreases the π -conjugation of the ligand, which decreases the MLCT and ILCT absorption band intensities. After photolysis, the emission wavelength is slightly blue-shifted and the luminescence is greatly reduced (~80%), resulting in a decreased excited-state lifetime (~65% lower). Both experimental results and theoretical calculations show that rather than forming a cis-cis isomer upon irradiation with UV-light, a trans-cis isomer is formed (Figure I-18). The initial trans-trans isomer and hence the initial photophysical properties can be restored by interacting with visible light.^[157, 165] The authors assume that emission and photoisomerization are competitive processes, i.e., the trans-cis isomerization probably involves a ³ILCT state, which is at equilibrium with the emissive

$^3\text{MLCT}$ state.^[156] These photoisomerizable complexes can be used as “switch on – switch off” components.^[156-157, 165]

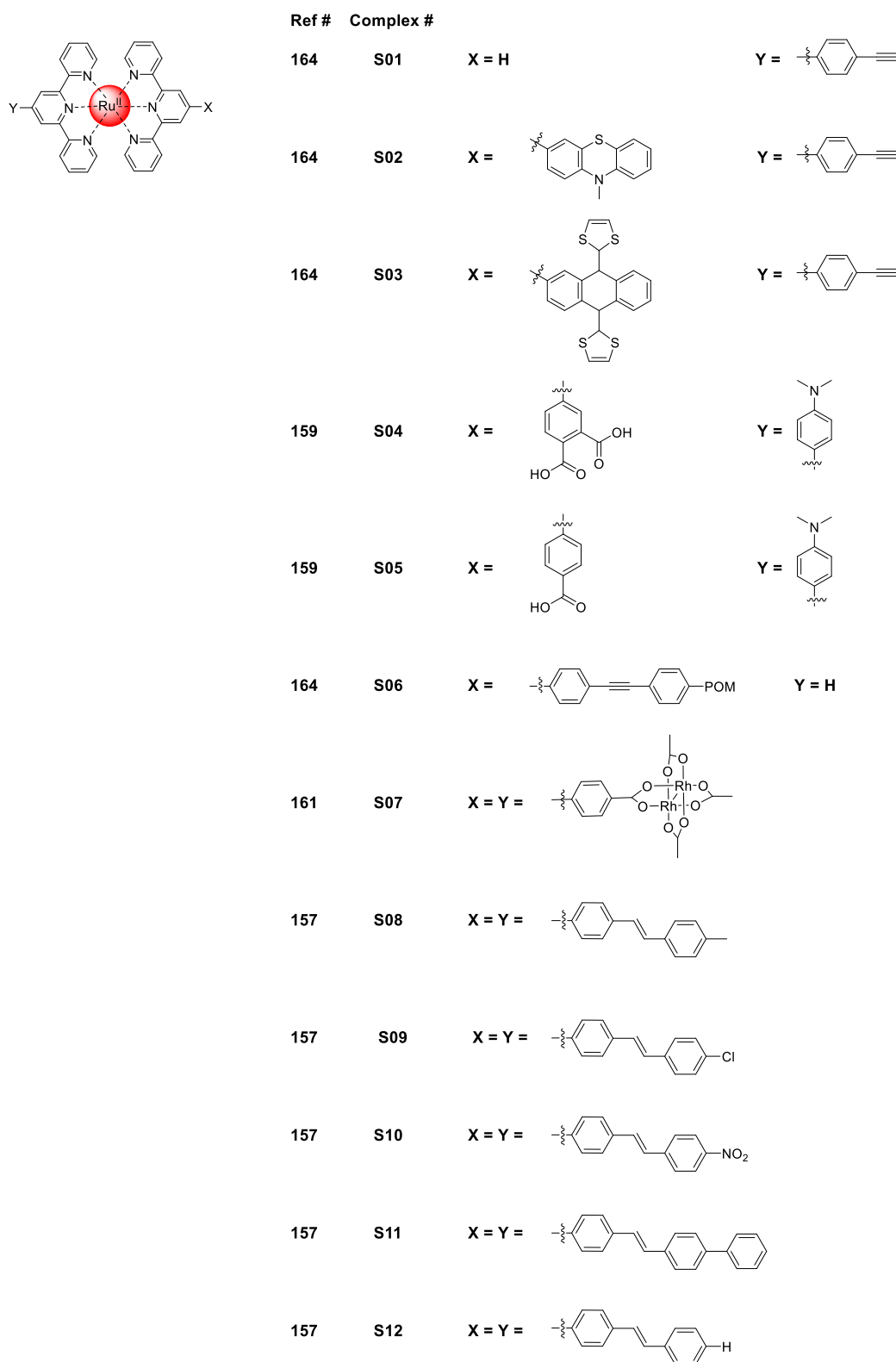


Figure I-17. Structures of complexes **S01** to **S12** bearing electron-donating and/or electron-withdrawing substituents.

Table I-2. Photophysical and electrochemical properties of [Ru(tpy)₂]²⁺ based complexes **S01** to **S12** depending on their substituents.

Complex	$\lambda_{\text{abs}}^{\text{a}}$ / nm	$\epsilon / 10^4 \text{ M}^{-1} \cdot \text{cm}^{-1}$	λ_{em} / nm	τ / ns	Φ	E_{ox} / V	$E_{\text{red}} / \text{V}$	Ref
[Ru(tpy) ₂] ²⁺	474	1.04	629 ^a	0.25	$\leq 5 \cdot 10^{-6}$	1.31 ^{b,f}	-1.23; -1.47	[166]
S01 ^c	490	2.23	660 ^{a,c}	n.d.	n.d.	0.82 ^{d,g}	-1.56; -1.81	[164]
S02 ^c	506	3.35	662 ^{a,c}	n.d.	n.d.	0.37 ^{d,g} ; 0.73 (irr); 0.78	-1.57; -1.80	[164]
S03 ^c	505	3.52	n-e	n.d.	n.d.	-0.03/ 0.84	-1.55; -1.76	[164]
S04 ^b	501	3.25	674 ^{a,b}	10.2	n.d.	0.90 ^{b,f} ; 1.32	-1.22; -1.52	[159]
S05 ^b	502	3.55	662 ^{a,b}	5.5	n.d.	0.90 ^{b,f} ; 1.34	-1.27; -1.51	[159]
S06 ^c	493	2.68	665 ^{a,c}	n.d.	n.d.	0.75 ^{d,g}	-1.46; -1.65; -1.84	[164]
S07 ^b	492	2.12	n-e	n-e	n-e	1.22 ^{b,f}	-1.18 (irr); -1.35 (irr); -1.63 (irr)	[161]
S08 ^b	497	2.71	659 ^{a,b}	6.0; 67.7	$10.5 \cdot 10^{-4}$	1.28 ^{b,e}	-1.16; -1.40	[157]
S09 ^b	496	3.06	660 ^{a,b}	3.8; 52.1	$8.20 \cdot 10^{-4}$	1.28 ^{b,e}	-1.03; -1.37	[157]
S10 ^b	498	3.71	669 ^{a,b}	1.4; 10.0	$6.80 \cdot 10^{-4}$	1.29 ^{b,e}	-0.91; -1.24; -1.47	[157]
S11 ^b	497	3.32	664 ^{a,b}	5.8; 64.3	$9.50 \cdot 10^{-4}$	1.28 ^{b,e}	-1.15; -1.35	[157]
S12 ^b	495	3.24	658 ^{a,b}	4.0; 54.5	$8.60 \cdot 10^{-4}$	1.29 ^{b,e}	-1.15; -1.39	[157]

a) at 298 K; b) in MeCN; c) in DMSO; d) in DMF; e) V vs. Ag/AgCl; f) V vs. SCE; g) V vs. Fc/Fc⁺; n.d.: not determined; n-e: non-emissive; irr: irreversible.

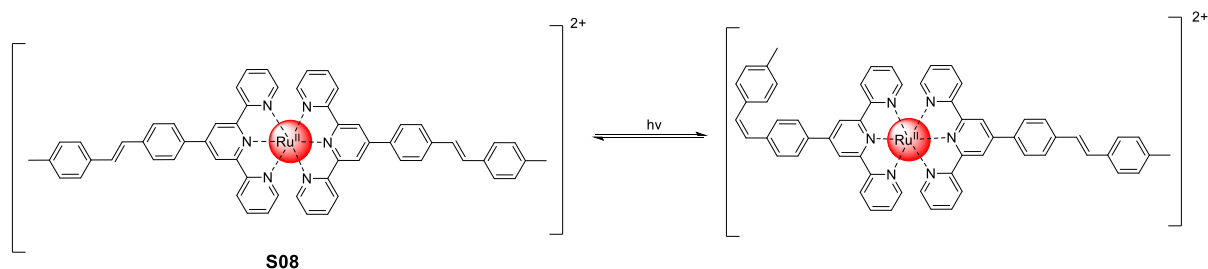


Figure I-18. Photoisomerization of the trans-trans complex **S08** to its cis-trans form upon irradiation with UV light.^[157]

Tridentate Ligands with Different N-Heterocycles. Apart from the implementation of EWG or EDG, the electron-accepting/donating character of the tridentate metal ion receptor can further be tuned by the introduction of other heterocycles, i.e., replacement of one or more of the pyridine rings in the terpyridine unit by other nitrogen containing heterocycles such as triazines, pyrimidines or *N*-heterocyclic carbenes (NHCs).

Cooke *et al.* replaced the center pyridine ring by a triazine ring (compare **N01** and **N02**, see Figure I-19 and Table I-3). Due to the additional nitrogen atoms, the formed ligand is more electron-accepting, which strongly stabilizes the ligand-centered LUMO. As a result, the electron density at the metal center of **N02** is reduced, the oxidation potential for the Ru(II)/Ru(III) couple is shifted anodically and the absorption as well as the emission are red shifted compared to **N01**. Even though a stabilization of the LUMO increases the energy gap between the ³MLCT state and the ³MC state, the emission of **N02** is quenched compared to **N01**. This observation is common for triazine containing ligands and can be explained by the energy gap law.^[155, 161, 167]

The introduction of additional nitrogen atoms to the central ring can also lead to a planarization of the metal-binding core and substituents (e.g., a phenyl ring) in the 4-position of the central ring due to hydrogen bonding. A higher planarity within the ligand leads to a more delocalized aromatic system and can further improve the photophysical properties due to reduced coupling of the ground state and the excited state. When comparing complexes **N03** and **N04**, the additional nitrogen atom in the central ring on one of the ligands leads to an anodic shift of the redox potentials, a red shift of the emission wavelength and an increased quantum yield and excited-state lifetime by an order of magnitude.^[162, 168-169]

Another possibility studied by several groups involves carbenes. Sinn *et al.* investigated complexes where one of the peripheral pyridine rings is exchanged by a 1,2,3-triazolide (**N05**) or a 1,2,3-triazolylidene (**N06**) ring, leading to cyclometalated complexes. The 1,2,3-triazolide ring acts as a strong σ -donor as well as π -donor, which leads to a destabilization of the ligand-centered LUMO. In contrast, the 1,2,3-triazolylidene ring is also a strong σ -donor but allows for weak π back-bonding and thus stabilizes the LUMO, therefore further increasing the $^3\text{MLCT}$ to ^3MC energy gap. Both complexes exhibit a drastic increase in excited-state lifetime as well as luminescence quantum yield, even in aerated solutions. The improved photophysical properties can be assigned to the destabilized ^3MC state due to the strong σ -donor character of both ligands.^[170] Even better results regarding the luminescence properties of Ru(II) complexes using carbene containing ligands were achieved by Torres *et al.* (**N07**). The use of NHCs leads to excited-state lifetimes in the μs region and emission quantum yields above 1%, making these complexes comparable to $[\text{Ru}(\text{bpy})_3]^{2+}$.^[171]

Table I-3. Photophysical and electrochemical properties of $[\text{Ru}(\text{tpy})_2]^{2+}$ based complexes **N01** to **N07** with different nitrogen containing heterocycles.

Complex	$\lambda_{\text{abs}}^{\text{a}}$ / nm	ϵ / 10^4 $\text{M}^{-1}\cdot\text{cm}^{-1}$	λ_{em} / nm	τ / ns	Φ	E_{ox} / V	E_{red} / V	Ref
N01 ^b	492	1.33	646 ^{a,b}	3.6	$1.0 \cdot 10^{-4}$	1.22 ^{b,c}	-1.27; -1.51; -1.70	[161]
N02 ^b	500	1.46	716 ^{a,b}	8.4	$3 \cdot 10^{-5}$	1.56 ^{b,c}	-0.68; -0.85; -1.47; -1.70	[161]
N03 ^b	497	3.4	658 ^{a,b}	3.8	$74 \cdot 10^{-5}$	0.89 ^{b,d}	-1.51; -1.81; -2.02	[169]
N04 ^b	490	2.3	738 ^{a,b}	30	$17.5 \cdot 10^{-4}$	1.36 ^{b,c}	-0.88; -1.35; -1.57	[168]
N05 ^b	505	1.21	730 ^{a,b}	35	$20 \cdot 10^{-4}$	0.25 ^{b,d}	-1.93	[170]
N06 ^b	480	1.04	650 ^{a,b}	45	$82 \cdot 10^{-4}$	0.70 ^{b,d}	-1.75	[170]
N07 ^b	383	1.29	532 ^{a,b}	1548	$10.5 \cdot 10^{-3}$	1.12 ^c	-1.93	[171]

a) at 298 K; b) in MeCN; c) V vs. SCE; d) V vs. Fc/Fc⁺.

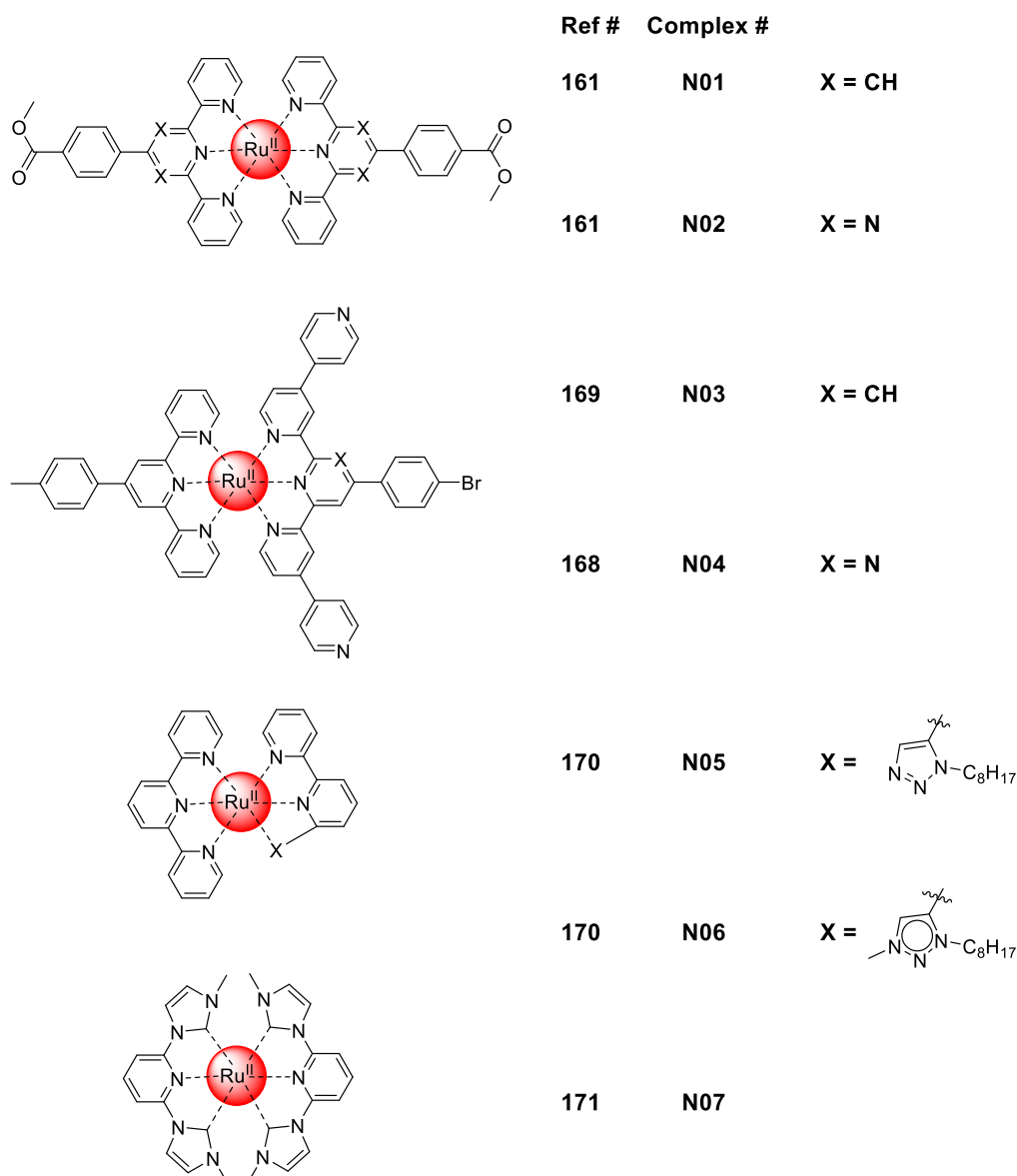


Figure I-19. Structures of complexes **N01** to **N07** involving different nitrogen containing heterocycles.

Bite Angle. As mentioned above, the decreased bite-angle of terpyridine metal ion receptors leads to a distorted octahedral coordination geometry and thus to a reduced ligand-field strength, which again results in an efficient non-radiative deactivation *via* the 3MC state.^[150] Thus, expanding the terpyridine metal ion receptor, either by introducing flexible bridges between the pyridine rings or by expanding the conjugated system, is an obvious approach to improve the photophysical properties of Ru(II) bis-terpyridine complexes.

Abrahamsson *et al.* followed this approach of expanding the bite-angle of the tridentate metal ion receptor by using 2,6-di(quinolin-8-yl)pyridine ligands to form Ru(II) complex **B01** (see Table I-4 and Figure I-20), which exhibits almost ideal octahedral symmetry. The study showed that the increased bite-angle leads to both an increased activation energy for the non-radiative decay *via* the metal-centered state as well as a decrease of the direct non-radiative decay from the $^3\text{MLCT}$ state. The latter effect is due to decreased singlet-triplet mixing and thus decreased rate constants for both the radiative and non-radiative decay from the $^3\text{MLCT}$ state back to the ground state. The complex exhibits an excited-state lifetime of 3 μs and an emission quantum yield of 2%.^[172]

An expanded metal ion receptor can furthermore allow for more flexibility, which can lead to different coordination modes. In the homoleptic complex **B02**, the ligands coordinate in a facial geometry, leading to the complex being non-emissive at room temperature due to a non-radiative decay *via* a ligand-to-metal charge transfer (LMCT) state. In the heteroleptic complex **B03** on the other hand, a meridional coordination as in bis-terpyridine complexes is observed. **B03** exhibits a red-shifted absorption and a strong emission compared to $[\text{Ru}(\text{tpy})_2]^{2+}$, as well as a longer excited-state lifetime. The combination of the increased bite-angle and the strong σ -donation from the expanded ligand leads to an increase in energy of the ^3MC state. The electron-accepting terpyridine ligand on the other hand results in a lowered $^3\text{MLCT}$ state, overall increasing the $^3\text{MLCT}$ - ^3MC gap.^[173]

An investigation of complexes **B04** und **B05** by our group also showed a similar impact of the coordination mode. While **B04** coordinates in a meridional fashion, the flexibility of the quinoline moiety in **B05** leads to several diastereomers, with the main isomer exhibiting a facial coordination geometry. Again, the *fac* isomer is not emissive due to the lowest energy level being a LMCT state, which leads to non-radiative deactivation.^[174]

To introduce even more flexibility, Brown *et al.* investigated sulfur-bridged terpyridine type metal ion receptors (see **B06**). The sulfur bridges lead to an irreversible reduction of the ligand in electrochemical experiments. Despite the increased bite-angle, the complex is non-emissive at room temperature due to deactivation *via* the metal-centered state.^[175] In contrast, the introduction of nitrogen and ketone bridges

(see **B07**) leads to a strong increase of both luminescence quantum yield (1.3%) and excited-state lifetime (477 ns) compared to $[\text{Ru}(\text{tpy})_2]^{2+}$. Theoretical calculations as well as comparison to other literature know compounds^[176] confirm that the ketone linker is in fact more beneficial to the photophysical properties compared to the nitrogen linker due to the different shape of the excited-state potentials and thus the excited-state dynamics it causes.^[177]

Complex **B08** is another example for a non-symmetric ligand with an increased bite-angle. The introduction of a methyl bridge increases the bite angle to close to 90° and red-shifts the $^1\text{MLCT}$ absorption band compared to an NHC containing complex without methyl linker. The coordination geometry, which is closer to a perfect octahedron, combined with the strong electron-donating properties of the NHC rings leads to a strong increase in the excited-state lifetime (250 ns in the solid state).^[178]

Table I-4. Photophysical and electrochemical properties of $[\text{Ru}(\text{tpy})_2]^{2+}$ based complexes **B01** to **B08** with expanded bite-angle ligands.

Complex	$\lambda_{\text{abs}}^{\text{a}}$ / nm	$\epsilon / 10^4 \text{ M}^{-1} \cdot \text{cm}^{-1}$	λ_{em} / nm	τ / ns	Φ	E_{ox} / V	E_{red} / V	Ref
B01	n.d.	n.d.	690 ^{a,c}	$3.0 \cdot 10^3$	0.02	n.d.	n.d.	[172]
B02^c	541	0.50	901 ^{a,c}	129	$1.0 \cdot 10^{-3}$	0.50 ^{c,d}	-1.47; -2.01	[173]
B03^c	564	0.19	n-e ^{a,c}	n-e	n-e	1.18 ^{c,d}	-0.29	[173]
B04^c	578	0.71	795 ^{a,c}	7.5	n.d.	1.47 ^{c,d} ; 0.28	-1.48; -1.72; -2.26	[174]
B05^c	506	1.34	n-e ^{a,c}	n-e	n-e	0.31 ^{c,d}	-1.48; -1.80; -2.29 (irr)	[174]
B06^c	452	n.d.	612 ^{b,g}	n.d.	n.d.	1.01 ^{c,e}	-1.91 (irr); -2.09 (irr)	[175]
B07^c	549	0.52	709 ^{a,c}	477	$1.3 \cdot 10^{-2}$	0.92 ^{c,e}	-1.29; -1.46; -2.12; -2.27	[177]
B08^c	407	2.3	558 ^g	250; 5800	n.d.	1.72 ^{c,f} ; 0.89	-1.85; -2.22	[178]

a) at 298K; b) at 77 K; c) in MeCN; d) V vs. SCE; e) V vs. Fc/Fc⁺; f) V vs. Ag/AgCl; g) solid state n.d.: not determined; n-e: not emissive; irr: irreversible.

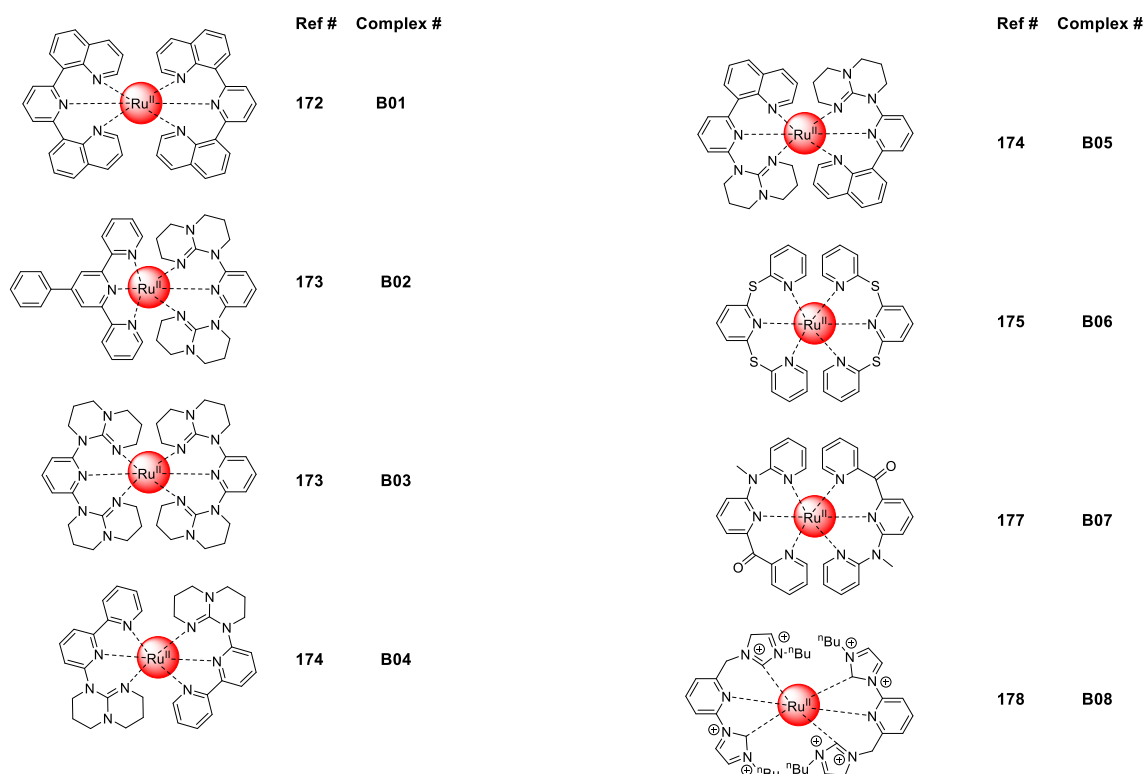


Figure I-20. Structures of complexes **B01** to **B08** with ligands with expanded bite-angles.

Homoleptic vs. Heteroleptic Design. The complexes discussed in the previous sections include both homoleptic, i.e., with identical ligands, and heteroleptic complexes, i.e., with different ligands. As mentioned previously, the use of different ligands, one being electron-accepting and one being electron-donating, can lead to light-induced charge separation, which can be beneficial for certain applications, including photosensitizers in hydrogen evolution photocatalysis.^[160] So far there is no simple relationship between structural design and luminescence properties of these complexes. In fact, the properties of the complex under investigation depend in a non-trivial way on the overall structure, including electron-withdrawing or donating substituents and geometry. Hence, the impact a homoleptic or heteroleptic design has on the photophysical and electrochemical properties of Ru(II) complexes is best studied by direct comparison.

Comparing the homoleptic complex **S08** (see Figure I-17 and Table I-2) with the heteroleptic complex **H01** (see Figure I-21 and Table I-4) or the homoleptic complex **H02** with the heteroleptic complex **H03**, the measured excited-state lifetimes as well as the luminescence quantum yields are increased in the homoleptic complexes. This

observation is attributed to a higher conjugation of the terpyridine ligand induced by the introduction of an additional styrylbenzene or anthraimidazoledione moiety in the homoleptic complexes, respectively, leading to a stabilization of the $^3\text{MLCT}$ state.^[165, 179] Interestingly, the observed trend of the quantum yield depending on the electron-donating character of the substituent seen in complexes **S08** to **S12** is different for a respective series of heteroleptic complexes. The reversed trend is due to the tolyl-substituted terpyridine ligand on the heteroleptic complexes, which is electron donating and destabilizes the ^3MC state. Thus, electron-accepting substituents on the opposite ligand enhance the photophysical properties of the complexes, i.e., they increase the excited-state lifetime by stabilizing the $^3\text{MLCT}$ state.^[157, 165]

A comparison of the heteroleptic complex **N03** (Table I-3 and Figure I-19) with both its homoleptic analogues **H04** and **H05** highlights the impact each ligand has on the properties of the complex. The electron-withdrawing ligand, which further exhibits a larger delocalized system, mainly affects the emissive $^3\text{MLCT}$ state and with it the energy gap to the non-emissive ^3MC state. Hence, both complexes **N03** and **H05** bearing pyridine-substituents exhibit similar emission properties, with excited-state lifetimes (2.4–3.8 ns) and quantum yields ($74\text{--}78 \times 10^{-5}$) increased by an order of magnitude compared to **H04** ($\tau < 1$ ns; $\Phi = 3 \times 10^{-5}$). The electron-donating tolyl-substituted ligand on the other hand has a slight HOMO-destabilizing effect, which results in an increasing cathodic shift of the oxidation potential with increasing number of tolyl-substituted ligands.^[162, 169]

When comparing the homoleptic complexes **N01** and **S07** with the heteroleptic complex **H06**, the excited-state lifetime decreases with increasing number of dirhodium dimer units. These moieties act as electron reservoirs and electron transfer from the ruthenium core to the dirhodium dimers quenches the luminescence, leading to a barely emissive heteroleptic complex **H06**.^[161]

Overall, these examples underscore the importance to take the properties of all ligands into consideration as they affect the electronic structure of the complex relatively independently. Hence, the heteroleptic design offers vast opportunities to tune the properties of the Ru(II) complexes for the desired application.

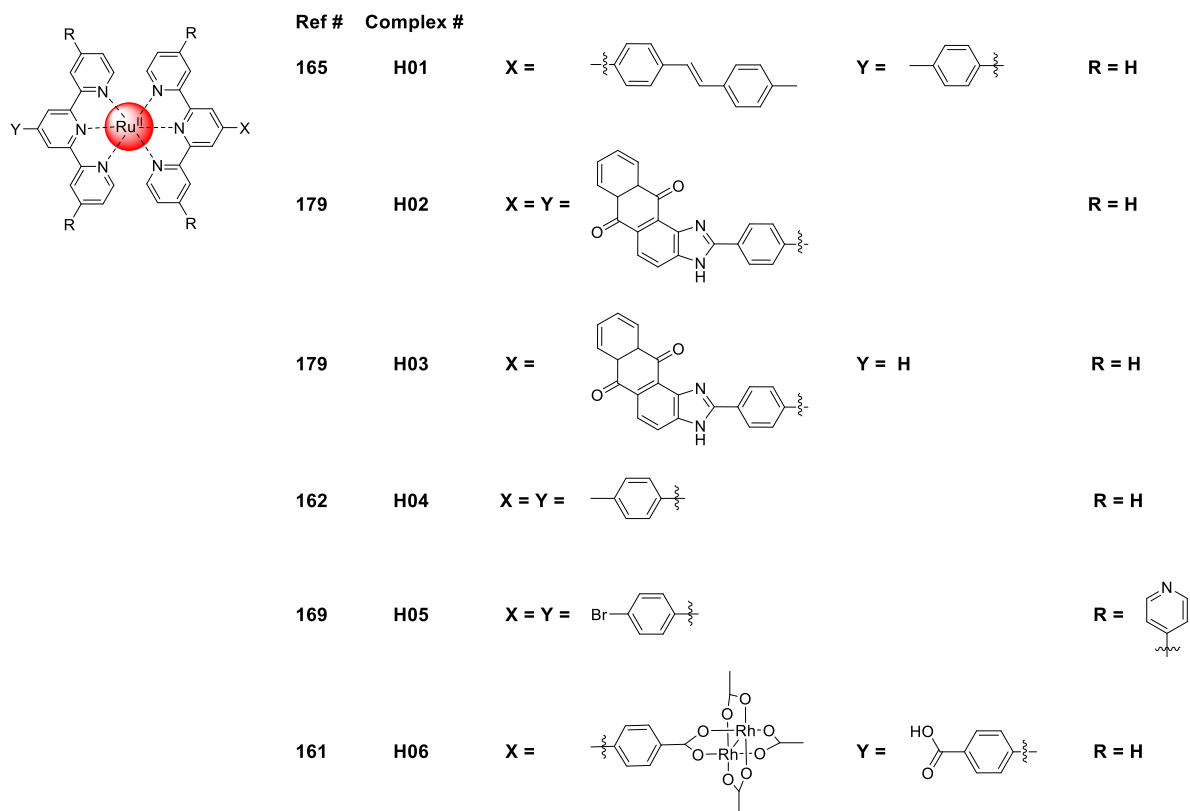


Figure I-21. Structures of homoleptic and heteroleptic complexes H01 to H06.

Table I-5. Photophysical and electrochemical properties of $[\text{Ru}(\text{tpy})_2]^{2+}$ based homoleptic and heteroleptic complexes **H01** to **H06**.

Complex	$\lambda_{\text{abs}}^{\text{a}}$ / nm	$\epsilon /$ 10^4 $\text{M}^{-1}\cdot\text{cm}^{-1}$	λ_{em} / nm	τ / ns	Φ	E_{ox} / V	$E_{\text{red}} / \text{V}$	Ref
H01 ^b	495	1.83	662 ^{a,b}	1.50, 8.43	$4.3 \cdot 10^{-4}$	1.28 ^{a,e}	-1.17; -1.40; -1.84; -2.12	[165]
H02 ^b	496	3.91	658 ^{a,b}	9.8	$3.1 \cdot 10^{-3}$	1.28 ^{b,e}	-1.01; -1.30; -1.49; -1.91	[179]
H03 ^b	488	2.35	653 ^{a,b}	2.0; 5.2	$1.2 \cdot 10^{-3}$	1.30 ^{b,e}	-1.02; -1.31; -1.51	[179]
H04 ^b	491	2.3	646 ^{a,b}	0.74	$3 \cdot 10^{-5}$	1.22 ^{b,c}	-1.24; -1.48	[162]
H05 ^b	502	3.0	649 ^{a,b}	2.4	$78 \cdot 10^{-5}$	0.94 ^{b,d}	-1.45; -1.64; -1.92; -2.06	[169]
H06 ^b	492	1.43	658 ^{a,b}	2.9	$2 \cdot 10^{-5}$	1.26 ^{b,c}	-1.24(irr); -1.46 (irr); -1.60 (irr)	[161]

a) at 298 K; b) in MeCN; c) V vs. SCE; d) V vs. Fc/Fc⁺; e) V vs. Ag/AgCl; irr: irreversible.

Other Chromophoric Units. Besides electron-acceptors or donors, substituents at the metal ion receptor can exhibit further functionality, such as photoisomerization already seen in the example of **S08**. On the other hand, organic chromophores as substituents placed judiciously in the periphery of the terpyridine ligands can lead to vectorial electron or energy transfer.

Puntoriero *et al.* investigated a bichromophoric system with one Ru(II) bis-terpyridine unit connected to a fused expanded bipyridinium unit (see **C01**, Figure I-22 and Table I-6). While the chromophore is not emissive at room temperature, it exhibits photo-induced electron transfer between the components. Both chromophores can be excited selectively at different wavelengths, leading to different excited-state decays. If the MLCT transition of the terpyridine unit is excited, oxidative photo-induced electron transfer takes place, followed by rapid charge recombination. If the organic dye is excited, a charge-separated state can be formed *via* reductive photo-induced charge separation.^[64]

A study by Eberhard *et al.* on another bichromophoric system highlights the influence of the spacer between the two chromophoric units. If the Ru(II) bis-terpyridine unit is coupled directly to the acridinium dye (**C02**), the organic chromophore acts as an EWG, leading to a shift of the redox potentials to more positive voltages. In complexes **C03** and **C04**, however, the spacer counterbalances the electron-withdrawing character of the acridinium group or leads to an electronic decoupling of the metal center and the dye. Furthermore, the absorptivity of the complexes depends on the spacers. **C03**, with a phenyl spacer, exhibits a stronger absorption, a blue-shifted emission, and a longer excited-state lifetime compared to **C02** with no spacer. The thionyl spacer in **C04** on the other hand leads to a red-shifted absorption and emission and a shorter excited-state lifetime in comparison with **C02**. None of these complexes is emissive at room temperature. The reason are both thermally activated non-radiative decay processes *via* the ^3MC state and the ^3LC state.^[163]

Table I-6. Photophysical and electrochemical properties of $[\text{Ru}(\text{tpy})_2]^{2+}$ complexes **C01** to **C04**, incorporating an organic chromophore.

Complex	$\lambda_{\text{abs}}^{\text{a}}$ / nm	$\epsilon / 10^4 \text{ M}^{-1} \cdot \text{cm}^{-1}$	λ_{em} / nm	τ / ns	Φ	E_{ox} / V	$E_{\text{red}} / \text{V}$	Ref
C01 ^c	493	3.70	636 ^{b,c}	13.7	n.d.	1.23 ^{cd}	-0.42	[64]
C02 ^c	493	2.50	664 ^{b,c}	20.2*10 ⁵ ; 1.15*10 ⁵	n.d.	1.01 ^{ce}	-0.77; -1.14; -1.34; -1.90	[163]
C03 ^c	493	3.91	648 ^{b,c}	95.0*10 ⁵ ; 12.0*10 ⁵	n.d.	0.88 ^{ce}	-0.89	[163]
C04 ^c	510	4.74	672 ^{b,c}	14.3*10 ⁵ ; 0.99*10 ⁵	n.d.	0.88 ^{ce}	-0.79; -1.15 (irr); -1.24 (irr)	[163]

a) at 298 K; b) at 77 K; c) in MeCN; d) V vs. SCE; e) V vs. Fc/Fc⁺; n.d.: not determined; irr: irreversible.

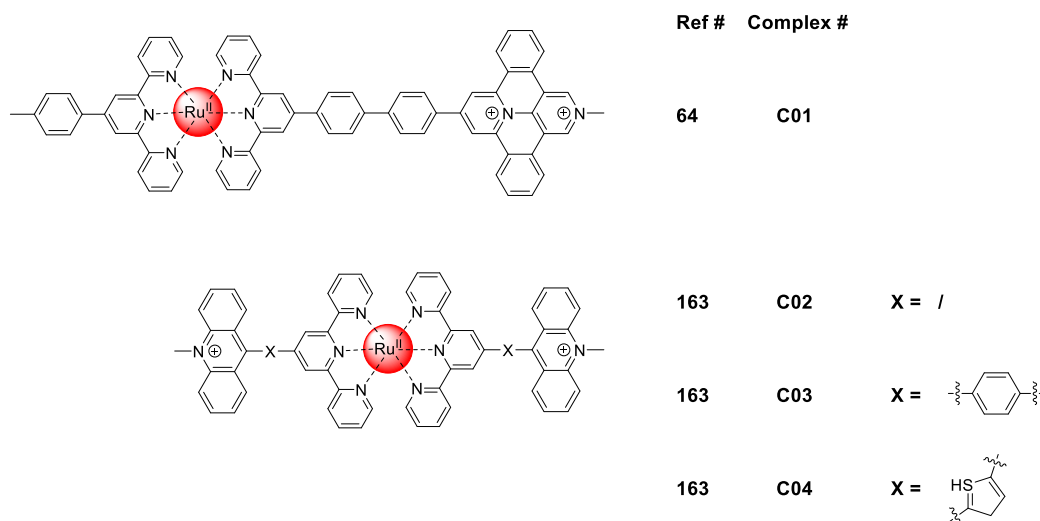


Figure I-22. Structures of terpyridine complexes incorporating an organic chromophore **C01** to **C04**.

I.7.2. Supramolecular Systems

In natural photosynthesis, chlorophyll acts as the main light absorbing species. Chlorophyll is a mononuclear porphyrin-like complex with a Mg^{2+} center. In nature, there is a great excess of the number of light absorbing molecules compared to the number of reaction centers.^[25] Hence, most chlorophyll molecules do not absorb light themselves but rather act as antennas, i.e., an excited chlorophyll molecule passes the absorbed energy to another chlorophyll molecule *via* exciton transfer. An energy gradient, with the lowest excited-state energy being located close to the reaction center, allows for a directional energy transfer.^[180] To achieve similar light harvesting artificial systems, which offer directional electron or energy transfer, many studies have focused on supramolecular systems. One of the attractive properties of terpyridine units as metal ion receptor is the possibility to design a variety of polytopic ligands, i.e., ligands with more than one metal binding site. In contrast to 2,2'-bipyridine ligands, the terpyridine unit allows for easy design of linear structures, which offer interesting opportunities for directional energy or electron transfer, e.g., in molecular wires.^[181]

To induce electron or energy transfer, the polynuclear system needs to exhibit dissymmetry, which can be introduced either by different binding sites leading to different electronic environments for the metal centers, or coordination of different metal ions within one structure. The energy transfer occurs from the chromophore site

with a larger HOMO-LUMO gap towards the chromophore site with a smaller HOMO-LUMO energy gap as the lower energy of the latter makes this process thermodynamically favorable.^[182] Careful ligand design, i.e., varying the coordination sites and thus fine-tuning the electronic environments, and/or implementation of different metal centers, can thus lead to directional energy transfer in antenna like systems.^[183] Different strategies to implement energy and electron transfer within polynuclear complexes are discussed in the following sections.

The energy transfer in polynuclear systems can follow two different mechanisms. The Förster resonance energy transfer (Chapter I.4.1) becomes particularly important if the chromophore units are well separated or the spacer between them is saturated.^[183] The Dexter energy transfer on the other hand takes place at much shorter distances. Hence, for this energy transfer mechanism to occur within a polynuclear structure, the spacer between the chromophore centers needs to be highly conjugated or very short, as the electron exchange requires sufficient overlap of the wave functions of the donor and the acceptor parts. Which energy transfer mechanism takes place greatly depends on the design of the spacer.^[56-57] In the following sections, several examples of polynuclear and polychromophoric systems are discussed.

Homometallic. As mentioned above, to observe directional energy transfer between different metal centers in a polynuclear system, their electronic surrounding needs to be different. In the octanuclear complex **P01** (see Figure I-23 and Table I-7) all metal centers share an identical environment. Furthermore, due to the great distance between the metal centers and the saturated linkers, no coupling is observed between the metal centers, i.e., the reduction potential as well as the luminescence properties of **P01** are very similar to those of an analogous mononuclear complex.^[184]

The presence of non-equivalent metal centers, e.g., in complex **P02**, can result in energy transfer. In the case of **P02**, a broad absorption band in the visible region is observed, indicating that there is more than one absorbing MLCT state. However, both at room temperature and at 77 K only one emission with a mono-exponential decay is observed. Cerfontaine *et al.* thus conclude a very fast energy transfer (on a fs timescale), following a Dexter mechanism from the peripheral coordination sites to the

central metal center. Due to the large delocalization of the excited state across the bridging ligand, an increase of two orders of magnitude for both the excited-state lifetime and the quantum yield are observed compared to a mononuclear analogue.^[184]

Another example for energy transfer within a binuclear complex with chemically very similar environments of the coordination sites was studied by Kreitner *et al.* Complex **P03** exhibits a dual emission at room temperature, which is excitation-wavelength independent. At 77 K, only one emission is observed, which leads the researchers to the conclusion that a thermally activated electron transfer, involving the bridging ligand, is responsible for the dual emission observed at room temperature.^[185]

The comparison of **P04** and **P05** highlights again the impact of the bridging ligand. These complexes use a similar bridging ligand but in **P04** the imidazole is not directly coordinated while in **P05** a ruthenium ion is coordinated directly by one of the imidazole nitrogen atoms. Both complexes exhibit a biexponential decay with the longer excited-state lifetime coming from the bipyridine coordinated ruthenium metal center and the shorter excited-state lifetime being assigned to the terpyridine unit. However, **P04** is strongly luminescent at room temperature ($\Phi = 11.1 \cdot 10^{-2}$) while the emission of **P05** is greatly reduced ($\Phi = 4 \cdot 10^{-3}$). The low emission of **P05** is due to energy transfer from the peripheral metal centers to the center terpyridine unit.^[186-187]

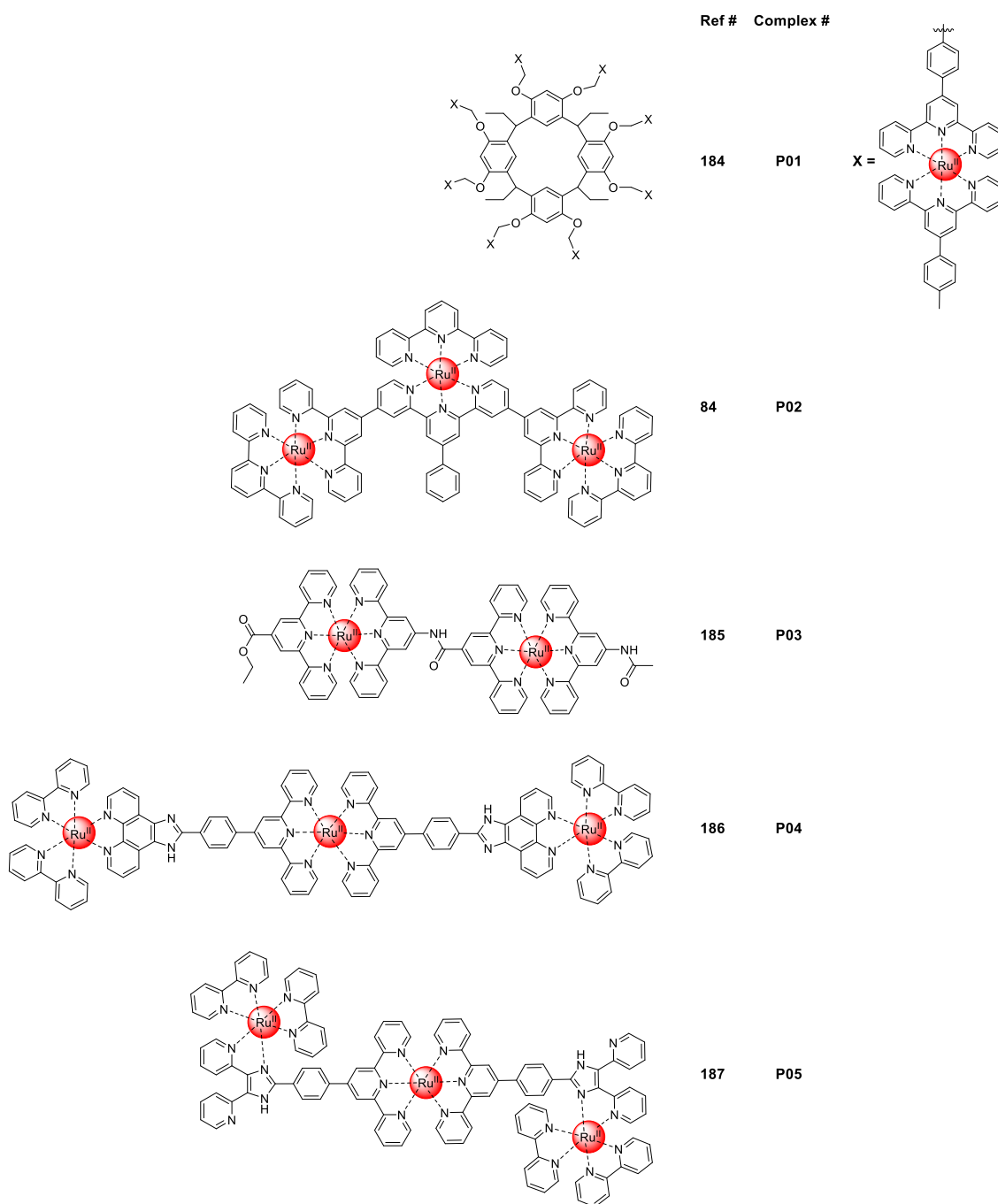


Figure I-23. Structures of polynuclear terpyridine complexes incorporating only ruthenium metal centers **P01** to **P05**.

Table I-7. Photophysical and electrochemical properties of [Ru(tpy)₂]²⁺ based polynuclear complexes **P01** to **P05**, incorporating only ruthenium metal centers.

Complex	$\lambda_{\text{abs}}^{\text{a}}$ / nm	$\epsilon / 10^4 \text{ M}^{-1} \cdot \text{cm}^{-1}$	λ_{em} / nm	τ / ns	Φ	E_{ox} / V	E_{red} / V	Ref
P01 ^b	491	26.6	n.d.	5.30	n.d.	1.25 ^{b,d}	-1.19; -1.41	[184]
P02 ^b	497	4.10	682 ^{a,b}	101	$1.4 \cdot 10^{-3}$	1.39 ^{b,d}	-0.64 ^{c,d} ; -0.96; -1.30	[84]
P03 ^b	504	6.30	684 ^{a,b}	24; 44	$3.2 \cdot 10^{-4}$	0.91 ^{b,e}	-1.49; -1.78	[185]
P04 ^b	496	5.32	599 ^{a,b}	9.70; 112	$1.11 \cdot 10^{-1}$	0.86 ^{b,d} ; 1.34	-1.45; -1.70; -1.92	[186]
P05 ^b	490	3.11	694 ^{a,b}	1.5; 52	$4.16 \cdot 10^{-3}$	1.01 ^{b,d} ; 1.20; 1.27	-1.40; -1.67; -1.98	[187]

a) at 298 K; b) in MeCN; c) in DMF; d) V vs. Ag/AgCl; e) V vs. Fc/Fc⁺; n.d.: not determined.

Heterometallic. As energy or electron transfer oftentimes is desired within a polynuclear complex, many studies focus on using different metal ions within the same structure. Cerfontaine *et al.* expanded the structure of **P02** discussed above to receive the heptanuclear complex **P06** (see Figure I-24 and Table I-8). The complex absorbs strongly in the visible region and exhibits an even longer excited-state lifetime (161 ns) than **P02** (101 ns). The photoluminescence properties of **P06** are in line with those of an analogous Os(II) complex with no residual luminescence from the ruthenium metal centers. Thus, efficient energy transfer from the peripheral ruthenium units to the central ruthenium units and from there to the osmium metal center is taking place. The photoluminescence is mainly determined by the properties of the final energy acceptor.^[188]

The previous example highlights that the energy transfer within a polynuclear complex always takes place from the larger towards the smaller HOMO-LUMO energy gap. In heteronuclear species, i.e., in polynuclear complexes with different metal ions, this means that energy is usually transferred from, e.g., Ru(II) to Os(II) or Fe(II).^[189-190] However, a study by our group showed that by careful ligand design, the HOMO-LUMO energies can be tuned to invert the electron or energy flow. The peripheral hexahydro-pyrimidopyrimidine ligands in complex **P07** are strong electron donors and thus lead to a strong red shift of the emission compared to an Os(II) reference. **P07** exhibits a relatively short excited-state lifetime of only 5.6 ns with a mono-exponential decay, indicating an efficient energy transfer from the central osmium metal center to the peripheral ruthenium units.^[191]

Polynuclear structures containing Fe(II) metal centers are usually non-emissive due to luminescence quenching *via* the ³MC state. However, if the energy transfer from the Ru(II) to the Fe(II) coordination site is not quantitatively, as in **P08** and **P09**, the longer lived ³MLCT state of the ruthenium metal center can still be observed. In addition, in both **P08** and **P09**, the extension of the conjugated system leads to a stabilized ³MLCT state and hence to a relatively long-lived iron-centered ³MLCT state with 300 ps for **P08** and 23 ps for **P09**.^[187, 192]

Furthermore, there are several studies combining Ru(II) bis-terpyridine units and lanthanide metal ions. Within these structures, energy transfer can take place either from or to the ruthenium metal center, depending on the lanthanide ion used. In **P10** energy transfer from the ⁵D₄ Tb(III) metal-centered state to the Ru(II) ³MLCT state occurs *via* a FRET mechanism. As a result, the excited-state lifetime of the ³MLCT emission is slightly extended to 1.2 ns.^[193] Moore *et al.* studied a series of trinuclear complexes with Ru(II) and lanthanide bis-terpyridine units. The emission intensity and excited-state lifetimes are increased for all lanthanide containing complexes compared to a mononuclear Ru(II) analogue and the effect is strongest when Gd(III) (**P11**) is used. The authors argue that the increase is due to rigidification of the complex and the shorter excited-state lifetimes of **P12** to **P14** compared to **P11** are due to a Dexter energy transfer from the Ru(II) center to the lanthanide center. Hence, the Ru(II) centers in these complexes act as sensitizers for the lanthanide near-infrared emission.^[194]

Furthermore, Ru(II) bis-terpyridine complexes can be used in larger supramolecular structures such as supramolecular cages, e.g., **P15**. A study on these ruthenium-palladium cages showed that the single terpyridine units used in the assembly do not couple with each other and no energy transfer is observed. Instead, the cage structure exhibits the same absorption and emission wavelengths as the monomer they are built from, as well as a comparable excited-state lifetime of 1.21 ns for complex **P15** and 1.26 ns for the monomer.^[195]

In contrast, the multicomponent metal-organic framework constructed from Ru(II) bis-terpyridine complexes linked *via* zinc naphthalene-2,6-dicarboxylic acid units **P16** studied by Luo *et al.* shows a strongly increased room-temperature luminescence with 0.6% quantum yield and an excited-state lifetime of 22 ns, which corresponds to an increase of two orders of magnitude compared to the corresponding mononuclear bis-terpyridine complex.^[196]

Table I-8. Photophysical and electrochemical properties of [Ru(tpy)₂]²⁺ based polynuclear complexes **P06** to **P16**, incorporating different metal ions.

Complex	$\lambda_{\text{abs}}^{\text{a}}$ / nm	$\epsilon / 10^4 \text{ M}^{-1} \cdot \text{cm}^{-1}$	$\lambda_{\text{em}} / \text{nm}$	τ / ns	Φ	E_{ox} / V	$E_{\text{red}} / \text{V}$	Ref
P06 ^b	497	7.79	736 ^{a,b}	161	$1.2 \cdot 10^{-2}$	0.91 ^{b,d} ; 1.31	-0.93; -0.99; -1.20; -1.40	[188]
P07 ^b	n.d.	n.d.	807 ^{a,b}	5.6	n.d.	0.92 ^{c,e} ; 0.72	-1.11; -1.26; -1.44	[191]
P08 ^b	572	3.54	644 ^{a,b}	0.3; 35	$1.23 \cdot 10^{-3}$	0.89 ^{b,d} ; 1.21	-1.22; -1.38	[187]
P09 ^b	486; 574	8.5 ^f	n-e ^{a,b}	129	n-e	n.d.	n.d.	[192]
P10 ^b	490	3.63	687 ^{a,b}	1.2	n.d.	0.93 ^{b,d}	-1.24; -1.73	[193]
P11 ^b	492	n.d.	667 ^{a,b}	2.43	n.d.	n.d.	n.d.	[194]
P12 ^b	492	n.d.	670 ^{a,b,f}	1.76	n.d.	n.d.	n.d.	[194]
P13 ^b	492	n.d.	670 ^{a,b,f}	2.37	n.d.	n.d.	n.d.	[194]
P14 ^b	492	n.d.	670 ^{a,b,f}	2.21	n.d.	n.d.	n.d.	[194]
P15	490	n.d.	640	1.21	n.d.	0.90 ^{b,d}	-1.53 (irr); -1.77	[195]
P16	500	n.d.	686	22.09	$0.6 \cdot 10^{-2}$	n.d.	n.d.	[196]

a) at 298 K; b) in MeCN; c) V vs. SCE; d) V vs. Ag/AgCl; e) in DMF; f) rounded value; n.d.: not determined; irr: irreversible; n-e: not-emissive.

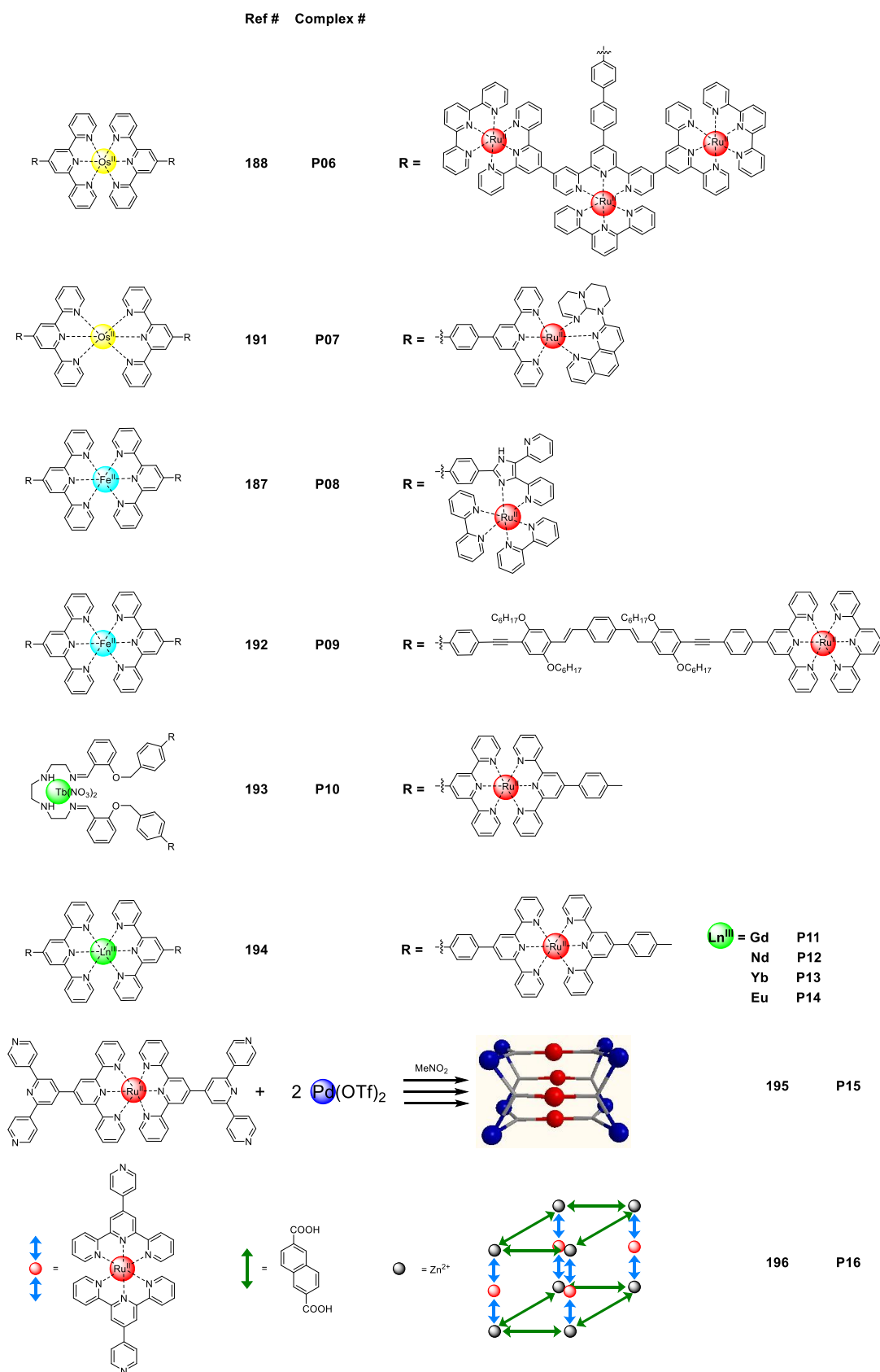


Figure I-24. Structures of polynuclear terpyridine complexes incorporating different metal ions P06 to P16.

1.8. Conclusion

Photocatalytic water splitting to convert and store solar energy in chemical bonds is a promising and widely studied field of research, which aims at contributing to the decarbonization of the energy sector. Typical molecular systems used for artificial photosynthesis consist of three main components: A catalyst, a SED/SEA and a PS. There is a wide variety of studies on each of these components as discussed in this chapter, many of which use $[\text{Ru}(\text{bpy})_3]^{2+}$ and its analogues as a benchmark PS. The terpyridine analogues $[\text{Ru}(\text{tpy})_2]^{2+}$ on the other hand have been mostly disregarded for the application as PS in photocatalytic water splitting due to their poor photophysical properties. However, as the review of recent advances in the literature shows, there are multiple strategies to enhance the photophysical properties of Ru(II) complexes with tridentate metal ion receptors, particularly terpyridine-like ligands. The introduction of electron-accepting and/or electron-donating substituents allows fine-tuning the molecular orbital energies and thus the photophysical properties. Different heterocycles such as NHCs can further act as strong σ -donors and drastically increase the luminescence of the complex. Similar results can be achieved by increasing the bite-angle of the coordinating ligands to reach a coordination geometry closer to a regular octahedron. However, the linker used to expand the ligand has a strong impact on the excited-state decay pathways.

The use of polynuclear complexes opens further energy and electron transfer pathways and the possibility to form antenna systems. The structure of terpyridines makes it a versatile building block for a variety of supramolecular structures such as metal cages^[195] or metallo-supramolecular polymers.^[197-198] Depending on the bridge between the terpyridine units, the coupling of the individual metal centers and energy or electron transfer pathways can be tuned.

Overall, a combination of the discussed strategies enables researchers to design molecules with specific target properties, with excited-state lifetimes up to several microseconds, for a variety of applications such as, organic photocatalysis,^[196] “switch on – switch off” compounds^[186], ion sensing^[179], photodynamic therapy^[199], or nuclear forensics^[200], and of course artificial photosynthesis.^[162]

II. Objective and Scope of this Thesis

The benchmark photosensitizer $[\text{Ru}(\text{bpy})_3]^{2+}$ and its derivatives have found wide applicability in photocatalytic water splitting experiments. However, drawbacks due to chiral structures, a relatively short-lived hydrogen evolution activity, and a rather narrow absorption band are all reasons to search for alternative PSs. The advances in the design of Ru(II) complexes with tridentate ligands and the impact the ligand design has on the photophysical and electrochemical properties are discussed in detail in the previous Chapter I.7. While there are numerous studies following a variety of different strategies to fine-tune the properties of these kinds of complexes, little work has been put into employing them as PSs in photocatalytic systems for hydrogen evolution. This thesis aims at filling this gap and at gaining some insight into the impact ligand design has not only on the photophysical and electrochemical properties, but also how this affects the performance as PS in artificial photosynthetic hydrogen evolution.

The presented studies investigate Ru(II) complexes with a number of altered terpyridine or tridentate ligands, following several strategies, which have been introduced in the introduction. An investigation of the photophysical and electrochemical properties of the complexes is used to verify if the requirements for an efficient PS are met. The experimental results are further used to estimate the driving forces for electron transfer processes in the catalytic system. Photocatalytic experiments are then used to analyze the actual performance as PS. The goal is to understand how the ligand design affects the thermodynamics of the electron transfer processes involving the PS and how the changes are reflected in the activity as PS in hydrogen evolution experiments.

Chapter III discusses the impact of electron-donating and electron-withdrawing substituents, while **Chapter IV** investigates the role of a homoleptic vs. heteroleptic complex design. **Chapter V** focusses on the introduction of additional charge via *N*-methylation on the ligands. In **Chapter VI**, the center pyridine ring of the terpyridine unit is exchanged with a pyrimidine ring and the impact of the different nitrogen-containing heterocycle is investigated. In **Chapter VII**, this pyrimidine design is expanded and dinuclear complexes are formed. These dinuclear species are investigated as a model for larger, polynuclear oligomers and the influence of multiple

metal centers on the activity as PS is analyzed. Finally, in **Chapter VIII**, a brief summary of the presented results is given.

III. Effect of Electron-Donating and Electron-Withdrawing Groups on Ru(II) bis-Terpyridine Complexes

Parts of the presented research were previously published under the title
“Photocatalytic Hydrogen Evolution Driven by a Heteroleptic Ruthenium(II)
Bis(terpyridine) Complex” in *Inorganic Chemistry*.

Reproduced with permission of American Chemical Society from *Inorganic
Chemistry*, **2019**, *58*, 9127-9134.

and

Mira T. Rupp; Daniel Chartrand, Garry S. Hanan, Dirk G. Kurth, CCDC 2090569:
Experimental Crystal Structure Determination, **2021**

Contributions:

Mira T. Rupp: Project design, synthesis, and characterization of ligand and complex, analysis of photophysical and electrochemical properties, article writing.

Thomas Auvray: Project design, collection, and refinement of X-ray diffraction crystal structure, DFT and TD-DFT calculations, revision of the article.

Elodie Rousset: Optimization of the synthesis of the precursor 2-acetyl-4,4'-bipyridine.

Gabriel M. Mercier: Optimization of the synthesis of the precursor 2-acetyl-4,4'-bipyridine.

Daniel Chartrand: Collection and treatment of X-ray diffraction crystal structure

Garry S. Hanan: Supervision, project design, revision of the article.

Dirk G. Kurth: Supervision, project design, revision of the article.

III.1. Introduction

In this chapter, the impact of electron-withdrawing and electron-donating substituents in Ru(II) bis-terpyridine complexes on the photophysical and electrochemical properties as well as on the activity and performance as PS in hydrogen evolution experiments is discussed. A photosensitizer for photocatalytic water splitting needs to exhibit reversible redox behavior as well as strong absorbance of light, and a high luminescence quantum yield alongside an extended excited-state lifetime (see Chapter 1.4 for more details).^[49] Therefore, an evaluation of the electrochemical and photophysical properties can give a good indication whether a complex might be suitable for the application as photosensitizer in photocatalytic water splitting.

Chart III-1 shows the structures of the heteroleptic complexes **III-C1** and **III-C2** under discussion in this chapter. Complex **III-C1** has one terpyridine ligand with two pyridine substituents, which makes this ligand more electron accepting. The extended aromatic system as well as the electron-withdrawing character of the ligand are expected to improve the photophysical properties due to a stabilization of the emissive ³MLCT state, hence decreasing luminescence quenching *via* the non-emissive ³MC state. In addition, the heteroleptic design, with the other ligand bearing a tolyl substituent, making this ligand more electron donating, could result in a directional energy transfer upon excitation. Furthermore, the pyridine substituents might be able to coordinate to the catalyst, enabling more efficient electron transfer from the excited PS to the catalyst.

Complex **III-C2** on the other hand has two electron-donating *tert*-butyl substituents. With two electron-donating ligands, no or a much weaker improvement regarding the photophysical properties is expected as the ³MLCT to ³MC energy gap is not increased. Furthermore, energy transfer towards the ligands in the excited state is expected to be not or less directional. The effect these changes in the ligand design have on the activity as PS is investigated in the following sections.

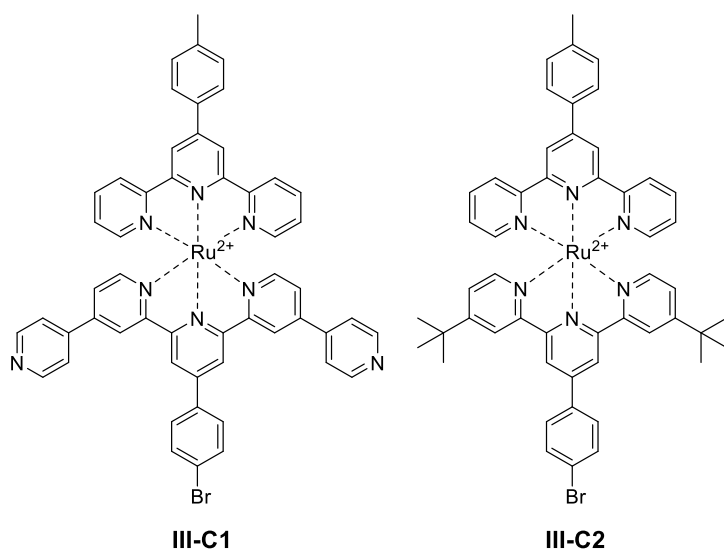


Chart III-1. Structures of the heteroleptic Ru(II) complexes **III-C1** and **III-C2** discussed in this chapter; the PF_6^- counterions are omitted for clarity.

III.2. Results and Discussion

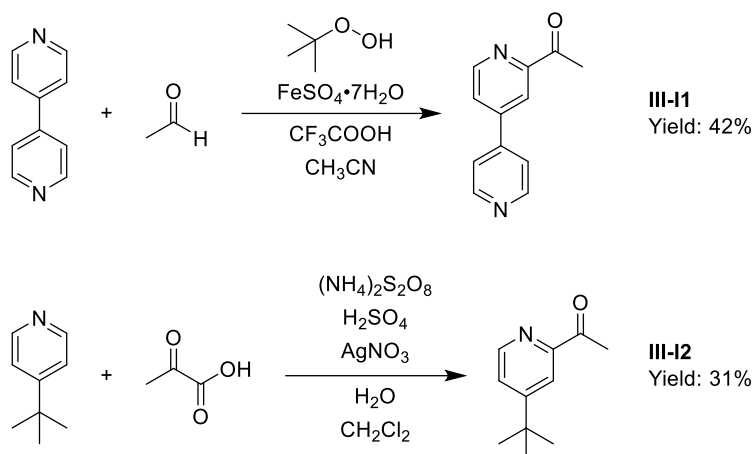
III.2.1. Synthesis

The synthesis of the terpyridine ligands follows a Kroehnke-like synthesis, which involves a 2-acetylpyridine and a benzaldehyde derivative.^[201] Functional groups on both the 2-acetylpyridine and the benzaldehyde allow the introduction of substituents into the terpyridine ligand. While many functionalized benzaldehydes are commercially available, most 2-acetylpyridine derivatives need to be synthesized starting from the pyridine precursor, following a metal catalyzed radical mechanism.

The synthesis of 2-acetyl-4,4'-bipyridine **III-I1** starts from 4,4'-bipyridine and acetaldehyde, using Fe(II) sulfate as a catalyst and *tert*-butyl hydroperoxide as a radical starter (Scheme III-1).^[162] While the reaction conditions used are optimized in order to reduce the amount of polyacetylated product, a mixture of products is received nonetheless. The desired monoacetylated product can be isolated by column chromatography to yield **III-I1** as an off-white solid in 42% yield.

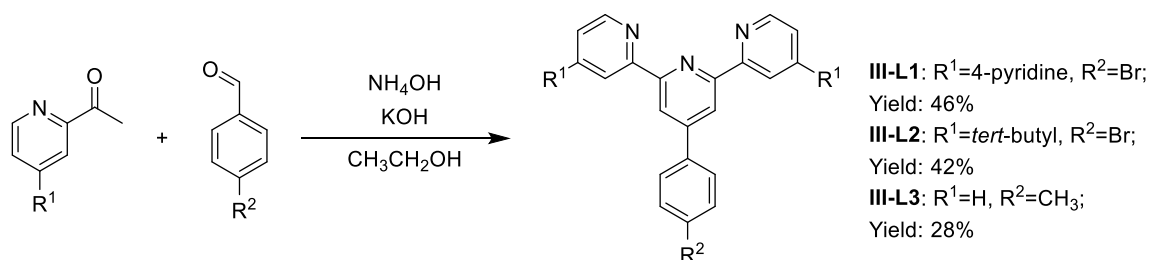
The precursor 2-acetyl-4-*tert*-butylpyridine **III-I2** is synthesized starting from 4-*tert*-butylpyridine using silver nitrate as a catalyst and ammonium persulfate as a radical starter. Following a procedure by Perera *et al.* pyruvic acid is used as carboxylic

acid to supply the acetyl group.^[202] The reaction yields again mono- and polyacetylated products, which can be separated by a series of extractions at different pH values.^[160] The desired product **III-I2** can be isolated as a yellow oily liquid (31% yield).



Scheme III-1. Synthesis of 2-acetylpyridine derivatives **III-I1** and **III-I2**.

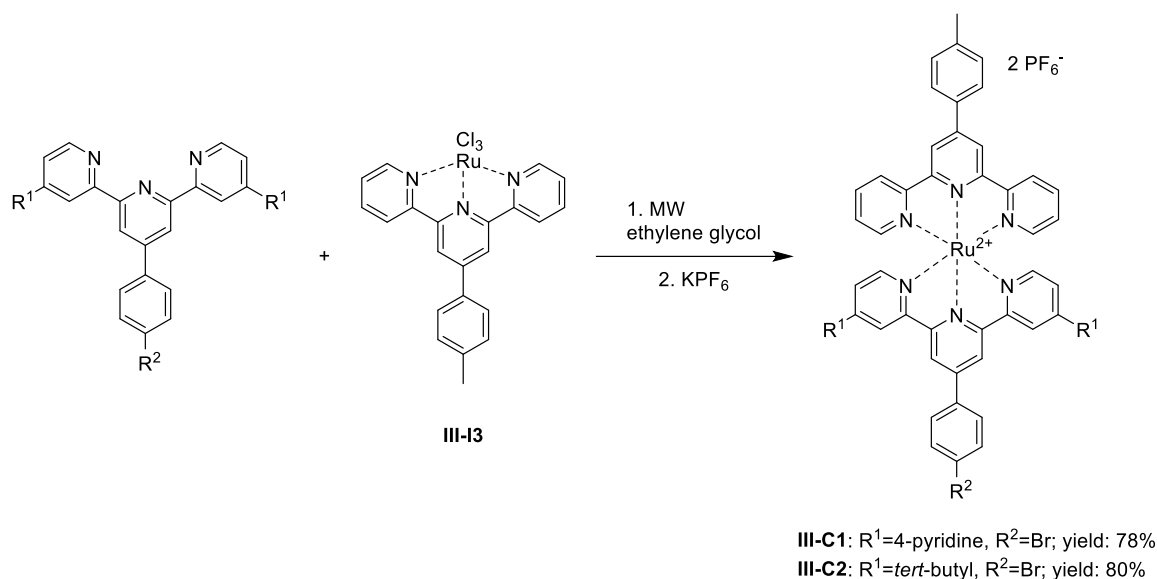
The 2-acetylpyridine derivatives **III-I1** and **III-I2** are used in a one-pot synthesis, analogous to a procedure described by Wang and Hanan^[201], reacting with 4-bromobenzaldehyde in the presence of aqueous ammonia and potassium hydroxide to form the 2,2':6',2''-terpyridine ligands Bipytpy **III-L1** and tButpy **III-L2**, respectively (Scheme III-2).^[162, 203] The crude products can be purified by recrystallization or washing with methanol.



Scheme III-2. Synthesis of terpyridine derivatives **III-L1**, **III-L2** and **III-L3**.

The ligand Tolytpy **III-L3** is synthesized by using 2-acetylpyridine and 4-methylbenzaldehyde as precursors. The heteroleptic complexes are subsequently prepared in a two-step procedure adapted from Fallahpour *et al.*^[204] The ligand **III-L3** is reacted with Ru(III) chloride trihydrate to form a Ru(III) complex. Complex **III-I3** is

used in the microwave assisted reaction with either Bipytpy **III-L1** or tButpy **III-L2** (Scheme III-3), resulting in a mixture of the respective homoleptic complexes as side products and the heteroleptic complex as main product. The desired heteroleptic complex is purified by column chromatography and isolated as hexafluorophosphate salt as a dark red solid. The complexes are analyzed using NMR spectroscopy, elemental analysis, and high-resolution mass spectrometry.



Scheme III-3. Microwave assisted (MW) synthesis of the heteroleptic Ru(II) complexes **III-C1** and **III-C2**.

III.2.2. Structural Analysis

Single crystals of **III-C1** and **III-C2** are obtained by slow diffusion of diethyl ether into a concentrated acetonitrile solution of the respective complex. The X-ray diffraction results are shown in Figure III-1, the refinement parameters are described in the Appendix (Chapter IX.4). In both complexes, the Ru(II) ion is coordinated by the two terpyridine ligands in a distorted octahedral coordination sphere. The distortion is a result of the restricted bite angle of the two meridionally coordinated ligands, leading to N-Ru-N *trans* angles between 157° and 158° instead of 180°. Furthermore, the bromophenyl and tolyl rings are not co-planar with the rest of the ligand structures, with torsion angles between 14° and 18° in **III-C1** and around 30° in **III-C2**. In complex **III-**

C1, the pyridine rings are also distorted with torsion angles of 24° and 42° , and the tolyl-substituted ligand is slightly bent due to intramolecular interactions, such as weak stacking between the tolyl ring and the pyridine rings of a neighboring Tolyltpy ligand as well as hydrogen bonding with pyridine substituents of neighboring complexes. A similar bending in the crystal structure of heteroleptic ruthenium bis-terpyridine complexes has been reported by Beves *et al.*^[205] In complex **III-C2**, no such bending of either ligand is observed due to a lack of hydrogen bond acceptors. Overall, crystal structure analysis is in full agreement with the other analytical data and confirms the expected structures of the complexes.

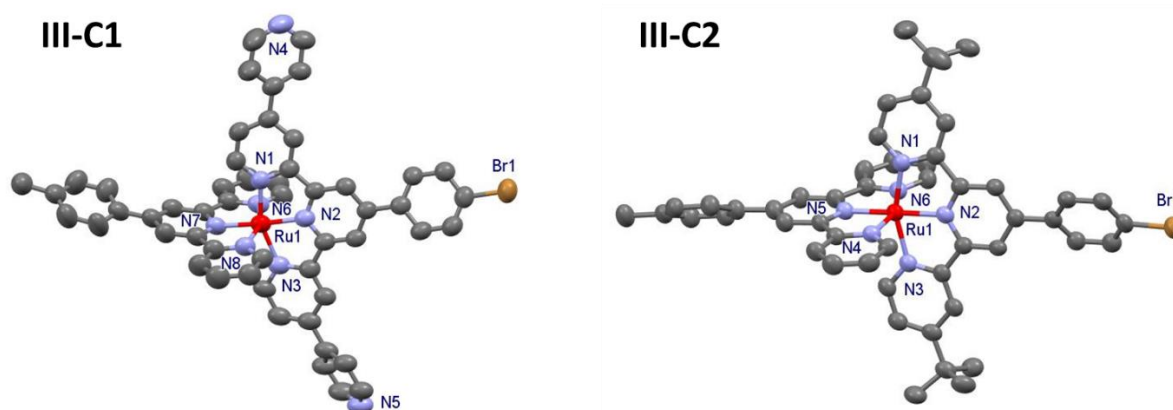


Figure III-1. Ellipsoid representation of complexes **III-C1** (left) and **III-C2** (right) at 50% probability. Hydrogen atoms, PF_6^- counter ions and co-crystallized solvent molecules are omitted for clarity.

III.2.3. Photophysical Properties

The photophysical properties of the complexes **III-C1** and **III-C2** are analyzed using UV-vis absorption and emission spectroscopy in acetonitrile solutions. Figure III-2 shows the absorption spectra (solid lines) of the complexes alongside their emission spectra (dashed lines). Both complexes exhibit several absorption bands in the UV region, which correspond to LC transitions. The pyridine-substituted complex **III-C1** shows an additional absorption band at 233 nm, which is assumed to correspond to a $\pi\text{-}\pi^*$ transition of the pyridine substituent. Furthermore, both complexes show a strong absorption in the visible region, which is responsible for the dark red color of the

complexes. This absorption band corresponds to a metal-to-ligand charge transfer (MLCT) transition. Complex **III-C1** absorbs at slightly longer wavelengths (498 nm) compared to complex **III-C2** (490 nm). This red-shifted absorption is presumably due to a stabilization of the ligand-centered LUMO, and with it the excited MLCT states, due to the electron-accepting character of the pyridine substituents as well as an extension of the aromatic system. A similar red shift from 642 nm for **III-C2** to 656 nm for **III-C1** can be observed in the emission spectra. The observed red shift in both the absorption and emission spectra of **III-C2** is relatively small despite the expected LUMO and $^3\text{MLCT}$ -stabilizing effect of the Bipytpy ligand **III-L1**. This observation is due to the electron-donating character of the *tert*-butyl groups in **III-C2**, resulting in a destabilization of the metal-centered HOMO and with it of the ground state. Table III-1 summarizes the data.

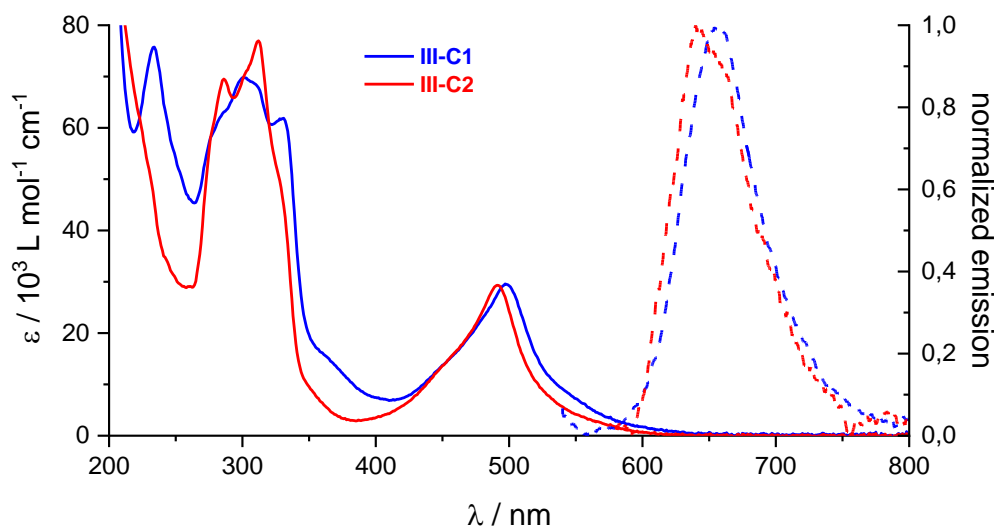


Figure III-2. UV-vis absorption (solid lines) and emission spectra (dashed lines) of complexes **III-C1** (blue) and **III-C2** (red); spectra measured in acetonitrile; emission experiments are conducted under inert gas atmosphere at 20 °C and emission spectra are rescaled so that the intensity at $\lambda_{\text{max em}}$ is 1.

The emission properties of the complexes are further analyzed regarding the luminescence quantum yield and the excited-state lifetime. As described in Chapter I.7, a stabilization of the LUMO by electron-withdrawing groups induces a stabilization of the emitting $^3\text{MLCT}$ state and, therefore, increases the surface crossing

barrier towards the non-emissive ^3MC state.^[159] Electron-donating groups on the other hand do not affect the energy gap between the $^3\text{MLCT}$ and the ^3MC state^[157] and hence do not increase the luminescence quantum yield or excited-state lifetime.

Indeed, complex **III-C1** exhibits an increased luminescence quantum yield (0.074%) compared to complex **III-C2** (0.013%). The excited-state lifetimes on the other hand are relatively similar with 3.8 ns and 3.1 ns for complexes **III-C1** and **III-C2**, respectively. These emission properties translate into similar non-radiative decay rates k_{nr} for both complexes, while the radiative decay rate k_{r} of **III-C1** is increased more than five-fold compared to **III-C2**.

Table III-1. UV-vis absorption and emission data of complexes **III-C1** and **III-C2** (spectra are measured in acetonitrile at 20 °C).^a

	$\lambda_{\text{max abs}} / \text{nm} (\epsilon / 10^3 \text{ L mol}^{-1} \text{ cm}^{-1})$	$\lambda_{\text{max em}} / \text{nm}$	$\Phi_{\text{c}} / 10^{-5}$	$\tau_{\text{c}} / \text{ns}$	$k_{\text{r}} / 10^4 \text{ s}^{-1}$	$k_{\text{nr}} / 10^8 \text{ s}^{-1}$	
	LC	MLCT					
III-C1	233 (76), 301 (70), 330 (62)	498 (29)	656	74±33	3.8 ± 0.1	19.5	2.63
III-C2	287 (69), 312 (77)	490 (29)	642	13±6	3.1 ± 0.2	4.19	3.23

^amaximum absorption wavelength $\lambda_{\text{max abs}}$; extinction coefficient ϵ ; maximum emission wavelength $\lambda_{\text{max em}}$; luminescence quantum yield Φ ; excited-state lifetime τ ; radiative decay rate $k_{\text{r}} = \Phi/\tau$; non-radiative decay rate $k_{\text{nr}} = (1-\Phi)/\tau$; emission data is collected in inert gas-purged solutions.

III.2.1. Electrochemical Properties

In the following, the complexes are further investigated regarding their electrochemical properties using cyclic voltammetry (CV). The CV experiments are carried out in dry acetonitrile under nitrogen atmosphere. Tetrabutylammonium hexafluorophosphate (TBAPF₆, 0.1 M) is used as electrolyte salt. The experimental set-up consists of a glassy carbon working electrode (WE), a platinum wire as counter electrode (CE), and a silver wire is used as pseudo-reference electrode (RE). Ferrocene is added to the sample solutions to act as an internal reference. The CV spectra are shown in Figure III-3 with the data being summarized in Table III-2.

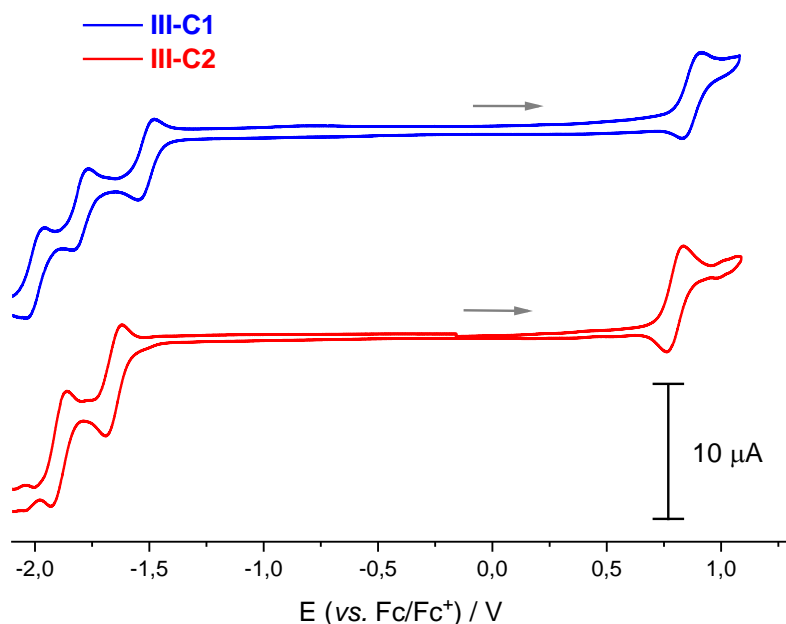


Figure III-3. Cyclic voltammograms of complexes **III-C1** (1.0 mM, blue) and **III-C2** (1.0 mM, red) in dry acetonitrile under inert gas atmosphere, with 0.1 M TBAPF₆; scan rate 100 mV/s; scans start at 0°V vs. reference in anodic direction.

Both complexes exhibit a one-electron reversible oxidation process, which is assigned to the oxidation from Ru(II) to Ru(III).^[49, 206] Furthermore, complex **III-C1** exhibits three reversible reduction processes, while **III-C2** only shows two reversible reduction processes in the investigated window. These reductions are assumed to be ligand centered.^[49] The anodically shifted potentials of the reduction processes in **III-C1** compared to **III-C2** support this assignment, as the more electron-accepting character of the Bipytpy ligand **III-L1** makes the complex easier to reduce. The cathodically shifted oxidation potential of **III-C2** (+0.79 V) compared to that of **III-C1** (+0.89 V) indicates a destabilization of the HOMO by the electron-donating *tert*-butyl substituents.

The difference between the oxidation potential and the first reduction potential can give an approximation of the HOMO-LUMO energy gap. For complex **III-C1** this energy gap is smaller than that of complex **III-C2**, which is the same trend observed in the photophysical properties, i.e., the MLCT absorption and emission wavelengths.

Table III-2. Electrochemical half-wave redox potentials $E_{1/2}$ in V vs. Fc/Fc⁺ (ΔE_p / mV) for complexes **III-C1** and **III-C2** in nitrogen-purged acetonitrile.^a

	Oxidation		Reduction	
III-C1	+0.89 (69)	-1.51 (62)	-1.81 (75)	-2.02 (104)
III-C2	+0.79 (69)	-1.66 (57)	-1.89 (80)	

^aRedox potentials are reported vs. ferrocene (Fc/Fc⁺); the differences between the anodic and cathodic peak potentials ΔE_p are given in parentheses in millivolts; measurements in inert gas-purged acetonitrile solutions containing 0.1 M tetrabutylammonium hexafluorophosphate at a sweep rate of 100 mV/s.

III.2.2. Spectroelectrochemistry

To gain a deeper understanding of the processes taking place when oxidizing and reducing the heteroleptic complexes **III-C1** and **III-C2**, they are additionally investigated by spectroelectrochemical experiments. The experimental set-up consists of a quartz glass cell with a path length of 1.0 mm, a platinum mesh WE, a platinum wire CE, and an Ag/Ag⁺ in acetonitrile RE. The measurements are conducted in argon-purged dry acetonitrile with 0.1 M TBAPF₆ as supporting electrolyte. The potential is changed in 0.1 V steps and kept constant while the UV-vis spectrum is recorded.

Figure III-4 shows the spectral changes upon oxidation of complexes **III-C1** and **III-C2**. The most significant change in both cases is the decrease of the MLCT absorption band around 500 nm, which is presumably due to the removal of the metal-centered electron, which would be excited at this wavelength.^[207] Furthermore, upon oxidation the increase of an absorption band around 400 nm can be observed for both complexes **III-C1** and **III-C2**. This absorption band can be assigned to a ligand-to-metal charge-transfer transition, probably due to the oxidation of the metal-centered HOMO.

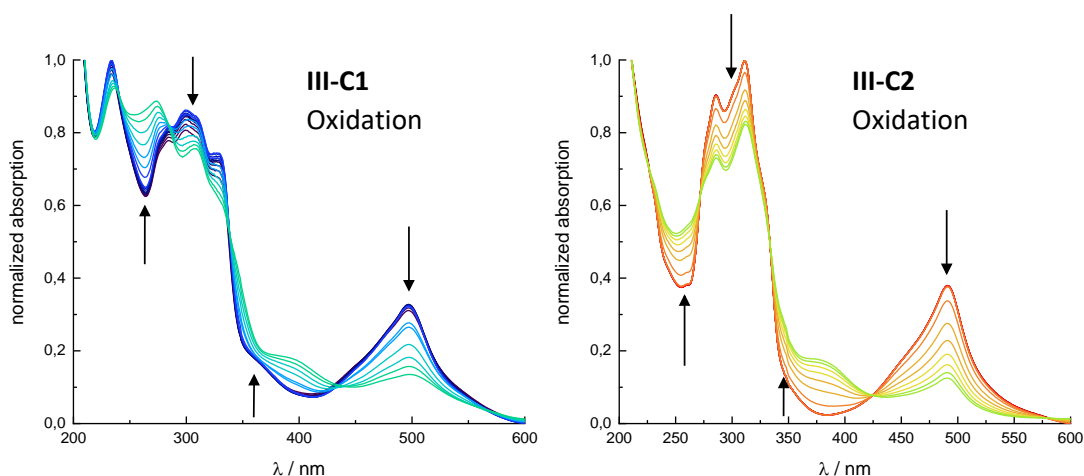


Figure III-4. UV-vis absorption spectra of **III-C1** (left) and **III-C2** (right) in argon-purged acetonitrile (0.1 M TBAPF₆) at oxidation potentials from +0.0 V to +1.5 V vs. Ag/Ag⁺; arrows indicate change of absorption bands upon oxidation.

When the complexes are reduced, hardly any change regarding the MLCT absorption intensity is observed (Figure III-5). Instead, the absorption band in the visible region is broadened. While no clear assignment of the appearing and increasing absorption bands between 350 nm and 600 nm is possible simply based on these spectroelectrochemical experiments, it is assumed that LMCT transitions as well as red-shifted LC transitions are partly responsible. Overall, the reduction of the complexes appears to result in fundamental changes to the electronic structure of the complexes.

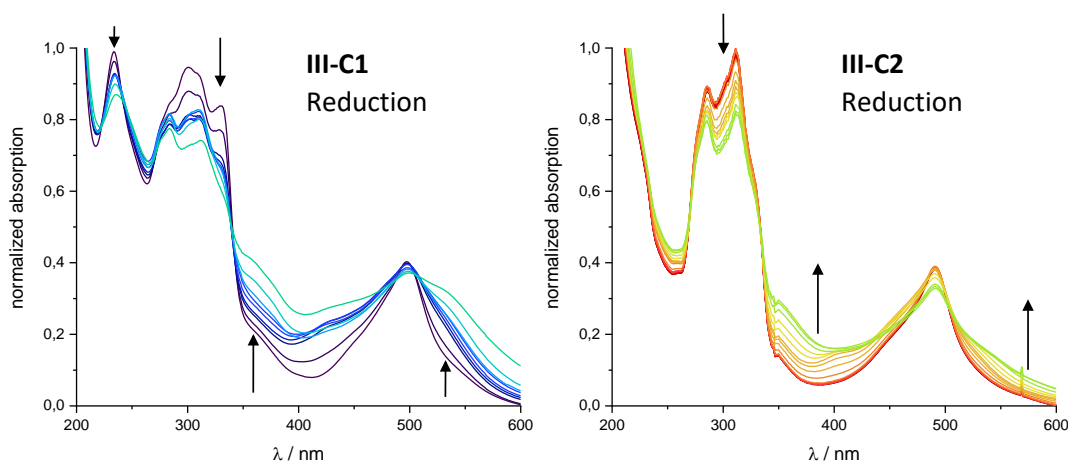


Figure III-5. UV-vis absorption spectra of **III-C1** (left) and **III-C2** (right) in argon-purged acetonitrile (0.1 M TBAPF₆) at reduction potentials from +0.0 V to -2.0 V vs. Ag/Ag⁺; arrows indicate change of absorption bands upon reduction.

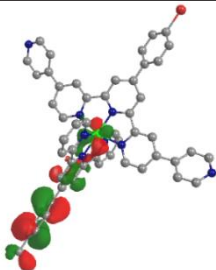
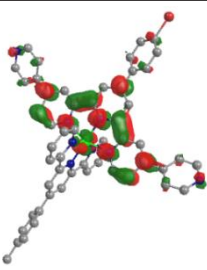
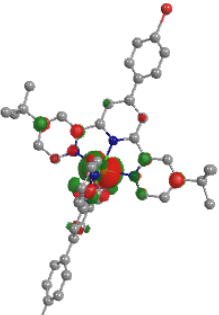
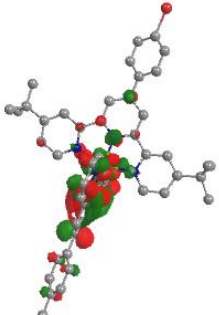
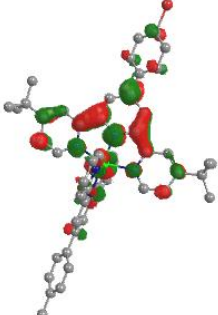
III.2.1. DFT Calculations

In addition to the experimental investigations, theoretical density functional theory (DFT) and time-dependent DFT (TD-DFT) calculations are conducted. Table III-3 shows the contributions to the molecular orbitals in the HOMO and LUMO for complexes **III-C1** and **III-C2**. In the HOMO, most of the electron density is located on the Ru(II) metal with equal contributions from both ligands. In the LUMO, the electron density is shifted towards the ligands. In the *tert*-butyl substituted complex **III-C2**, two very close lying LUMO states exist. These states can be regarded as degenerate, with one having the main contribution from **III-L2** and one from **III-L3**. In the pyridine substituted complex **III-C1** on the other hand, most of the electron density in the LUMO is delocalized over **III-L1** due to its more electron-accepting character. Only in the LUMO+1 at higher energy is the tolyl-substituted ligand **III-L3** contributing. This clear separation shows that the heteroleptic design with one electron-accepting and one electron-donating ligand does indeed result in a directional electron density transfer. Furthermore, the LUMO can be associated with the first reduction of the complexes. In **III-C1**, it can hence be assumed that the first reduction process takes place at the pyridine-substituted ligand. In **III-C2**, no clear attribution of the reduction processes

observed in CV can be made based on the presented calculations. In addition, the calculations confirm the MLCT character of the absorption around 500 nm.

When looking at the HOMO and LUMO energies more closely, a strong stabilization of the LUMO in **III-C1** (-3.00 eV) compared to **III-C2** (-2.74 eV) can be observed. The destabilization of the HOMO in complex **III-C2** (-6.41 eV) compared to **III-C1** (-6.53 eV) is less pronounced. The HOMO-LUMO energy gap of the pyridine-substituted **III-C1** is thus smaller (3.53 eV) than that of **III-C2** (3.67 eV). This result matches well with the experimental observations discussed above, i.e., a smaller gap between oxidation and reduction potential for **III-C1** as well as blue-shifted absorption and emission wavelengths for **III-C2**.

Table III-3. Contributions to molecular orbitals for complexes **III-C1** and **III-C2**.

	HOMO	LUMO	
III-C1	 -6.53 eV Ru: 66% III-L1 : 19%; III-L3 : 15%	 -3.00 eV Ru: 7% III-L1 : 92%; III-L3 : 1%	
III-C2	 -6.41 eV Ru: 67% III-L2 : 17%; III-L3 : 15%	 -2.74 eV Ru: 8% III-L2 : 18%; III-L3 : 74%	 -2.72 eV Ru: 8% III-L2 : 74%; III-L3 : 18%

III.2.2. Hydrogen Evolution Experiments

The investigated photophysical and electrochemical properties are used to estimate if the complexes will act as PS in hydrogen evolution experiments. Herein a system for photocatalytic hydrogen evolution is assumed, which follows the scheme as described in Figure I-7, where a PS is excited, and the absorbed energy is used to transfer an electron from a SED to the excited PS and the reduced PS is subsequently re-oxidized by electron transfer to the HEC. A PS in this system should exhibit a long-excited state lifetime and high luminescence quantum yield to ensure that the absorbed energy can be used efficiently to transfer electrons, i.e., from the SED to the excited PS. Furthermore, reversible redox behavior is needed to ensure that the PS is not altered upon electron transfer and restoration to its initial form after electron transfer to the catalyst is possible. In addition, the relative energy of the excited and reduced states of the PS needs to allow electron transfer from the SED to the excited PS and from the reduced PS to the catalyst.^[49] The driving forces for the photoinduced electron transfer ΔG^0_{ET} from the SED (TEOA, $E_{Ox} = +0.42$ V vs. Fc/Fc⁺^[208]) to the excited PS can be estimated using Equation I-4 to Equation I-6. The results are summarized in Table III-4.

A negative ΔG^0_{ET} value indicates that the electron transfer process is exergonic and thus thermodynamically favorable. The estimated driving forces are positive for both complexes, with the electron transfer towards **III-C2** being even more endergonic than towards **III-C1**. The estimated driving forces together with the photophysical properties indicate that **III-C1** will perform as the superior PS than **III-C2**.

Table III-4. Excited-state redox potentials and estimated free Gibbs energy ΔG^0_{ET} for photoinduced electron transfer from TEOA to the excited complexes **III-C1** and **III-C2**.

	E_{ox}^* / V vs. Fc/Fc ⁺	E_{red}^* / V vs. Fc/Fc ⁺	$\Delta G^0_{ET} / eV$
III-C1	-1.00	+0.38	+0.04
III-C2	-1.17	+0.25	+0.17

Hydrogen evolution experiments are carried out in DMF solutions containing 0.1 mM PS, 1 M TEOA as SED, aqueous tetrafluoroboric acid (HBF₄) as proton source

and a catalyst. The sample is irradiated with blue light (LED centered at 445 nm) and the gaseous phase above the sample is probed using gas chromatography. A detailed description of the experimental set-up can be found in the Appendix (Chapter 0). The amount of hydrogen produced is monitored over time and is reported as turn-over frequency (TOF), i.e., the rate of hydrogen production per unit of time, and turn-over number (TON), i.e., the overall amount of hydrogen produced up to a point in time.

When no PS, no catalyst or no light are applied during the experiments, no hydrogen evolution is observed. When **III-C1** is used as PS with [Co(dmgh)(dmgh₂)Cl₂] (dmgh = dimethylglyoxime) hydrogen is produced at a stable rate for at least 12 days (Figure III-6). The maximum activity decreases from 50 to 40 mmol_{H₂} mol_{PS}⁻¹ min⁻¹ over the course of almost 300 h, without any change or addition of components in the reaction mixture.

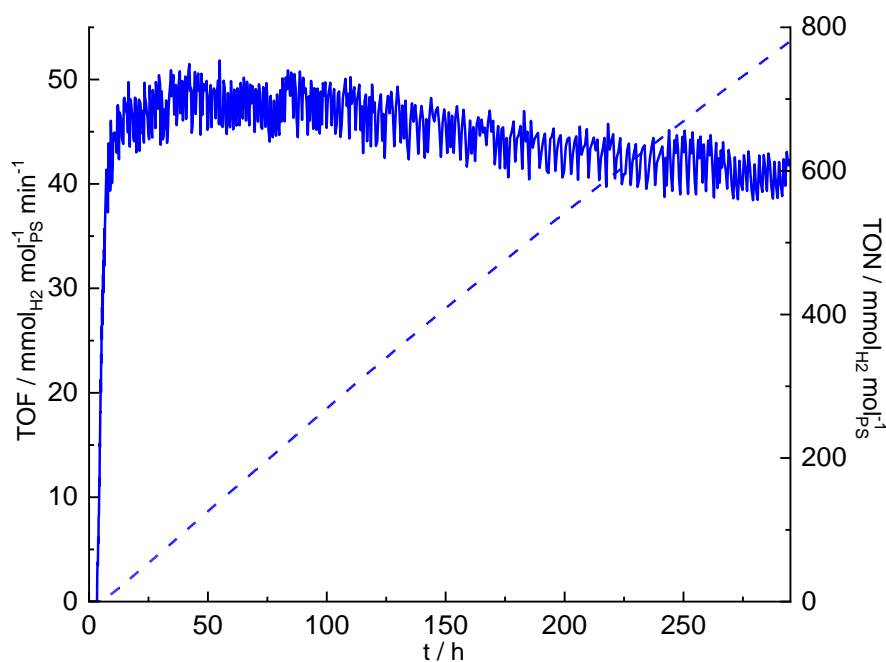


Figure III-6. Hydrogen photoproduction with complex **III-C1** as PS (0.1 mM) under blue light irradiation (LED centered at 445 nm); with TEOA as sacrificial electron donor (1 M) and HBF₄ as proton source (0.1 M), [Co(dmgh)(dmgh₂)Cl₂] as catalyst (1 mM), with dmgh₂ (6 mM) in DMF; TOF: solid line; TON: dashed line; adapted from *Inorganic Chemistry*, **2019**, 58, 9127-9134. Reproduced with permission of American Chemical Society.^[162]

If this result is compared to the benchmark PS $[\text{Ru}(\text{bpy})_3]^{2+}$, it becomes apparent that the hydrogen evolution profile looks very differently (see Figure III-7) compared to that of **III-C1**. The maximum TOF (TOF_{max}) with $[\text{Ru}(\text{bpy})_3]^{2+}$ under the same conditions is increased by two orders of magnitude ($\text{TOF}_{\text{max}} = 6850 \text{ mmol}_{\text{H}_2} \text{ mol}_{\text{PS}}^{-1} \text{ min}^{-1}$). However, the TOF decreases rapidly, and the system becomes catalytically inactive after only a few hours, i.e., reaching its half-life time in less than an hour. Addition of catalyst after the hydrogen evolution has ceased does not show any further hydrogen evolution. Addition of PS on the other hand does partly restore the hydrogen evolution activity of the system. This observation indicates that there is still active catalyst present in the reaction mixture while the PS has decomposed, e.g., via photo-substitution.^[70-71] Considering the longevity of **III-C1** as PS, after the duration of the performed experiment, the overall amount of hydrogen produced ($\text{TON}(296 \text{ h}) = 764 \text{ mmol}_{\text{H}_2} \text{ mol}_{\text{PS}}^{-1}$) is similar to that of $[\text{Ru}(\text{bpy})_3]^{2+}$ ($\text{TON}(9.5 \text{ h}) = 750 \text{ mmol}_{\text{H}_2} \text{ mol}_{\text{PS}}^{-1}$). The results are summarized in Table III-5.

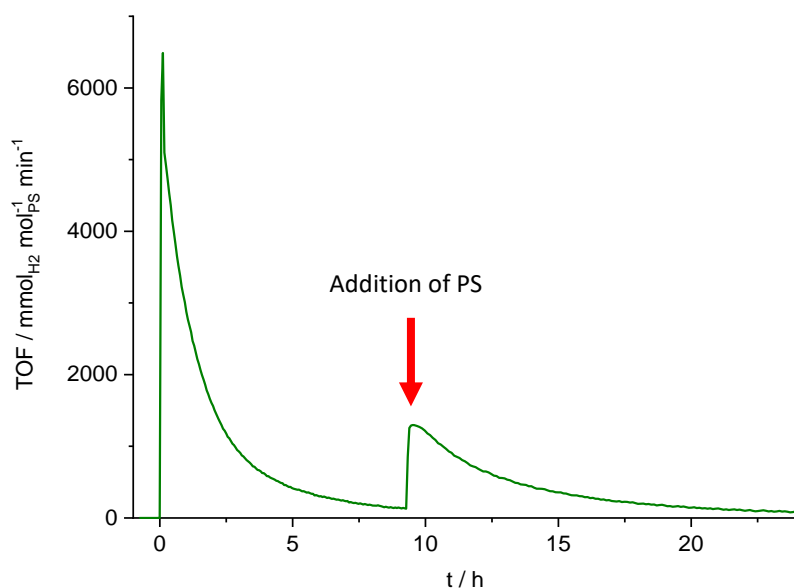


Figure III-7. Hydrogen photoproduction with complex $[\text{Ru}(\text{bpy})_3]^{2+}$ as PS (0.1 mM) under blue light irradiation (LED centered at 445 nm); with TEOA as sacrificial electron donor (1 M) and HBF_4 as proton source (0.1 M), $[\text{Co}(\text{dmgH})(\text{dmgH}_2)\text{Cl}_2]$ as catalyst (1 mM), with dmgH_2 (6 mM) in DMF; addition of same amount of $[\text{Ru}(\text{bpy})_3]^{2+}$ in 0.25 mL DMF after 9 hours (highlighted by red arrow); adapted from *Inorganic Chemistry*, **2019**, 58, 9127-9134. Reproduced with permission of American Chemical Society.^[162]

Furthermore, complex **III-C1** is tested under different catalytic conditions. The results are presented in Figure III-8 and Table III-5. The use of the Co(III) complex $[\text{Co}(\text{dmgH})(\text{dmgH}_2)\text{Cl}_2]$ in different concentrations, the Co(II) complex $[\text{Co}(\text{dmgH})_2(\text{H}_2\text{O})_2](\text{BF}_4)_2$, which is prepared *in-situ* from $[\text{Co}(\text{H}_2\text{O})_6](\text{BF}_4)_2$ and dmgH_2 , or colloidal platinum, which is prepared *in-situ* from $\text{K}_2[\text{PtCl}_4]$, leads to very similar TOF_{max} around $50 \text{ mmol}_{\text{H}_2} \text{ mol}_{\text{PS}}^{-1} \text{ min}^{-1}$. This observation indicates that the rate-limiting step does not involve the catalyst and is hence the reductive quenching of the PS. This explanation also accounts for the relatively low activity and matches the estimated driving force for this electron transfer step.

Interestingly, the hydrogen evolution longevity differs slightly between the different catalysts used. A faster decrease of hydrogen evolution activity (20% in 44 h) is observed when colloidal platinum or a lower concentration of cobaloxime catalyst is used. The lower hydrogen evolution longevity is presumably due to a concentration mismatch of the PS and the catalyst, leading to photodegradation of the system.

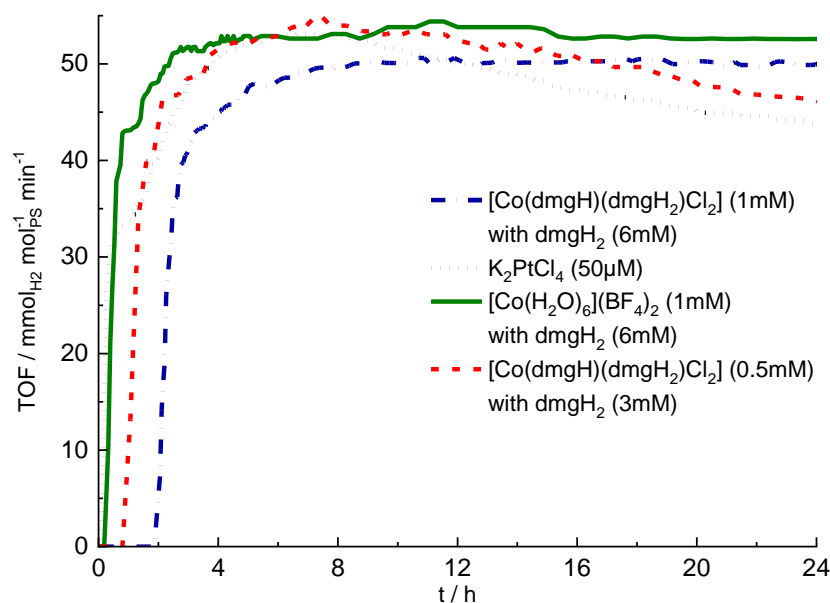
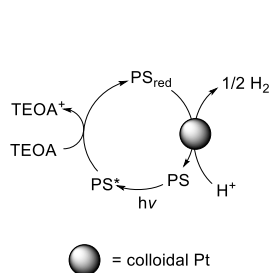


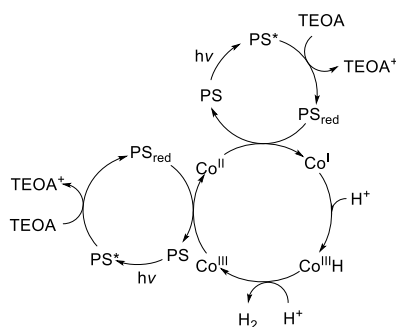
Figure III-8. Hydrogen photoproduction with complex **III-C1** as PS (0.1 mM) under blue light irradiation (LED centered at 445 nm); with TEOA as sacrificial electron donor (1 M) and HBF_4 as proton source (0.1 M) in DMF; different catalysts are used: $[\text{Co}(\text{dmgH})(\text{dmgH}_2)\text{Cl}_2]$ (1 mM) with dmgH_2 (6 mM) (blue, dashed/dotted line), K_2PtCl_4 (50 μM) as pre-catalyst to form *in-situ* colloidal Pt (black, dotted line), $[\text{Co}(\text{H}_2\text{O})_6](\text{BF}_4)_2$ as pre-catalyst (1 mM), with dmgH_2 (6 mM) (green, solid line), $[\text{Co}(\text{dmgH})(\text{dmgH}_2)\text{Cl}_2]$ (0.5 mM) with dmgH_2 (3 mM) (red, dashed line); adapted from *Inorganic Chemistry*, **2019**, *58*, 9127-9134. Reproduced with permission of American Chemical Society.^[162]

Furthermore, not all catalytic systems investigated start to produce hydrogen instantly when the light is switched on, i.e., at time 0 h. Instead, when a Co(III) complex is used, an induction period is observed. This induction period depends on the concentration of the catalyst used and is absent when a Co(II) complex or colloidal platinum are used as catalyst. This observation can be understood when looking at the catalytic cycles, which have been proposed for these kind of systems (Scheme III-4).^[129, 131] When a cobalt complex is used as catalyst, in both the mechanism including a Co^{III}-H intermediate and a Co^{II}-H intermediate the active species is a Co(I) complex. Hence, if a Co(III) catalyst is used, the Co(II) intermediate must be accumulated first before it can be reduced to Co(I). Otherwise, any Co(I) species would be subject to comproportionation reactions. The need to first reduce all of the Co(III) catalyst to Co(II) before forming any Co(I) species, which can produce hydrogen, does explain the observed induction period and why it depends on the concentration of the Co(III) catalyst. It also explains why no (or a much shorter) induction period is observed when using a Co(II) complex. The short remaining induction period is presumably due to some oxidation of the catalyst happening during preparation under air.

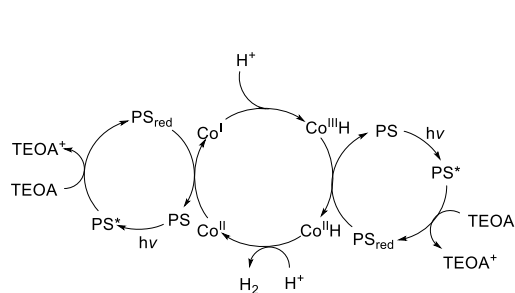
a) Mechanism for a heterogeneous catalyst



b) Mechanism for a Co(III)-H intermediate



c) Mechanism for a Co(II)-H intermediate



Scheme III-4. Proposed photocatalytic cycles for different catalysts used: a) heterogeneous catalyst such as colloidal Pt; b) Co(III) catalyst such as $[\text{Co}(\text{dmgH})(\text{dmgH}_2)\text{Cl}_2]$; c) Co(II) catalyst such as $[\text{Co}(\text{dmgH})_2(\text{H}_2\text{O})_2](\text{BF}_4)_2$.

Complex **III-C2** is tested as PS using either colloidal platinum or $[\text{Co}(\text{dmgH})_2(\text{H}_2\text{O})_2](\text{BF}_4)_2$ as catalyst. As **III-C2** exhibits a lower luminescence quantum yield than **III-C1** and the estimated free Gibbs energy for the electron transfer from the

SED to the excited complex suggests this electron transfer step to be less exergonic than with **III-C1**, the *tert*-butyl substituted complex **III-C2** is not expected to be active as PS. Indeed, no hydrogen production can be observed.

Table III-5. Hydrogen production results of complexes discussed in this chapter.^a

PS	(pre)catalyst	duration / h	TOF _{max} / mmol _{H₂} mol _{PS} ⁻¹ min ⁻¹	TON / mmol _{H₂} mol _{PS} ⁻¹	induction / h
III-C1	[Co(dmgh)(dmgh ₂)Cl ₂]	296	51	764	3.4
III-C1	[Co(dmgh)(dmgh ₂)Cl ₂]	44	53	122	1.9
III-C1	[Co(dmgh)(dmgh ₂)Cl ₂] ^b	44	54	119	0.8
III-C1	[Co(dmgh)(dmgh ₂)Cl ₂] ^c	44	not detected	not detected	
III-C1	[Co(H ₂ O) ₆](BF ₄) ₂	44	57	134	0.2
III-C1	K ₂ [PtCl ₄] ^d	44	56	116	<0.1
III-C1	none	44	not detected	not detected	
III-C2	[Co(H ₂ O) ₆](BF ₄) ₂	24	not detected	not detected	
III-C2	K ₂ [PtCl ₄] ^d	24	not detected	not detected	
[Ru(bpy)₂]²⁺	[Co(dmgh)(dmgh ₂)Cl ₂]	9.5	6850	750	<0.1

^aunless otherwise stated, all experiments are carried out using 0.1 mM PS, 1 M TEOA as SED, 0.1 M HBF₄ as proton source and 1 mM catalyst with 6 mM dmgh₂ in DMF, irradiation with blue light (LED centered at 445 nm, 62 mW), reported values are averages of multiple runs; ^b0.5 mM catalyst and 3 mM dmgh₂; ^cno light irradiation; ^dused as precursor for colloidal platinum, concentration 50 μM.

III.3. Conclusion

In this chapter, the synthesis of two novel terpyridine ligands, one with electron-accepting pyridine substituents and one with electron-donating *tert*-butyl substituents, following a Kroehnke-like one-pot procedure is described. These ligands are used to form the heteroleptic Ru(II) complexes **III-C1** and **III-C2**. The crystal structures of these complexes confirm the distorted octahedral coordination, which is typical for terpyridine complexes.

The pyridine substituents in **III-C1** have a LUMO-stabilizing effect, which is reflected in a red-shifted absorption and emission. The stabilization of the emissive ³MLCT state furthermore leads to an increase of the energy gap between ³MLCT and

^3MC state, which yields a higher luminescence quantum yield and a longer excited-state lifetime compared to complexes without electron-withdrawing substituents. Furthermore, the potential of the first reduction process observed in CV experiments is anodically shifted. The *tert*-butyl substituents in **III-C2** on the other hand have a HOMO-destabilizing effect, also leading to a red shift of absorption and emission wavelengths. However, the energy gap to the ^3MC state is not increased compared to unsubstituted complexes, hence not significantly improving the luminescence properties of **III-C2**. The destabilization of the LUMO results in a cathodic shift of the oxidation potential of the complex.

The driving forces for the photoinduced electron transfer from the SED to the excited complex are estimated for both **III-C1** and **III-C2**. This electron transfer process is expected to not be thermodynamically favorable for **III-C2**, which is indeed not active as PS under the presented photocatalytic conditions. For complex **III-C1**, the photoinduced electron transfer is estimated to be more exergonic in comparison to **III-C2**, but still not highly thermodynamically favorable. In photocatalytic hydrogen evolution experiments, **III-C1** acts as a PS under various catalytic conditions. The rate of hydrogen production observed is relatively low. However, the longevity of the system involving **III-C1** as PS is by far superior compared to the benchmark PS $[\text{Ru}(\text{bpy})_3]^{2+}$. The catalytic studies, alongside the estimated driving forces and the still relatively low luminescence quantum yield, lead to the conclusion that the reductive quenching of the excited complex **III-C1** is the rate-limiting step in this system.

III.4. Experimental

Details on instrumentation, crystal structure analysis, and DFT calculations as well as NMR spectra with peak assignments can be found in the Appendix (Chapter IX). References are given for known compounds. The properties of the known compounds agree with the ones published.

2-Acetyl-4,4'-bipyridine III-I1^[209]

A solution of 4,4'-bipyridine (3.00 g, 19.2 mmol, 1 eq), Fe(II) sulfate

heptahydrate (267 mg, 960 μ mol, 0.05 eq), acetaldehyde (5.40 mL, 4.23 g, 96.0 mmol, 5 eq), *tert*-butylhydroperoxide (70%w in H₂O, 26.6 mL, 17.3 g, 192 mmol, 10 eq) and trifluoroacetic acid (7.40 mL, 11.0 g, 96.0 mmol, 5 eq) in acetonitrile (60 mL) was heated to reflux for 90 minutes. Subsequently, the acetonitrile was removed under reduced pressure and the pH of the residue was raised to approximately 9 by adding 1 M aqueous sodium carbonate. After extraction with dichloromethane, the organic phase was dried over magnesium sulfate and the solvent removed under reduced pressure. The crude product was purified by column chromatography (silica gel, ethyl acetate) to yield the pure product as an off-white solid (1.60 g, 8.07 mmol, 42%).

¹H-NMR (400 MHz, CDCl₃): δ = 8.81 (d, 1H, ³J = 5.1 Hz), 8.77 (dd, 2H, ³J = 4.4 Hz, ⁴J = 1.6 Hz), 8.31 (d, 1H, ⁴J = 1.2 Hz), 7.72 (dd, 1H, ³J = 5.1 Hz, ⁴J = 1.9 Hz), 7.59 (dd, 2H, ³J = 4.5 Hz, ⁴J = 1.7 Hz) and 2.78 ppm (s, 3H). ¹³C{¹H}-NMR (101 MHz, CDCl₃): δ = 199.9, 154.5, 150.9, 150.1, 146.7, 144.9, 124.6, 121.5, 119.4 and 26.0 ppm. ESI-MS: m/z [M+Na]⁺ calc. for C₁₂H₁₀N₂NaO 221.0685; found 221.0685. Anal. calc. for C₁₂H₁₀N₂O: C 72.71, H 5.08, N 14.13; found: C 72.43, H 5.11, N 13.67.

2-Acetyl-4-tert-butylpyridine III-12^[202]

A solution of 4-*tert*-butylpyridine (4.13 mL, 3.81 g, 28.2 mmol, 1 eq), pyruvic acid (5.48 mL, 6.95 g, 79.0 mmol, 2.8 eq) and silver nitrate (383 mg, 2.26 mmol, 0.08 eq) in 40.0 mL dichloromethane and 7.00 mL water was cooled to 0 °C. Subsequently, a solution of sulfuric acid (2.33 mL, 4.29 g, 43.7 mmol, 1.55 eq) and ammonium persulfate (9.65 g, 42.3 mmol, 1.5 eq) in 33.0 mL water was slowly added. The reaction mixture was refluxed for 4 hours, cooled to room temperature, and neutralized with 10 mol/L sodium hydroxide solution. After filtration, the phases were separated, and the aqueous phase extracted with dichloromethane. The combined organic phases were dried over magnesium sulfate and the solvent was removed under reduced pressure. The residue was then dissolved in diethyl ether and extracted first with 0.75 mol/L citric acid and subsequently with 1 mol/L hydrochloric acid. The hydrochloric acid phase was neutralized with 10 mol/L sodium hydroxide solution and extracted with diethyl ether. The organic phase was filtered through a silica plug and

the solvent removed under pressure to yield a light-yellow liquid (2.05 g, 11.6 mmol, 31%). ^1H NMR (CDCl_3 , 300 MHz): δ = 8.56 (dd, 3J = 5.2 Hz, 5J = 0.7 Hz, 1H), 8.04 (dd, 4J = 2.0 Hz, 5J = 0.7 Hz, 1H), 7.44 (dd, 3J = 5.2 Hz, 4J = 2.0 Hz, 1H), 2.70 (s, 3H) and 1.32 ppm (s, 9H). ^{13}C NMR (75 MHz, CDCl_3) δ = 200.73, 161.36, 153.72, 149.08, 124.29, 118.86, 35.15, 30.61 and 26.12 ppm.

4'-(4-Bromophenyl)-4,4''':4'',4''''-di-pyridinyl-2,2':6',2''-terpyridine Bipyty III-L1

To a solution of 2-acetyl-4,4'-bipyridine **III-I1** (500 mg, 2.52 mmol, 2.5 eq) in 25.0 mL ethanol, 4-bromobenzaldehyde (187 mg, 1.01 mmol, 1 eq), potassium hydroxide (283 mg, 5.04 mmol, 5 eq) and aqueous ammonia (28%w, 7.02 mL, 6.32 g, 50.4 mmol, 50 eq) were added. The reaction mixture was heated to reflux for two weeks. Subsequently, water was added to precipitate the product, which was filtered over celite, washed with water and methanol, and dissolved in dichloromethane. The solution was dried over magnesium sulfate and the solvent was removed under reduced pressure. The crude product was suspended in methanol and the slurry filtered to give the product as a white solid (251 mg, 463 μmol , 46%). ^1H -NMR (300 MHz, CDCl_3): δ = 8.89 (d, 2H, 4J = 1.8 Hz), 8.86 (dd, 2H, 3J = 5.1 Hz, 4J = 0.7 Hz), 8.80 (dd, 4H, 3J = 4.5 Hz, 4J = 1.7 Hz), 8.79 (s, 2H), 7.81 (dd, 3J = 6.6 Hz, 4J = 2.0 Hz, 2H), 7.68 (m, 6H) and 7.62 ppm (dd, 3J = 5.1 Hz, 4J = 1.8 Hz, 2H). $^{13}\text{C}\{^1\text{H}\}$ -NMR (100 MHz, CDCl_3): δ = 157.1, 156.0, 150.9, 150.3, 149.6, 146.8, 146.1, 137.3, 132.4, 129.0, 123.9, 121.8, 121.7, 119.5 and 119.3 ppm. ESI-MS: m/z $[\text{M} + \text{H}]^+$ calc. for $\text{C}^{31}\text{H}^{20}\text{BrN}^5$: 542.0975; found: 542.0887; difference: 16.2 ppm.

4'-(4-Bromophenyl)-4,4''-di-tert-butyl-2,2':6',2''-terpyridine tButpy III-L2^[203]

To a solution of 4-bromobenzaldehyde (418 mg, 2.26 mmol, 1 eq) in 40.0 mL ethanol, 2-acetyl-4-*tert*-butylpyridine **III-I2** (1.00 g, 5.64 mmol, 2.5 eq), potassium hydroxide (380 mg, 6.77 mmol, 3 eq) and aqueous ammonia (28%w, 7.85 mL, 7.06 g, 56.4 mmol, 25 eq) were added. The reaction mixture was stirred at room temperature for 5 days in which additional aqueous ammonia (28%w, 7.85 mL, 7.06 g, 56.4 mmol, 25 eq) was added after 3 days. Subsequently, water was added to precipitate the product, which was then filtered over celite, washed with water, and dissolved in

dichloromethane. The solution was dried over magnesium sulfate and the solvent removed under reduced pressure. The crude product was purified by recrystallization in methanol to yield an off-white solid (474 mg, 947 μmol , 42%). $^1\text{H-NMR}$ (300 MHz, CDCl_3): δ = 8.79 (dd, 4J = 2.0 Hz, 5J = 0.6 Hz, 2H), 8.69 (s, 2H), 8.63 (dd, 3J = 5.2 Hz, 5J = 0.6 Hz, 2H), 7.79 (dd, 3J = 6.6 Hz, 4J = 2.0 Hz, 2H), 7.63 (dd, 3J = 6.6 Hz, 4J = 2.0 Hz, 2H), 7.37 (dd, 3J = 5.2 Hz, 4J = 2.0 Hz, 2H) and 1.45 ppm (s, 18H). $^{13}\text{C}\{^1\text{H}\}$ -NMR (75 MHz, CDCl_3): δ = 161.0, 156.3, 156.1, 149.3, 149.2, 137.7, 132.2, 129.1, 123.6, 121.4, 118.5, 118.4, 35.1 and 30.7 ppm. ESI-MS: m/z $[\text{M} + \text{H}]^+$ calc. for $\text{C}_{29}\text{H}_{30}\text{BrN}_3$: 500.1696; found: 500.1675; difference: 4.2 ppm.

p-Tolyl-2,2':6',2''-terpyridine Tolytpty **III-L3**^[201]

To a solution of 4-methylbenzaldehyde (496 mg, 4.13 mmol, 1 eq) in 20.0 mL of ethanol 2-acetylpyridine (1.00 g, 8.25 mmol, 2 eq), potassium hydroxide (463 mg, 8.25 mmol, 2 eq) and aqueous ammonia (28%w, 1.44 mL, 10.3 mmol, 2.5 eq) were added. After the solution was stirred at room temperature for 4.5 hours deionized water was added, and the precipitate was filtered and washed with water. The crude product was recrystallized from chloroform/methanol to yield a pale-yellow solid (374 mg, 1.16 mmol, 28%). $^1\text{H-NMR}$ (300 MHz, CDCl_3) δ = 8.73 (s, 4H), 8.67 (d, 3J = 8.0 Hz, 2H), 7.92 – 7.79 (m, 4H), 7.34 (dd, 3J = 12.2, 6.8 Hz, 4H) and 2.43 ppm (s, 3H).

$[\text{Ru}(\text{Tolytpty})\text{Cl}_3]$ **III-I3**^[210]

A solution of Ru(III) chloride trihydrate (261 mg, 1.00 mmol, 1 eq) and Tolytpty **III-L3** (323 mg, 1.00 mmol, 1 eq) in ethanol (125 mL) was heated to reflux for 3 hours. Subsequently, the reaction mixture was filtered, and the residue washed with ethanol to yield a red-brown solid (470 mg, 885 μmol , 89%). The product was used without further purification.

$[\text{Ru}(\text{Tolytpty})(\text{Bipytpy})](\text{PF}_6)_2$ **III-C1**

A suspension of $[\text{RuCl}_3(\text{Tolytpty})]$ **III-I3** (75.0 mg, 141 μmol , 1 eq), Bipytpy **III-L1** (76.6 mg, 141 μmol , 1 eq) and four drops of triethylamine in 15.0 mL ethylene glycol was heated to 170 $^\circ\text{C}$ for 25 minutes using microwave irradiation. After cooling to room

temperature water and aqueous KPF_6 solution were added to the solution and the precipitate filtered off over celite. After washing with water, it was dissolved in acetonitrile, dried over magnesium sulfate and the solvent was removed under reduced pressure. Traces of ethylene glycol were removed by washing the crude product with water. It was further purified by column chromatography (silica gel, MeCN:aqu. KNO_3 7:1) to yield a dark red solid (138 mg, 110 μmol , 78%). $^1\text{H-NMR}$ (400 MHz, CD_3CN): δ = 9.22 (s, 2H), 9.06 (s, 2H), 8.99 (d, 4J = 1.6 Hz, 2H), 8.79 (dd, 3J = 4.5 Hz, 4J = 1.6 Hz, 4H), 8.70 (d, 3J = 8.1 Hz, 2H), 8.25 (d, 3J = 8.6 Hz, 2H), 8.16 (d, 3J = 8.2 Hz, 2H), 7.99 (m, 4H), 7.76 (dd, 3J = 4.5 Hz, 4J = 1.7 Hz 4H), 7.63 (d, 3J = 7.9 Hz, 2H), 7.60 (d, 3J = 5.9 Hz, 2H), 7.54 (dd, 3J = 5.9 Hz, 4J = 2.0 Hz, 2H), 7.48 (d, 3J = 4.9 Hz, 2H), 7.23 (ddd, 3J = 7.1 Hz, 3J = 5.6 Hz, 4J = 1.2 Hz, 2H) and 2.55 ppm (s, 3H). $^{13}\text{C}\{^1\text{H}\}$ -NMR (151 MHz, CD_3CN): δ = 159.9, 159.2, 156.6, 156.3, 155.6, 153.8, 153.5, 151.8, 149.8, 148.2, 148.0, 143.7, 142.1, 139.2, 136.9, 133.8, 131.3, 130.6, 128.7, 128.5, 125.9, 125.5, 123.4, 123.3, 122.9, 122.5, 122.5 and 21.4 ppm. ESI-MS: m/z $[\text{M} - \text{PF}_6]^+$ calc. for $\text{C}_{53}\text{H}_{37}\text{BrF}_6\text{N}_8\text{PRu}$: 1111.10044; found: 1111.09792; difference: 3.1 ppm. Anal. calc. for $\text{C}_{53}\text{H}_{37}\text{BrF}_{12}\text{N}_8\text{P}_2\text{Ru}\cdot 2\text{H}_2\text{O}$: C, 49.24; H, 3.20; N, 8.67. Found: C, 48.84; H, 3.06; N, 8.36.

[Ru(Tolyltpy)(tButpy)](PF₆)₂ III-C2

A suspension of $[\text{RuCl}_3(\text{Tolyltpy})]$ **III-I3** (50.0 mg, 94.2 μmol , 1 eq) and tButpy **III-L2** (47.1 mg, 94.2 μmol , 1 eq) in 15.0 mL ethylene glycol was heated to 180 °C for 20 minutes using microwave irradiation. After cooling to room temperature, water and aqueous KPF_6 solution were added to the solution. The precipitate was filtered off over celite, washed with water and dissolved in acetonitrile. The solution was dried over magnesium sulfate and the solvent removed under reduced pressure. The crude product was purified by washing with diethyl ether and column chromatography (silica gel, MeCN:aqu. KNO_3 9:1) to yield a dark red solid (91.0 mg, 75.0 μmol , 80%). $^1\text{H-NMR}$ (300 MHz, CD_3CN): δ = 9.06 (s, 2H), 8.99 (s, 2H), 8.64 (d, 3J = 8.1 Hz, 2H), 8.60 (d, 4J = 2.0 Hz, 2H), 8.19 (d, 3J = 8.4 Hz, 2H), 8.11 (d, 3J = 8.0 Hz, 2H), 7.94 (m, 4H), 7.58 (d, 3J = 8.2 Hz, 2H), 7.41 (d, 3J = 5.6 Hz, 2H), 7.29 (d, 3J = 5.9 Hz, 2H), 7.17 (m, 4H) 2.54 (s, 3H) and 1.32 ppm (s, 18H). $^{13}\text{C}\{^1\text{H}\}$ -NMR (100 MHz, CD_3CN): δ = 164.0,

159.2, 158.7, 156.7, 156.3, 153.3, 152.7, 149.0, 147.9, 142.0, 128.9, 137.1, 134.9, 133.5, 131.3, 130.8, 128.6, 128.4, 125.4, 125.4, 125.3, 123.2, 122.4, 122.3, 36.2, 30.4 and 21.4 ppm. ESI-MS: m/z $[M - PF_6]^+$ calc. for $C_{51}H_{47}BrF_6N_6PRu$: 1069.17254; found: 1069.16866; difference: 4.4 ppm. Anal. calc. for $C_{51}H_{47}BrF_{12}N_6P_2Ru$: C, 50.42; H, 3.90; N, 6.92. Found: C, 50.40; H, 3.96; N, 6.62.

IV. Effect of Homoleptic vs. Heteroleptic Design of Ru(II) bis-Terpyridine Complexes

Parts of the presented research were previously published under the title “Electrochemical and photophysical study of homoleptic and heteroleptic methylated ruthenium(II) bis-terpyridine complexes” in *European Journal of Inorganic Chemistry*.

Reproduced with permission of Wiley-VCH, from *Electrochemical and photophysical study of homoleptic and heteroleptic methylated ruthenium(II) bis-terpyridine complexes*, Mira T. Rupp, Thomas Auvray, Garry S. Hanan, Dirk G. Kurth, *European Journal of Inorganic Chemistry* **2021**, 2021 (28), 2822-2829.

Contributions:

Mira Rupp: Project design, synthesis, and characterization of ligands and complexes, collection and refinement of X-ray diffraction crystal structures, analysis of photophysical and electrochemical properties, article writing.

Thomas Auvray: Project design, DFT and TD-DFT calculations, revision of the article.

Garry S. Hanan: Supervision, project design, revision of the article.

Dirk G. Kurth: Supervision, project design, revision of the article.

IV.1. Introduction

Electron-withdrawing or donating substituents on the terpyridine ligand can alter the electronic structure of the corresponding Ru(II) complex. In heteroleptic complexes with ligands of different electron-accepting character, e.g., **III-C1** (Chart IV-1), effects of both ligands can be observed. While electron-donating ligands usually have a greater impact on the metal-centered orbitals, electron-withdrawing ligands affect the ligand-centered orbitals (see Chapter I.7.1 for further reading). Hence, in a heteroleptic complex, both the HOMO and LUMO energies and with that the photophysical and electrochemical properties can be altered.

In this chapter, the heteroleptic complex **III-C1** is compared to its homoleptic counterparts, **IV-C1** and **IV-C2** (Chart IV-1), to investigate the effect of the substitution pattern on the photophysical and electrochemical properties. Furthermore, the impact of a directional charge separation in the excited complex, as observed for the heteroleptic complex **III-C1** (see Chapter III for more details), on the performance as PS in photocatalytic hydrogen evolution is investigated.

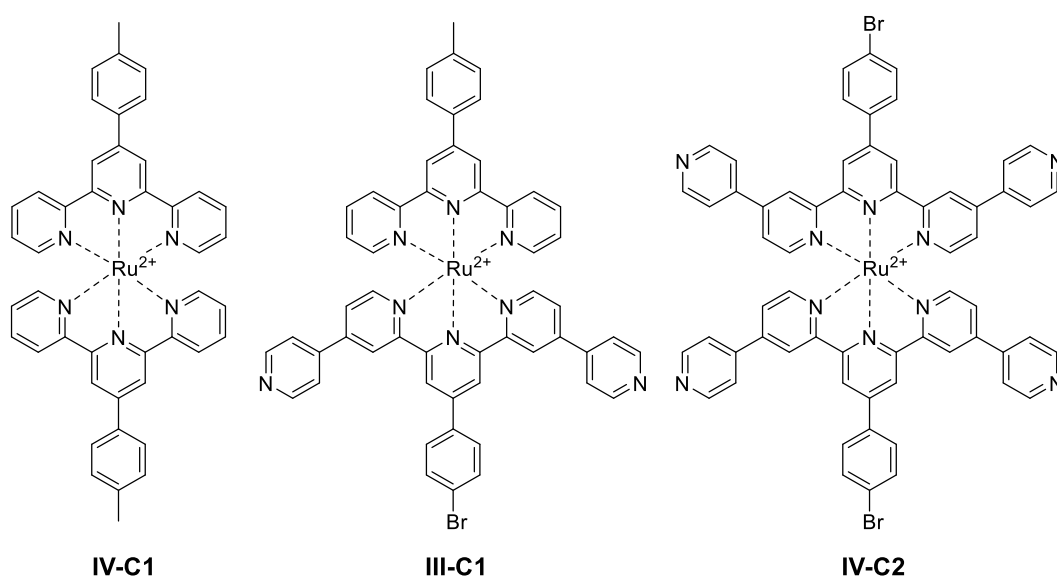
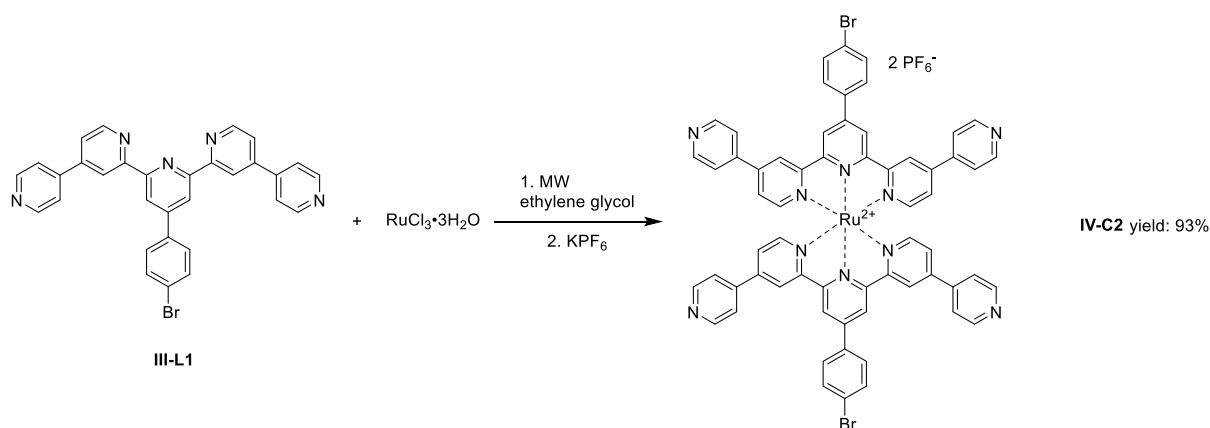


Chart IV-1. Structures of the homoleptic Ru(II) complexes **IV-C1** and **IV-C2** discussed in this chapter alongside **III-C1**; the PF₆⁻ counterions are omitted for clarity.

IV.2. Results and Discussion

IV.2.1. Synthesis and Structural Analysis

As shown in Chart IV-1, there are two respective homoleptic complexes corresponding to the pyridine-substituted heteroleptic complex discussed in Chapter III. To form the first homoleptic complex $[\text{Ru}(\text{Tolytpty})_2]^{2+}$ **IV-C1**, the intermediate $\text{Ru}(\text{Tolytpty})\text{Cl}_3$ **III-I3** is reacted with another equivalent of Tolytpty **III-L3**, analogous to the synthesis of the heteroleptic complex **III-C1**. The homoleptic complex $[\text{Ru}(\text{Bipytpy})_2]^{2+}$ **IV-C2** on the other hand is formed in a one-step synthesis, reacting two equivalents of Bipytpy **III-L1** with Ru(III) chloride using microwave irradiation to form the homoleptic complex **IV-C2** in good yield (93%, Scheme IV-1). An analogue one-step procedure is also possible for the synthesis of **IV-C1**.



Scheme IV-1. Microwave assisted (MW) synthesis of homoleptic complex **IV-C2** starting from **III-L1**.

Single crystals suitable for X-ray diffraction analysis of **IV-C2** are obtained by slow evaporation of a solution of the complex in an acetonitrile/water mix. The experimentally determined structure is depicted in Figure IV-1, the refinement parameters are described in the Appendix (Chapter IX.4). The central Ru(II) ion is coordinated by the two terpyridine ligands **III-L1** in a distorted octahedral coordination sphere. The distortion is a result of the restricted bite angle of the two meridionally coordinated ligands, leading to a N-Ru-N *trans* angle of around 158° instead of 180°. Furthermore, as shown in Figure IV-1, the pyridine substituents as well as the

bromophenyl rings are not co-planar with the rest of the ligand structure, with torsion angles between 20° and 35°. Overall, crystal structure analysis confirms the expected structure of the complex **IV-C2**.

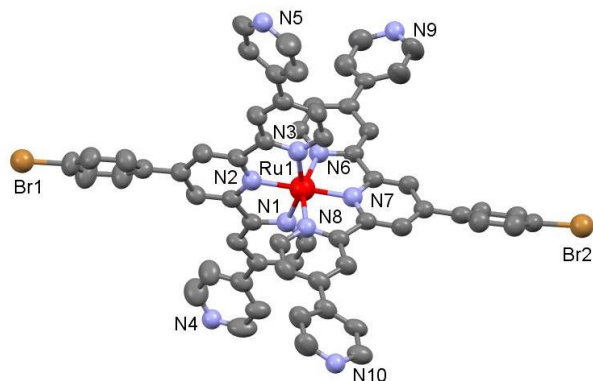


Figure IV-1. Ellipsoid representation of complex **IV-C2** at 50% probability. Hydrogen atoms, PF₆⁻ counter ions and co-crystallized solvent molecules are omitted for clarity.

IV.2.2. Photophysical Properties

Acetonitrile solutions of the complexes are investigated using UV-vis and emission spectroscopy. The spectra can be seen in Figure IV-2 and the data is summarized in Table IV-1. The absorption spectra of the complexes **III-C1**, **IV-C1** and **IV-C2**, look very similar with strong LC absorption bands between 280 nm and 330 nm, and a strong MLCT absorption band around 500 nm. The pyridine substituents bearing complexes **III-C1** and **IV-C2**, furthermore, have a LC absorption band around 235 nm. This absorption band is more intense for the homoleptic complex **IV-C2** (Figure IV-2, green curve), which is expected as it is assigned to a π - π^* transition of the pyridine substituents.

The emission maxima are slightly red-shifted going from the homoleptic complex **IV-C1** to the homoleptic complex **IV-C2** to the heteroleptic complex **III-C1**. This observation matches well with the tolyl substituent being electron donating and hence destabilizing the HOMO and the pyridine substituents being electron withdrawing, hence stabilizing the LUMO. The presence of two different ligands with two different effects leads to both a destabilization of the HOMO and a stabilization of the LUMO and thus a decrease in the HOMO-LUMO energy gap. However, the

observed shifts are very small and other parameters could also affect the emission energy.

Indeed, the absorption spectra do not exhibit the same trend regarding the MLCT absorption maxima of the three complexes, i.e., the MLCT absorption of the heteroleptic complex **III-C1** is slightly blue-shifted compared to the homoleptic complex **IV-C2**. This difference compared to the emission properties is presumably due to the fact that absorption results not only in an electronic transition but also vibrational excitation, i.e., a vibronic transition, while according to Kasha's rule, only the lowest vibrational mode is emissive.^[211]

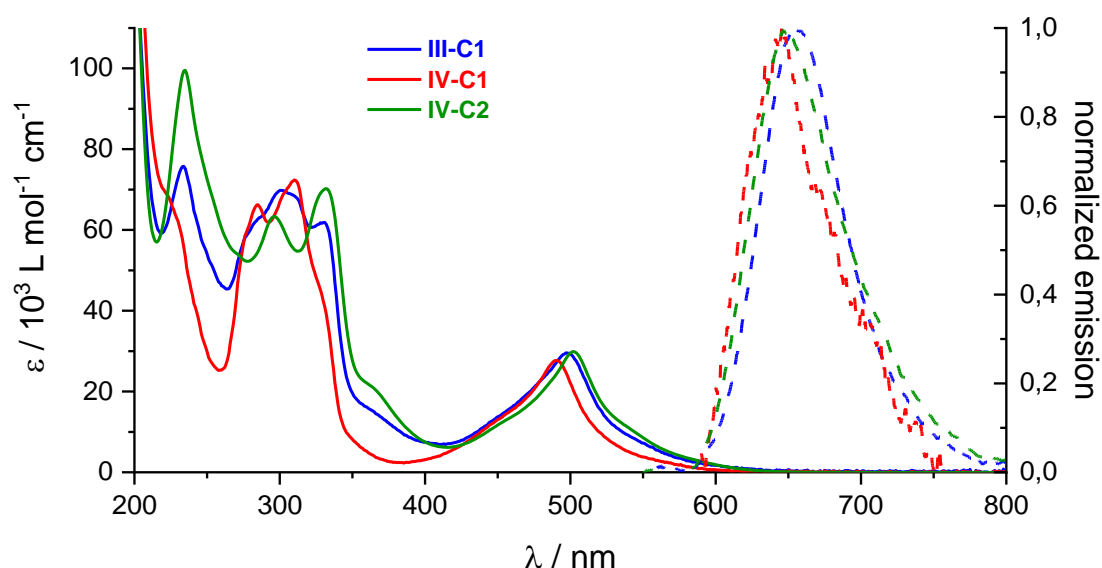


Figure IV-2. UV-vis absorption (solid lines) and emission spectra (dashed lines) of complexes **IV-C1** (red) and **IV-C2** (green) alongside complex **III-C1** (blue); spectra recorded in acetonitrile; emission experiments are conducted under inert gas atmosphere at 20 °C and emission spectra are rescaled so that the intensity at $\lambda_{\max \text{em}}$ is 1.

Table IV-1 shows the luminescence quantum yields as well as the excited-state lifetimes of the homoleptic and heteroleptic complexes. As already discussed in the previous chapters, the pyridine substituted complexes are expected to show stronger luminescence due to the stabilized MLCT state and thus less efficient excited-state quenching *via* the ^3MC state. Indeed, both pyridine-substituted complexes **III-C1** and **IV-C2** exhibit similar photophysical properties ($\tau = 3.8$ ns and 2.4 ns for **III-C1** and **IV-**

C2, respectively; $\Phi = 70\text{--}80 \cdot 10^{-5}$), while the homoleptic complex **IV-C1** has both an excited-state lifetime ($\tau < 1$ ns) and luminescence quantum yield ($\Phi = 3 \cdot 10^{-5}$) decreased by an order of magnitude. The beneficial effect of the pyridine substituents on the photophysical properties is furthermore reflected in the non-radiative decay rates, which are decreased three to five-fold compared to **IV-C1**.

Table IV-1. UV-vis absorption and emission data of complexes **IV-C1** and **IV-C2** alongside complex **III-C1** (spectra measured in acetonitrile at 20 °C).^a

	$\lambda_{\text{max abs}} / \text{nm} (\epsilon / 10^3 \text{ L mol}^{-1} \text{ cm}^{-1})$		$\lambda_{\text{max em}} / \text{nm}$	$\Phi / 10^{-5}$	τ_c / ns	$k_r / 10^4 \text{ s}^{-1}$	$k_{\text{nr}} / 10^8 \text{ s}^{-1}$
	LC	MLCT					
III-C1	233 (76), 301 (70), 330 (62)	498 (29)	656	74 ± 33	3.8 ± 0.1	19.5	2.63
IV-C1	285 (66), 310 (72)	491 (28)	646	3 ± 1^b	0.74 ± 0.02^b	4.05	13.5
IV-C2	235 (100), 296 (63), 332 (70)	502 (30)	649	78 ± 32	2.4 ± 0.2	32.5	4.16

^amaximum absorption wavelength $\lambda_{\text{max abs}}$, extinction coefficient ϵ , maximum emission wavelength $\lambda_{\text{max em}}$, luminescence quantum yield Φ , excited-state lifetime τ ; radiative decay rate $k_r = \Phi/\tau$, non-radiative decay rate $k_{\text{nr}} = (1-\Phi)/\tau$; emission data is collected in inert gas-purged solutions. ^bData taken from Spettel *et al.*^[212]

IV.2.3. Electrochemical Properties

The homoleptic complexes **IV-C1** and **IV-C2** are analyzed using cyclic voltammetry. Figure IV-3 shows the recorded cyclic voltammograms of the homoleptic complexes alongside the heteroleptic complex **III-C1**. The potentials are reported vs. ferrocene (Fc/Fc^+) and the data is summarized in Table IV-2.

All complexes exhibit one reversible, metal-centered oxidation process.^[49, 206] The heteroleptic complex **III-C1** is easier to oxidize (+0.89 V vs. Fc/Fc^+) than the homoleptic complex **IV-C2** (+0.94 V vs. Fc/Fc^+). This shift of the oxidation potential is due to the absence of an electron-donating Tolytpy ligand in the homoleptic complex **IV-C2**, and hence less destabilization of the metal-centered HOMO. The homoleptic complex **IV-C1** on the other hand has two electron-donating tolyl substituents, leading to a further destabilization of the HOMO compared to the heteroleptic complex **IV-C1**, hence resulting in a cathodic shift of the oxidation potential (+0.84 V vs. Fc/Fc^+).

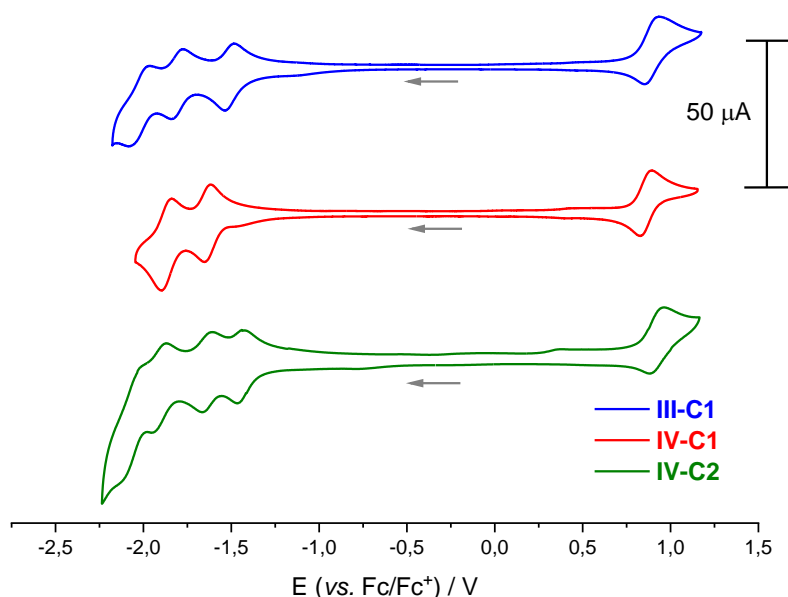


Figure IV-3. Cyclic voltammograms of complexes **IV-C1** (0.5 mM, red) and **IV-C2** (0.5 mM, green) alongside complex **III-C1** (0.5 mM, blue) in dry acetonitrile under inert gas atmosphere, with 0.1 M TBAPF₆; scan rate 100 mV/s; scans start at 0°V vs. reference in cathodic direction.

All complexes exhibit several reversible reduction processes, which are assumed to be ligand centered. The reduction potentials can give an indication about the relative energy of the LUMO of the complexes. More electron-withdrawing substituents make the complex easier to reduce, i.e., the reduction potentials shift anodically. Comparing the different reduction potentials with each other, in complex **III-C1** the first reduction (-1.51 V) is assumed to take place at the pyridine-substituted terpyridine ligand, the second one (-1.81 V) on the tolyl-substituted ligand, and the third one (-2.02 V) on the pyridine-substituted ligand again. For the homoleptic complex **IV-C2**, another reduction process at even lower potentials (-2.09 V) is observed, i.e., the CV shows a total of four reduction processes as each ligand is reduced two times.

The difference between the first oxidation and the first reduction potential can give an indication about the HOMO-LUMO energy gap. The pyridine-substituted complexes **III-C1** and **IV-C2** exhibit a very similar potential difference (2.40 V and 2.39 V, respectively), while the homoleptic complex **IV-C1** has a larger oxidation-reduction potential difference (2.47 V). The observed trend is similar to that of the

MLCT absorption wavelengths, i.e., **IV-C1** exhibits both a smaller potential difference and a blue-shifted absorption wavelength compared to the pyridine-substituted complexes **III-C1** and **IV-C2**. However, the observed differences between the complexes are again relatively small and other factors might need to be taken into consideration.

Table IV-2. Electrochemical half-wave redox potentials $E_{1/2}$ in V vs. Fc/Fc⁺ (ΔE_p / mV) for complexes **IV-C1** and **IV-C2** alongside complex **III-C1** in nitrogen-purged acetonitrile.^a

	Oxidation		Reduction		
III-C1	+0.89 (69)	-1.51 (62)	-1.81 (75)	-2.02 (104)	
IV-C1	+0.84 (47)	-1.63 (50)	-1.85 (65)		
IV-C2	+0.94 (69)	-1.45 (61)	-1.64 (61)	-1.92 (83)	-2.06 (98)

^aRedox potentials are reported vs. ferrocene (Fc/Fc⁺); the differences between the anodic and cathodic peak potentials ΔE_p are given in parentheses in millivolts; measurements in inert gas-purged acetonitrile solutions containing 0.1 M tetrabutylammonium hexafluorophosphate at a sweep rate of 100 mV/s.

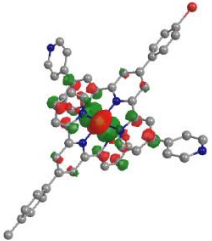
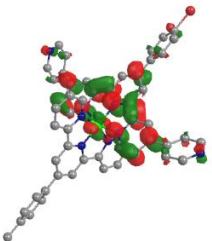
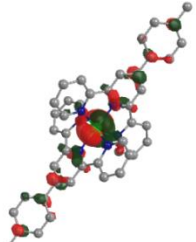
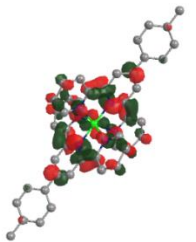
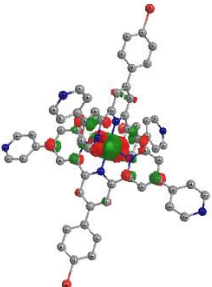
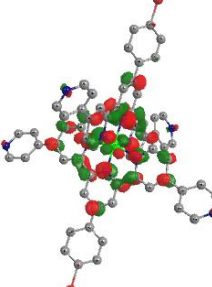
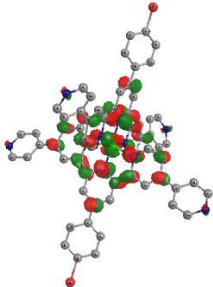
IV.2.4.DFT Calculations

To further understand and rationalize the experimental results discussed above, theoretical DFT calculations are used. Table IV-3 shows the calculated contributions of electron density to the molecular orbitals. In the HOMO, most of the electron density is located on the Ru(II) metal center with equal contributions from both ligands. In the LUMO, the electron density is shifted towards the ligands. As already discussed in the previous Chapter III, in the heteroleptic complex **III-C1**, the electron density is mainly localized on the electron-accepting pyridine-substituted ligand **III-L1**. In the homoleptic complexes however, the electron density is equally distributed over both ligands, regardless of the electron-accepting or donating character of the ligand. Interestingly, it appears as if in the heteroleptic complex **III-C1** more electron density is shifted towards the pyridine substituents compared to the homoleptic complex **IV-C2**.

Taking a closer look at the calculated HOMO and LUMO energies, the pyridine-carrying complexes **III-C1** and **IV-C2** have a very similar calculated HOMO-LUMO energy gap (3.55 eV and 3.53 eV, respectively). In contrast, the homoleptic complex

IV-C1 exhibits a larger HOMO-LUMO energy gap of 3.71 eV. These calculated energy gaps match well with the observed oxidation-reduction potential differences in the electrochemical experiments.

Table IV-3. Contributions to molecular orbitals for complexes **III-C1**, **IV-C1** and **IV-C2**.

	HOMO	LUMO	
III-C1	 -6.53 eV Ru: 66% III-L1: 19%; III-L3: 15%	 -3.00 eV Ru: 7% III-L1: 92%; III-L3: 1%	
IV-C1	 -6.47 eV Ru: 59% III-L3: 41%	 -2.76 eV Ru: 7% III-L3: 93%	
IV-C2	 -6.58 eV Ru: 64% III-L1: 36%	 -3.03 eV Ru: 7% III-L1: 93%	 -3.03 eV Ru: 7% III-L1: 93%

IV.2.5. Hydrogen Evolution Experiments

In the following section the hydrogen evolution activity of complexes **IV-C1** and **IV-C2** is presented, while **III-C1** is already described in Chapter III. The similar photophysical properties of complex **IV-C2** compared to **III-C1** could possibly make this homoleptic complex another promising candidate for the role as PS in photocatalytic hydrogen evolution. As has been stated previously, the rate-limiting step in the hydrogen evolution catalytic cycle is assumed to be the reductive quenching of **III-C1**. As complex **IV-C2** is slightly easier to reduce, this first step could be facilitated. Equation I-4 to Equation I-6 are used to estimate the driving forces ΔG^0_{ET} for the photoinduced electron transfer from the sacrificial electron donor (TEOA, $E_{Ox} = +0.42$ V vs. Fc/Fc^[208]) to the excited PS. The results are summarized in Table IV-4.

Indeed, complex **IV-C2** exhibits a higher estimated driving force compared to the heteroleptic complex **III-C1**. For the tolyl-substituted homoleptic complex **IV-C1** on the other hand the photoinduced electron transfer is estimated to be even less exergonic. The estimated driving force (+0.13 eV) is similar to that of complex **III-C2** ($\Delta G^0_{ET} = +0.17$ eV), which is found to be inactive as PS (see Chapter III). This observation coupled with the poor photophysical properties of **IV-C1** lead to the assumption that this complex is also not active as PS in hydrogen evolution experiments.

Table IV-4. Excited-state redox potentials and estimated free Gibbs energy ΔG^0_{ET} for photoinduced electron transfer from TEOA to the complexes **III-C1**, **IV-C1** and **IV-C2**.

	E_{ox}^* / V vs. Fc/Fc ⁺	E_{red}^* / V vs. Fc/Fc ⁺	$\Delta G^0_{ET} / eV$
III-C1	-1.00	+0.38	+0.04
IV-C1	-1.08	+0.29	+0.13
IV-C2	-0.97	+0.46	-0.04

Hydrogen evolution experiments are carried out under comparable conditions to the studies described in the previous chapter, using [Co(dmgH)₂(H₂O)₂](BF₄)₂, prepared *in-situ* from [Co(H₂O)₆](BF₄)₂ (1 mM) and dmgH₂ (6 mM), or colloidal

platinum, prepared *in-situ* from K_2PtCl_4 , and blue light irradiation (LED centered at 445 nm). Under these conditions, complex **IV-C1** is inactive as PS. Complex **IV-C2**, however, does act as PS and leads to hydrogen evolution (Figure IV-4). Yet, despite the slightly higher estimated driving force for the reductive quenching, the activity of the homoleptic complex **IV-C2** is lower than that of the heteroleptic complex **III-C1**, with a maximum TOF around $35 \text{ mmol}_{H_2} \text{ mol}_{PS}^{-1} \text{ mol}^{-1}$, regardless of the catalyst used. Furthermore, the homoleptic complex leads to a less stable hydrogen evolution activity. With the cobaloxime catalyst, the hydrogen evolution reaches its half-life time after 5.2 h and with colloidal platinum after 8.0 h.

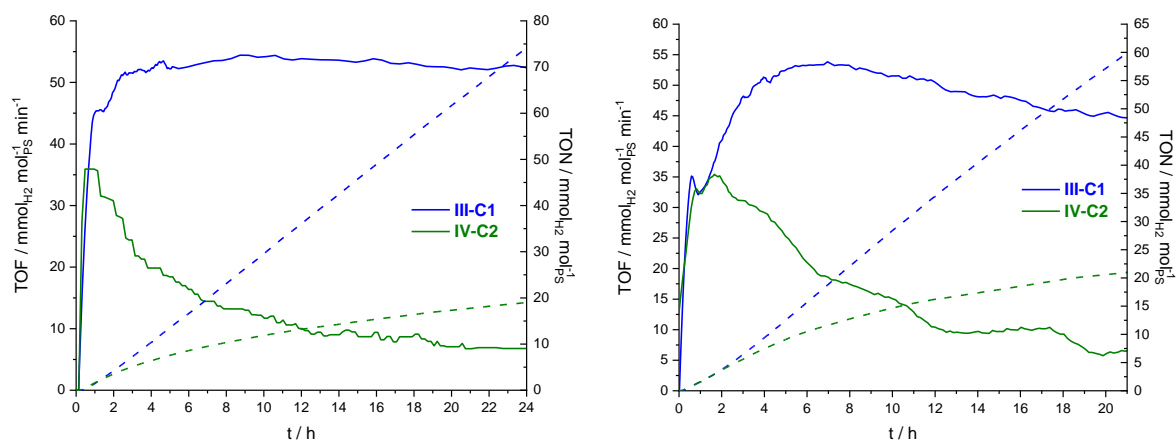


Figure IV-4. Hydrogen photoproduction with complexes **III-C1** and **IV-C2** as PS (0.1 mM) under blue light irradiation (LED centered at 445 nm); with TEOA as sacrificial electron donor (1 M) and HBF_4 as proton source (0.1 M) in DMF; left: $[Co(H_2O)_6](BF_4)_2$ as pre-catalyst (1 mM), with $dmgH_2$ (6 mM); right: K_2PtCl_4 as pre-catalyst to form *in-situ* colloidal Pt (0.05 mM); TOF: solid lines; TON: dashed lines; adapted from *Electrochemical and photophysical study of homoleptic and heteroleptic methylated ruthenium(II) bis-terpyridine complexes*, Mira T. Rupp, Thomas Auvray, Garry S. Hanan, Dirk G. Kurth, *European Journal of Inorganic Chemistry* **2021**, 2021 (28), 2822-2829. Reproduced with permission of Wiley-VCH.^[169]

UV-vis absorption experiments of the reaction mixtures with **IV-C2** before and after irradiation are shown in Figure IV-5. The spectra before and after vary only slightly, with the overall absorption profile of **IV-C2** unchanged. This observation leads to the conclusion that the complex does not decompose under the catalytic conditions, and that instead other components of the reaction mixture, such as the catalyst or the oxidized SED, are responsible for the loss of hydrogen evolution activity over time.

The hydrogen evolution experiments using **III-C1** as PS lead to the conclusion that the rate-limiting step does not involve the catalyst and that the low activity is due to the reductive quenching being thermodynamically unfavorable because of the relatively poor photophysical properties and low driving forces. The fact that the maximum activity of **IV-C2** as PS remains unchanged regardless of the catalyst used points towards the photoinduced electron transfer being the critical step in this system as well. However, as mentioned above, the slightly improved estimated driving force for the reductive quenching alongside with similar photophysical properties as **III-C1** should be reflected in a higher activity of complex **IV-C2**. The observed lower activity and reduced longevity of the hydrogen production of the homoleptic complex **IV-C2** compared to the heteroleptic complex **III-C1** hence lead to the conclusion that the heteroleptic design is somehow beneficial to the electron transfer processes involved in the hydrogen evolution catalytic cycle. The non-symmetrical electron density distribution in the LUMO of the heteroleptic complex **III-C1**, as calculated by DFT, could induce a directionality, which might be beneficial for electron transfer, making it a more efficient and stable PS than **IV-C2**. However, more detailed studies are needed to investigate this effect.

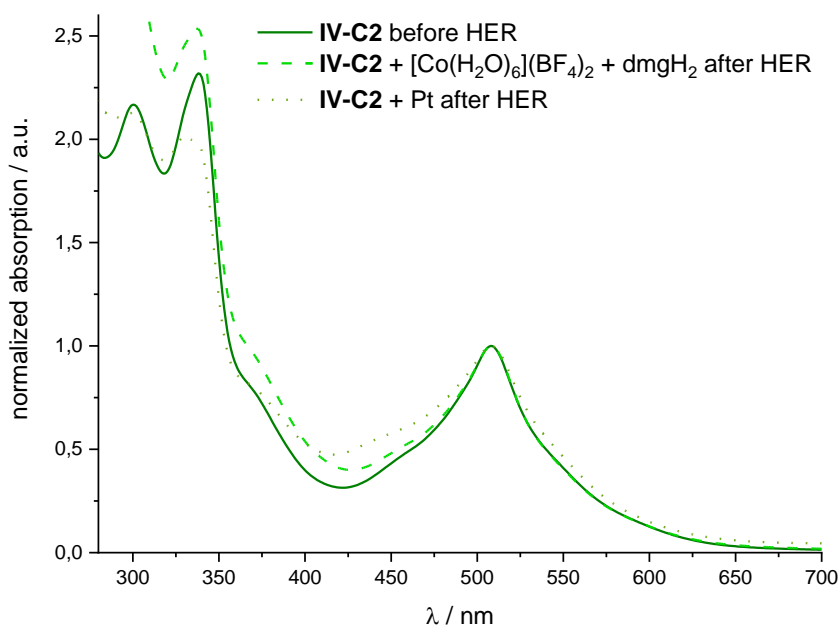


Figure IV-5. UV-vis absorption spectra of DMF solutions containing **IV-C2** (0.1 mM); TEOA (1 M) and HBF₄ (0.1 M) before light irradiation (solid line) alongside reaction mixtures additionally containing (a) [Co(H₂O)₆](BF₄)₂ (1 mM) and dmgH₂ (6 mM) (dashed line) or (b) K₂PtCl₄ (dotted line) after blue light irradiation (LED centered at 445 nm); absorptions are normalized to the MLCT absorption peak; adapted from *Electrochemical and photophysical study of homoleptic and heteroleptic methylated ruthenium(II) bis-terpyridine complexes*, Mira T. Rupp, Thomas Auvray, Garry S. Hanan, Dirk G. Kurth, *European Journal of Inorganic Chemistry* **2021**, 2021 (28), 2822-2829. Reproduced with permission of Wiley-VCH.^[169]

IV.3. Conclusion

In this chapter, the heteroleptic complex **III-C1** is compared to its homoleptic counterparts **IV-C1** and **IV-C2**. The LUMO-stabilizing effect of the electron-accepting pyridine substituents as well as the HOMO-destabilizing effect of the electron-donating tolyl substituents are reflected both in the photophysical and electrochemical experiments. Stabilization of the ligand-centered LUMO is accompanied by an increase of the ³MLCT to ³MC gap and hence an increase of the luminescence of the pyridine-bearing complexes **III-C1** and **IV-C2**. These two complexes exhibit very similar photophysical properties. However, the homoleptic complex **IV-C2** is slightly easier to reduce, which leads to a higher estimated driving force from the sacrificial electron donor TEOA to the excited complex. However, in hydrogen evolution experiments, the homoleptic complex **IV-C2** leads to a weaker and shorter-lived hydrogen evolution

activity. The observed activity is identical for both a cobaloxime and a colloidal platinum catalyst, which indicates that the catalyst is not involved in the rate-limiting step. Overall, the presented study suggests that the directionality induced by the heteroleptic design of complex **III-C1** is beneficial for the activity as PS in hydrogen evolution.

IV.4. Experimental

Details on instrumentation, crystal structure analysis, and DFT calculations as well as NMR spectra with peak assignments can be found in the Appendix (Chapter IX). References are given for known compounds. The properties of the known compounds agree with the ones published.

[Ru(Tolyltpy)₂](PF₆)₂ IV-C1^[213]

A suspension of [RuCl₃(Tolyltpy)] **III-I3** (75.0 mg, 141 μmol, 1 eq) and Tolyltpy **III-L3** (45.7 mg, 141 μmol, 1 eq) in 15.0 mL ethylene glycol was heated to 180 °C for 20 minutes using microwave irradiation. After cooling to room temperature, water and aqueous KPF₆ solution were added to the solution. The precipitate was filtered off over celite, washed with water and dissolved in acetonitrile. The solution was dried over magnesium sulfate and the solvent removed under reduced pressure to yield the product as a red solid (96.4 mg, 92.9 μmol, 66%).

¹H-NMR (300 MHz, CD₃CN): δ = 8.99 (s, 4H), 8.64 (d, ³J = 8.2 Hz, 4H), 8.11 (d, ³J = 8.2 Hz, 4H), 7.94 (td, ³J = 7.9 Hz, ⁴J = 1.4 Hz, 4H), 7.58 (d, ³J = 8.3 Hz, 4H), 7.43 (d, ³J = 5.5 Hz, 4H), 7.17 (m, 4H) and 2.54 ppm (s, 6H). ¹³C{¹H}-NMR (75 MHz, CD₃CN): δ = 159.2, 156.4, 153.4, 149.3, 142.0, 139.0, 134.9, 131.3, 128.6, 128.4, 125.4, 122.3 and 21.4 ppm.

[Ru(Bipytpy)₂](PF₆)₂ IV-C2

A suspension of Ru(III) chloride trihydrate (11.8 mg, 45.0 μmol, 1 eq) and Bipytpy **III-L1** (50.0 mg, 92.2 μmol, 2.05 eq) in 7.00 mL ethylene glycol was heated to 150 °C for 40 minutes using microwave irradiation. After cooling to room temperature, water and aqueous KPF₆ solution were added to the solution and the precipitate was

filtered off over celite. After washing with water, the solid was dissolved in acetonitrile, dried over magnesium sulfate and the solvent was removed under reduced pressure. The crude product was purified by washing with dichloromethane to yield the product as a dark red solid (62.0 mg, 42.0 μmol , 93%).

$^1\text{H-NMR}$ (400 MHz, CD_3CN): δ = 9.24 (s, 4H), 8.99 (s, 4H), 8.77 (d, 3J = 5.7 Hz, 8H), 8.24 (d, 3J = 8.4 Hz, 4H), 8.01 (d, 3J = 8.3 Hz, 4H), 7.79 (d, 3J = 5.6 Hz, 8H), 7.61 (d, 3J = 5.9 Hz, 4H) and 7.54 ppm (d, 3J = 5.7 Hz, 4H). $^{13}\text{C}\{^1\text{H}\}\text{-NMR}$ (125 MHz, CD_3CN): δ = 159.8, 156.5, 154.0, 151.8, 148.4, 148.3, 143.6, 136.8, 133.7, 130.6, 125.9, 125.6, 123.4, 123.1 and 122.5 ppm. ESI-MS: m/z $[\text{M}]^{2+}$ calc. for $\text{C}_{62}\text{H}_{40}\text{Br}_2\text{N}_{10}\text{Ru}$: 592.04183; found: 592.04471; difference: 4.9 ppm.

V. Effect of N-Methylation of Ru(II) bis-Terpyridine Complexes

Parts of the presented research were previously published under the title “Electrochemical and photophysical study of homoleptic and heteroleptic methylated ruthenium(II) bis-terpyridine complexes” in *European Journal of Inorganic Chemistry*.

Reproduced with permission of Wiley-VCH, from *Electrochemical and photophysical study of homoleptic and heteroleptic methylated ruthenium(II) bis-terpyridine complexes*, Mira T. Rupp, Thomas Auvray, Garry S. Hanan, Dirk G. Kurth, *European Journal of Inorganic Chemistry* **2021**, 2021 (28), 2822-2829.

Contributions:

Mira Rupp: Project design, synthesis and characterization of ligands and complexes, collection and refinement of X-ray diffraction crystal structures, analysis of photophysical and electrochemical properties, article writing.

Thomas Auvray: Project design, DFT and TD-DFT calculations, revision of the article.

Garry S. Hanan: Supervision, project design, revision of the article.

Dirk G. Kurth: Supervision, project design, revision of the article.

V.1. Introduction

Pyridine substituents in the periphery of the terpyridine metal ion receptor offer the possibility for further functionalization on the nitrogen atom, e.g., *via* *N*-methylation. The concept is demonstrated on the complexes **III-C1** and **IV-C2** from the previous chapters III and IV. The functionalization of the peripheral pyridine-substituents can introduce a charge to the ligand, which alters not only the solubility but also the electron-accepting character of the ligand and with that the photophysical and electrochemical properties of the complex. Furthermore, in a heteroleptic complex, the previously observed non-symmetrical distribution to the electron density in the excited state would be further promoted.

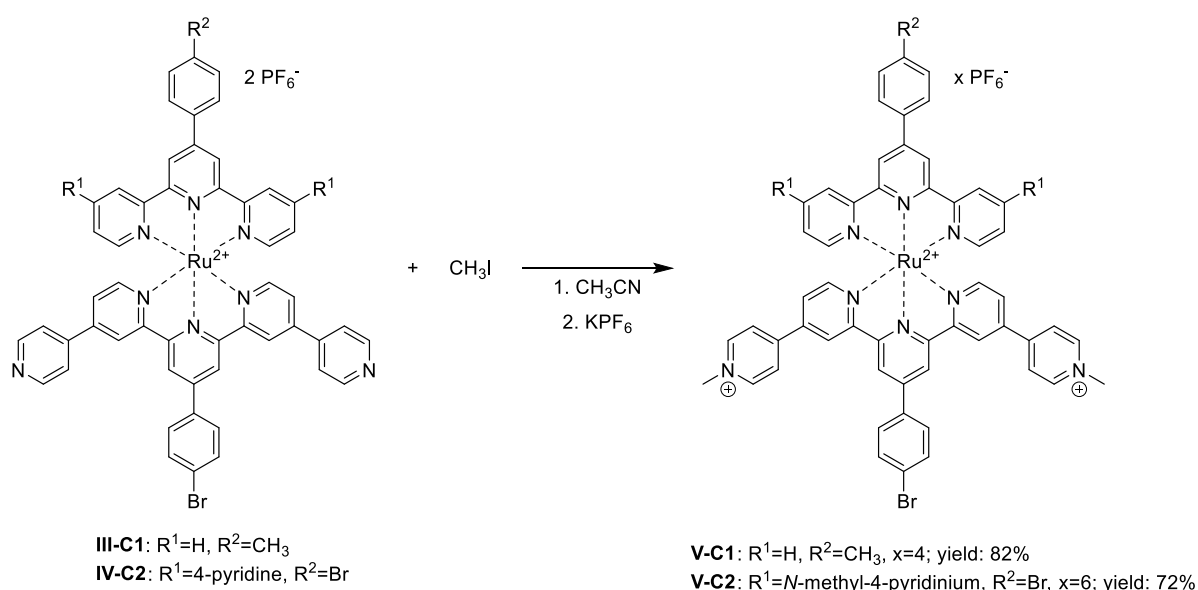
There are several studies of Constable and coworkers, who investigate *N*-alkylation on a pyridine ring in 4'-position of the terpyridine ligand and the effects on ruthenium, osmium and iron bis-terpyridine complexes.^[86, 214-222] By introducing different *N*-substituents, they could alter the properties of these complexes, e.g., the redox behavior, emission wavelength and excited-state lifetime.

In this chapter, the complexes **III-C1** and **IV-C2** are *N*-methylated on the pyridine substituents in 4- and 4''-position to form complexes **V-C1** and **V-C2** (Scheme V-1). Their photophysical and electrochemical properties are compared to similar structures from the literature and their possible application as PS is discussed.

V.2. Results and Discussion

V.2.1. Synthesis and Structural Analysis

The pyridine substituted homoleptic and heteroleptic complexes **III-C1** and **IV-C2** are reacted with excess of iodomethane to form the desired complexes **V-C1** and **V-C2** (Scheme V-1). The complexes are isolated as hexafluorophosphate salts and are analyzed using NMR spectroscopy and high-resolution mass spectrometry.

Scheme V-1. Synthesis of methylated complexes **V-C1** and **V-C1**.

Complex **V-C1** is furthermore analyzed using X-ray diffraction. Single crystals are received by slow diffusion of diethyl ether into a concentrated acetonitrile solution of **V-C1**. The received structure is shown in Figure V-1 and the refinement parameters are described in the Appendix (IX.4). The Ru(II) ion is meridionally coordinated by the two terpyridine ligands in a distorted octahedral sphere, with a N-Ru-N *trans* angle of 158° . In contrast to complex **III-C1**, the tolyl substituted ligand in **V-C1** is not bent, presumably due to the fact that no hydrogen bonding with the pyridine substituents of neighboring complexes in the crystal is possible because of the methylation. As observed in other Ru(II) bis-terpyridine crystal structures, the bromophenyl, pyridine and tolyl substituents are not co-planar with the rest of the ligands but distorted to a certain degree ($8\text{--}30^\circ$). Overall, the crystal structure analysis confirms the expected structure of complex **V-C1**.

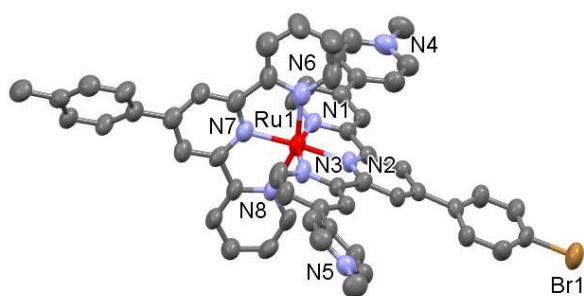


Figure V-1. Ellipsoid representation of complex **V-C1** at 50% probability. Hydrogen atoms, PF_6^- counterions and co-crystallized solvent molecules are omitted for clarity.

V.2.2. Photophysical Properties

The photophysical properties of the methylated complexes **V-C1** and **V-C2** in acetonitrile solution are investigated and compared to those of their non-methylated counterparts **III-C1** and **IV-C2**. The UV-vis absorption spectra alongside the room-temperature emission spectra are shown in Figure IV-2 and the data is summarized in Table V-1. The methylated complexes exhibit a broader and red-shifted MLCT absorption band compared to the non-methylated complexes with a maximum around 515 nm. These broader MLCT absorption bands have a lower absorptivity compared to the ones of the non-methylated analogues and they overlap with other, higher-energy transitions around 400 nm, which are presumably ligand-centered. The heteroleptic complex **V-C1** further exhibits a shoulder around 470 nm, which is assumed to stem from a MLCT transition, mainly involving the tolyl-substituted ligand.

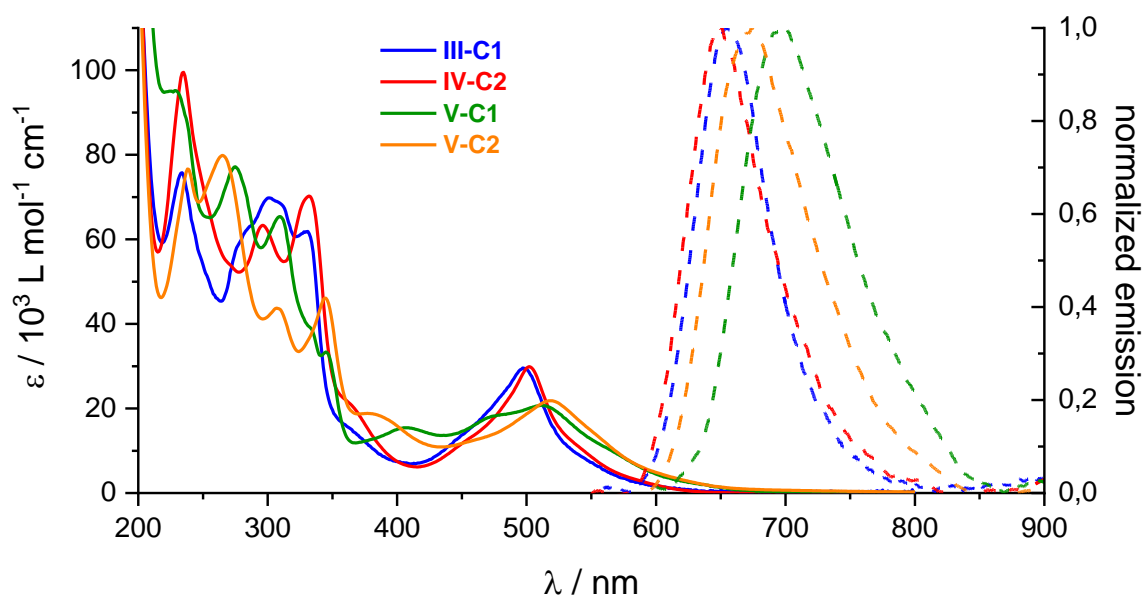


Figure V-2. UV-vis absorption (solid lines) and emission spectra (dashed lines) of methylated complexes **V-C1** (green) and **V-C2** (orange) alongside non-methylated complexes **III-C1** (blue) and **IV-C2** (red); spectra recorded in acetonitrile; adapted from *Electrochemical and photophysical study of homoleptic and heteroleptic methylated ruthenium(II) bis-terpyridine complexes*, Mira T. Rupp, Thomas Auvray, Garry S. Hanan, Dirk G. Kurth, *European Journal of Inorganic Chemistry* **2021**, 2021 (28), 2822-2829. Reproduced with permission of Wiley-VCH.^[169]

The emission of the methylated complexes is red-shifted by 25–40 nm compared to the non-methylated analogues. This bathochromic shift relates to a stabilized ³MLCT state, presumably due to the more electron-accepting methylated ligand stabilizing the ligand-centered LUMO. As has been discussed in previous chapters, a stabilized ³MLCT state should further lead to increased luminescence. Indeed, both the quantum yields and excited-state lifetimes of complexes **V-C1** and **V-C2** ($\Phi = 295\text{--}405 \cdot 10^{-5}$; $\tau = 35\text{--}40$ ns) are increased by an order of magnitude compared to **III-C1** and **IV-C2** ($\Phi = 70\text{--}80 \cdot 10^{-5}$; $\tau = 2\text{--}4$ ns).

Constable and coworkers investigated *N*-alkylated 4'-pyridyl substituted bis-terpyridine complexes and they found similar quantum yields around $40 \cdot 10^{-4}$.^[87] However, the excited-state lifetimes of the complexes investigated by Constable *et al.* were found to be increased by a factor of three to four compared to complexes **V-C1** and **V-C2**, and the emission wavelengths to be red-shifted to around 720 nm. This

further red shift of another 25–45 nm of the *N*-alkylated 4'-pyridyl substituted complexes compared to the complexes discussed in this chapter, indicates an even smaller gap between the ground state and the excited state. The energy gap law states that the natural logarithm \ln of the non-radiative decay constant, $\ln(k_{nr})$, varies linearly with the emission energy.^[155] Therefore, a red-shifted emission should result in a shorter excited-state lifetime. The observed inconsistency of the emission energy and excited-state lifetime relation for the complexes studied by Constable *et al.* as well as the complexes discussed in this thesis indicates that the non-radiative decay is not governed by the energy gap law. Instead, a non-radiative decay *via* the 3MC state is assumed to be the main contributor to the quenching of the excited 3MLCT state. Hence, a smaller energy gap between the ground state and the 3MLCT state resulting mainly from a stabilized LUMO could lead to a larger energy barrier for internal conversion to the non-radiative 3MC state, leading to longer excited-state lifetimes. Compared to the non-methylated complexes **III-C1** and **IV-C2**, the increased electron-accepting character of the ligands due to methylation leading to a stabilization of the 3MLCT state and with that to less luminescence quenching *via* the 3MC state, i.e., higher quantum yield and longer excited-state lifetimes is indeed observed. However, within the series of *N*-methylated and *N*-alkylated complexes no clear relationship between the emission wavelength and the quantum yield or excited-state lifetime can be identified and it is assumed that there are further aspects that influence the emission behavior of these complexes.

Table V-1. UV-vis absorption and emission data of methylated complexes **V-C1** and **V-C2** alongside non-methylated complexes **III-C1** and **IV-C2** (spectra measured in acetonitrile at 20 °C).^a

	$\lambda_{\max \text{ abs}} / \text{nm} (\epsilon / 10^3 \text{ L mol}^{-1} \text{ cm}^{-1})$		$\lambda_{\max \text{ em}} / \text{nm}$	$\Phi_c / 10^{-5}$	τ_c / ns	$k_r / 10^4 \text{ s}^{-1}$	$k_{nr} / 10^8 \text{ s}^{-1}$
	LC	MLCT					
III-C1	233 (76), 301 (70), 330 (62)	498 (29)	656	74±33	3.8±0.1	19.5	2.63
IV-C2	235 (100), 296 (63), 332 (70)	502 (30)	649	78±32	2.4±0.2	32.5	4.16
V-C1	228 (95), 275 (77), 309 (65), 405 (15)	511 (21)	697	295±128	36±1	8.19	0.28
V-C2	238 (77), 265 (80), 307 (44), 377 (19)	519 (22)	675	405±160	39±1	10.4	0.26

^amaximum absorption wavelength $\lambda_{\max \text{ abs}}$, extinction coefficient ϵ , maximum emission wavelength $\lambda_{\max \text{ em}}$, luminescence quantum yield Φ , excited-state lifetime τ ; radiative decay rate $k_r = \Phi/\tau$, non-radiative decay rate $k_{nr} = (1-\Phi)/\tau$; emission data is collected in inert gas-purged solutions.

V.2.3. Electrochemical Properties

The *N*-methylated complexes **V-C1** and **V-C2** are further investigated regarding their electrochemical properties using cyclic voltammetry. The cyclic voltammograms in nitrogen-purged acetonitrile are shown in Figure V-3 and the data is summarized in Table V-3. The potentials are reported vs. ferrocene and scans start in cathodic direction. Both the methylated and non-methylated complexes exhibit one reversible oxidation process corresponding to an oxidation of the Ru(II) metal center. The potential of these oxidation processes is anodically shifted by 50–100 mV for the methylated complexes **V-C1** and **V-C2** compared to their non-methylated counterparts **III-C1** and **IV-C2**. This observation is a result of the more electron-withdrawing character of the *N*-methyl-pyridine substituents compared to a pyridine substituent, which leads to a stronger stabilizing effect of the metal-centered HOMO.^[206]

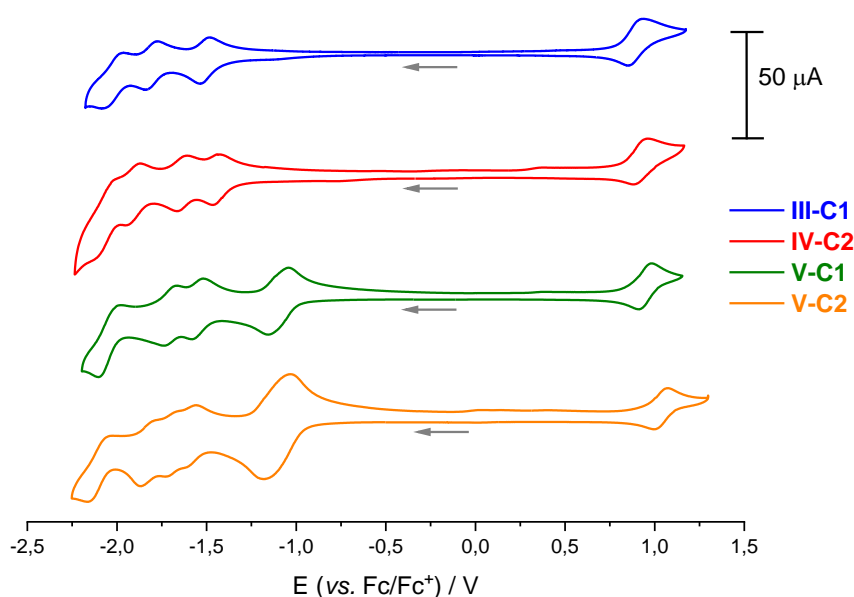


Figure V-3. Cyclic voltammograms of complexes **V-C1** (0.5 mM, green) and **V-C2** (0.5 mM, orange) alongside complexes **III-C1** (0.5 mM, blue) and **IV-C2** (0.5 mM, red) in dry acetonitrile under inert gas atmosphere, with 0.1 M TBAPF₆; scan rate 100 mV/s; scans start at 0°V vs. reference in cathodic direction.

While the electron-accepting character of the ligands also affects the HOMO, it influences the LUMO energy to a greater degree. The *N*-methylated complexes exhibit a first ligand-centered reduction process, or rather several overlapping processes, at -1.1 V vs. Fc/Fc⁺, which corresponds to an anodic shift of 350–400 mV compared to the non-methylated complexes. Square wave voltammetry experiments (see Figure V-4) identify this first oxidation event to be a two-electron process in the case of the heteroleptic complex **V-C1**, and a four-electron process in the case of the homoleptic complex **V-C2**. The strong anodic shift as well as the observation of multi-electron processes lead to the assignment of this first reduction to take place at the pyridinium ions.^[215] Furthermore, the redox potentials match well with those observed in a study on homoleptic *N*-methylated 4'-pyridinium Ru(II) bis-terpyridine complexes by Constable and Cargill Thompson. However, they observed two separate reduction processes corresponding to the pyridinium sites.^[215] Their results support the assumption that here the first reduction process indeed consists of several overlapping processes, which also accounts for the large peak separation (>100 mV).

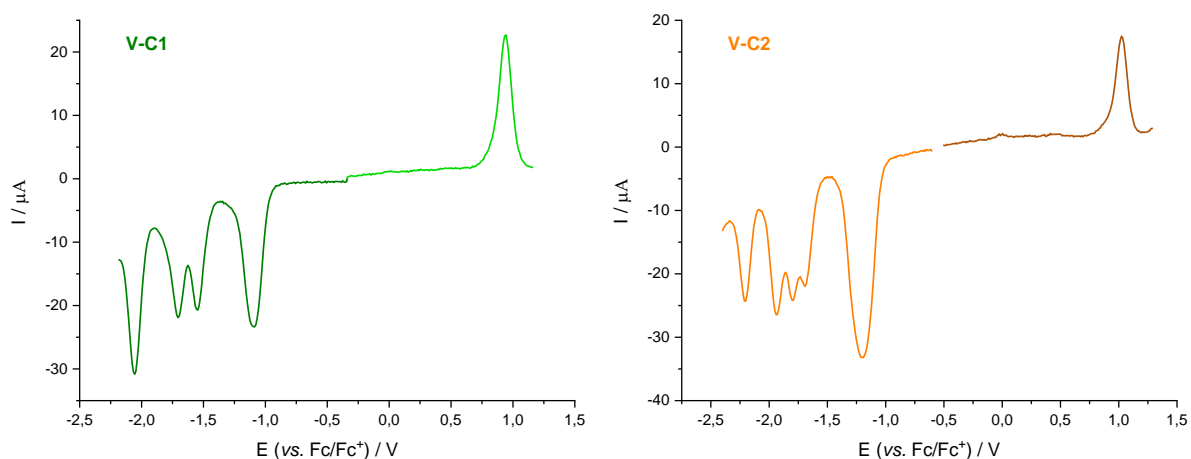


Figure V-4. Square wave voltammetry of complex **V-C1** (left) and **V-C2** (right) in dry acetonitrile under inert gas atmosphere, with 0.1 M TBAPF₆; scan rate 100 mV/s; scans start at 0 V vs. reference electrode; adapted from *Electrochemical and photophysical study of homoleptic and heteroleptic methylated ruthenium(II) bis-terpyridine complexes*, Mira T. Rupp, Thomas Auvray, Garry S. Hanan, Dirk G. Kurth, *European Journal of Inorganic Chemistry* **2021**, 2021 (28), 2822-2829. Reproduced with permission of Wiley-VCH.^[169]

The *N*-methylated complexes **V-C1** and **V-C2** furthermore exhibit three and four more reduction processes, respectively. Following the assignment of the reduction processes described in previous chapters, it is assumed that in complex **V-C1**, the reductions occurring at -1.55 V and -2.04 V vs. Fc/Fc⁺ take place at the pyridinium-substituted ligand, while the reduction event at -1.70 V takes place at the tolyl-substituted ligand. In the homoleptic complex **V-C2**, the four reductions below -1.5 V correspond to each ligand being reduced twice.

Table V-2. Table III-6. Electrochemical half-wave redox potentials $E_{1/2}$ in V vs. Fc/Fc⁺ (ΔE_p / mV) for methylated complexes **V-C1** and **V-C2** alongside non-methylated complexes **III-C1** and **IV-C2** in nitrogen-purged acetonitrile.^a

	Oxidation		Reduction			
	$E_{1/2}$ (mV)	ΔE_p (mV)	$E_{1/2}$ (mV)	ΔE_p (mV)	$E_{1/2}$ (mV)	ΔE_p (mV)
III-C1	+0.89 (69)	-1.51 (62)	-1.81 (75)	-2.02 (104)		
IV-C2	+0.94 (69)	-1.45 (61)	-1.64 (61)	-1.92 (83)	-2.06 (98)	
V-C1	+0.94 (71)	-1.10 (102)	-1.55 (62)	-1.70 (71)	-2.04 (139)	
V-C2	+1.04 (73)	-1.11 (114)	-1.58 (66)	-1.69 (70)	-1.82 (84)	-2.09 (142)

^aRedox potentials are reported vs. ferrocene (Fc/Fc⁺); the differences between the anodic and cathodic peak potentials ΔE_p are given in parentheses in millivolts; measurements in inert gas-purged acetonitrile solutions containing 0.1 M tetrabutylammonium hexafluorophosphate at a sweep rate of 100 mV/s.

V.2.4. DFT Calculations

The experimental investigations are supported by theoretical calculations using DFT and TD-DFT. Figure V-5 shows the calculated HOMO and LUMO energies of complexes **V-C1** and **V-C2** alongside **III-C1** and **IV-C2**. The energy of the LUMOs of the methylated complexes is decreased significantly compared to the non-methylated counterparts. This stabilization matches well the observed anodic shift of the reduction potentials of **V-C1** and **V-C2**. Furthermore, the HOMOs of the methylated complexes are stabilized compared to **III-C1** and **IV-C2**, which again agrees well with the observed anodic shift of the oxidation potentials. The HOMO-LUMO energy gaps of the methylated complexes are significantly smaller than those of the non-methylated analogues, which matches the red shift in emission wavelength described above,

indicating that the $^3\text{MLCT}$ state is affected by the *N*-methylation in a similar fashion as the LUMO (Table V-1).

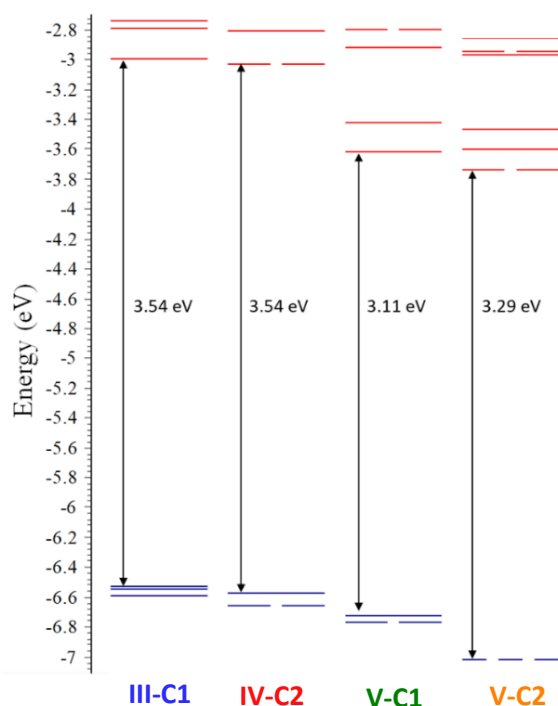


Figure V-5. Energy diagram of the calculated frontier orbitals of the methylated complexes **V-C1** and **V-C2** alongside the non-methylated complexes **III-C1** and **IV-C2** with energy gaps highlighted (degeneracy threshold of 15 meV); adapted from *Electrochemical and photophysical study of homoleptic and heteroleptic methylated ruthenium(II) bis-terpyridine complexes*, Mira T. Rupp, Thomas Auvray, Garry S. Hanan, Dirk G. Kurth, *European Journal of Inorganic Chemistry* **2021**, 2021 (28), 2822-2829. Reproduced with permission of Wiley-VCH.^[169]

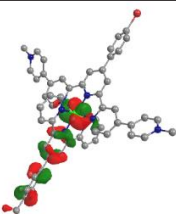
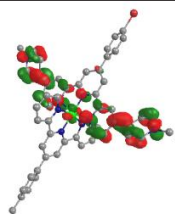
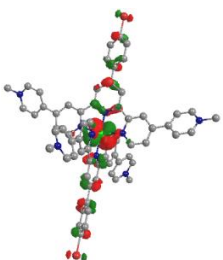
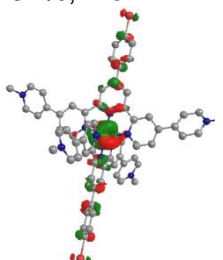
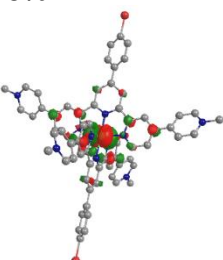
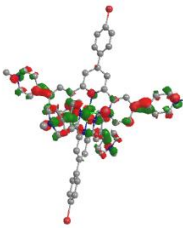
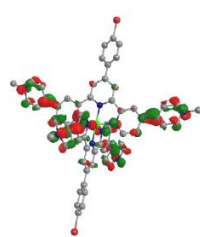
Table V-3 shows the calculated contributions to the molecular orbitals. In the HOMO, most of the electron density is located on the metal center, with smaller contributions from the ligands. Interestingly, compared to the non-methylated complex **III-C1**, **V-C1** has a slightly lower calculated contribution from the metal center and instead the contribution from the TolyItpy ligand **III-L3** is doubled. In the homoleptic complex **V-C2**, the electron density contribution of the ligands in the HOMO is also increased.

In the LUMO, the electron density is shifted almost completely towards the ligands. As already discussed in the previous Chapter IV, in the heteroleptic complexes, the electron density is mainly localized on one, the more electron-

accepting, ligand, while in the homoleptic complexes it is equally distributed over both ligands. The *N*-methylation leads to a larger contribution of electron density from the pyridinium substituents, which agrees with the pyridinium-centered reductions observed in the cyclic voltammograms.

TD-DFT calculations investigating the nature of the excited state of **V-C1** and **V-C2** show that the excited states correspond to MLCT states with minor contributions from LC states (see Appendix IX.5.1). As already seen in Table V-3, the delocalization is extended towards the pyridinium substituents upon methylation. However, these substituents have only a minor contribution to the excited state, with no contribution from the methyl groups. These results are similar to those described by Constable and coworkers for comparable systems.^[87]

Table V-3. Contributions to molecular orbitals for complexes **V-C1** and **V-C2**.

	HOMO			LUMO	
V-C1	 -6.73 eV Ru: 52% III-L3: 32%; Me-III-L1: 16%			 -3.62 eV Ru: 4% III-L3: 3%; Me-III-L1: 93%	
V-C2	 -7.02 eV Ru: 55% Me-III-L1: 45%	 -7.02 eV Ru: 56% Me-III-L1: 44%	 -7.03 eV Ru: 65% Me-III-L1: 35%	 -3.74 eV Ru: 4% Me-III-L1: 96%	 -3.74 eV Ru: 4% Me-III-L1: 96%

V.2.5. Hydrogen Evolution Experiments

Complex **IV-C2** is less active and less long-lived as photosensitizer in hydrogen evolution experiments (see Chapter IV), despite similar photophysical properties compared to **III-C1** and being easier to reduce. While this is presumably due to a certain directionality of charge transfer within the heteroleptic complex **III-C1**, a less negative reduction potential could still make the electron transfer from sacrificial electron donor to the excited PS more exergonic. Equation I-4 to Equation I-6 are used to estimate the driving forces for this photoinduced electron transfer process for the methylated complexes. The results are summarized in Table V-4. The free Gibbs energy for **V-C1** and **V-C2** shows that indeed the reductive quenching of these PSs should be significantly more exergonic compared to the non-methylated complexes. However, the potential difference between the reduced PS and the reduction potential of the used cobaloxime catalyst ($[\text{Co}(\text{dmgH})_2(\text{H}_2\text{O})_2](\text{BF}_4)_2$, $E_{\text{Red}}(\text{Co}^{\text{II/I}}) = -1.43 \text{ V vs. Fc/Fc}^+$) leads to the conclusion that this second electron transfer step is thermodynamically highly unfavorable. It is hence questionable if these complexes can act as PS despite their improved photophysical properties.

Table V-4. Excited-state redox potentials and estimated free Gibbs energy $\Delta G^{\circ}_{\text{ET}}$ for photoinduced electron transfer from TEOA to the complexes **III-C1**, **IV-C2**, **V-C1** and **V-C2**.

	$E_{\text{ox}}^* / \text{V vs. Fc/Fc}^+$	$E_{\text{red}}^* / \text{V vs. Fc/Fc}^+$	$\Delta G^{\circ}_{\text{ET}} / \text{eV}$
III-C1	-1.00	+0.38	+0.04
IV-C2	-0.97	+0.46	-0.04
V-C1	-0.84	+0.68	-0.26
V-C2	-0.80	+0.73	-0.31

Hydrogen evolution experiments are carried out under the same conditions as described in the previous chapters with $[\text{Co}(\text{dmgH})_2(\text{H}_2\text{O})_2](\text{BF}_4)_2$, prepared *in-situ* from $[\text{Co}(\text{H}_2\text{O})_6](\text{BF}_4)_2$ (1 mM) and dmgH_2 (6 mM), and colloidal platinum, prepared *in-situ* from K_2PtCl_4 , and blue light irradiation (LED centered at 445 nm). The homoleptic complex **V-C2** is not active as PS under the investigated conditions. Using the cobalt catalyst, complex **V-C1** does lead to photocatalytic hydrogen evolution. However, the maximum TOF ($\text{TOF}_{\text{max}} = 22 \text{ mmol}_{\text{H}_2} \text{ mol}_{\text{PS}}^{-1} \text{ min}^{-1}$) is even lower than that of the

homoleptic complex **IV-C2** ($\text{TOF}_{\text{max}} = 35 \text{ mmol}_{\text{H}_2} \text{ mol}_{\text{PS}}^{-1} \text{ min}^{-1}$) (Figure V-6). Furthermore, the system with **V-C1** reaches its half-lifetime after only 2.9 h, with 5.02 h for **IV-C2**.

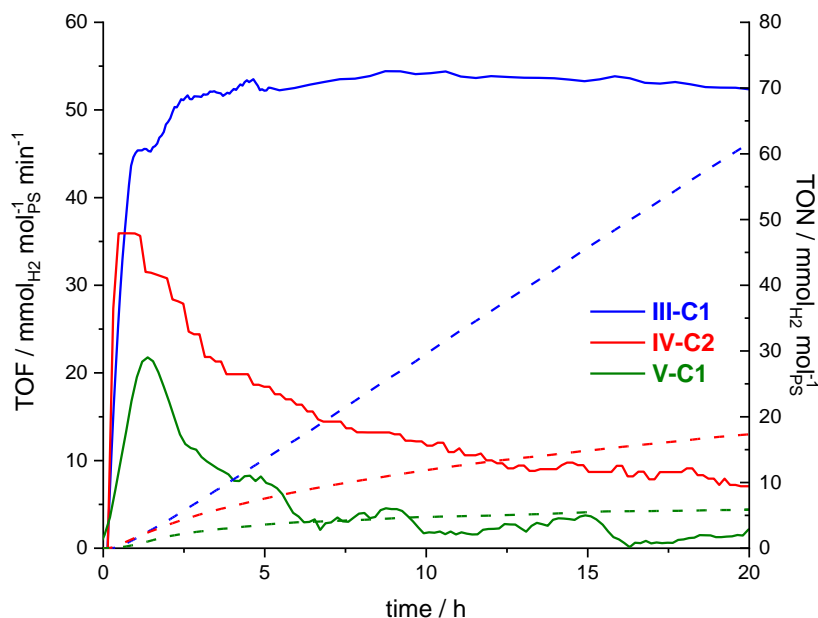


Figure V-6. Hydrogen photoproduction with complexes **III-C1**, **IV-C2** and **V-C1** as PS (0.1 mM) under blue light irradiation (LED centered at 445 nm); with $[\text{Co}(\text{H}_2\text{O})_6](\text{BF}_4)_2$ as pre-catalyst (1 mM), with dmgH_2 (6 mM), TEOA as sacrificial electron donor (1 M) and HBF_4 as proton source (0.1 M) in DMF; TOF: solid lines; TON: dashed lines; adapted from *Electrochemical and photophysical study of homoleptic and heteroleptic methylated ruthenium(II) bis-terpyridine complexes*, Mira T. Rupp, Thomas Auvray, Garry S. Hanan, Dirk G. Kurth, *European Journal of Inorganic Chemistry* **2021**, 2021 (28), 2822-2829. Reproduced with permission of Wiley-VCH.^[169]

When colloidal platinum is used as catalyst, the hydrogen evolution profile with **V-C1** looks very different (Figure V-7). Instead of reaching the peak of its hydrogen production activity shortly after the light is turned on (time = 0 h), a slow increase in activity is observed, eventually reaching a plateau TOF similar to that of **III-C1**. It should be noted however that the exact profile of the hydrogen evolution activity of **V-C1** varies between batches of freshly prepared colloidal platinum solutions.

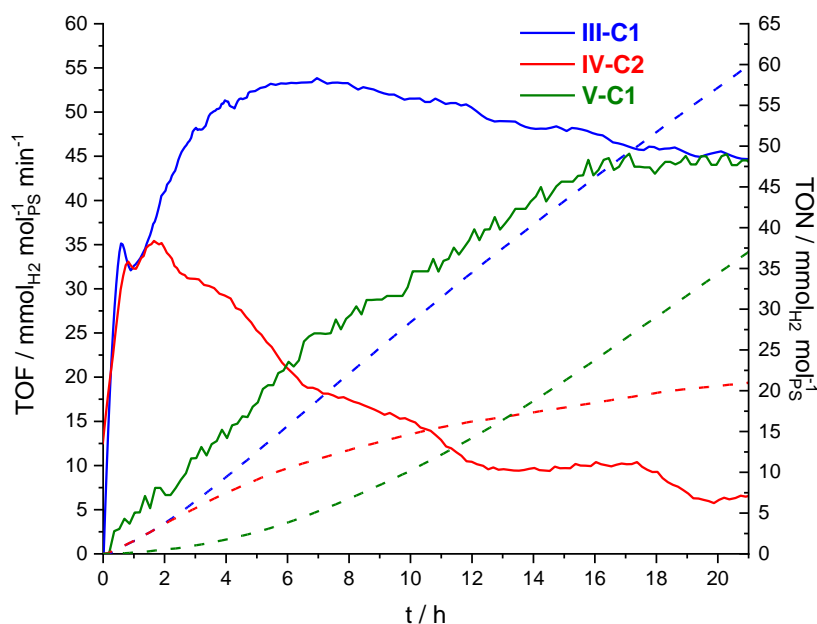


Figure V-7. Hydrogen photoproduction of complexes **III-C1**, **IV-C2** and **V-C1** (0.1 mM) under blue light irradiation (LED centered at 445 nm); using $\text{K}_2(\text{PtCl}_4)$ as pre-catalyst to form *in-situ* colloidal Pt (0.05 mM), TEOA as sacrificial electron donor (1 M) and HBF_4 as proton source (0.1 M) in DMF; TOF: solid lines; TON: dashed lines; adapted from *Electrochemical and photophysical study of homoleptic and heteroleptic methylated ruthenium(II) bis-terpyridine complexes*, Mira T. Rupp, Thomas Auvray, Garry S. Hanan, Dirk G. Kurth, *European Journal of Inorganic Chemistry* **2021**, 2021 (28), 2822-2829. Reproduced with permission of Wiley-VCH.^[169]

To gain some insights into what is happening during the hydrogen evolution experiments, UV-vis absorption spectra of the reaction mixtures with **V-C1** as PS are recorded before and after irradiation with light. The spectra are shown in Figure V-8. The absorption profile of the complex differs greatly before and after the hydrogen evolution experiment. The MLCT absorption band after light irradiation is blue-shifted and is now similar to the absorption profile of **III-C1**. While no detailed analysis of the composition of the reaction mixture after the experiment could be performed, the UV-vis spectra suggest that the PS decomposes under the catalytic conditions, presumably *via* loss of its methyl groups. This assumption would explain why the hydrogen production activity with colloidal platinum increases over time when using **V-C1** and eventually yields a similar activity to the non-methylated analogue **III-C1**. It is further assumed that the cobaloxime catalyst reacts with the free methyl groups, which deactivates it, leading to a loss of hydrogen evolution activity as seen in Figure V-6.

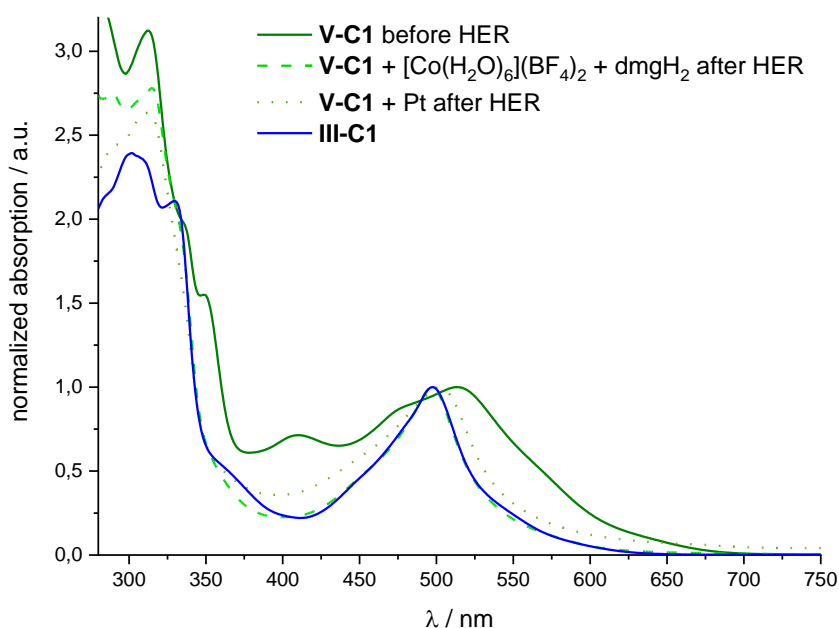


Figure V-8. UV-vis absorption spectra of DMF solutions containing **V-C1** (0.1 mM); TEOA (1 M) and HBF₄ (0.1 M) before light irradiation (green solid line) alongside reaction mixture additionally containing (a) [Co(H₂O)₆](BF₄)₂ (1 mM) and dmgH₂ (6 mM) (dashed line) or (b) K₂PtCl₄ (dotted line) after blue light irradiation (LED centered at 445 nm); the absorption spectrum of **III-C1** (blue line) is given for comparison; absorptions are normalized to the MLCT absorption peak; adapted from *Electrochemical and photophysical study of homoleptic and heteroleptic methylated ruthenium(II) bis-terpyridine complexes*, Mira T. Rupp, Thomas Auvray, Garry S. Hanan, Dirk G. Kurth, *European Journal of Inorganic Chemistry* **2021**, 2021 (28), 2822-2829. Reproduced with permission of Wiley-VCH.^[169]

UV-vis absorption experiments of the catalytic mixtures containing **V-C2** before and after light irradiation are shown in Figure V-9. Again, a change in the absorption profile can be observed. The resulting profile is similar regardless of the catalyst used but does not exactly match that of the non-methylated analogue **IV-C2**. The observed change could be a result of decomposition of the complex, e.g., *via* demethylation, or of reduction of the complex.

Overall, the anodically shifted reduction potentials of the methylated complexes does not seem to be beneficial for the activity as PS. This is presumably due to the previously mentioned fact that they are now easily reduced upon excitation but lack driving force to forward the electron to the catalyst. While the cyclic voltammograms showed reversible redox processes it is evident that under catalytic conditions, i.e., the

presence of other reagents as well as light irradiation, decomposition of the methylated complexes, e.g., *via* loss of the methyl groups, occurs.

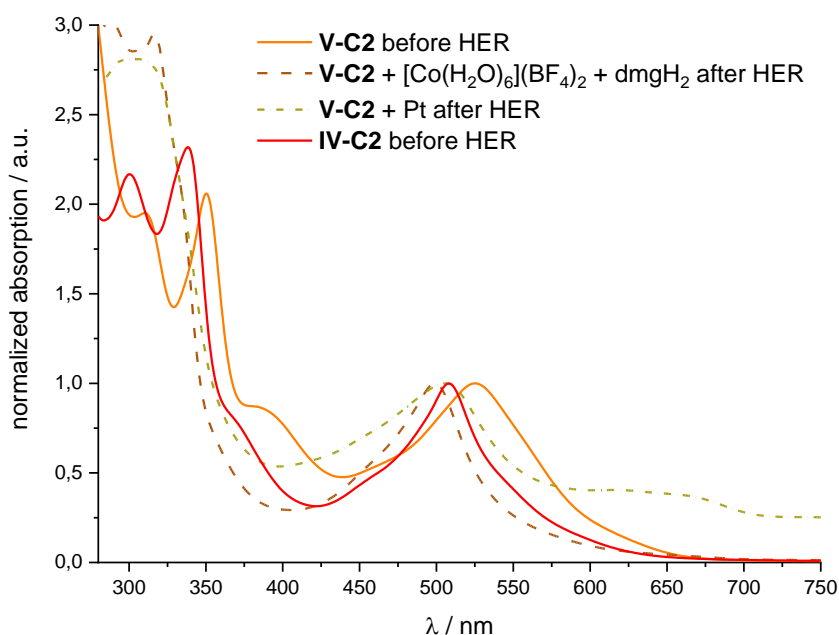


Figure V-9. UV-vis absorption spectra of DMF solutions containing **V-C2** (0.1 mM); TEOA (1 M) and HBF₄ (0.1 M) before light irradiation (orange solid line) alongside reaction mixture additionally containing (a) [Co(H₂O)₆](BF₄)₂ (1 mM) and dmgH₂ (6 mM) (dashed line) or (b) K₂PtCl₄ (dash-dotted line) after blue light irradiation (LED centered at 445 nm); the absorption spectrum of **IV-C2** (red line) is given for comparison; absorptions are normalized to the MLCT absorption peak; adapted from *Electrochemical and photophysical study of homoleptic and heteroleptic methylated ruthenium(II) bis-terpyridine complexes*, Mira T. Rupp, Thomas Auvray, Garry S. Hanan, Dirk G. Kurth, *European Journal of Inorganic Chemistry* **2021**, 2021 (28), 2822-2829. Reproduced with permission of Wiley-VCH.^[169]

However, the anodically shifted oxidation potentials of the methylated complexes could make them suitable candidates as PS in photocatalytic water oxidation experiments. As discussed in the introduction (see Figure I-7), in systems for water oxidation, the excited PS is typically oxidized by a sacrificial electron acceptor or reduced directly by the water oxidation catalyst. Studies on *N*-alkylated Ru(II) bis-terpyridine complexes by Constable and coworkers show that these complexes can indeed act as PS in photocatalytic water oxidation systems and reach oxygen evolution activities similar to that of the benchmark PS [Ru(bpy)₃]²⁺.^[86-87] Hence, complexes **V-C1** and **V-C2** could also be tested for this application.

V.3. Conclusion

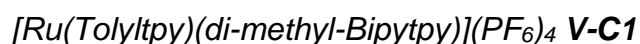
In this chapter, the homoleptic and heteroleptic pyridine-substituted complexes **IV-C2** and **III-C1** are further functionalized by *N*-methylation to form **V-C1** and **V-C2**. Photophysical and electrochemical analysis show that *N*-methylation leads to red-shifted absorption and emission wavelengths, increases the luminescence quantum yields and extends the excited-state lifetimes. Furthermore, it increases the electron-accepting character of the ligand and leads to a strong anodic shift of the reduction potential of the respective complex.

The *N*-methylated complexes both decompose under photocatalytic water reduction experiments, presumably involving demethylation. While the homoleptic complex **V-C2** shows no hydrogen evolution activity at all, **V-C1** does lead to a certain hydrogen evolution activity. UV-vis spectroscopy conducted on the reaction mixtures before and after light irradiation suggests that in the case of **V-C1** the non-methylated parent complex **III-C1** is formed and that this is actually the species acting as PS in the system. This demethylation leads to a slow increase in activity when colloidal platinum is used as catalyst with **V-C1** as PS, but only very low and short-lived activity with a cobaloxime catalyst, which might be due to the cobalt complex reacting with the decomposition products.

In summary, the lack of stability under the photocatalytic conditions as well as the lack of driving forces for the electron transfer from the reduced PS to the catalyst make the *N*-methylated complexes **V-C1** and **V-C2** unsuitable as PS in photocatalytic hydrogen evolution despite their improved photophysical properties.

V.4. Experimental

Details on instrumentation, crystal structure analysis, and DFT calculations as well as NMR spectra with peak assignments can be found in the Appendix (Chapter IX).



To a solution of $[\text{Ru}(\text{Bipytpy})(\text{TolyItpy})](\text{PF}_6)_2$ **III-C1** (65.0 mg, 27.9 μmol , 1 eq) in 10.0 mL acetonitrile, iodomethane (807 mg, 350 μl , 5.69 mmol, 110 eq) was added.

The reaction mixture was heated to 75 °C over night. The product was isolated by removal of the solvent and excess iodomethane under vacuum. To exchange the iodide counter ions, the dark red solid was dissolved in acetonitrile and water and aqueous KPF₆ solution and water were added. The precipitate was filtered off and washed with water (67 mg, 42.5 μmol, 82%).

¹H-NMR (300 MHz, CD₃CN): δ = 9.25 (s, 2H), 9.04 (m, 4H), 8.76 (d, ³J = 6.4 Hz, 4H), 8.69 (d, ³J = 8.1 Hz, 2H), 8.34 (d, ³J = 6.4 Hz, 4H), 8.23 (d, ³J = 8.4 Hz, 2H), 8.15 (d, ³J = 8.0 Hz, 2H), 7.98 (m, 4H), 7.74 (d, ³J = 5.9 Hz, 4H), 7.61 (d, ³J = 7.4 Hz, 4H), 7.44 (d, ³J = 5.1 Hz, 2H), 7.21 (m, 2H), 4.35 (s, 6H) and 2.56 ppm (s, 3H). ¹³C{¹H}-NMR (75 MHz, CD₃CN): δ = 160.4, 159.1, 156.4, 156.1, 154.4., 153.7, 152.0, 150.3, 148.2, 147.0, 143.7, 143.7, 142.2, 139.5, 136.8, 134.7, 133.8, 131.3, 130.6, 128.7, 128.5, 126.9, 126.5, 125.7, 125.6, 123.7, 123.4, 122.7, 49.2 and 21.4 ppm. ESI-MS: m/z [M]²⁺ calc. for C₅₅H₄₃BrN₈Ru: 498.09133; found: 498.0926; difference: 2.6 ppm.

[Ru(di-methyl-Bipytpy)₂](PF₆)₆ V-C2

To a solution of [Ru(Bipytpy)₂](PF₆)₂ **IV-C2** (40.0 mg, 27.1 μmol, 1 eq) in 10.0 mL acetonitrile, iodomethane (385 mg, 167 μL, 2.71 mmol, 100 eq) was added. The reaction mixture was heated to reflux for 4 hours. The product was isolated by removal of the solvent and excess iodomethane under vacuum. To exchange the iodide counter ions, the dark red solid was dissolved in acetonitrile and aqueous KPF₆ solution and water were added. The precipitate was filtered off and washed with water (41.0 mg, 19.4 μmol, 72%).

¹H-NMR (500 MHz, CD₃CN): δ = 9.29 (s, 4H), 9.06 (s, 4H), 8.76 (d, ³J = 6.8 Hz, 8H), 8.33 (d, ³J = 6.8 Hz, 8H), 8.25 (d, ³J = 8.4 Hz, 4H), 8.02 (d, ³J = 8.4 Hz, 4H), 7.74 (d, ³J = 6.0 Hz, 4H), 7.62 (dd, ³J = 6.0 Hz, ⁴J = 1.8 Hz, 4H) and 4.34 ppm (s, 12H). ¹³C{¹H}-NMR (125 MHz, CD₃CN): δ = 160.3, 156.2, 154.8., 151.9, 149.1, 147.0, 144.2, 136.7, 133.8, 130.6, 126.9, 126.6, 125.8, 123.9, 123.7 and 49.2 ppm. ESI-MS: m/z [M+3H]³⁺ calc. for C₆₆H₅₂Br₂N₁₀Ru: 415.73350; found: 415.72972; difference: 9.1 ppm.

VI. Effect of other Heterocycles in Ru(II) Complexes of Tridentate Ligands

Parts of the presented research have been previously published under the title “Substituted 2,4-Di(pyridin-2-yl)pyrimidine-Based Ruthenium Photosensitizers for Hydrogen Photoevolution under Red Light” in *Inorganic Chemistry*.

Reproduced with permission of American Chemical Society from *Inorganic Chemistry*, **2021**, 60, 292-302.

Contributions:

Mira Rupp: Project design, synthesis and characterization of ligands and complexes, collection and refinement of X-ray diffraction crystal structures, analysis of photophysical and electrochemical properties, article writing.

Thomas Auvray: Project design, DFT and TD-DFT calculations, revision of the article.

Natali Shevchenko: Synthesis of some precursors and ligands.

Lukas Swoboda: Synthesis of some ligands and complexes.

Garry S. Hanan: Supervision, revision of the article.

Dirk G. Kurth: Supervision, revision of the article.

VI.1. Introduction

The introduction of strongly electron-accepting *N*-methyl-pyridinium substituents has a big influence on the electrochemical and photophysical properties of the respective Ru(II) bis-terpyridine complexes, i.e., increasing the luminescence quantum yield and excited-state lifetime, and making the complex easier to reduce. However, the strong anodic shift of the reduction potential due to the methylation leads to a lack of driving forces for the electron transfer from the reduced PS to the catalyst as well as a lack of stability of the complexes under the catalytic conditions. Hence, a different approach to improve the photophysical properties and to adjust the electrochemical properties is necessary to increase the activity of the PS.

One possibility is the introduction of different *N*-heterocycles, e.g., pyrimidine or triazine rings. The additional nitrogen atoms present in pyrimidine or triazine rings can lead to intra-ligand hydrogen bonding, resulting in a more planar ligand structure. Fang *et al.* previously reported that Ru(II) complexes with pyrimidine-substituent terpyridine ligands exhibit improved photophysical properties due to reduced electronic coupling of the ground state and the excited state.^[223-224] The introduction of triazine rings on the other hand oftentimes leads to luminescence quenching due to the energy gap law.^[161, 167]

Based on these reports, a series of ligands, in which the central pyridine ring is exchanged for a pyrimidine ring, and their respective heteroleptic Ru(II) complexes **VI-C1** to **VI-C4** (Chart VI-1) are discussed in this chapter. The introduction of a pyrimidine ring in this position leads to a non-symmetrical design. Hence, the impact of the position of a pyridine substituent is further investigated. The possibility of intra-ligand hydrogen bonding is expected to improve the photophysical properties. Furthermore, the pyrimidine ring should make the ligand more electron-accepting, thus stabilizing the ³MLCT state and increasing the energy gap to the non-emissive ³MC state, further improving the photophysical properties and making the complex easier to reduce. The impact these changes in the structure and properties have on the performance of the complexes as PS is further investigated.

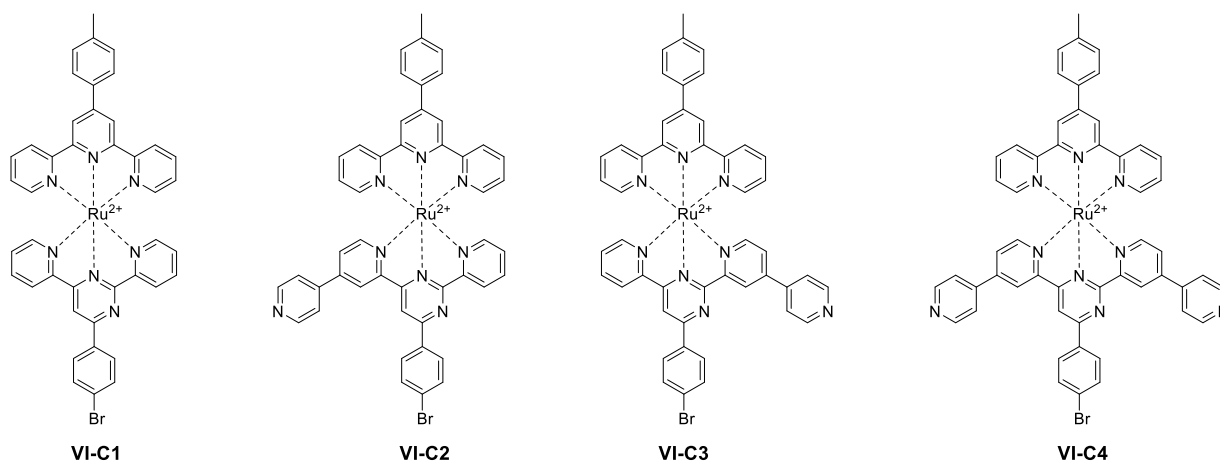
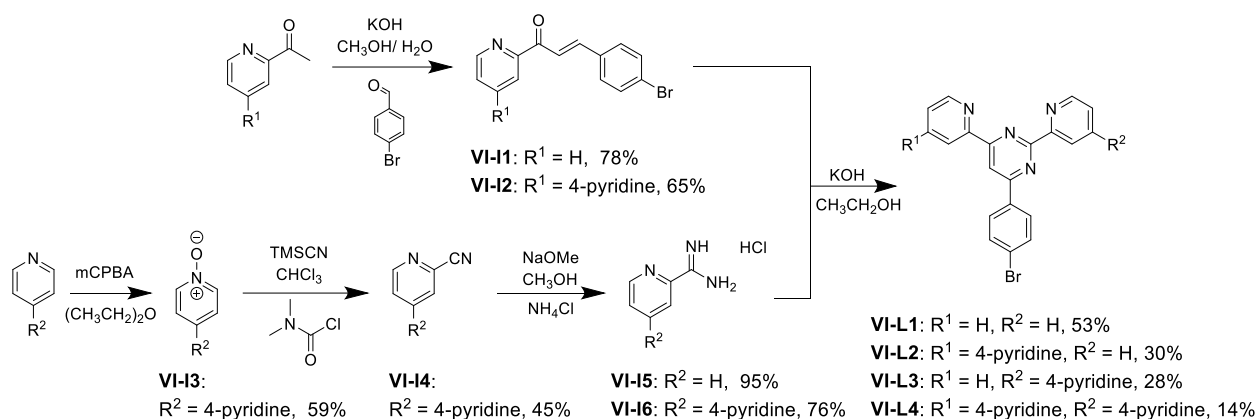


Chart VI-1. Structures of the pyrimidine containing complexes **VI-C1** to **VI-C4**; the PF_6^- counterions are omitted for clarity.

VI.2. Results and Discussion

VI.2.1. Synthesis and Structural Analysis

The synthesis of the complexes follows a multistep procedure (Scheme VI-1), analogous to a procedure described by Pai *et al.*^[225] Starting with 2-acetylpyridine derivatives, which are reacted with 4-bromobenzaldehyde in the presence of potassium hydroxide to form the enones **VI-I1** and **VI-I2**. These enones are then used to form the pyrimidine containing ligands **VI-L1** to **VI-L4** by reacting with a 2-pyridinecarboxamide derivative. The synthesis of 2-pyridinecarboxamide **VI-I5** starts from pyridine-2-carbonitrile. As 4,4'-bipyridine-2-carbonitrile **VI-I4** is not commercially available, it is synthesized from 4,4'-bipyridine. First, 4,4'-bipyridine-*N*-oxide **VI-I3** is formed using *meta*-chloroperoxybenzoic acid (mCPBA). Second, the *N*-oxide is reacted with trimethylsilyl cyanide (TMSCN) and *N,N*-dimethyl carbamoyl chloride, following a procedure by Brunner *et al.*,^[226] resulting in the formation of 4,4'-bipyridine-2-carbonitrile **VI-I4**. The carboxamides **VI-I5** and **VI-I6** are subsequently formed as hydrochlorid acid adducts analogous to a synthesis described by Sun *et al.*^[227]



Scheme VI-1. Synthesis of the precursors **VI-I1** to **VI-I6** as well as the ligands **VI-L1** to **VI-L4**; adapted from *Inorganic Chemistry*, **2021**, *60*, 292-302. Reproduced with permission of American Chemical Society.^[168]

The synthesized ligands **VI-L1** to **VI-L4** are used to form the heteroleptic complexes **VI-C1** to **VI-C4** (Chart VI-1) analogous to the procedure described in Chapter III. The complexes are isolated as hexafluorophosphate salts and are analyzed using NMR spectroscopy, high-resolution mass-spectrometry, and elemental analysis.

Furthermore, single crystals of complexes **VI-C1** and **VI-C4** are obtained by slow evaporation of an acetonitrile/water mixture for **VI-C1** or by slow diffusion of diethyl ether into a concentrated acetonitrile solution of **VI-C4**, respectively. The single crystals are analyzed using X-ray diffraction and the received structures are shown in Figure VI-1 with refinement parameters described in the Appendix (Chapter IX.4). As in the bis-terpyridine complexes, which are discussed in the previous chapters, the Ru(II) ion has a distorted octahedral coordination sphere with N-Ru-N *trans* angles around 157° in both complexes **VI-C1** and **VI-C4**. As mentioned above, one of the reasons to introduce a pyrimidine ring instead of a pyridine ring to the tridentate metal ion receptor is the possibility of intra-ligand hydrogen bonding between the nitrogen atom of the pyrimidine ring and the C-H group of the bromophenyl ring, which could lead to a more planarized structure. Hence, the torsion angle between the pyrimidine and the bromophenyl ring indicates the presence of hydrogen bonding within the crystal structure, i.e., it is assumed that a smaller torsion angle relates to a higher degree of hydrogen bonding in the structure. In complex **VI-C1**, the torsion angle between the

pyrimidine and the bromophenyl ring is 13° while the torsion angle of the tolyl ring on the terpyridine ligand is 36° . The decreased torsion angle on the pyrimidine-containing ligand confirms the presence of hydrogen bonding. In complex **VI-C4** on the other hand, torsion angles of 22° and 29° for the bromophenyl and the tolyl ring are observed, respectively. The smaller difference indicates that in the case of **VI-C4** the intra-ligand hydrogen bonding is less pronounced. It should be noted that disorder has to be taken into account when modelling the crystal structures of both **VI-C1** and **VI-C4** and thus the actual torsion angles might indeed differ from the ones observed.

Similar to the bis-terpyridine complex **III-C1**, the peripheral pyridine-substituents in complex **VI-C4** are distorted with torsion angles of 32° and 28° . Furthermore, the tolyl-substituted terpyridine ligand is bent due to interactions in the crystal packing with neighboring complex molecules but also co-crystallized solvent molecules.

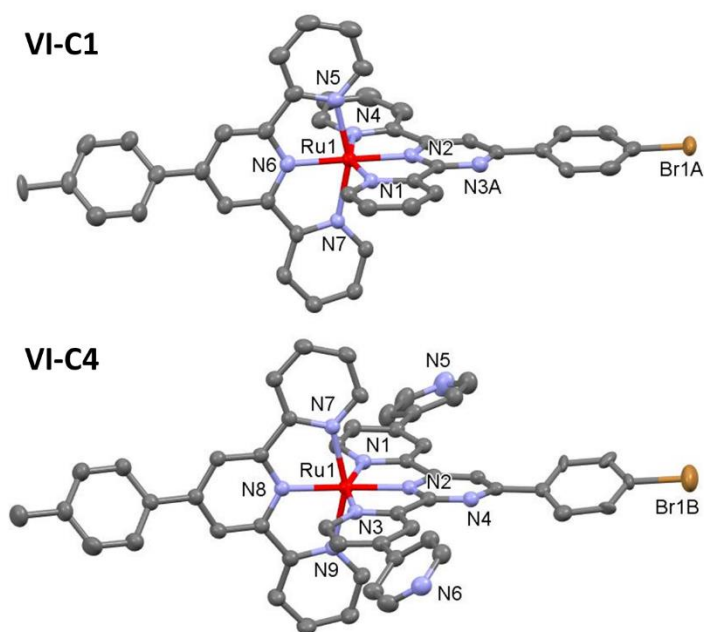


Figure VI-1. Ellipsoid representation of complexes **VI-C1** (top) and **VI-C4** (bottom) at 50% probability. Hydrogen atoms, PF_6^- counter ions and co-crystallized solvent molecules are omitted for clarity; adapted from *Inorganic Chemistry*, **2021**, *60*, 292-302. Reproduced with permission of American Chemical Society.^[168]

VI.2.2. Photophysical Properties

The photophysical properties of complexes **VI-C1** to **VI-C4** in acetonitrile solution are analyzed and the results are shown in Figure VI-2 and Table VI-1. All

complexes exhibit a MLCT absorption band in the visible region and several LC absorption bands in the UV region. The complexes bearing one or two pyridine substituents, i.e., all complexes except **VI-C1**, have an additional LC absorption band around 230–240 nm. The MLCT absorption band of the pyrimidine-containing complexes **VI-C1** to **VI-C4** is slightly blue-shifted to 485–490 nm compared to that of the bis-terpyridine complex **III-C1** (498 nm). The MLCT absorption of the homoleptic tolyl-substituted complex **IV-C1** (491 nm) matches that of the pyrimidine-containing complexes relatively well, leading to the conclusion that the maximum MLCT absorption has strong contributions from an excitation involving the tolyl-substituted ligand **III-L3**. The complexes bearing a pyridine-substituent in the 4-pyrimidine position, i.e., **VI-C2** and **VI-C4**, exhibit a shoulder around 530 nm, which is assumed to correspond to a MLCT towards the pyrimidine-containing ligand.

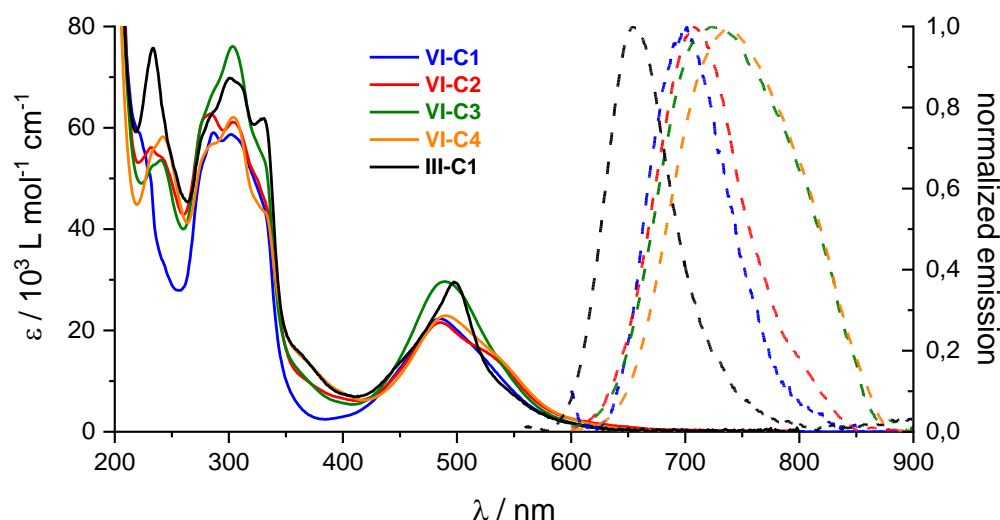


Figure VI-2. UV-vis absorption (solid lines) and emission spectra (dashed lines) of complexes **VI-C1** to **VI-C4** alongside complex **III-C1**; spectra measured in acetonitrile; emission experiments are conducted under inert gas atmosphere at 20 °C and emission spectra are rescaled so that the intensity at $\lambda_{\text{max em}}$ is 1.

Emission spectra are recorded in acetonitrile under inert gas atmosphere. The maximum emission wavelengths of the pyrimidine-containing complexes are strongly red-shifted compared to the bis-terpyridine complex **III-C1**, with the complexes bearing a pyridine substituent in the 2-pyrimidine position (**VI-C3** and **VI-C4**) exhibiting a stronger red shift than those without a substituent in this position. However, the excited-

state lifetime and luminescence quantum yield appears to depend on the substituent in the 4-pyrimidine position. While **VI-C1** and **VI-C3** exhibit very similar lifetimes and quantum yields, comparable to bis-terpyridine complex **III-C1**, complexes **VI-C2** and **VI-C4** show a three-fold increase of both parameters. This increase in excited-state lifetimes and luminescence quantum yield is further reflected in lower non-radiative decay rates k_{nr} .

As described in the Chapter I.4 (Equation I-2), the non-radiative decay rate has two main contributions: k_{nr}^0 describes the decay from the excited MLCT state directly to the ground state; k'_{nr} on the other hand describes the non-radiative decay *via* the 3MC state. In Ru(II) bis-terpyridine complexes, the second term k'_{nr} is usually assumed to be the main contributor to the luminescence quenching due to the small 3MLCT to 3MC energy gap, which results in fast internal conversion at room temperature.^[224, 228] The rate constant k_{nr}^0 depends on the electronic coupling of the excited and the ground state. As mentioned above, Fang *et al.* reported that planarization of the ligands leads to a better delocalization of the ligand acceptor orbital, which in return results in smaller Frack-Condon factors for the non-radiative decay described by k_{nr}^0 .^[224] As the pyrimidine rings in the herein presented complexes offer the possibility of intra-ligand hydrogen bonding, whose presence to a certain degree is also confirmed by crystal structure analysis, it is assumed, that the photophysical properties of complexes **VI-C1** to **VI-C4** are not solely improved due to the more electron-accepting character but also the structure of the ligands and the impact this has on the electronic coupling of the ground state and the excited state.

Table VI-1. UV-vis absorption and emission data of complexes **VI-C1** to **VI-C4** alongside complex **III-C1** (spectra are measured in acetonitrile at 20 °C).^a

	$\lambda_{\max \text{ abs}} / \text{nm} (\epsilon / 10^3 \text{ L mol}^{-1} \text{ cm}^{-1})$		$\lambda_{\max \text{ em}} / \text{nm}$	$\Phi / 10^{-5}$	τ_c / ns	$k_r / 10^4 \text{ s}^{-1}$	$k_{nr} / 10^8 \text{ s}^{-1}$
	LC	MLCT					
VI-C1	287 (59), 302 (59)	485 (22)	703	42 ± 17	8.8 ± 1	4.77	1.14
VI-C2	232 (56), 284 (63), 303 (61)	485 (22)	709	169 ± 63	34 ± 5	4.97	0.29
VI-C3	240 (54), 303 (76)	490 (30)	723	49 ± 20	11 ± 0.5	4.45	0.91
VI-C4	242 (58), 304 (62)	490 (23)	738	175 ± 67	30 ± 1	5.83	0.33
III-C1	233 (76), 301 (70), 330 (62)	498 (29)	656	74±33	3.8±0.1	19.5	2.63

^amaximum absorption wavelength $\lambda_{\max \text{ abs}}$, extinction coefficient ϵ , maximum emission wavelength $\lambda_{\max \text{ em}}$, luminescence quantum yield Φ , excited-state lifetime τ ; radiative decay rate $k_r = \Phi/\tau$, non-radiative decay rate $k_{nr} = (1-\Phi)/\tau$; emission data is collected in inert gas-purged solutions.

VI.2.3. Electrochemical Properties

The redox behavior of complexes **VI-C1** to **VI-C4** is investigated using cyclic voltammetry. The results are shown in Figure VI-3 and Table VI-2. The lower current flow of complexes **VI-C3** and **VI-C4** is due to a lower concentration of the complex in the electrolyte, which is chosen due to the limited solubility of these complexes in the electrolyte. Analogous to the previously discussed bis-terpyridine complexes, the pyrimidine-containing complexes exhibit a reversible, metal-centered oxidation process. The half-wave potential of this process is anodically shifted compared to bis-terpyridine analogues, presumably due to a HOMO-stabilizing effect of the more electron-accepting pyrimidine-containing ligands.

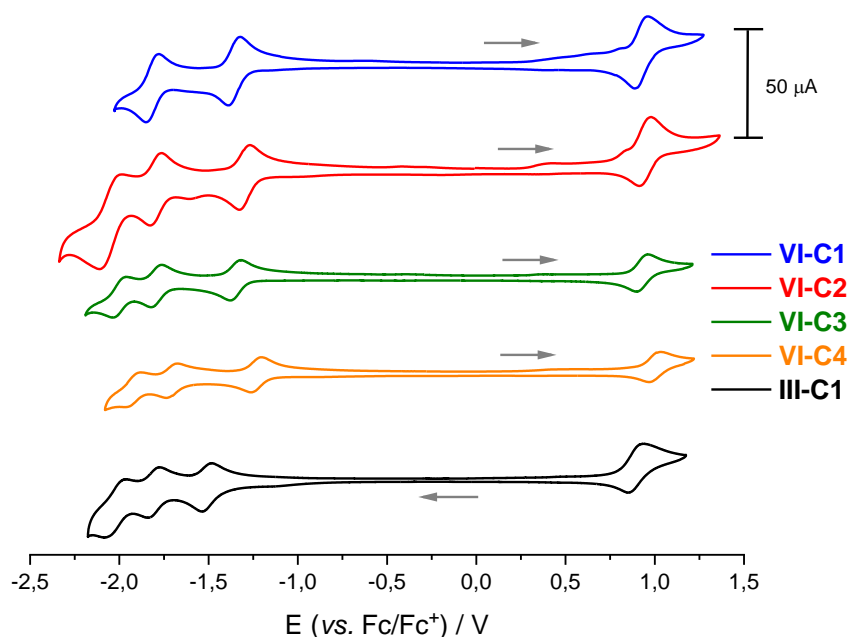


Figure VI-3. Cyclic voltammograms of complexes **VI-C1** (1 mM, blue), **VI-C2** (1 mM, red), **VI-C3** (0.5 mM, green) and **VI-C4** (0.5 mM, orange) alongside complex **III-C1** (0.5 mM, black) in dry acetonitrile under inert gas atmosphere, with 0.1 M TBAPF₆; scan rate 100 mV/s; scans start at 0 V vs. reference in anodic or cathodic direction as indicated by arrows.

Furthermore, all complexes exhibit several reversible ligand-centered reduction processes. The first reduction potential of complexes **VI-C1** to **VI-C4** is anodically shifted by 150–230 mV compared to the reference bis-terpyridine complex **III-C1**. Based on assignments of the reduction processes in the previous chapters, the reductions occurring around -1.80 V vs. Fc/Fc^+ are assigned to the tolyl-substituted ligand. The less negative reduction processes around -1.40 V are assumed to involve the pyrimidine-containing ligands as their more electron-accepting character makes them easier to reduce. The complexes bearing a pyridine-substituent exhibit a third reduction process in the investigated potential window, which is presumably involving the pyridine substituent as the potential for this reduction process is very similar for both pyrimidine-containing and bis-terpyridine complexes. The complexes bearing a pyridine substituent in the 4-pyrimidine position, i.e., **VI-C2** and **VI-C4**, are both slightly easier to reduce than those with no substituent in this position.

The potential difference between the oxidation potential and the first reduction potential can give an indication about the HOMO-LUMO energy gap. This potential

difference is identical for complexes **VI-C1** and **VI-C3** (2.28 V) and slightly larger than that of **VI-C2** (2.26 V) and **VI-C4** (2.24 V), showing again the impact of the substituent position in these complexes. The potential difference for all pyrimidine containing complexes is smaller compared to that of the bis-terpyridine complex **III-C1** (2.40 V).

Table VI-2. Electrochemical half-wave redox potentials $E_{1/2}$ in V vs. Fc/Fc⁺ (ΔE_p / mV) for complexes **VI-C1** to **VI-C4** alongside complex **III-C1** in nitrogen-purged acetonitrile.^a

	Oxidation		Reduction	
VI-C1	+0.92 (69)	-1.36 (67)	-1.81 (71)	
VI-C2	+0.96 (60)	-1.30 (58)	-1.80 (64)	-2.04 (123)
VI-C3	+0.94 (61)	-1.34 (54)	-1.78 (58)	-1.99 (77)
VI-C4	+0.96 (69)	-1.28 (62)	-1.75 (59)	-1.97 (99)
III-C1	+0.89 (69)	-1.51 (62)	-1.81 (75)	-2.02 (104)

^aRedox potentials are reported vs. ferrocene (Fc/Fc⁺); the differences between the anodic and cathodic peak potentials ΔE_p are given in parentheses in millivolts; measurements in inert gas-purged acetonitrile solutions containing 0.1 M tetrabutylammonium hexafluorophosphate at a sweep rate of 100 mV/s.

VI.2.4.DFT Calculations

To understand the observed photophysical and electrochemical properties better DFT and TD-DFT calculations are conducted. Figure VI-4 shows the calculated frontier orbitals of complexes **VI-C1** to **VI-C4**. The introduction of a pyridine-substituent in the 4-pyrimidine position appears to have a stronger impact on the energy of the calculated HOMOs and LUMOs than that of a pyridine-substituent in the 2-pyrimidine position. The calculated HOMO-LUMO energy gap of complex **VI-C1** is identical to that of **VI-C3** (3.46 eV), while that of complexes **VI-C2** and **VI-C4** is slightly smaller (3.40 eV) and that of the bis-terpyridine complex **III-C1** is even larger (3.53 eV). These differences match very well with the oxidation to reduction potential differences in the CV experiments. The reduced HOMO-LUMO energy gap for complexes **VI-C2** and **VI-C4** is due to a stronger stabilization of the LUMOs compared to the HOMOs in these complexes and can be related to the red-shifted shoulder on the MLCT absorption band. The stabilization of the LUMOs is expected to also result in a stabilized ³MLCT state and hence an increased energy gap to the non-emissive ³MC state, potentially

explaining the longer excited-state lifetimes and higher quantum yields of **VI-C2** and **VI-C4**.

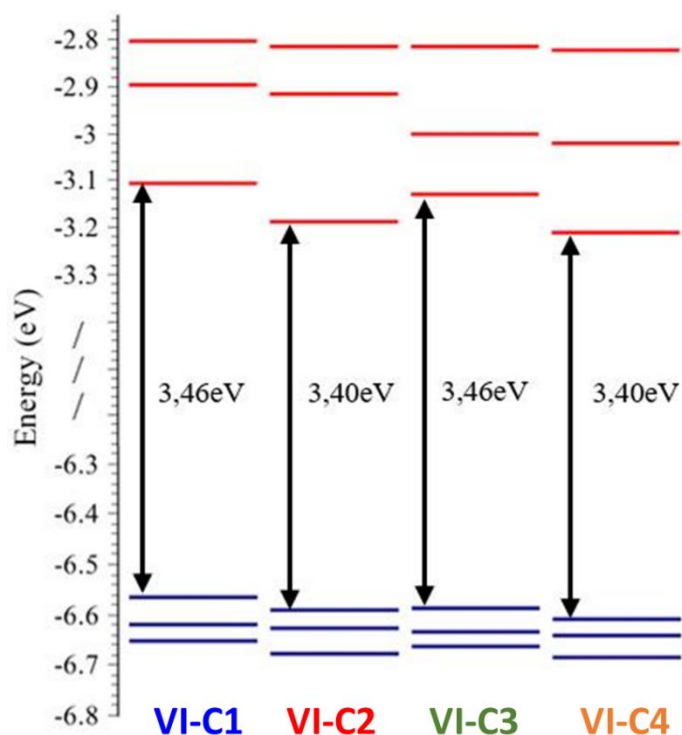
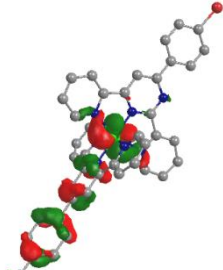
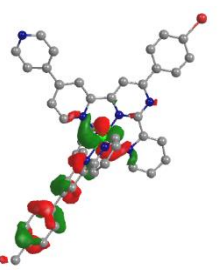
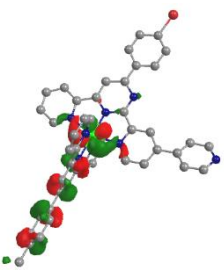
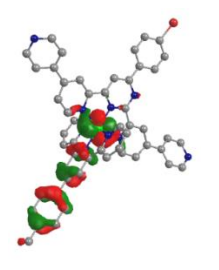
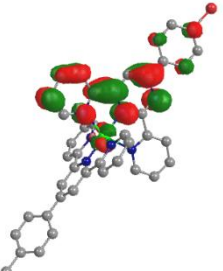
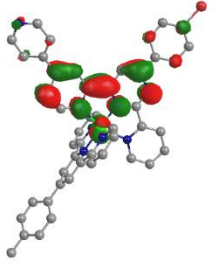
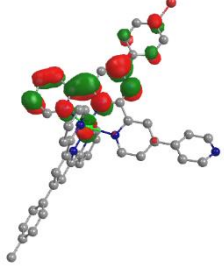
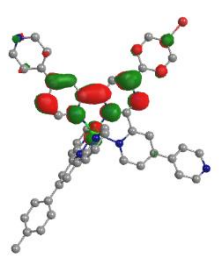
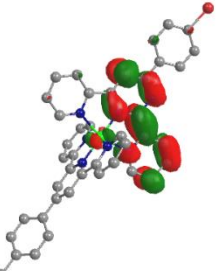
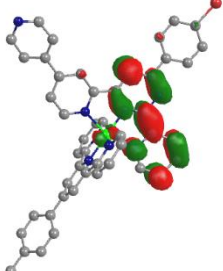
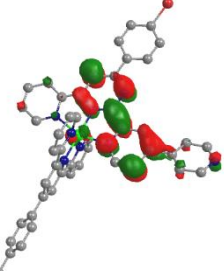
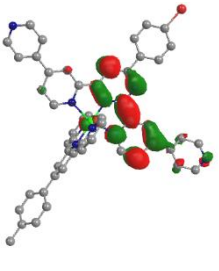


Figure VI-4. Energy diagram of the calculated frontier orbitals of complexes **VI-C1** to **VI-C4** with energy gaps highlighted (degeneracy threshold of 15 meV); adapted from *Inorganic Chemistry*, 2021, 60, 292-302. Reproduced with permission of American Chemical Society.^[168]

The impact of the substituent position can be further understood when looking at the contributions to the molecular orbitals presented in Table VI-3. As discussed in previous chapters, in the HOMO most of the electron density in the heteroleptic complexes is localized on the metal center. While for bis-terpyridine complexes relatively equal contributions from both ligands, almost regardless of their substituents, is observed, here, the terpyridine ligand **III-L3** contributes to the HOMOs much stronger (36%) than the pyrimidine containing ligands (8%). In the LUMO, the electron density shifts towards the more electron-accepting ligands **VI-L1** to **VI-L4**. As the ligand is itself not symmetrical, the electron density is localized on the side of the ligand pointing away from the additional nitrogen atom. This unequal distribution could explain why the pyridine substituents in 2-pyrimidine position less affect the energy and photophysical properties of the complexes.

Table VI-3. Contributions to molecular orbitals for complexes **VI-C1** to **VI-C4**; adapted from *Inorganic Chemistry*, **2021**, *60*, 292-302. Reproduced with permission of American Chemical Society.^[168]

	VI-C1	VI-C2	VI-C3	VI-C4
HOMO	 -6.57 eV Ru: 56% III-L3: 36% VI-L1: 8%	 -6.59 eV Ru: 56% III-L3: 36% VI-L2: 8%	 -6.59 eV Ru: 56% III-L3: 36% VI-L3: 8%	 -6.61 eV Ru: 55% III-L3: 37% VI-L4: 8%
LUMO	 -3.11 eV Ru: 6% III-L3: 1% VI-L1: 93%	 -3.19 eV Ru: 7% III-L3: 1% VI-L2: 92%	 -3.13 eV Ru: 7% III-L3: 1% VI-L3: 92%	 -3.21 eV Ru: 7% III-L3: 1% VI-L4: 92%
LUMO+1	 -2.90 eV Ru: 4% III-L3: 2% VI-L1: 94%	 -2.92 eV Ru: 4% III-L3: 2% VI-L2: 94%	 -3.00 eV Ru: 3% III-L3: 2% VI-L3: 95%	 -3.02 eV Ru: 4% III-L3: 1% VI-L4: 95%

In the emission experiments, a relatively strong red shift of the emission wavelength can be observed for complexes **VI-C3** and **VI-C4**, which is not reflected in

the HOMO-LUMO energy gap calculations as the involved orbitals do not directly correspond to the ground and excited states. Theoretical investigations of spin-forbidden singlet-triplet transitions are conducted to give a better understanding of the emissive state in the complexes. Figure VI-5 shows the natural transition orbitals analysis for the lowest singlet-triplet transition in **VI-C1**, which inverted corresponds to the emissive state according to Kasha's rule.^[211] Natural transition orbitals analysis of complexes **VI-C2** to **VI-C4** can be found in the Appendix (Chapter IX.5.1). The transition shown in Figure VI-5 has both MLCT and intra-ligand character, both involving the pyrimidine-containing ligand. When the electron density contributions to the singlet state (left), which corresponds to the singlet ground state, are compared to the electron density contributions to the HOMO for **VI-C1** (Table VI-3), it can be seen that they are not identical. While the HOMO mainly has contributions from the metal and the tolyl-substituted ligand, the singlet state features contributions mainly from the metal and the pyrimidine-containing ligand. This observation highlights the difference between the electronic states involved in photophysical transitions and the HOMOs and LUMOs. It should be noted that while for some compounds the same trend can be observed in the emission properties and the HOMO-LUMO energy gaps, the two experiments do not involve the same states, and hence differences in the observed trends can differ between photophysical and electrochemical properties.

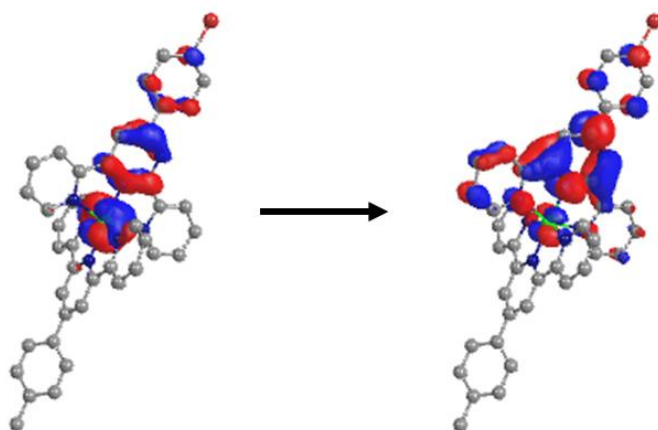


Figure VI-5. Natural transition analysis of the lowest singlet (left) to triplet (right) transition for complex **VI-C1**; adapted from *Inorganic Chemistry*, **2021**, *60*, 292-302. Reproduced with permission of American Chemical Society.^[168]

VI.2.5. Hydrogen Evolution Experiments

The results from the photophysical and electrochemical experiments are used to estimate the redox potentials in the excited state and the driving force for the photoinduced electron transfer from the SED to the excited PS. The results are summarized in Table VI-4. Interestingly, despite the more electron-accepting character of the pyrimidine-containing ligands and the resulting less negative reduction potentials, the reduction potentials in the excited state are very similar to that of **III-C1**, resulting in comparable driving forces. Furthermore, no relation between the position of the pyridine-substituent and the driving force can be observed. Based on these estimations, the electron transfer step from the SED to the PS is expected to be most exergonic for complex **VI-C2** ($\Delta G_{ET}^0 = -0.03$ eV), while it is the least unfavorable for **VI-C3** and the bis-terpyridine complex **III-C1** ($\Delta G_{ET}^0 = +0.04$ eV).

The electron transfer step from the reduced PS to the catalyst depends on the reduction potential of the PS in the ground state. Hence, this process is expected to be least favorable for complexes **VI-C2** and **VI-C4**. Overall, there is no clear trend regarding the thermodynamical considerations of all electron transfer steps involving the PS as to which complex will perform best under photocatalytic conditions.

Table VI-4. Excited-state redox potentials and estimated free Gibbs energy ΔG_{ET}^0 for photoinduced electron transfer from TEOA to the complexes **VI-C1** to **VI-C4** and **III-C1**.

	E_{ox}^* / V vs. Fc/Fc ⁺	E_{red}^* / V vs. Fc/Fc ⁺	$\Delta G_{ET}^0 / eV$
VI-C1	-0.84	+0.40	+0.02
VI-C2	-0.79	+0.45	-0.03
VI-C3	-0.78	+0.38	+0.04
VI-C4	-0.72	+0.40	+0.02
III-C1	-1.00	+0.38	+0.04

Photocatalytic hydrogen evolution experiments are carried out analogous to the previous chapters with TEOA (1 M) as SED, HBF₄ (0.1 M) as proton source, [Co(dmgh)₂(H₂O)₂](BF₄)₂ as catalyst prepared *in-situ* from [Co(H₂O)₆](BF₄)₂ (1 mM) and dmgh₂ (6 mM) in DMF solution, containing 0.1 mM of the respective complex as PS and being irradiated with blue light at 445 nm. The results of these experiments

with complexes **VI-C1** to **VI-C4** are shown in Figure VI-6 and a summary can be found in Table VI-5.

All pyrimidine-containing complexes are active as PSs, leading to maximum TOFs, which are increased by an order of magnitude ($\text{TOF}_{\text{max}} = 300\text{--}700 \text{ mmol}_{\text{H}_2} \text{ mol}^{-1}_{\text{PS}} \text{ min}^{-1}$) compared to the bis-terpyridine complex **III-C1** ($\text{TOF}_{\text{max}} = 50 \text{ mmol}_{\text{H}_2} \text{ mol}^{-1}_{\text{PS}} \text{ min}^{-1}$). However, the hydrogen evolution activity of the catalytic systems using **VI-C1** to **VI-C4** as PS is less long-lived and decreases rapidly within a few hours. Interestingly, both complexes bearing a pyridine-substituent in 4-pyrimidine position, i.e., **VI-C2** and **VI-C4**, exhibit even shorter half-life times (2.1 h and 2.4 h, respectively) than complexes **VI-C1** and **VI-C3** (half-life times 4.5 h and 5.6 h, respectively). The decreased longevity of the catalytic systems using **VI-C2** and **VI-C4** as PS leads to lower overall amounts of hydrogen produced after 24 h of these systems compared to those with **VI-C1** and **VI-C3** despite their initially slightly higher activity.

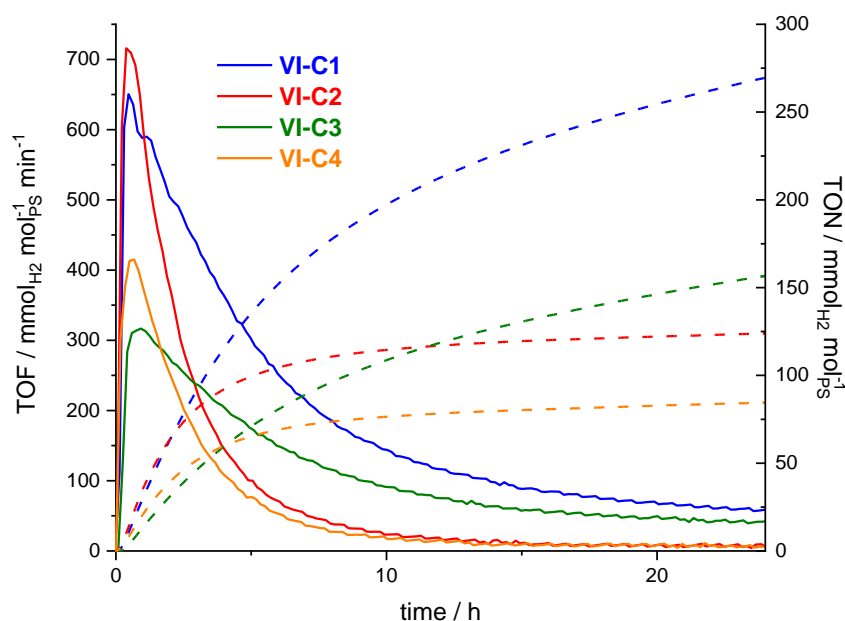


Figure VI-6. Hydrogen photoproduction with complexes **IV-C1** to **IV-C4** as PS (0.1 mM) under blue light irradiation (LED centered at 445 nm); with $[\text{Co}(\text{H}_2\text{O})_6](\text{BF}_4)_2$ as pre-catalyst (1 mM), with dmgH_2 (6 mM), TEOA as sacrificial electron donor (1 M) and HBF_4 as proton source (0.1 M) in DMF; TOF: solid lines; TON: dashed lines; adapted from *Inorganic Chemistry*, **2021**, *60*, 292-302. Reproduced with permission of American Chemical Society.^[168]

One of the drawbacks of the benchmark PS $[\text{Ru}(\text{bpy})_3]^{2+}$ is the lack of absorptivity in the red despite more than half of the solar energy being carried in the

red and infra-red part of the solar spectrum.^[229] This lack of absorptivity results in $[\text{Ru}(\text{bpy})_3]^{2+}$ being almost completely inactive as PS under red light irradiation at 630 nm ($\text{TOF}_{\text{max}} = 30 \text{ mmol}_{\text{H}_2} \text{ mol}^{-1}_{\text{PS}} \text{ min}^{-1}$).^[76] The pyrimidine containing complexes **VI-C1** to **VI-C4** on the other hand exhibit a red-shifted absorption with stronger absorptivity at 630 nm and hence promise to be more active under these catalytic conditions.

Figure VI-7 shows the results of hydrogen evolution experiments under red light (LED centered at 630 nm) using complexes **VI-C1** to **VI-C4** as PSs. All complexes are active as PS under these catalytic conditions. While the activity is reduced compared to experiments carried out under blue light irradiation, the longevity of the hydrogen evolution is increased with half-life times of up to 31 h for **VI-C3**. The decreased activity under red light irradiation roughly corresponds to the decreased light harvesting efficiency (LHE) at 630 nm (LHE = 11–28%) compared to 445 nm (LHE = 89–94%), which is calculated using the following equation, with transmission T_λ and absorption A .

$$\text{LHE} = 1 - T_\lambda = 1 - 10^{-A}$$

Equation VI-1

The fact that the TOF_{max} decreases by approximately the same degree as the LHE when switching from blue to red light irradiation, indicates that the excited PS is involved in a critical step of the catalytic cycle.

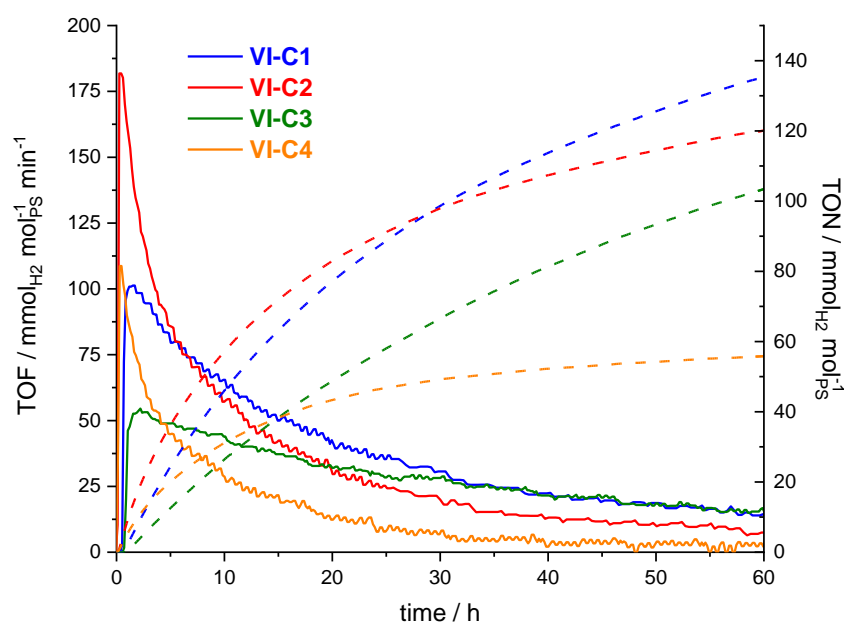


Figure VI-7. Hydrogen photoproduction with complexes **IV-C1** to **IV-C4** as PS (0.1 mM) under red light irradiation (LED centered at 630 nm); with $[\text{Co}(\text{H}_2\text{O})_6](\text{BF}_4)_2$ as pre-catalyst (1 mM), with dmgH_2 (6 mM), TEOA as sacrificial electron donor (1 M) and HBF_4 as proton source (0.1 M) in DMF; TOF: solid lines; TON: dashed lines; adapted from *Inorganic Chemistry*, **2021**, *60*, 292-302. Reproduced with permission of American Chemical Society.^[168]

The complexes **VI-2** and **VI-4**, both bearing a pyridine-substituent in the 4-pyrimidine position, exhibit a higher luminescence quantum yield and an extended excited-state lifetime. These improvements do not seem to affect directly the performance as PS, i.e., stronger luminescence and longer excited-state lifetimes are not reflected in a higher hydrogen evolution activity. However, a similar grouping with regard to the substituent in 4-pyrimidine position can be observed regarding the longevity of the hydrogen evolution activity, both under blue and red light irradiation, i.e., systems using complexes with a pyridine-substituent in the 4-pyrimidine position as PS lose their hydrogen production activity more quickly.

Taking the estimated driving forces from Table VI-4 back into consideration, complexes **VI-C1** and **VI-C2** are expected to perform better than **VI-C3** and **VI-C4**, respectively, due to both electron transfer steps to and from the PS being thermodynamically more favorable. This estimation is indeed reflected in the experiments under blue light irradiation. The faster decrease of the activity of the catalytic systems using **VI-C2** and **VI-C4** as PS on the other hand could be related to

the electron transfer from the reduced PS to the catalyst being thermodynamically more hindered than for complexes **VI-C1** and **VI-C3**. A possible explanation for the observed behavior is that the rate-limiting step in the systems using pyrimidine-containing PSs is the electron transfer from the reduced PS to the catalyst rather than the reductive quenching from the SED. Hence, if the electron transfer step from the SED to the excited PS is faster than the electron transfer from the reduced PS to the catalyst, an accumulation of reduced PS can occur. Such an accumulation of reduced complexes could lead to a decomposition or loss of activity as PS over time.

To verify that it is indeed the PS that causes the loss of hydrogen evolution activity, either PS or catalyst are added to the reaction mixture after the hydrogen evolution activity has ceased. Figure VI-8 shows that addition of PS results in a partly restoration of the hydrogen evolution activity, meaning that there is still active catalyst in the system while the PS has become inactive. Addition of catalyst does not result in increased hydrogen evolution. These experiments confirm that deactivation of the PS is the result for the decreased longevity of the hydrogen evolution.

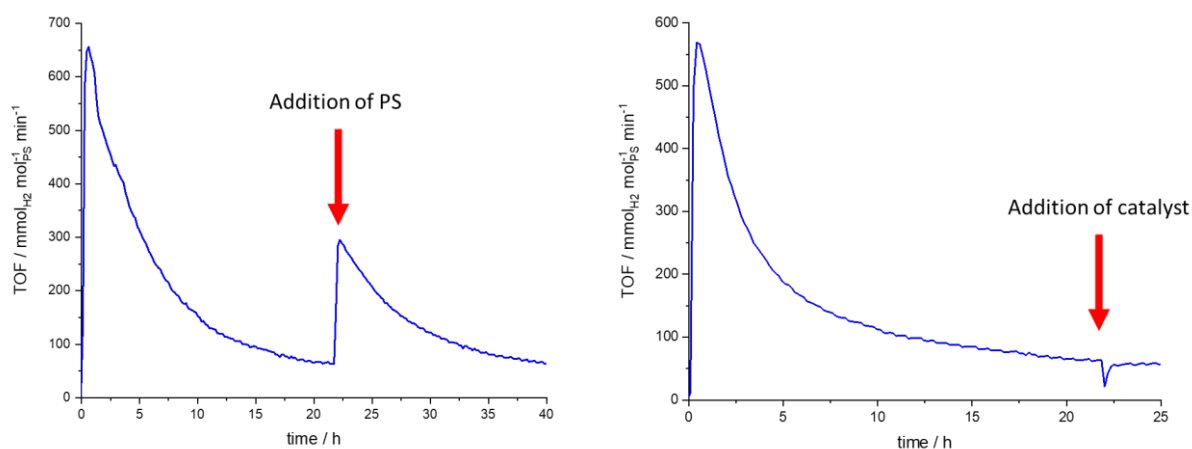


Figure VI-8. Hydrogen photoproduction with complex **VI-C1** as PS (0.1 mM) under blue light irradiation (LED centered at 445 nm); with TEOA as sacrificial electron donor (1 M) and HBF_4 as proton source (0.1 M), $\text{Co}(\text{H}_2\text{O})_6(\text{BF}_4)_2$ (1 mM), with dmgH_2 (6 mM) in DMF; left: addition of same amount of **VI-C1** in 0.25 mL DMF after 22 hours (highlighted by red arrow); right: addition of same amount of $[\text{Co}(\text{H}_2\text{O})_6](\text{BF}_4)_2$ and dmgH_2 in 0.25 mL DMF after 22 hours (highlighted by red arrow); adapted from *Inorganic Chemistry*, **2021**, *60*, 292-302. Reproduced with permission of American Chemical Society.^[168]

To test the hypothesis that the rate-limiting step involves the catalyst, complex **VI-C1** is tested with different catalytic species (Figure VI-9). The cobaloxime catalyst

[Co(dmgBF₂)L₂] (L = solvent molecule) is reported to have a less negative reduction potential for the Co(II) to Co(I) reduction at -0.95 V vs. Fc/Fc⁺[133] than [Co(dmgH)₂(H₂O)₂](BF₄)₂ (-1.43 V vs. Fc/Fc⁺).^[129] Therefore, the electron transfer step from the reduced PS to the catalyst should be more exergonic for [Co(dmgBF₂)L₂]. Yet, the observed TOF_{max} (301 mmol_{H₂} mol⁻¹_{PS} min⁻¹) is less than half compared to the *in-situ* prepared [Co(dmgH)₂(H₂O)₂](BF₄)₂ (TOF_{max} = 650 mmol_{H₂} mol⁻¹_{PS} min⁻¹). Furthermore, when K₂PtCl₄ is used as a precursor for colloidal platinum, barely any hydrogen evolution can be observed (TOF_{max} = 20 mmol_{H₂} mol⁻¹_{PS} min⁻¹). These results indicate two things. First, the catalyst is involved in the rate-limiting step of the hydrogen evolution reaction. Second, the electron transfer process is not solely governed by thermodynamic parameters.

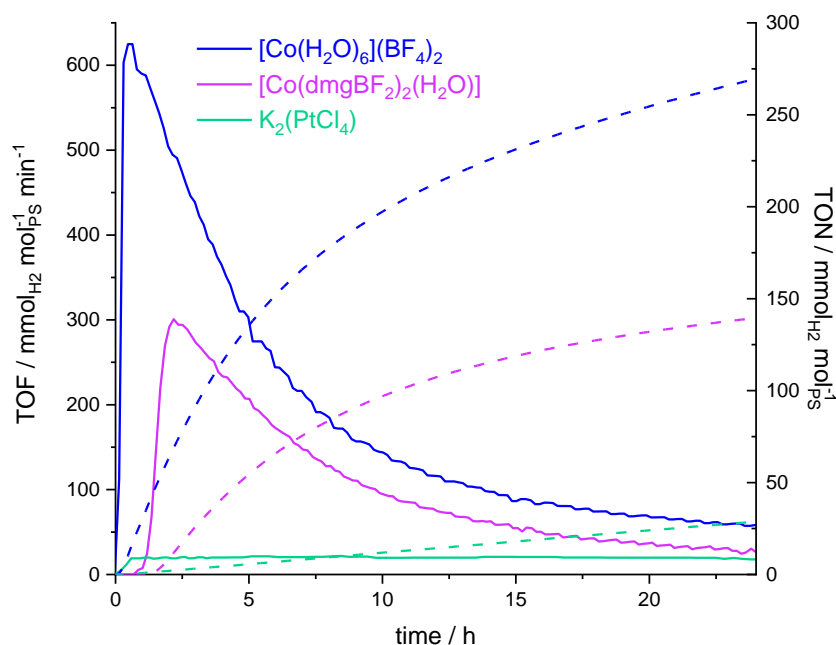


Figure VI-9. Hydrogen photoproduction with complex **IV-C1** as PS (0.1 mM) under blue light irradiation (LED centered at 445 nm); with TEOA as sacrificial electron donor (1 M) and HBF₄ as proton source (0.1 M) and different catalysts in DMF; blue: [Co(H₂O)₆](BF₄)₂ as pre-catalyst (1 mM), with dmgH₂ (6 mM); pink: [Co(dmgBF₂)₂(H₂O)] (1 mM), with dmgH₂ (6 mM); K₂(PtCl₄) as pre-catalyst to form *in-situ* colloidal Pt (0.05 mM); TOF: solid lines; TON: dashed lines.

UV-vis spectroscopy of the reaction mixtures before and after light irradiation (Figure VI-10) reveals a blue shift of the MLCT absorption maximum, regardless of the catalyst used. This observation leads to the conclusion that the decomposition or deactivation of the PS does not involve the catalyst, hence, supporting the hypothesis

that the PS is reductively quenched and then the reduced PS decomposes over time.

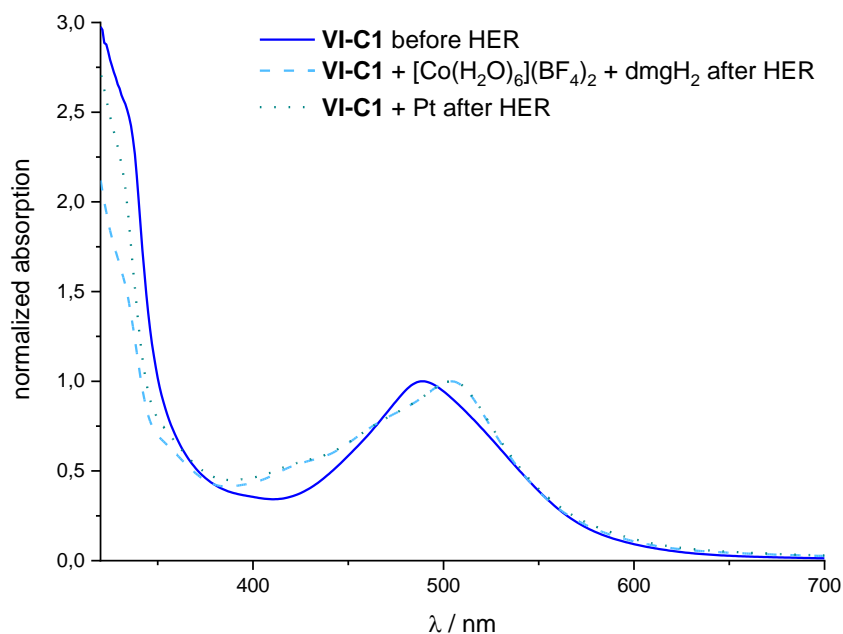


Figure VI-10. UV-vis absorption spectra of DMF solutions containing **VI-C1** (0.1 mM); TEOA (1 M) and HBF₄ (0.1 M) before light irradiation (solid line) alongside reaction mixtures additionally containing (a) [Co(H₂O)₆](BF₄)₂ (1 mM) and dmgH₂ (6 mM) (dashed line) or (b) K₂PtCl₄ (dotted line) after blue light irradiation (LED centered at 445 nm); absorptions are normalized to the MLCT absorption peak.

Table VI-5. Hydrogen production results of complexes discussed in this chapter.^a

PS	catalyst	λ_{exc} / nm	duration / h	TOF _{max} / mmol _{H₂} mol _{PS} ⁻¹ min ⁻¹	TON / mmol _{H₂} mol _{PS} ⁻¹
VI-C1	[Co(dmgH) ₂ (H ₂ O) ₂](BF ₄) ₂ ^b	445	24	650	269
VI-C1	[Co(dmgH) ₂ (H ₂ O) ₂](BF ₄) ₂ ^b	630	60	101	135
VI-C1	[Co(dmgBF ₂) ₂ (H ₂ O)]	445	24	301	139
VI-C1	colloidal Pt ^c	445	24	20	29
VI-C1	none	445	24	not detected	not detected
VI-C2	[Co(dmgH) ₂ (H ₂ O) ₂](BF ₄) ₂ ^b	445	24	715	124
VI-C2	[Co(dmgH) ₂ (H ₂ O) ₂](BF ₄) ₂ ^b	630	60	182	120
VI-C3	[Co(dmgH) ₂ (H ₂ O) ₂](BF ₄) ₂ ^b	445	24	317	157
VI-C3	[Co(dmgH) ₂ (H ₂ O) ₂](BF ₄) ₂ ^b	630	60	54	103
VI-C4	[Co(dmgH) ₂ (H ₂ O) ₂](BF ₄) ₂ ^b	445	24	415	84
VI-C4	[Co(dmgH) ₂ (H ₂ O) ₂](BF ₄) ₂ ^b	630	60	109	56
[Ru(bpy)₃]²⁺d	[Co(dmgH) ₂ (H ₂ O) ₂](BF ₄) ₂ ^b	445	9.5	6850	750
[Ru(bpy)₃]²⁺d	[Co(dmgH) ₂ (H ₂ O) ₂](BF ₄) ₂ ^b	630	20	30	30
III-C1	[Co(dmgH) ₂ (H ₂ O) ₂](BF ₄) ₂ ^b	445	24	46	57
III-C1	[Co(dmgH)(dmgH ₂)Cl ₂]	445	296	51	764

^aunless otherwise stated, all experiments are carried out using 0.1 mM PS, 1 M TEOA as SED, 0.1 M HBF₄ as proton source and 1 mM catalyst with 6 mM dmgH₂ in DMF, irradiation with blue light (LED centered at 445 nm, 62 mW), reported values are averages of multiple runs; ^bprepared *in-situ* from [Co(H₂O)₆](BF₄)₂ and dmgH; ^cprepared *in-situ* from K₂[PtCl₄] (0.05 mM); ^ddata taken from Rupp *et al.*^[162] and Rousset *et al.*^[76].

VI.3. Conclusion

In this chapter, a series of pyrimidine containing ligands with pyridine-substituents in different positions is synthesized following a multistep procedure. The ligands are used to form the heteroleptic complexes **VI-C1** to **VI-C4**. Photophysical and electrochemical experiments confirm the more electron accepting nature of these ligands, which leads to red-shifted emission, longer excited-state lifetimes, higher quantum yields, and anodically shifted reduction potentials. Interestingly, the pyridine-substituents in 4-pyrimidine position appear to have a stronger impact on both photophysical and electrochemical properties. These experimental findings are supported by DFT and TD-DFT calculations.

An estimation of the driving forces for the electron transfer processes from the SED to the excited PS and from the reduced PS to the catalyst gives no clear overall trend. Reductive quenching of complex **VI-C2** is expected to be more exergonic compared to the other pyrimidine-containing complexes as well as **III-C1**. Yet, the electron transfer to the catalyst is expected to be less favorable.

Hydrogen evolution experiments under blue and red light irradiation show that all pyrimidine-containing complexes act as PS, with a TOF_{max} increased by an order of magnitude compared to the bis-terpyridine complex **III-C1**. However, the PSs decompose under the catalytic conditions, leading to a loss of hydrogen evolution activity. The complexes with a pyridine-substituent in 4-pyrimidine position, which exhibit superior photophysical properties, are not more active than the complexes with shorter excited-state lifetimes but rather have a decreased longevity under catalytic conditions. Experiments using different catalysts support the hypothesis that the rate-limiting step in these systems is not the reductive quenching but does involve the catalyst.

VI.4. Experimental

Details on instrumentation, crystal structure analysis, and DFT calculations as well as NMR spectra with peak assignments and natural transition analysis can be found in the Appendix (Chapter IX). References are given for known compounds. The properties of the known compounds agree with the ones published.

3-(4-bromophenyl)-1(pyridine-2-yl)-prop-2-en-1-one VI-I1^[230]

To a solution of potassium hydroxide (278 mg, 4.95 mmol, 1.2 eq) in 10.0 mL methanol and 1.00 mL deionized water 4-bromobenzaldehyde (840 mg, 4.56 mmol, 1.1 eq) and 2-acetylpyridine (463 μL , 500 mg, 4.13 mmol, 1 eq) were added. The reaction mixture was stirred at room temperature for 2.5 h. The precipitate was filtered off over celite and washed with methanol and water. The solid was dissolved in dichloromethane and dried over magnesium sulfate to yield the product as a yellow solid (929 mg, 3.22 mmol, 78%).

$^1\text{H-NMR}$ (300 MHz, CDCl_3) δ = 8.74 (m, 1H), 8.29 (d, 3J = 16.1 Hz, 1H), 8.19

(m, 1H), 7.87 (m, 2H), 7.53 (m, 5H).

1-([4,4'-bipyridine]-2-yl)-3-(4-bromophenyl)-prop-2-en-1-one VI-I2

To a solution of potassium hydroxide (170 mg, 3.03 mmol, 1.2 eq) in 10.0 mL methanol and 1.00 mL deionized water 4-bromobenzaldehyde (513 mg, 2.77 mmol, 1.1 eq) and 2-acetyl-4,4'-bipyridine (500 mg, 2.52 mmol, 1 eq) were added. The reaction mixture was stirred at room temperature for 5 hours. The precipitate was filtered off and washed with water to yield the product as a beige solid (599 mg, 1.64 mmol, 65%). The product was used without further purification.

¹H-NMR (400 MHz, CDCl₃) δ = 8.86 (dd, ³J = 5.0 Hz, ⁵J = 0.5 Hz, 1H), 8.78 (dd, ³J = 4.5 Hz, ⁴J = 1.6 Hz, 2H), 8.45 (d, ⁴J = 1.1 Hz, 1H), 8.33 (d, ³J = 16.0 Hz, 1H), 7.90 (d, ³J = 16.1 Hz, 1H), 7.74 (dd, ³J = 5.0 Hz, ⁴J = 1.8 Hz, 1H) and 7.60 ppm (m, 6H). ¹³C{¹H}-NMR (100 MHz, CDCl₃) δ = 189.0, 155.1, 151.0, 150.0, 147.0, 145.0, 143.9, 134.1, 132.3, 130.4, 125.2, 124.6, 121.6, 121.4 and 120.8 ppm. ESI-MS: m/z [M+H]⁺ calc. for C₁₉H₁₃BrN₄O: 365.0284; found: 365.02906; difference: 1.8 ppm.

4,4'-Bipyridine-N-oxide VI-I3^[226]

A solution of 4,4'-bipyridine (2.00 g, 12.8 mmol, 1 eq) and *meta*-chloroperoxybenzoic acid (73%w, 3.63 g, 15.4 mmol, 1.2 eq) in 80 mL diethyl ether was stirred at room temperature for 4.5 h. The white precipitate was collected by filtration. Mono and bis-*N*-oxide were separated by column chromatography (silica gel, acetone:methanol 4:1) to receive the desired product as a white solid (1.30 g, 7.57 mmol, 59%).

¹H-NMR (300 MHz, DMSO-d₆): δ = 8.68 (d, ³J = 6.2 Hz, 2H), 8.34 (d, ³J = 7.4 Hz, 2H), 7.93 (d, ³J = 7.4 Hz, 2H) and 7.81 ppm (d, ³J = 6.2 Hz, 2H).

4,4'-Bipyridine-2-carbonitrile VI-I4^[226]

Under inert gas atmosphere a suspension of 4,4'-bipyridine-*N*-oxide VI-I3 (546 mg, 3.17 mmol, 1 eq) and trimethylsilyl cyanide (478 μL, 378 mg, 3.81 mmol, 1.2 eq) in 20.0 mL dry chloroform was stirred at room temperature for 5 min. After adding *N,N*-dimethyl carbamoyl chloride (321 μL, 375 mg, 3.49 mmol, 1.1 eq), the reaction mixture was stirred at room temperature for 48 h. The solvent was removed

under reduced pressure and 70.0 mL of an aqueous 10% potassium carbonate solution were added. The suspension was stirred for 4.5 h and the precipitate was filtered off. More product was retrieved by extracting the filtrate with dichloromethane. The combined crude product was purified using column chromatography (silica gel, ethyl acetate) to yield the desired product as a white solid (256 mg, 1.41 mmol, 45%).

$^1\text{H-NMR}$ (300 MHz, CDCl_3): δ = 8.85 (d, 3J = 5.1 Hz, 1H, H⁶), 8.81 (dd, 3J = 4.5 Hz, 4J = 1.6 Hz, 2H, H^{2',6'}), 7.94 (m, 1H, H³), 7.75 (dd, 3J = 5.1 Hz, 4J = 1.8 Hz, 1H, H⁴) and 7.53 ppm (dd, 3J = 4.5 Hz, 4J = 1.6 Hz, 2H^{3',5'}).

2-Pyridinecarboxamide hydrochloride VI-15^[231]

Under inert gas atmosphere, a solution of pyridine-2-carbonitrile (1.85 mL, 2.00 g, 19.2 mmol, 1 eq) and sodium methoxide (25%w, 440 μL , 104 mg, 1.92 mmol, 0.1 eq) in 20.0 mL methanol was stirred at room temperature overnight. Subsequently, ammonium chloride (1.13 g, 21.1 mmol, 1.1 eq) was added and the reaction mixture was heated to reflux for 6 h. The volume of solvent was reduced to half and diethyl ether was added. The mixture was cooled, and the precipitate was filtered off to yield the desired product as a white solid (2.87 g, 18.2 mmol, 95%).

$^1\text{H-NMR}$ (300 MHz, DMSO-d_6): δ = 9.50 (s, 3H, NH), 8.83 (ddd, 3J = 4.7 Hz, 4J = 1.7 Hz, 5J = 0.9 Hz, 1H), 8.37 (dt, 3J = 8.0 Hz, 4J = 1.0 Hz, 1H), 8.16 (dt, 3J = 7.8 Hz, 4J = 1.7 Hz, 1H) and 7.79 ppm (ddd, 3J = 7.7 Hz, 4J = 4.7 Hz, 5J = 1.0 Hz, 1H).

4,4'-Bipyridine-2-carboxamide hydrochloride VI-16

Under inert gas atmosphere, a suspension of 4,4'-bipyridine-2-carbonitrile **VI-14** (200 mg, 1.10 mmol, 1 eq) and sodium methoxide (25%w, 25.2 μL , 5.96 mg, 110 μmol , 0.1 eq) in 5.0 mL methanol was stirred at room temperature overnight. Subsequently, ammonium chloride (64.9 mg, 1.21 mmol, 1.1 eq) was added and the reaction mixture was heated to reflux for 6 hours. The volume of solvent was reduced to half and diethyl ether was added. The mixture was cooled, and the precipitate was filtered off to yield the desired product as an off-white solid (197 mg, 839 μmol , 76%).

$^1\text{H-NMR}$ (300 MHz, DMSO-d_6): δ = 9.50 (s, 3H, NH), 8.83 (ddd, 3J = 4.7 Hz, 4J = 1.7 Hz, 5J = 0.9 Hz, 1H), 8.37 (dt, 3J = 8.0 Hz, 4J = 1.0 Hz, 1H), 8.16 (dt,

$^3J = 7.8$ Hz, $^4J = 1.7$ Hz, 1H) and 7.79 ppm (ddd, $^3J = 7.7$ Hz, $^4J = 4.7$ Hz, $^5J = 1.0$ Hz, 1H). $^{13}\text{C}\{^1\text{H}\}$ -NMR (75 MHz, DMSO- d_6): $\delta = 162.0, 150.7, 146.3, 145.1, 143.0, 125.6, 121.6$ and 121.4 ppm. ESI-MS: m/z $[\text{M}+\text{H}]^+$ calc. for $\text{C}_{11}\text{H}_{10}\text{N}_4$: 199.09718; found: 199.09782; difference: 3.2 ppm.

6-(4-bromophenyl)-2,4-di(pyridin-2-yl)-pyrimidine VI-L1^[225]

A suspension of 3-(4-bromophenyl)-1-(pyridine-2-yl)-prop-2-en-1-one **VI-I1** (300 mg, 1.04 mmol, 1 eq), 2-pyridinecarboxamide hydrochloride **VI-I5** (164 mg, 1.04 mmol, 1 eq) and potassium hydroxide (87.6 mg, 1.56 mmol, 1.5 eq) in 40.0 mL ethanol was heated to reflux for 3 days. After cooling to room temperature, water was added, and the precipitate was filtered off over celite and washed with water. The solid was dissolved in dichloromethane and dried over magnesium sulfate. The crude product was purified by washing with methanol and column chromatography (Al_2O_3 + 6%w H_2O , dichloromethane) to yield the product as a white solid (214 mg, 550 μmol , 53%).

^1H -NMR (500 MHz, CDCl_3): $\delta = 8.92$ (d, $^3J = 4.7$ Hz, 1H), 8.84 (s, 1H), 8.78 (m, 2H), 8.72 (d, $^3J = 7.9$ Hz), 8.27 (d, $^3J = 8.6$ Hz, 2H), 7.93 (tt, $^3J = 7.7$ Hz, $^4J = 1.9$ Hz, 2H), 7.69 (d, $^3J = 8.6$ Hz, 2H) and 7.46 ppm (ddd, $^3J = 7.5$ Hz, $^3J = 4.7$ Hz, $^4J = 1.0$ Hz, 2H). $^{13}\text{C}\{^1\text{H}\}$ -NMR (125 MHz, CDCl_3): $\delta = 164.8, 164.7, 164.0, 155.5, 154.2, 150.3, 149.6, 137.3, 137.0, 136.1, 132.3, 129.3, 125.9, 125.8, 125.0, 124.3, 122.6$ and 111.9 ppm. ESI-MS: m/z $[\text{M}+\text{H}]^+$ calc. for $\text{C}_{20}\text{H}_{13}\text{BrN}_4$: 389.03966; found: 389.03964; difference: 0.1 ppm.

2-(6-(4-bromophenyl)-2-(pyridin-2-yl)-pyrimidin-4-yl)-4,4'-bipyridine VI-L2

A suspension of 1-([4,4'-bipyridine]-2-yl)-3-(4-bromophenyl)-prop-2-en-1-one **VI-I2** (270 mg, 739 μmol , 1 eq), potassium hydroxide (62.2 mg, 1.11 mmol, 1.5 eq), and 2-pyridinecarboxamide hydrochloride **VI-I5** (128 mg, 813 μmol , 1.1 eq) in 20.0 mL ethanol was heated to reflux for three days. After cooling to room temperature, water was added and the precipitate was filtered off over celite, washed with water and dissolved in dichloromethane. The organic solution was dried over magnesium sulfate and the solvent was reduced under vacuum. The crude product was washed with hot methanol to yield the product as an off-white solid (102 mg, 219 μmol , 30%).

$^1\text{H-NMR}$ (500 MHz, CDCl_3): δ = 9.00 (d, 4J = 1.0 Hz, 1H), 8.90 (m, 3H), 8.80 (dd, 3J = 4.5 Hz, 4J = 1.6 Hz, 2H), 8.71 (d, 3J = 7.9 Hz, 1H), 8.29 (d, 3J = 8.6 Hz, 2H), 7.95 (td, 3J = 7.8, 4J = 1.7 Hz, 1H), 7.70 (m, 5H) and 7.48 ppm (dd, 3J = 6.9 Hz, 4J = 5.3 Hz, 1H). $^{13}\text{C}\{^1\text{H}\}$ -NMR (125 MHz, CDCl_3): δ = 165.0, 164.3, 164.1, 155.3, 150.9, 150.4, 150.3, 147.2, 145.5, 137.1, 135.9, 132.3, 129.3, 126.1, 125.1, 124.4, 123.4, 121.8, 120.2 and 112.2 ppm. ESI-MS: m/z $[\text{M}+\text{H}]^+$ calc. for $\text{C}_{25}\text{H}_{16}\text{BrN}_5$: 466.06618; found: 466.06765; difference: 3.2 ppm.

2-(6-(4-bromophenyl)-4-(pyridin-2-yl)-pyrimidin-2-yl)-4,4'-bipyridine VI-L3

A suspension of 3-(4-bromophenyl)-1-(pyridine-2-yl)-prop-2-en-1-one **VI-I1** (123 mg, 426 μmol , 1 eq), 4,4'-bipyridine-2-carboxamidine hydrochloride **VI-I6** (100 mg, 426 μmol , 1 eq) and potassium hydroxide (35.9 mg, 639 μmol , 1.5 eq) in 15.0 mL ethanol was heated to reflux for three days. After cooling to room temperature, water was added and the precipitate was filtered off over celite, washed with water and dissolved in dichloromethane. The organic solution was dried over magnesium sulfate and the solvent was reduced under vacuum. The crude product was recrystallized from hot methanol to yield the product as an off-white solid (56.0 mg, 120 μmol , 28%).

$^1\text{H-NMR}$ (300 MHz, CDCl_3): δ = 9.03 (dd, 3J = 5.1 Hz, 5J = 0.8 Hz, 1H), 8.94 (dd, 4J = 1.8 Hz, 5J = 0.8 Hz, 1H), 8.87 (s, 1H), 8.82 (dd, 3J = 4.4 Hz, 4J = 0.8 Hz, 1H), 8.78 (m, 2H), 8.28 (d, 3J = 8.8, 2H), 7.94 (m, 1H), 7.94 (m, 5H) and 7.47 ppm (ddd, 3J = 7.6 Hz, 3J = 4.9 Hz, 4J = 1.1 Hz, 1H). $^{13}\text{C}\{^1\text{H}\}$ -NMR (100 MHz, CDCl_3): δ = 164.8, 164.6, 163.5, 156.4, 153.9, 151.0, 150.8, 149.5, 146.7, 145.7, 137.3, 135.8, 132.2, 129.2, 125.9, 125.7, 122.5, 122.4, 121.9, 121.6 and 112.1 ppm. ESI-MS: m/z $[\text{M}+\text{H}]^+$ calc. for $\text{C}_{25}\text{H}_{16}\text{BrN}_5$: 466.06618; found: 466.06794; difference: 3.8 ppm.

2,2''-(6-(4-bromophenyl)-pyrimidine-2,4-diyl)-di-4,4'-bipyridine VI-L4

A suspension of 1-([4,4'-bipyridine]-2-yl)-3-(4-bromophenyl)-prop-2-en-1-one **VI-I2** (100 mg, 274 μmol , 1 eq), 4,4'-bipyridine-2-carboxamidine hydrochloride **VI-I6** (64.3 mg, 274 μmol , 1 eq) and potassium hydroxide (46.1 mg, 821 μmol , 3 eq) in 10.0 mL ethanol was heated to reflux for two days. After cooling to room temperature, water was added and the precipitate was separated and washed with water using a centrifuge to yield the product as an off-white solid (21.0 mg, 38.6 μmol , 14%).

$^1\text{H-NMR}$ (500 MHz, CDCl_3): δ = 9.03 (d, 3J = 5.0 Hz, 1H), 9.00 (s, 1H), 8.92 (s, 2H), 8.90 (d, 3J = 5.0 Hz, 1H), 8.81 (m, 4H), 8.28 (d, 3J = 8.5, 2H) and 7.70 ppm (m, 8H). $^{13}\text{C}\{^1\text{H}\}\text{-NMR}$ (126 MHz, CDCl_3): δ = 165.0, 164.6, 163.8, 156.5, 155.2, 151.1, 151.0, 150.9, 150.5, 147.3, 146.9, 145.8, 145.5, 135.8, 132.4, 129.3, 126.2, 123.5, 122.7, 122.1, 121.8, 121.7, 120.3 and 112.6 ppm. ESI-MS: m/z $[\text{M}+\text{H}]^+$ calc. for $\text{C}_{30}\text{H}_{19}\text{BrN}_6$: 543.09273; found: 543.0906; difference: 3.9 ppm.

[Ru(Tolyltpy)(VI-L1)](PF₆)₂ **VI-C1**

A suspension of $[\text{Ru}(\text{Tolyltpy})\text{Cl}_3]$ **III-I3** (68.2 mg, 128 μmol , 1 eq) and **VI-L1** (50.0 mg, 128 μmol , 1 eq) in 7.00 mL ethylene glycol was heated to 180 °C for 15 minutes using microwave irradiation. After cooling to room temperature, water, and aqueous KPF_6 solution were added to the solution. The precipitate was filtered off over celite, washed with deionized water, and dissolved in acetonitrile. The solution was dried over magnesium sulfate and the solvent was removed under reduced pressure. The crude product was purified by column chromatography (silica, MeCN:aqu. KNO_3 7:1) to yield a dark red solid (122 mg, 111 μmol , 86%).

$^1\text{H-NMR}$ (500 MHz, CD_3CN): δ = 9.17 (s, 1H), 9.02 (s, 2H), 8.94 (d, J = 7.9 Hz, 1H), 8.83 (d, J = 8.0 Hz, 1H), 8.64 (m, 4H), 8.12 (d, J = 8.1 Hz, 2H), 8.05 (t, J = 7.6 Hz, 2H), 7.99 – 7.93 (m, 4H), 7.60 – 7.57 (m, 3H), 7.53 (d, J = 5.3 Hz, 1H), 7.42 (d, J = 5.5 Hz, 2H), 7.31 (m, 2H), 7.14 (t, J = 6.6 Hz, 2H) and 2.55 ppm (s, 3H). $^{13}\text{C}\{^1\text{H}\}\text{-NMR}$ (126 MHz, CD_3CN): δ = 164.45, 163.16, 162.42, 159.13, 157.43, 157.03, 156.25, 154.27, 154.02, 153.72, 149.82, 142.12, 139.42, 139.19, 139.15, 136.01, 134.73, 133.70, 131.25, 130.56, 129.94, 129.87, 128.63, 128.30, 127.55, 127.41, 127.30, 125.49, 122.37, 114.65 and 21.37 ppm. ESI-MS: m/z $[\text{M}]^{2+}$ calc. for $\text{C}_{42}\text{H}_{30}\text{BrN}_7\text{Ru}$: 406.53893; found: 406.54001; difference: 2.7 ppm. Anal. calc. for $\text{C}_{42}\text{H}_{30}\text{BrF}_{12}\text{N}_7\text{P}_2\text{Ru}$: C, 45.71; H, 2.74; N, 8.88. Found: C, 46.34; H, 2.83; N, 8.85.

[Ru(Tolyltpy)(VI-L2)](PF₆)₂ **VI-C2**

A suspension of $[\text{RuCl}_3(\text{Tolyltpy})]$ **III-I3** (185 mg, 429 μmol , 1 eq), **VI-L2** (200 mg, 429 μmol , 1 eq) and four drops of *N*-ethylmorpholine in 15.0 mL ethylene glycol was heated to 180 °C for 15 min using microwave irradiation. After cooling to room temperature, water, and aqueous KPF_6 were added to the solution and the

precipitate was filtered off over celite. After washing with water, it was dissolved in acetonitrile, dried over magnesium sulfate and the solvent was removed under reduced pressure. The product was purified by column chromatography (silica, MeCN:aqu. KNO₃ 7:1) to yield a dark red solid (150 mg, 136 μmol, 32%).

¹H-NMR (500 MHz, CD₃CN): δ = 9.31 (s, 1H), 9.12 (s, 1H), 9.03 (s, 2H), 8.96 (d, ³J = 7.9 Hz, 1H), 8.78 (d, ³J = 4.9 Hz, 2H), 8.66 (m, 4H), 8.14 (d, ³J = 7.5 Hz, 2H), 8.06 (t, ³J = 7.7 Hz, 1H), 8.00 (d, ³J = 7.6 Hz, 2H), 7.96 (t, ³J = 7.8 Hz, 2H), 7.75 (d, ³J = 5.0 Hz, 2H), 7.70 (d, ³J = 6.0 Hz, 1H), 7.61 (m, 3H), 7.54 (d, ³J = 5.5 Hz, 1H), 7.45 (d, ³J = 5.6 Hz, 2H), 7.34 (t, ³J = 6.5 Hz, 1H), 7.16 (t, ³J = 6.6 Hz, 2H) and 2.55 ppm (s, 3H). ¹³C{¹H}-NMR (176 MHz, CD₃CN): δ = 164.54, 163.13, 162.51, 159.14, 158.28, 156.97, 156.23, 154.7, 154.0, 153.8, 151.8, 150.0, 148.1, 143.5, 142.2, 139.5, 139.3, 136.0, 134.7, 133.8, 131.3, 130.5, 130.0, 128.7, 128.4, 127.7, 127.4, 127.2, 125.5, 125.3, 122.5, 114.9 and 21.4 ppm. ESI-MS: m/z [M]²⁺ calc. for C₄₇H₃₃BrN₈Ru: 445.0522; found: 445.05327; difference: 2.4 ppm. Anal. calc. for C₄₇H₃₃BrF₁₂N₈P₂Ru: C, 47.81; H, 2.82; N, 9.49. Found: C, 47.91; H, 2.91; N, 9.79.

[Ru(TolyItpy)(VI-L3)](PF₆)₂ **VI-C3**

A suspension of [RuCl₃(TolyItpy)] **III-I3** (59.2 mg, 112 μmol, 1 eq), **VI-L3** (52.0 mg, 112 μmol, 1 eq) and silver nitrate (56.8 mg, 335 μmol, 3 eq) in 15.0 mL ethylene glycol was heated to 150 °C for 15 minutes using microwave irradiation. After cooling to room temperature, 1-2 mL of hydrazine hydrate, water, and aqueous KPF₆ solution were added to the solution and the precipitate was filtered off over celite. After washing with water, it was dissolved in acetonitrile, dried over magnesium sulfate and the solvent was removed under reduced pressure. The product was purified by column chromatography (silica, MeCN:aqu. KNO₃ 12:1) to yield a dark red solid (65.0 mg, 55.1 μmol, 49%).

¹H-NMR (500 MHz, CD₃CN): δ = 9.22 (s, 1H), 9.20 (d, ³J = 1.6 Hz, 1H), 9.04 (s, 2H), 8.86 (d, ³J = 8.0 Hz, 1H), 8.76 (d, ³J = 5.6 Hz, 2H), 8.70 (d, ³J = 8.6 Hz, 2H), 8.68 (d, ³J = 8.1 Hz, 2H), 8.14 (d, ³J = 8.1 Hz, 2H), 8.07 (td, ³J = 7.9 Hz, ⁴J = 1.3 Hz, 1H), 7.96 (m, 4H), 7.75 (dd, ³J = 4.7 Hz, ⁴J = 1.5 Hz, 2H), 7.62 (m, 5H), 7.44 (d, ³J = 4.9 Hz, 2H), 7.32 (m, 1H), 7.16 (ddd, ³J = 7.2 Hz, ³J = 5.7 Hz, ⁴J = 1.1 Hz, 2H) and 2.55 ppm (s, 3H). ¹³C{¹H}-NMR (126 MHz, CD₃CN): δ = 164.4, 163.2, 162.5, 159.1, 157.9, 157.4,

156.2, 154.5, 154.3, 153.8, 151.7, 150.0, 148.5, 143.5, 142.1, 139.3, 139.3, 135.9, 134.7, 133.6, 131.3, 130.8, 129.9, 128.6, 128.3, 127.7, 127.5, 127.3, 125.5, 124.7, 122.6, 122.5, 114.8 and 21.4 ppm. ESI-MS: m/z $[M]^{2+}$ calc. for $C_{47}H_{33}BrN_8Ru$: 446.05118; found: 446.05341; difference: 2.0 ppm. Anal. calc. for $C_{47}H_{33}BrF_{12}N_8P_2Ru$: C, 47.81; H, 2.82; N, 9.49. Found: C, 47.34; H, 2.99; N, 9.35.

[Ru(TolyItpy)(VI-L4)](PF₆)₂ VI-C4

A suspension of $[RuCl_3(TolyItpy)]$ **III-I3** (37.1 mg, 69.9 μ mol, 1 eq), **VI-L4** (38.0 mg, 39.9 μ mol, 1 eq) and silver nitrate (35.6 mg, 210 μ mol, 3 eq) in 15.0 mL ethylene glycol was heated to 150 °C for 15 min using microwave irradiation. After cooling to room temperature 1-2 mL of hydrazine hydrate, water, and aqueous KPF₆ solution were added to the solution and the precipitate was filtered off over celite. After washing with water, it was dissolved in acetonitrile, dried over magnesium sulfate and the solvent was removed under reduced pressure. The product was purified by column chromatography (silica, MeCN:aqu. KNO₃ 12:1 to 8:1) to yield a dark red solid (16.0 mg, 12.7 μ mol, 18%).

¹H-NMR (400 MHz, CD₃CN): δ = 9.35 (s, 1H), 9.22 (m, 1H), 9.15 (d, ⁴J = 1.6 Hz, 9.05 (s, 2H), 8.76 (m, 6H), 8.69 (d, ³J = 8.0 Hz, 2H), 8.15 (d, ³J = 8.2 Hz, 2H), 7.98 (m, 4H), 7.75 (m, 4H), 7.71 (d, ³J = 5.9 Hz, 1H), 7.64 (m, 5H), 7.47 (dd, ³J = 5.6 Hz, ⁴J = 0.7 Hz, 2H), 7.18 (m, 2H) and 2.56 ppm (s, 3H). ¹³C{¹H}-NMR (100 MHz, CD₃CN): δ = 164.5, 163.2, 162.7, 159.2, 158.2, 157.8, 156.2, 154.6, 154.5, 153.9, 151.9, 151.8, 150.1, 148.6, 148.3, 143.5, 143.4, 142.2, 139.4, 135.9, 134.8, 133.7, 131.3, 130.7, 128.7, 128.4, 127.8, 127.4, 127.4, 125.6, 125.3, 124.8, 122.6, 122.6, 122.5, 115.1 and 21.4 ppm. ESI-MS: m/z $[M]^{2+}$ calc. for $C_{52}H_{36}BrN_9Ru$: 483.56548; found: 483.56737; difference: 3.9 ppm. Anal. calc. for $C_{52}H_{36}BrF_{12}N_9P_2Ru$: C, 49.66; H, 2.88; N, 10.02. Found: C, 49.82; H, 3.04; N, 9.69.

VII. Effect of Multiple Metal Centers in Ru(II) Complexes of Tridentate Ligands

Parts of the presented research were submitted as a full paper to
Dalton Transactions under the title
“Dinuclear 2,4-di(pyridin-2-yl)-pyrimidine based ruthenium photosensitizers for
hydrogen photo-evolution under red light”.

Contributions:

Mira Rupp: Project design, synthesis and characterization of ligands and complexes, analysis of photophysical and electrochemical properties, article writing.

Thomas Auvray: Project design, DFT and TD-DFT calculations, revision of the article.

Garry S. Hanan: Supervision, revision of the article.

Dirk G. Kurth: Supervision, revision of the article.

VII.1. Introduction

The exchange of the central pyridine ring in the terpyridine metal ion receptor with a pyrimidine ring in complexes **VI-C1** to **VI-C2** results in an increase of the hydrogen evolution activity by an order of magnitude. However, this increased activity comes at the cost of the longevity of the system as the PS is deactivated under catalytic conditions. In this chapter, the mononuclear pyrimidine-containing complexes are expanded using ditopic pyrimidine-containing ligands to form dinuclear complexes **VII-C1** and **VII-C2** (see Chart VII-1). The dinuclear complexes are investigated as models for larger, polynuclear assemblies to study the effect the introduction of a second Ru(II) ion into the structure has on the activity as PS.

As both coordination sites are identical, no electron or energy transfer is expected from one metal center to the other. However, due to the more electron accepting nature of the bridging pyrimidine-containing ligand compared to the capping terpyridine ligands a charge transfer towards the bridging ligand is expected upon excitation. The expansion of the conjugated system as well as the possibility to form intra-ligand hydrogen bonds is expected to reduce the non-radiative decay and hence increase the luminescence quantum yield. Furthermore, the presence of two chromophoric sites, i.e., two coordinated metal ions, in one structure is expected to increase the absorptivity.

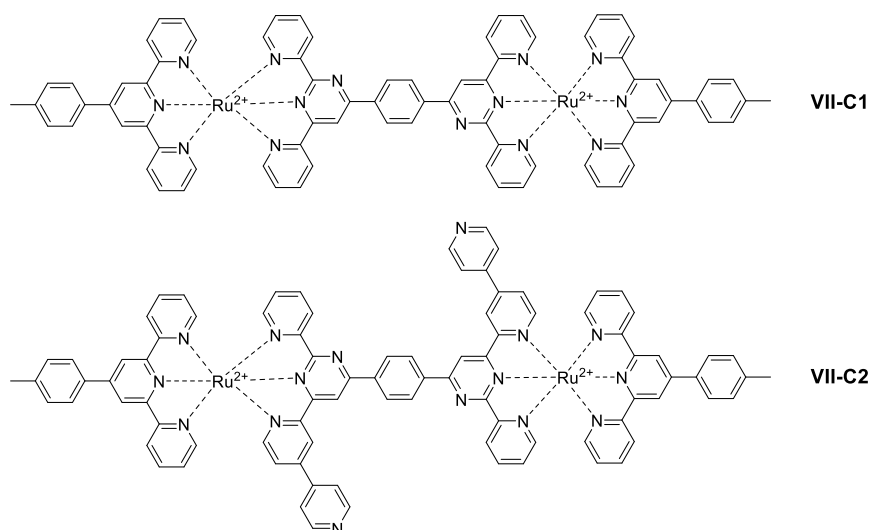
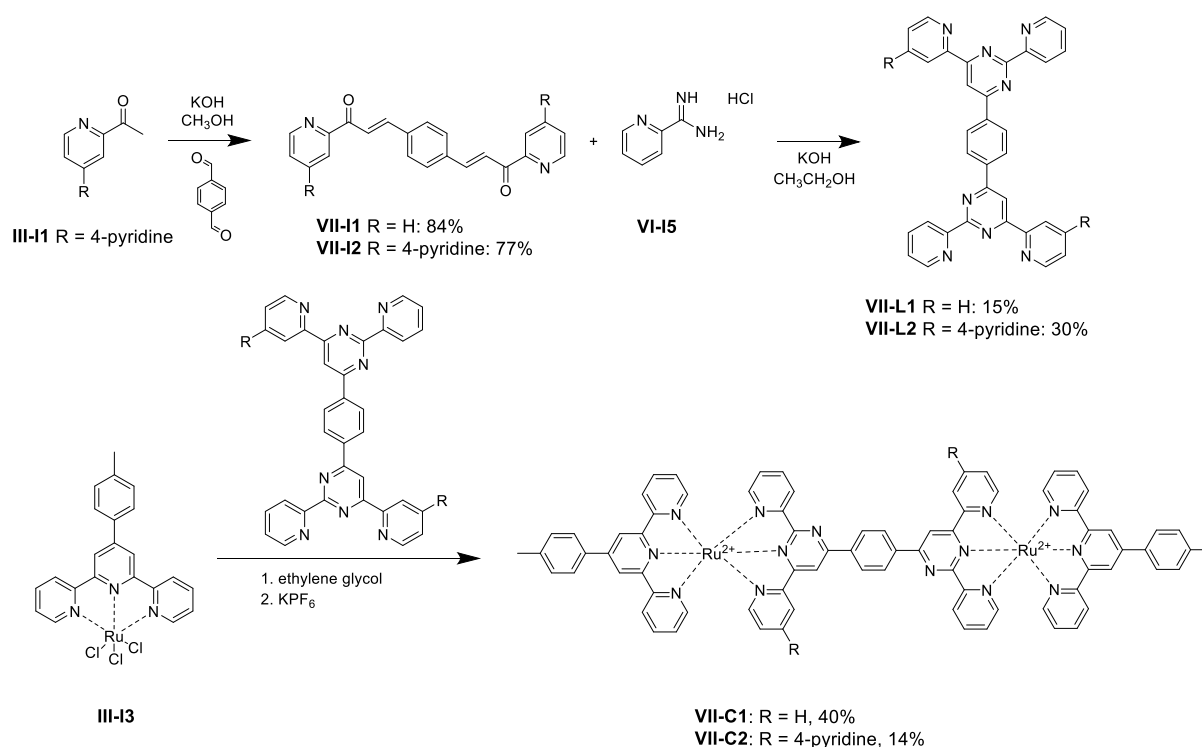


Chart VII-1. Structures of dinuclear complexes **VII-C1** and **VII-C2**; the PF_6^- counterions are omitted for clarity.

VII.2. Results and Discussion

VII.2.1. Synthesis

The ditopic ligands **VII-L1** and **VII-L2** are synthesized analogously to the monotopic ligands **VI-L1** and **VI-L2**. The synthesis can also be carried out in a one-pot procedure, i.e., combining the respective 2-acetylpyridine derivative with terephthalaldehyde and 2-pyridinecarboxamidine **VI-I5**, leading to comparable yields. The dinuclear complexes of the ditopic ligands are then received by reacting the ditopic ligands with the Ru(III) complex **III-I3**, either using microwave irradiation or regular heating. As in the synthesis of the mononuclear complexes, this procedure yields a mixture of products because of ligand scrambling. Due to the ditopic nature of **VII-L1** and **VII-L2**, different monometallic and polymetallic species are formed. The desired product is isolated and purified using column chromatography.



Scheme VII-1. Synthesis of bis-enones **VII-I1** and **VII-I2**, ditopic ligands **VII-L1** and **VII-L2**, and dinuclear complexes **VII-C1** and **VII-C2**.

The complexes are analyzed using NMR-spectroscopy, high-resolution mass-spectrometry, and elemental analysis. Despite several crystallization attempts under

various conditions, no suitable single crystals for X-ray analysis are obtained. However, theoretical calculations and structure optimizations, modelling the complexes **VII-C1** and **VII-C2** in acetonitrile solution, suggest that the pyrimidine rings of the ditopic bridging ligand form hydrogen bonds with the phenyl spacer to some degree, hence planarizing the ligand. The optimized structures exhibit torsion angles between 7° and 12° (Figure VII-1), which is similar to the torsion angle of 13° observed in **VI-C1** (Chapter VI.2.1).

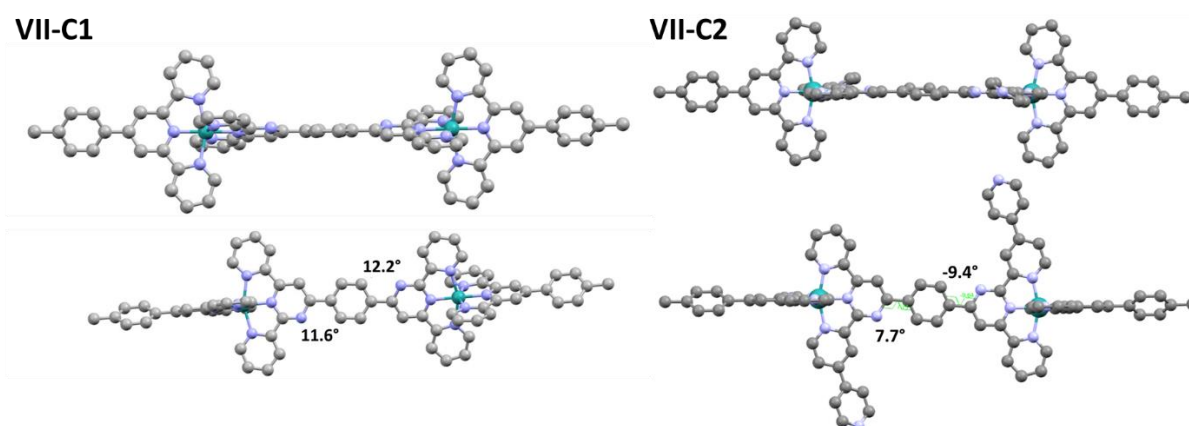


Figure VII-1. Optimized geometries of **VII-C1** (left) and **VII-C2** (right) with torsion angles between the pyrimidine rings and the phenyl spacer.

VII.2.2. Photophysical Properties

The photophysical properties of the dinuclear complexes **VII-C1** and **VII-C2** are investigated using UV-vis absorption and emission spectroscopy and are compared to their mononuclear analogues **VI-C1** and **VI-C2**. Spectra are recorded in acetonitrile and the results are summarized in Figure VII-2 and Table VII-1.

The dinuclear complexes exhibit a broad MLCT absorption band in the visible region with two shoulders, which both exhibit a red shift compared to the mononuclear complexes. This bathochromic shift is presumably due to the extended conjugated system, which leads to a stabilization of the ¹MLCT state. The absorption shoulder around 500 nm is assumed to correspond to an MLCT transition involving the terpyridine ligand, while the red-shifted shoulder around 530 nm involves the ditopic pyrimidine ligand. The LC absorption bands in the UV-region resemble those of the

mononuclear complexes, with an additional absorption band around 230 nm for complexes **VII-C2** and **VI-C2**, which both bear pyridine substituents. However, a hyperchromic effect is observed for both dinuclear complexes compared to the mononuclear ones. The increased absorptivity in **VII-C1** and **VII-C2** is expected due to the presence of two chromophoric sites.

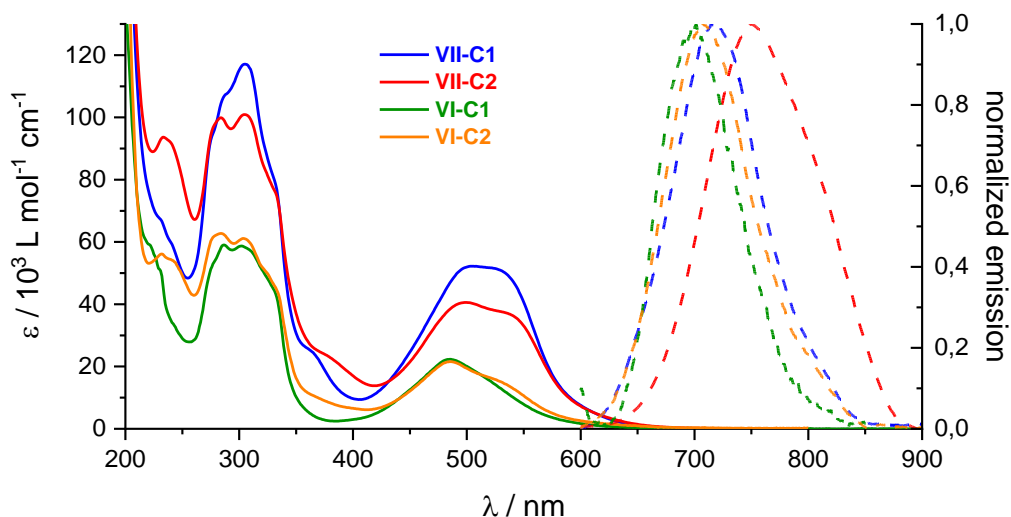


Figure VII-2. UV-vis absorption (solid lines) and emission spectra (dashed lines) of dinuclear complexes **VII-C1** (blue) and **VII-C2** (red), alongside the mononuclear complexes **VI-C1** (green) and **VI-C2** (orange); spectra measured in acetonitrile.

The emission of the dinuclear complexes is red-shifted compared to their mononuclear counterparts. Furthermore, the complexes with a pyridine-substituent **VII-C2** and **VI-C2** exhibit a stronger red shift of the emission wavelength than the unsubstituted complexes **VII-C1** and **VI-C1**, respectively. The red-shifted emission is presumably due to a stabilization of the emissive $^3\text{MLCT}$ state, which results in a larger $^3\text{MLCT}$ to ^3MC energy gap and hence improves the emission properties. Indeed, the dinuclear complexes exhibit increased excited-lifetimes (95–125 ns) and quantum yields ($210\text{--}350 \times 10^{-5}$), leading to decreased non-radiative decay rates (0.1×10^8), compared to the mononuclear complexes ($k_{\text{nr}} = 0.3\text{--}1.1 \times 10^8$). Furthermore, as described in Chapter VI, the possibility to form hydrogen bonds within the pyrimidine containing ligands is expected to also affect the photophysical properties as a result of reduced electronic coupling of the excited state and the ground state.

Table VII-1. UV-vis absorption and emission data of dinuclear complexes **VII-C1** and **VII-C2**, alongside the mononuclear complexes **VI-C1** and **VIC-2** (spectra measured in acetonitrile at 20 °C).^a

	$\lambda_{\max \text{ abs}} / \text{nm} (\epsilon / 10^3 \text{ L mol}^{-1} \text{ cm}^{-1})$		$\lambda_{\max \text{ em}} / \text{nm}$	$\Phi_c / 10^{-5}$	τ_c / ns	$k_r / 10^4 \text{ s}^{-1}$	$k_{\text{nr}} / 10^8 \text{ s}^{-1}$
	LC	MLCT					
VII-C1	305 (134)	504 (59) 526 (51)	720	212 ± 72	94 ± 4	2.26	0.11
VII-C2	233 (94), 283 (100), 305 (101)	499 (41) 534 (37)	752	350 ± 143	125 ± 5	2.80	0.08
VI-C1	287 (59), 302 (59)	485 (22)	703	42 ± 17	8.8 ± 1	4.77	1.14
VIC-2	232 (56), 284 (63), 303 (61)	485 (22)	709	169 ± 63	34 ± 5	4.97	0.29

^amaximum absorption wavelength $\lambda_{\max \text{ abs}}$, extinction coefficient ϵ , maximum emission wavelength $\lambda_{\max \text{ em}}$, luminescence quantum yield Φ , excited-state lifetime τ ; radiative decay rate $k_r = \Phi/\tau$, non-radiative decay rate $k_{\text{nr}} = (1-\Phi)/\tau$; emission data is collected in inert gas-purged solutions.

The photophysical properties of complex **VII-C1** are further investigated in different protic (methanol, acetic acid) and aprotic solvents (acetonitrile, acetone, dimethylsulfoxide (DMSO), DMF). The absorption and emission spectra are shown in Figure VII-3. Both the emission intensity and wavelength vary between solvents. Comparing the emission wavelength of **VII-C1** in acetonitrile ($\lambda_{\max \text{ em}} = 720 \text{ nm}$) to that in methanol ($\lambda_{\max \text{ em}} = 708 \text{ nm}$) a hypsochromic shift can be observed. While this shift represents negative solvatochromism no overall trend between the solvent properties and the emission properties of **VII-C1** in the respective solvent can be identified. In the absorption spectra the relative intensity of the MLCT absorption shoulders varies between solvents. This study underscores the dependence of the MLCT transition on the surrounding solvent.

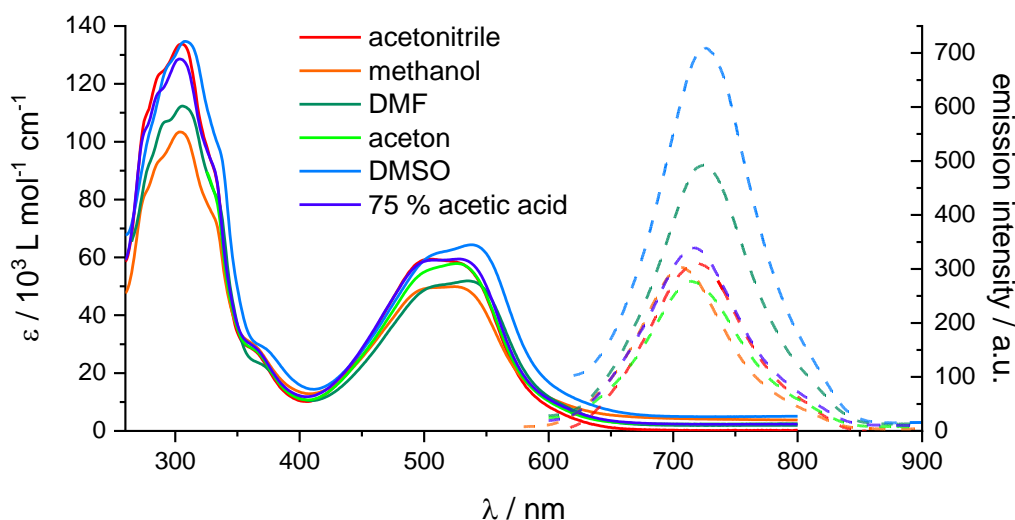


Figure VII-3. UV-vis absorption (solid lines) and emission spectra (dashed lines) of complex **VII-C1** in different inert gas-purged solvents; emission spectra are normalized with regard to the absorptivity of the sample solution at the excitation wavelength and the refractive index of the solvent.

In addition, the temperature-dependence of the emission of the dinuclear complexes **VII-C1** and **VII-C2** and the mononuclear analogues **VI-C1** and **VI-C2** is investigated. The temperature of inert gas purged-acetonitrile solutions is varied between +40 ° and -10 °C. The emission spectra are shown in Figure VII-4. Despite the electron-withdrawing character of the pyrimidine-containing ligands, the extended conjugated system, and the impact of ligand planarization, it is assumed that the non-radiative decay *via* the ^3MC state plays a major role in the emission of the complexes, nonetheless. Therefore, an increased luminescence is expected at lower temperatures. Indeed, all complexes discussed in this chapter exhibit a higher emission intensity at lower temperatures. Furthermore, in the investigated temperature range the emission wavelength is red-shifted by 5–15 nm with decreasing temperature.

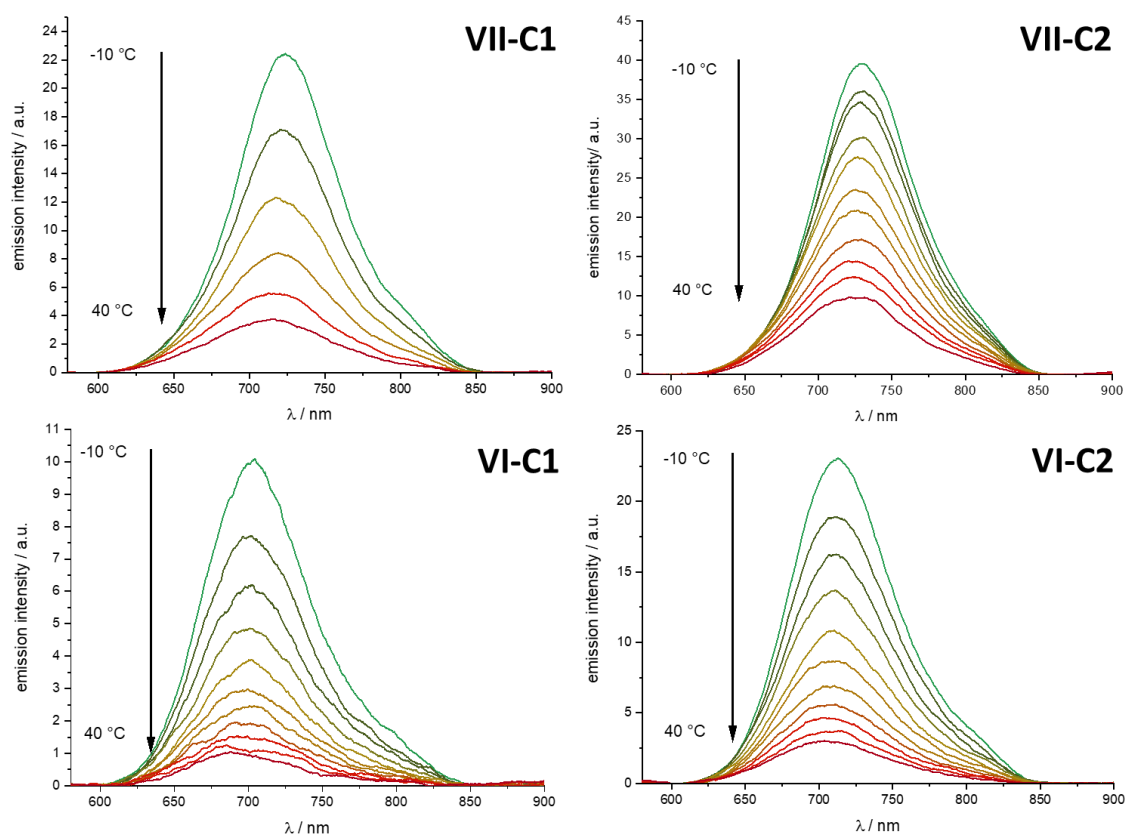


Figure VII-4. Emission spectra of the dinuclear complexes **VII-C1** and **VII-C2** as well as the mononuclear complexes **VI-C1** and **VI-C2** in inert gas-purged acetonitrile at different temperatures; temperatures vary between +40 °C and -10 °C.

Figure VII-5 shows the temperature-dependence of the emission quantum yield of the dinuclear and mononuclear complexes. The mononuclear complexes **VI-C1** and **VI-C2** exhibit an exponential dependency of the quantum yield on the temperature. Interestingly, in the analyzed temperature range, the relation between the quantum yield of the dinuclear complexes **VII-C1** and **VII-C2** and the temperature is almost linear. As described by Equation I-1, an exponential temperature-dependence of the emission is expected, and it is assumed that on a wider temperature range this behavior would also be observed for the dinuclear complexes. Overall, emission spectroscopy at different temperatures reveals that despite an expected stabilization of the emissive $^3\text{MLCT}$ state and with it an increased energy gap to the non-emissive ^3MC state, there is still an equilibrium between the $^3\text{MLCT}$ and the ^3MC state at room temperature, which results in luminescence quenching in both the mononuclear and dinuclear complexes.

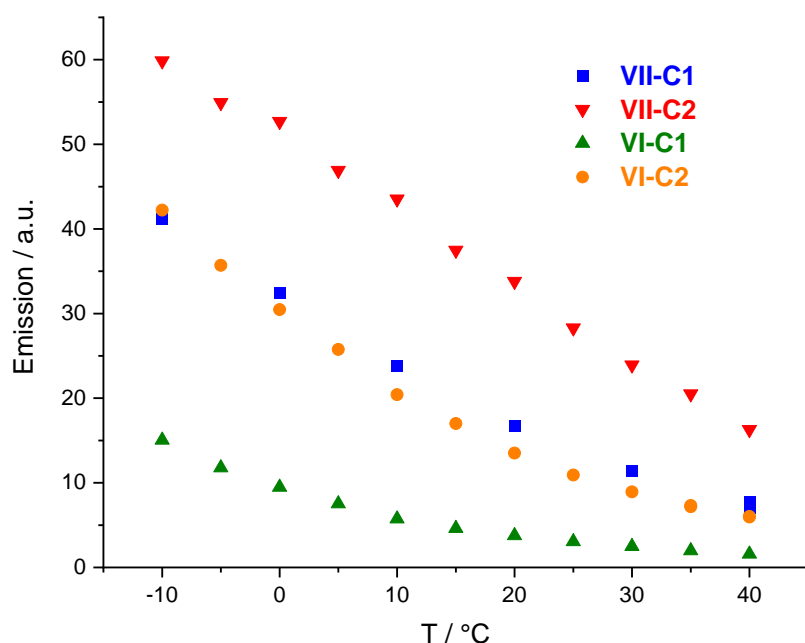


Figure VII-5. Temperature-dependence of the emission quantum yield of the dinuclear complexes **VII-C1** and **VII-C2** as well as the mononuclear complexes **VI-C1** and **VI-C2** in inert gas-purged acetonitrile.

For complex **VII-C1**, the excited-state lifetimes at different temperatures (243–298 K) are further investigated. The excited-state lifetime τ is increased from 94 ns at room temperature to 518 ns at -30 °C. The observed rate constant k_{obs} ($= 1/\tau$) is plotted against $1/T$ (Figure VII-6) and fitted using the simplified Arrhenius-type Equation I-1, shown again here:

$$k_{obs} = \frac{1}{\tau} = A \exp\left(-\frac{\Delta E_a}{RT}\right) + k'_0 \quad \text{Equation I-1}$$

with the preexponential factor A , gas constant R , temperature T and the term k'_0 , which accounts for the direct radiative and non-radiative decay from the excited state to the ground state at low temperature. ΔE_a represents the activation energy for the internal conversion between the $^3\text{MLCT}$ and the ^3MC state, i.e., it is related to the energy gap between the $^3\text{MLCT}$ and the ^3MC state.^[49] The value received from the fitted data of **VII-C1** yields an activation energy ΔE_a of 3080 cm^{-1} . As a comparison, the benchmark PS $[\text{Ru}(\text{bpy})_3]^{2+}$ exhibits an activation energy for the internal conversion

to the ^3MC state of 3560 cm^{-1} according to a study by Durham *et al.*^[71] A dinuclear terpyridine complex, analogous to **VII-C1** apart of the additional nitrogen atoms in the pyrimidine rings, previously investigated by Hammarström *et al.*, has an activation barrier of 2300 cm^{-1} .^[232] The larger ΔE_a value for $[\text{Ru}(\text{bpy})_3]^{2+}$ presumably stems from the stronger ligand field due to larger N-Ru-N *trans* angles in the complex, leading to a destabilization of the ^3MC state. The smaller ΔE_a value for the dinuclear terpyridine complex on the other hand underscores the $^3\text{MLCT}$ stabilizing effect of the pyrimidine ring in the herein discussed complex **VII-C1**.

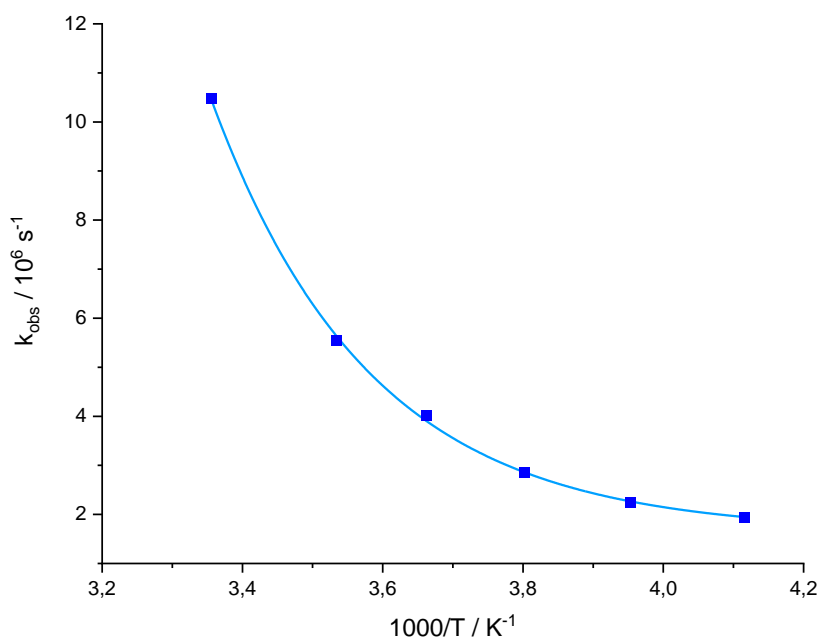


Figure VII-6. Plot of k_{obs} ($1/\tau$) vs. $1000/T$ for **VII-C1**. Curve fit according to Equation I-1 of the manuscript. Excited-state lifetimes are measured in nitrogen-purged acetonitrile solutions.

VII.2.3. Electrochemical Properties

Cyclic voltammetry of the dinuclear complexes **VII-C1** and **VII-C2** is carried out in acetonitrile solution and the results are presented in Figure VII-7 and Table VII-2. Due to solubility issues in the electrolyte, particularly for complex **VII-C1**, a lower sample concentration is chosen. The lower concentration as well as different experimental setups lead to different flow of current. Therefore, the scaling of the CV curves in Figure VII-7 is adjusted for clarity and the current flow is not to scale.

All complexes exhibit one reversible, metal-centered oxidation. In the dinuclear

complexes, the oxidation is a two-electron process as can be seen in square wave voltammetry (Figure VII-8). The presence of only one two-electron process means that both metal centers in the dinuclear complexes are oxidized simultaneously, indicating that there is no strong electronic coupling between the Ru(II) ions. Interestingly, the oxidation potentials are almost identical for the dinuclear and mononuclear complexes. If the oxidation potential is assumed to be related to the relative HOMO energy of the complexes the absence of a significant potential shift means that the HOMO is not or barely affected by the extended conjugated system or the addition of another metal coordination site in close proximity.

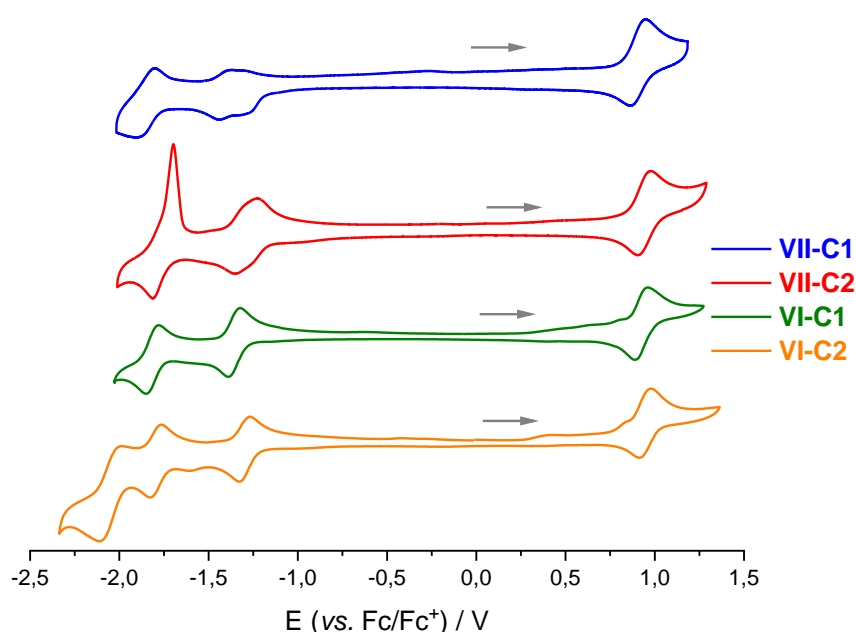


Figure VII-7. Cyclic voltammograms of complexes **VII-C1** (0.25 mM, blue), **VII-C2** (0.5 mM, red), **VI-C1** (1 mM, green) and **VI-C2** (1 mM, orange) in dry acetonitrile under inert gas atmosphere, with 0.1 M TBAPF₆; scan rate 100 mV/s; current flow is not to scale, altered for clarity; scans start at 0 V vs. reference in anodic direction.

The dinuclear complexes exhibit two very close lying LC reduction processes between -1.15 V and -1.45 V vs. Fc/Fc⁺, which are assumed to take place on the bridging pyrimidine ligand. There seems to be a certain degree of coupling between these reduction processes or adsorption and desorption processes on the glassy carbon disk WE taking place, which is particularly visible in the small peak separation of the first reduction process (4 meV) in **VII-C1**. In square wave voltammetry

experiments, the two first reduction processes are better resolved than in CV. Hence, the cathodic peak potentials, as determined by square wave voltammetry, are also given in Table VII-2. In the dinuclear complexes, a third reduction process is observed around -1.8 V. This reduction event is a two-electron event and likely taking place at the two tolyl-substituted terpyridine ligands. In complex **VII-C2**, the re-oxidation at -1.36 V appears as an unexpectedly sharp feature, which is presumably due to desorption from the glassy carbon WE.

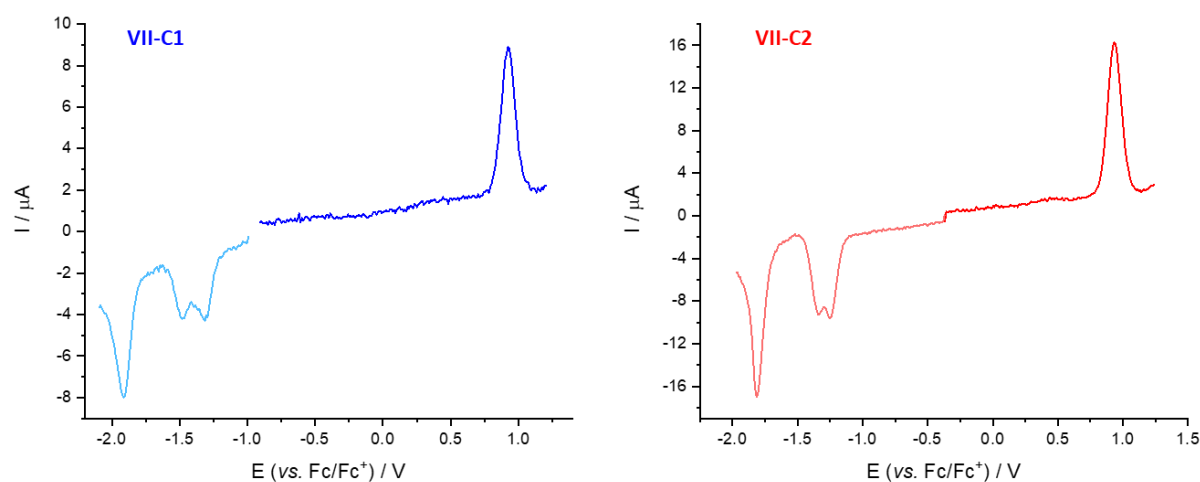


Figure VII-8. Square wave voltammetry of complex **VII-C1** (left) and **VII-C2** (right) in dry acetonitrile under inert gas atmosphere, with 0.1 M TBAPF₆; scan rate 100 mV/s; scans start at 0 V vs. reference electrode.

The first reduction potentials of the dinuclear complexes are anodically shifted compared to the mononuclear complexes, with a significantly stronger shift for complex **VII-C2**. It should be noted that the difference of the cathodic peak potentials in square wave voltammetry is smaller between the two complexes than when comparing the half-wave redox potentials.

The potential differences between the oxidation and first reduction of the complexes gives the same approximation for the HOMO-LUMO energy gap for **VII-C1** and **VI-C2** (2.26 V). The potential difference for **VII-C2** is smaller with 2.13 V.

Table VII-2. Electrochemical half-wave redox potentials $E_{1/2}$ in V vs. Fc/Fc⁺ (ΔE_p / mV) for dinuclear complexes **VII-C1** and **VII-C2** alongside mononuclear complexes **VI-C1** and **VI-C2** in nitrogen-purged acetonitrile.^a

	Oxidation	Reduction		
VII-C1	+0.94 (62)	-1.32 (4)	-1.42 (62)	-1.86 (112)
VII-C1^b	+0.92 ^b	-1.31 ^b	-1.48 ^b	-1.91 ^b
VII-C2	+0.95 (71)	-1.18 (94)	-1.32 (63)	-1.76 (108)
VII-C2	+0.93 ^b	-1.25 ^b	-1.34 ^b	-1.81 ^b
VI-C1	+0.92 (69)	-1.36 (67)	-1.81 (71)	
VI-C2	+0.96 (60)	-1.30 (58)	-1.80 (64)	-2.04 (123)

^aRedox potentials are reported vs. ferrocene (Fc/Fc⁺); the differences between the anodic and cathodic peak potentials ΔE_p are given in parentheses in millivolts; measurements in inert gas-purged acetonitrile solutions containing 0.1 M tetrabutylammonium hexafluorophosphate at a sweep rate of 100 mV/s; ^bcathodic peak potential as determined by square wave voltammetry.

VII.2.4. DFT Calculations

Theoretical calculations do not only give the optimized structures discussed above (Section VII.2.1) but also the HOMO and LUMO energies, which are shown in Figure VII-9. The calculations yield a stabilization of the HOMOs and LUMOs of the dinuclear complexes **VII-C1** and **VII-C2** compared to the mononuclear analogues. While in the previous chapters these calculations are found to match well with the electrochemical experiments, here, a discrepancy is observed. The stabilization of the LUMO does match the anodically shifted first reduction potential of **VII-C2**, but no adequately strong shift is observed for **VII-C1** to match the theoretical calculations. Furthermore, the stabilization of the HOMOs is not reflected in the CV experiments either. The HOMO-LUMO energy gaps for both dinuclear complexes are calculated to be significantly smaller than those of the mononuclear complexes. Again, the calculations do not match the experimental findings for **VII-C1**. Hence, it becomes clear that the applied model does not properly represent the dinuclear complexes. The observed discrepancy seems to be due to an over-planarization of the conjugated system in the ditopic ligand of **VII-C1**, which leads to an over-stabilization of the LUMO.

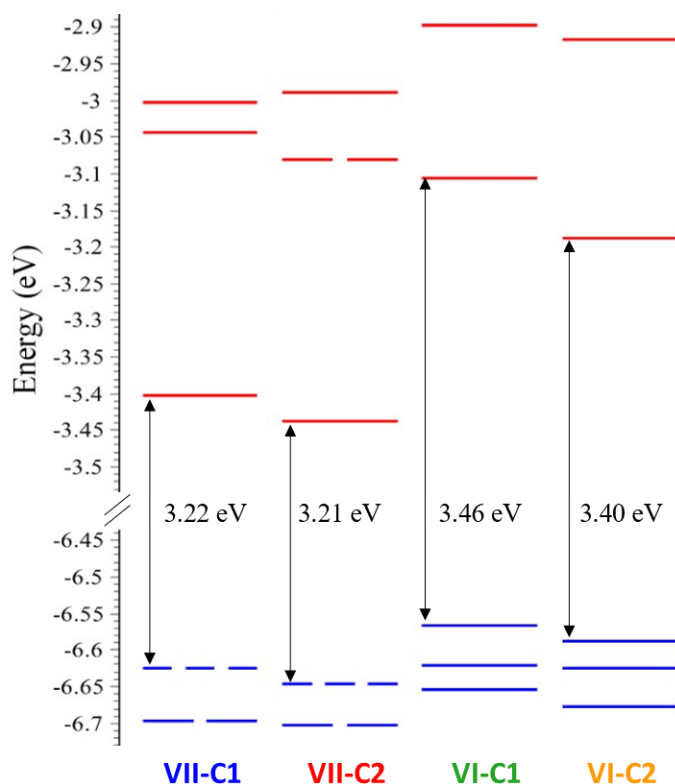


Figure VII-9. Energy diagram of the calculated frontier orbitals of dinuclear complexes **VII-C1** and **VII-C2** alongside the mononuclear analogues **VI-C1** and **VI-C2** with energy gaps highlighted (degeneracy threshold of 15 meV).

VII.2.5. Hydrogen Evolution Experiments

The photophysical and electrochemical experimental results are used to calculate the free Gibbs energy for the photoinduced electron transfer from the SED to the excited PS (Equation I-4 to Equation I-6). The results are summarized in Table VII-3. The estimated driving forces of the dinuclear complex **VII-C1** and its mononuclear analogue **VI-C1** are identical (+0.02 eV), while both **VII-C2** and **VI-C2** exhibit lower $\Delta G^{\circ}_{\text{ET}}$ values (-0.05 eV and -0.03 eV, respectively). The electron-transfer step to the catalyst is also expected to be similar with regards to thermodynamic considerations for both **VII-C1** and **VI-C1** as they exhibit similar potentials for the first reduction process ($E_{1/2} = -1.32$ and -1.36 V vs. Fc/Fc^+ , respectively). However, the anodically shifted reduction potential of **VII-C2** ($E_{1/2} = -1.18$ V vs. Fc/Fc^+) presumably leads to the electron transfer from the reduced complex to the catalyst being less thermodynamically favorable.

Table VII-3. Excited-state redox potentials and estimated free Gibbs energy ΔG^0_{ET} for photoinduced electron transfer from TEOA to the dinuclear complexes **VII-C1** and **VII-C2**, alongside the mononuclear analogues **VI-C1** and **VI-C2**.

	E_{ox}^* / V vs. Fc/Fc ⁺	E_{red}^* / V vs. Fc/Fc ⁺	$\Delta G^0_{ET} / eV$
VII-C1	-0.78	0.40	+0.02
VII-C2	-0.70	0.47	-0.05
VI-C1	-0.84	0.40	+0.02
VI-C2	-0.79	0.45	-0.03

Hydrogen evolution experiments are conducted with TEOA (1 M) as SED, HBF₄ (0.1 M) as proton source, [Co(dmgH)₂(H₂O)₂](BF₄)₂ as catalyst prepared *in-situ* from [Co(H₂O)₆](BF₄)₂ (1 mM) and dmgH₂ (6 mM) in DMF solution, with 0.1 mM of the respective complex as PS under blue (445 nm) and red light (630 nm) irradiation. The results are shown in Figure VII-10 and Figure VII-11 and are summarized in Table VII-4.

The maximum activity of the dinuclear complex **VII-C1** (TOF_{max} = 1518 mmol_{H₂} mol_{PS}⁻¹ min⁻¹) is increased by a factor of more than two compared to its mononuclear counterpart **VI-C1** (TOF_{max} = 650 mmol_{H₂} mol_{PS}⁻¹ min⁻¹). As the driving forces for both complexes are estimated to be very similar and the light harvesting efficiency at 445 nm is also in the same order of magnitude (LHE = 99% for **VII-C1** and 92% for **VI-C1**), it is assumed that either the superior emission properties of the dinuclear complex or kinetic aspects are responsible for the higher performance of **VII-C1**. The pyridine-substituted dinuclear complex **VII-C2** exhibits a lower hydrogen evolution activity (TOF_{max} = 496 mmol_{H₂} mol_{PS}⁻¹ min⁻¹) than both mononuclear complexes despite its increased quantum yield and excited-state lifetime. A possible explanation is the thermodynamically unfavorable electron transfer from the reduced PS to the catalyst.

Reaction mixtures using the dinuclear complexes as PS lose their hydrogen evolution activity within just a few hours with half-life times of 2.3 h for **VII-C1** and 1.8 h for **VII-C2**. While the mononuclear pyridine-substituted complex **VI-C2** exhibits a similar hydrogen evolution half-life time of 2.1 h, the catalytic system with complex **VI-C1** has a half-life time of 4.5 h. The prolonged activity leads to the overall amount of

hydrogen produced after 20 h for **VI-C1** ($254 \text{ mmol}_{\text{H}_2} \text{ mol}_{\text{PS}}^{-1}$) matching that of the previously more active **VII-C1** ($\text{TON}(20 \text{ h}) = 253 \text{ mmol}_{\text{H}_2} \text{ mol}_{\text{PS}}^{-1}$).

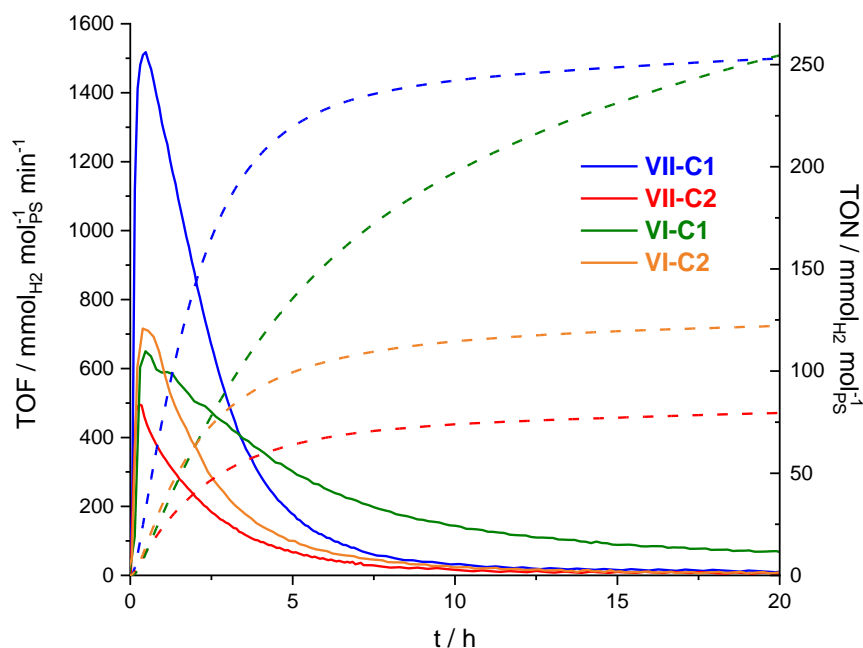


Figure VII-10. Hydrogen photoproduction with dinuclear complexes **VII-C1**, **VII-C2**, **VI-C1** and **VI-C2** as PS (0.1 mM) under blue light irradiation (LED centered at 445 nm); with $[\text{Co}(\text{H}_2\text{O})_6](\text{BF}_4)_2$ as pre-catalyst (1 mM), with dmgH_2 (6 mM), TEOA as sacrificial electron donor (1 M) and HBF_4 as proton source (0.1 M) in DMF; TOF: solid lines; TON: dashed lines.

When the reaction mixtures are irradiated with red light, the hydrogen evolution activity of all complexes is reduced. This decrease of TOF_{max} is expected as the PSs absorb less photons at 630 nm. The LHE of the dinuclear complexes **VII-C1** and **VII-C2** is decreased to 45% and 50%, respectively. The mononuclear complexes **VI-C1** and **VI-C2** exhibit a LHE of 14% and 28%, respectively. Despite the larger LHE of complexes **VII-C1** and **VII-C2**, the ratio of the activity of the dinuclear complexes **VII-C1** or **VII-C2** under blue and red light irradiation is much larger than for **VI-C2**. This stronger decrease upon switching the light source leads to comparable TOF_{max} of **VI-C2** ($\text{TOF}_{\text{max}} = 182 \text{ mmol}_{\text{H}_2} \text{ mol}_{\text{PS}}^{-1} \text{ min}^{-1}$) and **VII-C1** ($\text{TOF}_{\text{max}} = 243 \text{ mmol}_{\text{H}_2} \text{ mol}_{\text{PS}}^{-1} \text{ min}^{-1}$).

While the mononuclear complexes **VI-C1** and **VI-C2** exhibit longer hydrogen evolution half-life times under red light irradiation (14 h and 4.6 h, respectively) compared to blue light irradiation, the half-life times of the dinuclear complexes remain

similar to the experiments conducted under blue light around 2 hours. Hence, the mononuclear complexes outperform the dinuclear complexes by far, producing more overall hydrogen after only 4–8 hours.

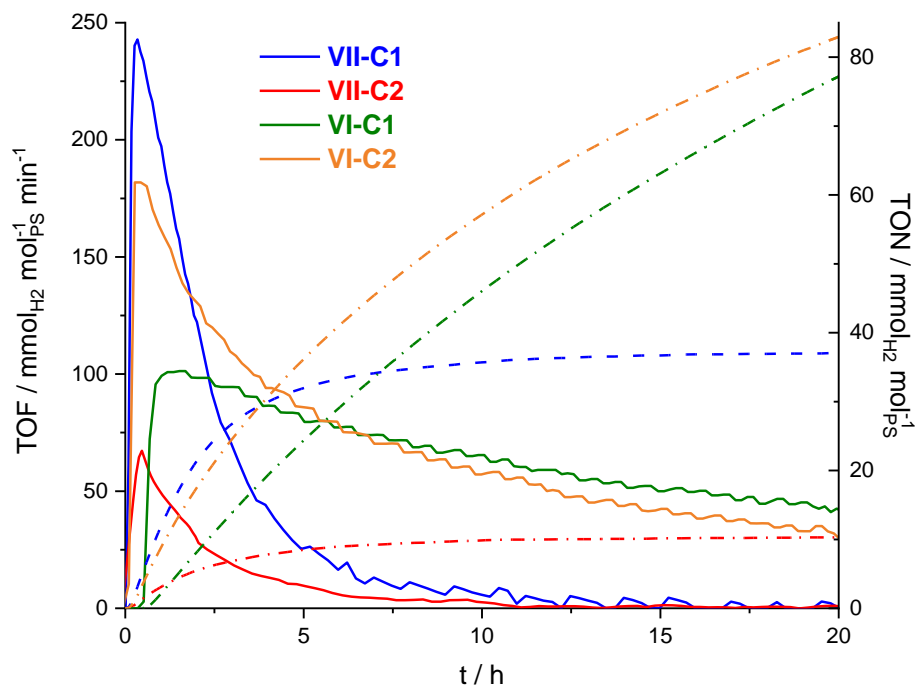


Figure VII-11. Hydrogen photoproduction with dinuclear complexes **VII-C1**, **VII-C2**, **VI-C1** and **VI-C2** as PS (0.1 mM) under red light irradiation (LED centered at 630 nm); with $[\text{Co}(\text{H}_2\text{O})_6](\text{BF}_4)_2$ as pre-catalyst (1 mM), with dmgH_2 (6 mM), TEOA as sacrificial electron donor (1 M) and HBF_4 as proton source (0.1 M) in DMF; TOF: solid lines; TON: dashed lines.

Addition of PS or catalyst to the catalytic reaction mixture after the hydrogen evolution has ceased is carried out for the catalytic system with **VII-C1**. Only when PS is added, the hydrogen evolution activity is partly restored, hence confirming that it is the PS that is rendered inactive under the catalytic conditions. UV-vis absorption spectra of the reaction mixtures with **VII-C1**, **VII-C2** and **VI-C1** before and after hydrogen evolution are shown in Figure VII-12. The MLCT absorption band of the complexes changes significantly during the photocatalytic experiment. The absorption of the dinuclear complexes is blue-shifted while that of the mononuclear complex **VI-C1** is red-shifted, resulting in relatively similar absorption profiles for all three complexes.

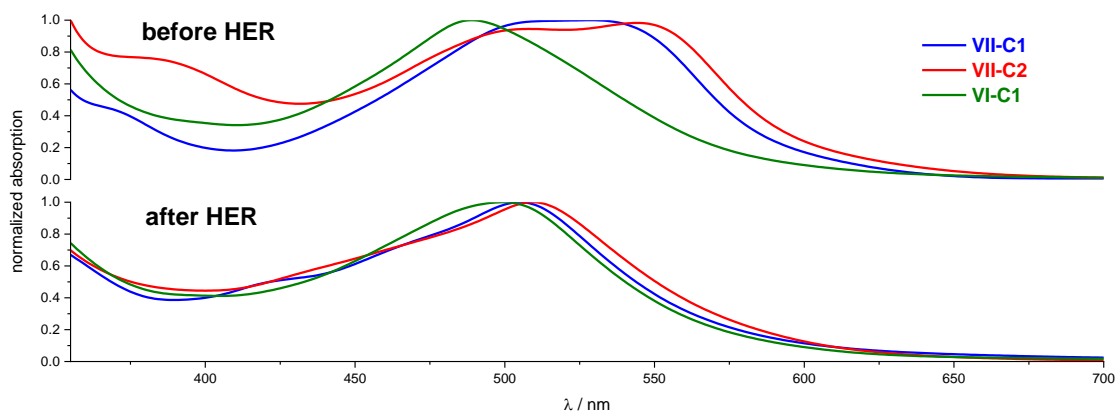


Figure VII-12. UV-vis absorption spectra of DMF solutions containing **VII-C1**, **VII-C2** or **VI-C1** (0.1 mM); $[\text{Co}(\text{H}_2\text{O})_6](\text{BF}_4)_2$ (1 mM), dmgH_2 (6 mM), TEOA (1 M) and HBF_4 (0.1 M) before (upper graph) and after (lower graph) 23 h under blue light irradiation (LED centered at 445 nm); absorptions are normalized to the MLCT absorption peak.

No changes in the absorption profile of **VII-C1** are observed upon light irradiation of a DMF solution with no other reagents present, ruling out a simple photodecomposition of the PS. However, a reaction mixture with **VII-C1** and only TEOA and HBF_4 present without any catalyst, which does not produce any hydrogen, exhibits an absorption profile after light irradiation identical to that of reaction mixtures, which do contain catalyst. This observation shows that the catalyst is not involved in the deactivation of the PS, while the presence of the SED and/or the proton source is required. The blue shift of the MLCT absorption band for the dinuclear complexes could indicate a decrease in delocalization, e.g., because of hydrogenation of the ligand. However, a detailed analysis of the reaction mixtures and the inactive form of the PSs could not be performed.

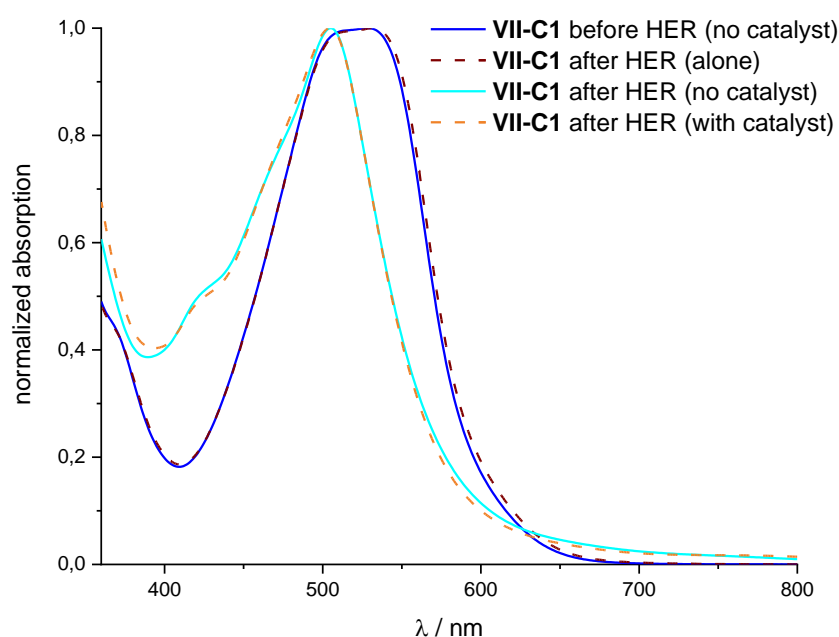


Figure VII-13. UV-vis absorption spectra of DMF solutions containing **VII-C1** (0.1 mM) (a) after 18 h blue light irradiation (LED centered at 445 nm) (dark red dashed line) alongside spectra of reaction mixtures additionally containing (b) TEOA (1 M) and HBF₄ (0.1 M) before light irradiation (dark blue solid line); (c) TEOA (1 M) and HBF₄ (0.1 M) after light irradiation (light blue solid line); (d) [Co(H₂O)₆](BF₄)₂ (1 mM), dmgH₂ (6 mM), TEOA (1 M) and HBF₄ (0.1 M) after light irradiation (orange dashed line); absorptions are normalized to the MLCT absorption peak.

Similar to the experiments on **VI-C1** or **III-C1** with different catalysts discussed in the previous Chapters III to VI, the dinuclear complexes are used as PS with chloro(pyridine)bis(dimethylglyoximate)cobalt(III) [Co(dmgH₂(py)Cl)] as the catalyst. This Co(III) catalyst is widely used in photocatalytic hydrogen evolution studies and hence allows for easy comparison of the performance as PS.^[74-75, 233] Its Co^{II}/Co^I reduction potential is identical to that of the *in-situ* prepared Co(II) catalyst [Co(dmgH)₂(H₂O)₂](BF₄)₂ (-1.43 V vs. Fc/Fc⁺) and the Co(III) complex can be prepared following a procedure by Lentz *et al.*^[234] The results with this Co(III) catalyst are shown in Figure VII-14. The maximum TOF is increased by more than 50% for both **VII-C1** and **VII-C2** compared to experiments with the *in-situ* prepared Co(II) catalyst, even though the efficiency of electron transfer to the different catalysts is expected to be the same from a thermodynamic point of view. The superior PS performance of **VII-C1** in the system with both catalysts indicates that the reduction potential of the PS and with

it the driving force for the electron transfer from the reduced PS to the catalyst impact the hydrogen evolution activity. However, it also becomes clear that the hydrogen evolution activity is not solely governed by thermodynamics of the electron transfer step to the catalyst and that other parameters influence the observed overall performance of the catalytic system.

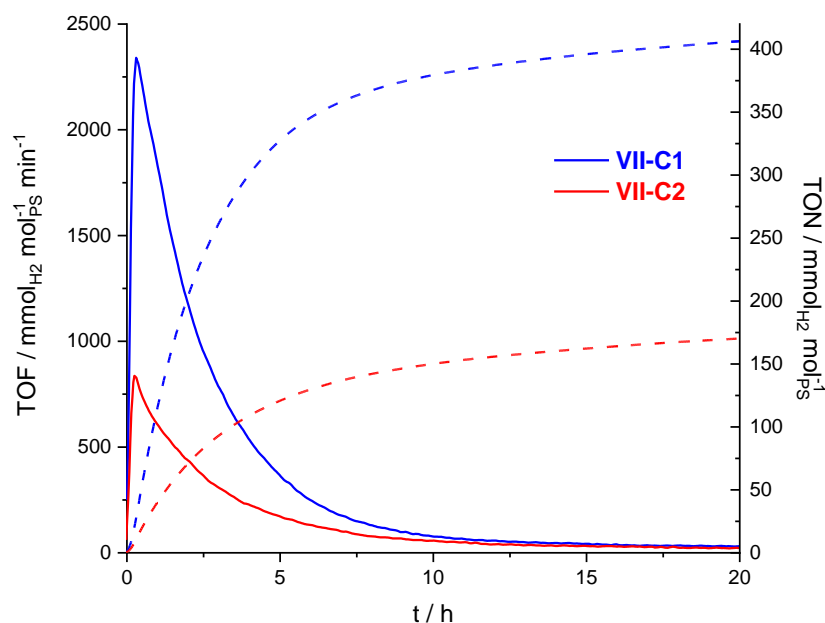


Figure VII-14. Hydrogen photoproduction with dinuclear complexes **VII-C1** and **VII-C2** as PS (0.1 mM) under blue light irradiation (LED centered at 445 nm); using [Co(dmgh)₂(py)Cl] as catalyst (1 mM), dmgh₂ (6 mM), TEOA as sacrificial electron donor (1 M) and HBF₄ as proton source (0.1 M) in DMF; TOF: solid lines; TON: dashed lines.

The photocatalytic system with **VII-C1** is further investigated by varying the PS concentration between 0.1 mM and 0.01 mM. Figure VII-15 shows that the maximum rate of hydrogen evolution does not change for concentrations as low as 0.03 mM when **VII-C1** is used as PS. At a concentration of 0.03 mM, the estimated LHE of the reaction mixture is decreased to 78% with no significant effect on the hydrogen production rate. Only at even lower concentrations of 0.01 mM, yielding a LHE of 40%, a decrease in hydrogen production can be observed. Due to the strong absorptivity of **VII-C1**, changing the concentration does not immediately affect the LHE and with it the amount of excited PS available for reductive quenching. Hence, the hydrogen production rate does only change if the concentration of **VII-C1** and with it the LHE is

lowered significantly. However, the observed maximum hydrogen production rate for a concentration of 0.01 mM **VII-C1** (max H₂ rate = 305 nmol min⁻¹) is still significantly larger than that under red light (max H₂ rate = 125 nmol min⁻¹) despite the similar LHE (40–45%). This discrepancy between the experiments indicates that the LHE, and with it the amount of excited PS, is not the key factor determining the hydrogen evolution activity in these systems. In contrast, when the benchmark PS [Ru(bpy)₃]²⁺ is used, the maximum rate of hydrogen produced decreases for lower PS concentrations. The maximum hydrogen evolution rate is found to linearly depend on the LHE in the investigated concentration range. As a lower LHE corresponds to a decreased amount of excited PS available to drive hydrogen evolution catalysis, these experiments indicate that in a system with [Ru(bpy)₃]²⁺ the excited PS is involved in the rate-limiting step.

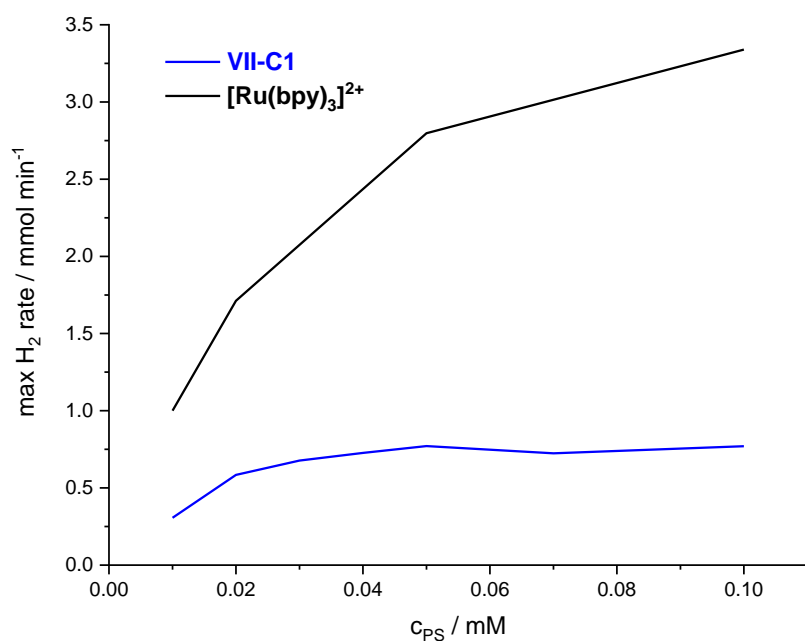


Figure VII-15. Maximum hydrogen production rate of dinuclear complex **VII-C1** (blue) in comparison with [Ru(bpy)₃]²⁺ (black) for different concentrations of PS in a DMF solution with [Co(H₂O)₆](BF₄)₂ as pre-catalyst (1 mM), dmgH₂ (6 mM), TEOA as sacrificial electron donor (1 M) and HBF₄ as proton source (0.1 M) under blue light irradiation (LED centered at 445 nm).

Table VII-4. Hydrogen production results of complexes discussed in this chapter.^a

PS	catalyst	λ_{exc} / nm	duration / h	TOF _{max} / mmol _{H2} mol _{PS} ⁻¹ min ⁻¹	TON / mmol _{H2} mol _{PS} ⁻¹
VII-C1	[Co(dmgh) ₂ (H ₂ O) ₂](BF ₄) ₂ ^b	445	20	1518	253
VII-C1	[Co(dmgh) ₂ (H ₂ O) ₂](BF ₄) ₂ ^b	630	20	243	37
VII-C1	[Co(dmgh) ₂ (py)Cl]	445	20	2340	406
VII-C1	none	445	20	not detected	not detected
VII-C2	[Co(dmgh) ₂ (H ₂ O) ₂](BF ₄) ₂ ^b	445	20	496	80
VII-C2	[Co(dmgh) ₂ (H ₂ O) ₂](BF ₄) ₂ ^b	630	20	66	10
VII-C2	[Co(dmgh) ₂ (py)Cl]	445	20	835	170
VI-C1	[Co(dmgh) ₂ (H ₂ O) ₂](BF ₄) ₂ ^b	445	20	650	254
VI-C1	[Co(dmgh) ₂ (H ₂ O) ₂](BF ₄) ₂ ^b	630	20	101	77
VI-C2	[Co(dmgh) ₂ (H ₂ O) ₂](BF ₄) ₂ ^b	445	20	715	122
VI-C2	[Co(dmgh) ₂ (H ₂ O) ₂](BF ₄) ₂ ^b	630	20	182	83
[Ru(bpy) ₃] ^{2+c}	[Co(dmgh) ₂ (H ₂ O) ₂](BF ₄) ₂ ^b	445	9.5	6850	750
[Ru(bpy) ₃] ^{2+c}	[Co(dmgh) ₂ (H ₂ O) ₂](BF ₄) ₂ ^b	630	20	30	30

^aunless otherwise stated, all experiments are carried out using 0.1 mM PS, 1 M TEOA as SED, 0.1 M HBF₄ as proton source and 1 mM catalyst with 6 mM dmgh₂ in DMF, irradiation with blue light (LED centered at 445 nm, 62 mW), reported values are averages of multiple runs; ^bprepared *in-situ* from [Co(H₂O)₆](BF₄)₂ and dmgh; ^cdata taken from Rupp *et al.*^[162] and Rousset *et al.*^[176].

VII.3. Conclusion

In this chapter, the synthesis of two dinuclear complexes, using a ditopic pyrimidine-containing ligand with a phenyl spacer, are synthesized analogously to the mononuclear complexes described in Chapter VI. While no crystal structures of the dinuclear species could be obtained, DFT structure optimizations suggest the presence of a certain degree of hydrogen bonding between the pyrimidine rings and the phenyl spacer, leading to a more planar ligand structure.

The presence of two chromophoric sites leads to a higher absorptivity. Furthermore, the MLCT absorption band is broadened due to two shoulders,

presumably as a result from different MLCT transitions involving either the bridging ligand or the peripheral terpyridine ligands. The emission of the dinuclear complexes is red-shifted compared to the mononuclear analogues, especially for the pyridine-substituted complex **VII-C2**. The excited-state lifetimes and luminescence quantum yields of the dinuclear complexes are furthermore increased in comparison to the mononuclear complexes. This observation can be explained by the larger conjugated system, which stabilizes the emissive $^3\text{MLCT}$ state and hence leads to an increased energy gap to the non-emissive ^3MC state. However, emission spectroscopy at different temperatures reveals a temperature-dependent luminescence behavior for all complexes, underscoring that at room temperature there is an equilibrium between the $^3\text{MLCT}$ and the ^3MC state for both the mononuclear and the dinuclear complexes discussed in this chapter.

Electrochemical experiments reveal one two-electron oxidation process for the dinuclear complexes, showing that there is no strong electronic coupling between the two metal centers. The dinuclear complexes furthermore show two very close-lying one-electron reduction processes, which are assigned to the bridging ligand, followed by one two-electron reduction process, corresponding to a simultaneous reduction of the two peripheral terpyridine ligands.

An estimation of the driving forces for the photoinduced electron transfer from the SED to the excited PS reveal very similar free Gibbs energy values for the dinuclear complexes their mononuclear analogues. However, the anodically shifted first reduction potential of **VII-C2** presumably makes the electron transfer from the reduced PS to the catalyst thermodynamically more challenging.

In hydrogen evolution experiments, the dinuclear pyridine-substituted complex **VII-C2** is indeed the least active as PS. The unsubstituted dinuclear complex **VII-C1** on the other hand shows an increased activity compared to the mononuclear ones. However, the longevity of the dinuclear complexes is further reduced, leading to less overall hydrogen production. Under red light irradiation, the activity of the dinuclear complexes is reduced greatly despite the high remaining LHE around 50%. Experiments using **VII-C1** in different concentrations show that the hydrogen evolution activity does only decrease for PS concentrations leading to a significantly lower LHE. Overall, the hydrogen evolution experiments show that the overall catalytic activity

does depend on the PS. However, improved photophysical properties, i.e., longer excited-state lifetimes and higher quantum yields, only result in an increase of activity when compared to other PSs, which exhibit similar driving forces for the electron transfer steps to and from the PS. Nonetheless, the overall activity of the catalytic systems with pyrimidine-containing ligands also depends on the catalyst used. Furthermore, it is also apparent that the activity of the system is not solely governed by thermodynamic considerations and that other aspects, e.g., the efficiency and kinetics of electron transfer, influence the overall hydrogen evolution performance of the catalytic system.

VII.4. Experimental

Details on instrumentation and DFT calculations as well as NMR spectra with peak assignments, natural transition analysis, and contributions to HOMOs and LUMOs can be found in the Appendix (Chapter IX). References are given for known compounds. The properties of the known compounds agree with the ones published.

3,3'-(1,4-phenylene)bis(1-(pyridin-2-yl)prop-2-en-1-one) **VII-I1**^[235]

A solution of 2-acetylpyridine (463 μ L, 500 mg, 4.13 mmol, 2.1 eq), terephthalaldehyde (264 mg, 1.97 mmol, 1 eq) and potassium hydroxide (276 mg, 4.91 mmol, 2.5 eq) in 20.0 mL methanol was stirred at room temperature over night. The precipitate was filtered off and washed with methanol to yield the product as a yellow solid (564 mg, 1.66 mmol, 84%). The product was used without further purification.

¹H-NMR (400 MHz, CDCl₃) δ = 8.76 (ddd, ³J = 4.7 Hz, ⁴J = 1.7 Hz, ⁵J = 0.9 Hz, 2H), 8.36 (d, ³J = 16.0 Hz, 2H), 8.20 (m, 1H), 7.90 (m, 4H), 7.77 (s, 4H) and 7.51 ppm (ddd, ³J = 7.6 Hz, ³J = 4.7 Hz, ⁴J = 1.3 Hz, 2H).

3,3'-(1,4-phenylene)bis(1-([4,4'-bipyridin]-2-yl)prop-2-en-1-one) **VII-I2**

A solution of 2-acetyl-4,4'-bipyridine **III-I1** (250 mg, 1.26 mmol, 2.2 eq), terephthalaldehyde (76.9 mg, 573 μ mol, 1 eq) and potassium hydroxide (70.8 mg, 1.26 mmol, 2.2 eq) in 5.00 mL methanol was stirred at room temperature for two days.

Water was added and the precipitate was filtered off and washed with water to yield the product as a brown solid (217 mg, 439 μmol , 77%). The product was used without further purification.

$^1\text{H-NMR}$ (500 MHz, CDCl_3) δ = 8.88 (d, 3J = 5.0 Hz, 2H), 8.80 (d, 3J = 6.0 Hz, 4H), 8.47 (s, 2H), 8.41 (d, 3J = 16.0 Hz, 4H), 8.00 (d, 3J = 16.0 Hz, 4H), 7.82 (s, 4H), 7.76 (dd, 3J = 5.0 Hz, 4J = 1.8 Hz, 2H) and 7.64 ppm (d, 3J = 6.0 Hz, 4H). ESI-MS: m/z $[\text{M}+\text{H}]^+$ calc. for $\text{C}_{32}\text{H}_{22}\text{N}_4\text{O}_2$: 495.18155; found: 495.18252; difference: 1.96 ppm.

1,4-bis(2,6-di(pyridin-2-yl)pyrimidin-4-yl)benzene VII-L1^[225]

A suspension of **VII-I1** (300 mg, 881 μmol , 1 eq), and 2-pyridinecarboxamidine hydrochloride **VI-I5** (278 mg, 1.76 mmol, 2 eq) and potassium hydroxide (124 mg, 2.20 mmol, 2.5 eq), in 40.0 mL ethanol was heated to reflux for four days. After cooling to room temperature, water was added and the precipitate was filtered off over celite, washed with water and was dissolved in dichloromethane. The organic solution was dried over magnesium sulfate and the solvent was removed under vacuum. The crude product was washed with hot methanol to yield the product as an off-white solid (72.0 mg, 133 μmol , 15%).

$^1\text{H-NMR}$ (300 MHz, CDCl_3): δ = 8.94 (m, 4H), 8.81 (m, 6H), 8.58 (s, 4H), 7.95 (m, 4H) and 7.48 ppm (m, 4H). $^{13}\text{C}\{^1\text{H}\}\text{-NMR}$ (75 MHz, CDCl_3): δ = 165.2, 164.7, 164.0, 155.6, 154.3, 150.3, 149.6, 139.6, 137.4, 137.1, 128.3, 125.7, 125.0, 124.4, 122.7 and 112.5 ppm. ESI-MS: m/z $[\text{M}+\text{H}]^+$ calc. for $\text{C}_{34}\text{H}_{22}\text{N}_8$: 543.20402; found: 543.20493; difference: 1.7 ppm.

1,4-bis(6-([4,4'-bipyridin]-2-yl)-2-(pyridin-2-yl)pyrimidin-4-yl)benzene VII-L2

A suspension of **VII-I2** (190 mg, 384 μmol , 1 eq), and 2-pyridinecarboxamidine hydrochloride **VI-I5** (132 mg, 838 μmol , 2.2 eq) and potassium hydroxide (64.7 mg, 1.15 mmol, 3 eq), in 20.0 mL ethanol was heated to reflux for four days. After cooling to room temperature, water was added and the precipitate was separated and washed with water and methanol using a centrifuge to yield the product as a brown solid (80.0 mg, 115 μmol , 30%).

$^1\text{H-NMR}$ (300 MHz, CDCl_3): δ = 9.03 (s, 4H), 8.99 (s, 4H), 8.93 (m, 6H), 8.80 (d, 3J = 5.8 Hz, 4H), 8.76 (d, 3J = 7.3 Hz, 2H), 8.60 (s, 4H), 7.97 (td, 3J = 7.8 Hz,

$^4J = 1.4$ Hz, 2H), 7.71 (m, 6H) and 7.49 ppm (dd, $^3J = 7.4$ Hz, $^4J = 4.8$ Hz, 2H). $^{13}\text{C}\{^1\text{H}\}$ -NMR (75 MHz, CDCl_3): $\delta = 165.2, 164.3, 164.1, 155.4, 150.9, 150.5, 150.3, 147.2, 145.5, 139.5, 137.2, 128.3, 125.1, 124.4, 123.3, 121.8, 121.4, 120.3$ and 112.8 ppm. ESI-MS: m/z $[\text{M}+\text{H}]^+$ calc. for $\text{C}_{44}\text{H}_{28}\text{N}_{10}$: 697.25712; found: 697.25607; difference: 1.5 ppm.

[{Ru(Tolyltpy)}₂(VII-L1)] VII-C1

A suspension of $[\text{RuCl}_3(\text{Tolyltpy})]$ **III-I3** (147 mg, 276 μmol , 2 eq), **VII-L1** (75.0 mg, 138 μmol , 1 eq) and four drops of *N*-ethylmorpholine in 5.00 mL ethylene glycol was heated to 180 °C for 15 minutes using microwave irradiation. After cooling to room temperature, water and aqueous KPF_6 solution were added to the solution and the precipitate was filtered off over celite. After washing with water, it was dissolved in acetonitrile, dried over magnesium sulfate and the solvent was removed under reduced pressure. The product was purified by column chromatography (silica gel, MeCN:aqu. KNO_3 7:1) to yield a dark red solid (108 mg, 54.8 μmol , 40%).

^1H -NMR (700 MHz, CD_3CN): $\delta = 9.43$ (s, 2H), 9.11 (s, 4H), 9.07 (m, 6H), 8.98 (d, $^3J = 8.0$ Hz, 2H), 8.70 (d, $^3J = 8.1$ Hz, 4H), 8.15 (d, $^3J = 7.8$ Hz, 4H), 8.11 (m, 4H), 7.98 (m, 4H), 7.64 (d, $^3J = 5.2$ Hz, 2H), 7.61 (d, $^3J = 7.6$ Hz, 4H), 7.58 (d, $^3J = 5.5$ Hz, 2H), 7.49 (d, $^3J = 5.6$ Hz, 4H), 7.37 (m, 4H), 7.19 (m, 4H) and 2.56 ppm (s, 6H). $^{13}\text{C}\{^1\text{H}\}$ -NMR (176 MHz, CD_3CN): $\delta = 164.56, 163.33, 162.12, 159.14, 157.49, 157.06, 156.20, 154.30, 154.06, 153.74, 149.91, 142.14, 140.12, 139.47, 139.25, 139.22, 134.71, 131.25, 130.01, 129.94, 129.89, 128.62, 128.34, 127.53, 127.34, 125.54, 122.40, 115.27$ and 21.36 ppm. ESI-MS: m/z $[\text{M}]^{4+}$ calc. for $\text{C}_{78}\text{H}_{56}\text{N}_{14}\text{Ru}_2$: 348.07194; found: 348.07353; difference: 4.6 ppm. Anal. calc. for $\text{C}_{78}\text{H}_{56}\text{F}_{18}\text{N}_{15}\text{O}_3\text{P}_3\text{Ru}_2 \cdot 2\text{H}_2\text{O}$: C, 48.68; H, 3.14; N, 10.92. Found: C, 48.72; H, 3.18; N, 10.73.

[{Ru(Tolyltpy)}₂(VII-L2)] VII-C2

A suspension of $[\text{RuCl}_3(\text{Tolyltpy})]$ **III-I3** (147 mg, 276 μmol , 2 eq), **VII-L2** (50.0 mg, 71.8 μmol , 1 eq) and silver nitrate (73.1 mg, 431 μmol , 6 eq) in 15.0 mL ethylene glycol was heated to 150 °C for 165 minutes. After cooling to room temperature, water and aqueous KPF_6 solution were added to the solution and the precipitate was filtered off over celite. After washing with water, it was dissolved in

acetonitrile, dried over magnesium sulfate and the solvent was removed under reduced pressure. The product was purified by column chromatography (silica gel, MeCN:aqu. KNO₃ 7:2) to yield a dark red solid (20.8 mg, 9.79 μmol, 14%).

¹H-NMR (400 MHz, CD₃CN): δ = 9.56 (s, 2H), 9.26 (s, 4H), 9.17 (s, 4H), 9.10 (m, 6H), 8.82 (d, ³J = 4.7 Hz, 4H), 8.71 (d, ³J = 7.9 Hz, 4H), 8.15 (m, 6H), 8.00 (t, ³J = 7.6 Hz, 4H), 7.81 (d, ³J = 5.1 Hz, 4H), 7.77 (d, ³J = 6.1 Hz, 2H), 7.64 (m, 8H), 7.53 (d, ³J = 5.2 Hz, 4H), 7.40 (t, ³J = 6.5 Hz, 2H), 7.22 (t, ³J = 6.3 Hz, 4H) and 2.57 ppm (s, 6H). ¹³C{¹H}-NMR (100 MHz, CD₃CN): δ = 164.7, 163.4, 162.3, 159.2, 158.4, 157.1, 156.2, 154.7, 154.1, 153.9, 151.9, 151.8, 150.1, 148.3, 143.4, 142.2, 140.2, 139.6, 139.4, 134.8, 131.3, 130.1, 130.0, 128.7, 128.4, 127.4, 127.2, 125.6, 125.5, 122.5, 115.7 and 21.4 ppm. ESI-MS: m/z [M+PF₆]³⁺ calc. for C₈₈H₆₂F₆N₁₆PRu₂: 563.77005; found: 563.77019; difference: 0.25 ppm. Anal. calc. for C₈₈H₆₂F₂₄N₁₆P₄Ru₂·3H₂O: C, 48.49; H, 3.14; N, 10.28. Found: C, 48.50; H, 3.48; N, 9.92.

VIII. Conclusion

Typical molecular systems used for artificial photosynthesis, i.e., the conversion of sun light into chemical energy, consist of three main components: A catalyst, a sacrificial electron acceptor or donor and a photosensitizer. In order for a compound to be capable to act as an efficient PS it needs to exhibit a strong absorption, preferably covering wide regions of the solar spectrum, a high luminescence quantum yield, a long excited-state lifetime, and reversible redox behaviour, with suitable ground-state and excited-state potentials with regard to the catalyst and SED or SEA. While Ru(II) tris-bipyridine $[\text{Ru}(\text{bpy})_3]^{2+}$ and its analogues are typically used as benchmark PSs, the terpyridine analogues $[\text{Ru}(\text{tpy})_2]^{2+}$ have been mostly disregarded for the application as PS in photocatalytic water splitting due to their poor photophysical properties. Despite numerous studies investigating multiple strategies, e.g., substitution with electron-withdrawing or donating groups, to enhance the photophysical properties of Ru(II) complexes with tridentate metal ion receptors, particularly terpyridine ligands, little work has been put into employing these complexes as PSs in photosynthetic hydrogen evolution. Hence, this thesis focusses on how ligand design of tridentate metal ion receptors affects not only the photophysical and electrochemical properties of the corresponding Ru(II) complexes but also their performance as PS in photocatalytic hydrogen evolution experiments. The following strategies are investigated for their impact on the properties of Ru(II) complexes: Electron-withdrawing and donating substituents, heteroleptic vs. homoleptic design, the implementation of different heterocycles, and multiple metal centers. The complexes are investigated regarding the photophysical and electrochemical properties, which are used to estimate the thermodynamic driving forces for the electron transfer processes during photocatalysis. Furthermore, the complexes are employed as PSs in photocatalytic hydrogen evolution experiments under different conditions.

Electron-withdrawing pyridine substituents on the terpyridine metal ion receptor result in a stabilization of the $^3\text{MLCT}$ state and hence an increase of excited-state lifetime and quantum yield ($\Phi = 74 \cdot 10^{-5}$; $\tau = 3.8 \text{ ns}$). This increase in luminescence leads to complex **III-C1** exhibiting activity as PS, being the first example in the literature of Ru(II) bis-terpyridine complexes used for homogeneous photocatalytic hydrogen evolution. While the maximum activity ($\text{TOF}_{\text{max}} = 57 \text{ mmol}_{\text{H}_2} \text{ mol}_{\text{PS}}^{-1} \text{ min}^{-1}$;

TON(44 h) = 134 mmol_{H₂} mol_{PS}⁻¹) is relatively low, the catalytic system is long-lived, losing only 20% of its activity over the course of 12 days (see Chapter III). Interestingly, the heteroleptic design in complex **III-C1** proves to be beneficial for the performance as PS, despite having comparable photophysical and electrochemical properties to the homoleptic complex **IV-C2** (TOF_{max} = 35 mmol_{H₂} mol_{PS}⁻¹ min⁻¹; TON(24 h) = 14 mmol_{H₂} mol_{PS}⁻¹) (see Chapter IV). While the heteroleptic design improves the efficiency of the electron transfer and with it the activity as PS, reductive quenching of the excited PS by the SED is identified as rate-limiting step in both the homoleptic and heteroleptic complex.

Hence, the ligands are designed to be more electron-accepting either *via N*-methylation of the peripheral pyridine substituents (see Chapter V) or introduction of a pyrimidine ring in the metal ion receptor (see Chapter VI). These changes further stabilize the ³MLCT state and lead to increased excited-state lifetimes ($\tau = 9\text{--}40$ ns) and luminescence quantum yields ($\Phi = 40\text{--}400 \times 10^{-5}$). However, the more electron-accepting character of the ligands also results in anodically shifted reduction potentials and with that a decreased driving force for the electron transfer from the reduced PS to the catalyst. Therefore, this electron transfer step is found to be a limiting factor to the overall performance of the PS. While higher TOF_{max} in hydrogen evolution experiments are observed for pyrimidine-containing PSs (TOF_{max} = 300–715 mmol_{H₂} mol_{PS}⁻¹ min⁻¹), the longevity for these systems is reduced with half-life times of 2–6 h.

Expansion of the pyrimidine-containing ligands to form dinuclear complexes(Chapter VII) yields a stronger absorptivity ($\epsilon = 100\text{--}135 \times 10^3$ L mol⁻¹ cm⁻¹), stronger luminescence ($\tau = 90\text{--}125$ ns, $\Phi = 210\text{--}350 \times 10^{-5}$) and can also result in higher TOF_{max} given sufficient driving force for electron transfer to the catalyst (TOF_{max} = 1500 mmol_{H₂} mol_{PS}⁻¹ min⁻¹ for **VII-C1**). The increased luminescence is found to be only beneficial for the use as PS if the driving forces otherwise remain unchanged, i.e., comparison of two complexes with similar driving forces shows a higher TOF_{max} for the stronger luminescing complex. Besides thermodynamic considerations, kinetic effects and electron transfer efficiency are assumed to impact the observed activity in hydrogen evolution.

Overall, this thesis shows that Ru(II) complexes of tridentate metal ion receptors, such as terpyridine derivatives, can act as PS in photocatalytic hydrogen evolution. The presented studies open this previously disregarded compound class for the application in photocatalysis, with the possibility of highly stable PSs. Furthermore, the importance of not only strong and long-lived luminescence but also sufficient driving forces for all electron transfer steps to and from the PS is highlighted.

IX. Appendix

This chapter consists of research previously published under the following titles:

“Photocatalytic Hydrogen Evolution Driven by a Heteroleptic Ruthenium(II) Bis(terpyridine) Complex” in *Inorganic Chemistry*.

Reproduced with permission of American Chemical Society from *Inorganic Chemistry*, **2019**, 58, 9127-9134.

“Electrochemical and photophysical study of homoleptic and heteroleptic methylated ruthenium(II) bis-terpyridine complexes” in *European Journal of Inorganic Chemistry*.

Reproduced with permission of Wiley-VCH, from *Electrochemical and photophysical study of homoleptic and heteroleptic methylated ruthenium(II) bis-terpyridine complexes*, Mira T. Rupp, Thomas Auvray, Garry S. Hanan, Dirk G. Kurth, *European Journal of Inorganic Chemistry* **2021**, 2021 (28), 2822-2829.

“Substituted 2,4-Di(pyridin-2-yl)pyrimidine-Based Ruthenium Photosensitizers for Hydrogen Photoevolution under Red Light” in *Inorganic Chemistry*.

Reproduced with permission of American Chemical Society from *Inorganic Chemistry*, **2021**, 60, 292-302.

CCDC 2090569: Experimental Crystal Structure Determination, **2021**

and

submitted to *Dalton Transactions* as a full paper under the title

“Dinuclear 2,4-di(pyridin-2-yl)-pyrimidine based ruthenium photosensitizers for hydrogen photo-evolution under red light.”

IX.1. Material

All reagents and solvents were obtained from commercial sources (VWR, Fisher Scientific, Acros, Sigma Aldrich, Merck, or Pressure Chemicals Inc.) and used as received, unless stated otherwise. For experiments under microwave irradiation, a Biotage Initiator or a Discover SP microwave synthesizer were used. Experiments were carried out under air except stated otherwise.

IX.2. Instrumentation Details

NMR experiments were performed on a Bruker AV-400 (^1H : 400 MHz and $^{13}\text{C}\{^1\text{H}\}$: 101 MHz, Montréal, Canada), a Fourier 300 (^1H : 300 MHz and $^{13}\text{C}\{^1\text{H}\}$: 75 MHz, Bruker Biospin, Rheinstetten, Germany), a Bruker Avance 500 (^1H : 500 MHz and $^{13}\text{C}\{^1\text{H}\}$: 126 MHz, Montréal, Canada), a Bruker Avance 700 (^1H : 700 MHz and $^{13}\text{C}\{^1\text{H}\}$: 176 MHz, Montréal, Canada), or a Bruker Avance III HD 600 (^1H : 600 MHz and $^{13}\text{C}\{^1\text{H}\}$: 151 MHz, Würzburg Germany) spectrometer at room temperature. The chemical shifts are reported in ppm relative to the residual peak of the solvent as the internal standard. Peak assignments were determined using 2D-NMR spectroscopy (COSY, HSQC, HMBC).

High-resolution mass spectrometry (HR-MS) was recorded either on a Q-Exactive orbitrap from ThermoFisher, a SYNAPT G2-Si spectrometer from Waters, or a Bruker Daltonics microTOF focus. Samples were ionized by electrospray ionization (ESI).

UV-vis absorption spectra were recorded on an Agilent Cary6000i or Cary5000 UV-Vis-NIR spectrometer or a Varian Cary50 spectrometer. Room-temperature emission spectra were recorded on a Jasco FP-8300 spectrometer equipped with a thermostating unit set to 20 °C or a LS 55 fluorescence spectrometer from PerkinElmer. Complexes were excited at 450 nm. The quantum yield was calculated using the dilute method^[236] using $[\text{Ru}(\text{TolyItpy})_2](\text{PF}_6)_2$ as reference.^[237] Solutions of absorbance ranging between 0.01 and 0.1 were used and the following equation was applied to obtain the quantum yield value. The reported value is an average from the different measurements.

$$\Phi_1 = \frac{S_1}{S_{ref}} \times \frac{A_{ref}}{A_1} \times \phi_{ref} \quad \text{Equation IX-1}$$

Where S_1 and S_{ref} are the area of the emission peak, A_1 and A_{ref} the absorbance of the corresponding solution and Φ_1 and Φ_{ref} the quantum yield of our complex and of the reference, $[\text{Ru}(\text{Tolyltpy})_2](\text{PF}_6)_2$ here.

For the luminescence lifetimes, an Edinburgh Instruments Mini-tau single-photon counting spectrometer, employing a Hamamatsu PLP2 laser diode as pulse (wavelength output, 408 nm; pulse width, 59 ps), or a FLS920 fluorescence spectrometer (Edinburgh Instruments) using a 405 nm centered (room-temperature measurements), or 508 nm centered (various temperature measurements) Hamamatsu diode laser was used. Sample solutions were degassed with nitrogen or argon prior to measuring emission or excited-state lifetimes.

Electrochemical experiments were carried out in a one-compartment cell, using a glassy carbon disk working electrode (3 mm or 6 mm diameter), a platinum wire counter electrode, and a silver wire as pseudo-reference electrode. The potential of the working electrode was controlled by an Autolab PGSTAT 100 potentiostat, or a SP-50 BioLogic potentiostat through a PC interface. The cyclic voltammograms were recorded with a sweep rate of 100 mV/s in dried acetonitrile. Tetrabutylammonium hexafluorophosphate (0.1 mol/L) was used as the supporting electrolyte, and the samples were purged by nitrogen before each measurement. Ferrocene was used as an internal standard.

Spectroelectrochemical experiments were carried out in a quartz glass cell with 1 mm path length. The three-electrode set-up consisted of a platinum mesh WE, a platinum wire CE and a Ag/Ag⁺ in acetonitrile RE. Measurements were conducted in argon-purged dry acetonitrile with 0.1 M TBAPF₆ as supporting electrolyte. The sample concentration was chosen to yield an absorptivity below 1. The potential was controlled by a Gamry Interface1010 potentiostat. The voltage was changed in 0.1 V steps, then kept constant while the UV-vis spectrum was recorded by an Agilent Cary 5000 UV-vis-NIR spectrometer.

IX.3. NMR Spectra

Higher-resolution graphics of the depicted NMR spectra (Figure IX-1 to Figure IX-54) can be found in the **Digital Appendix**.

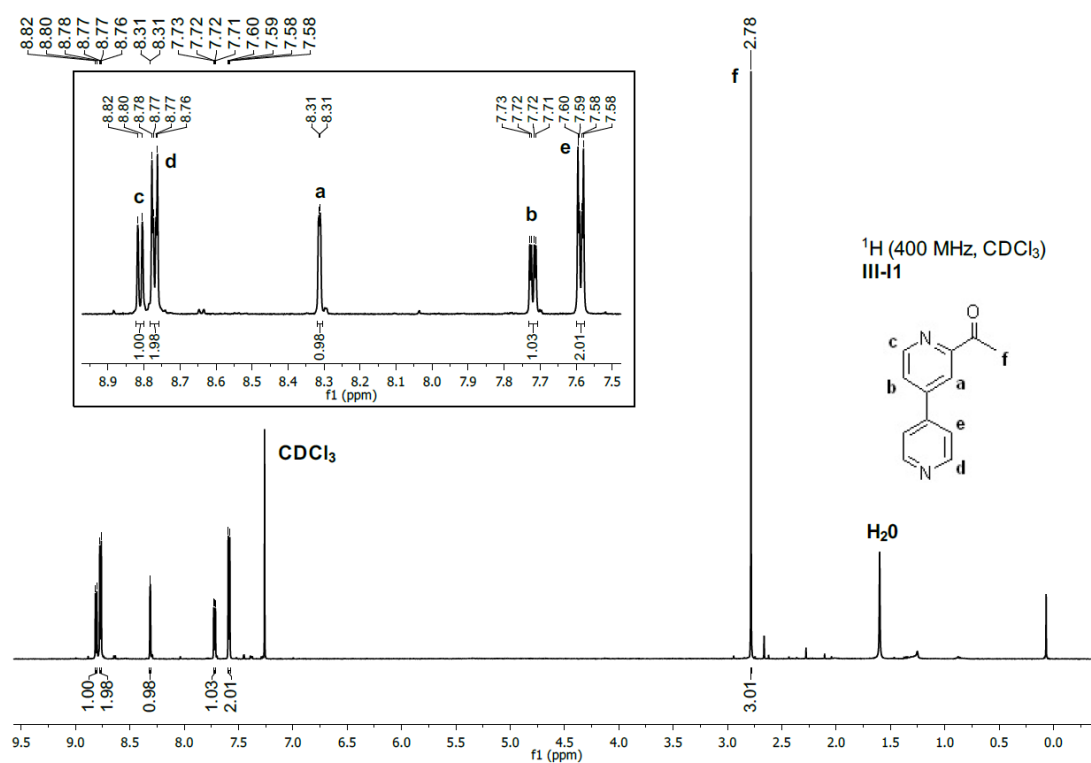
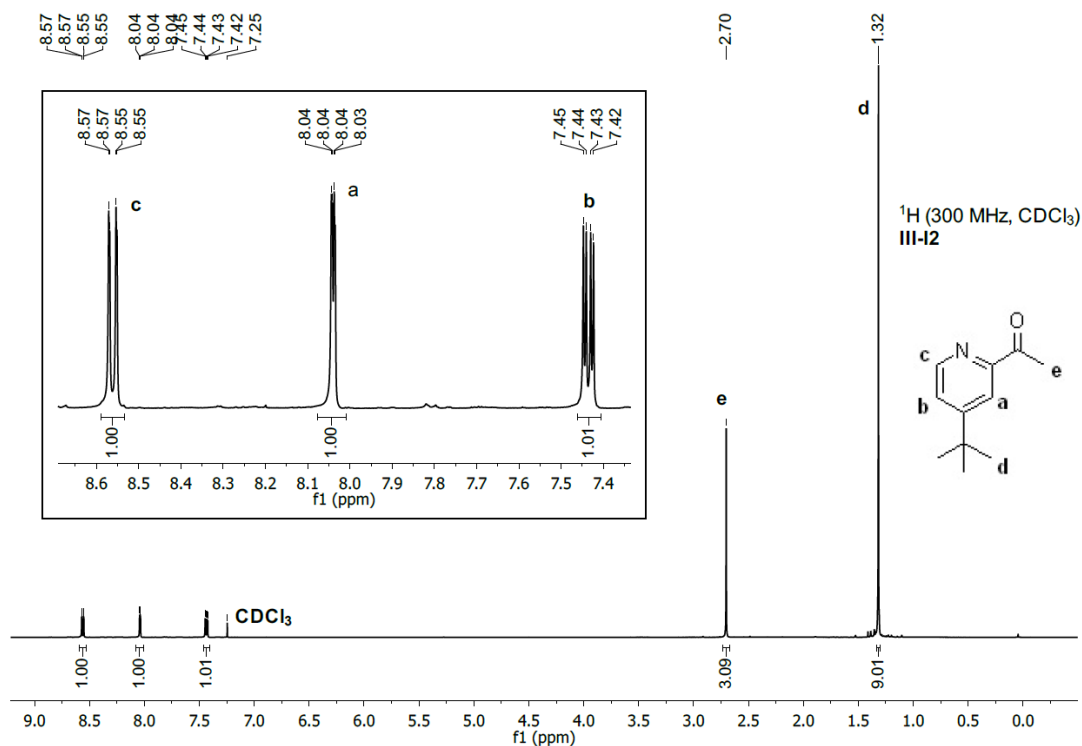
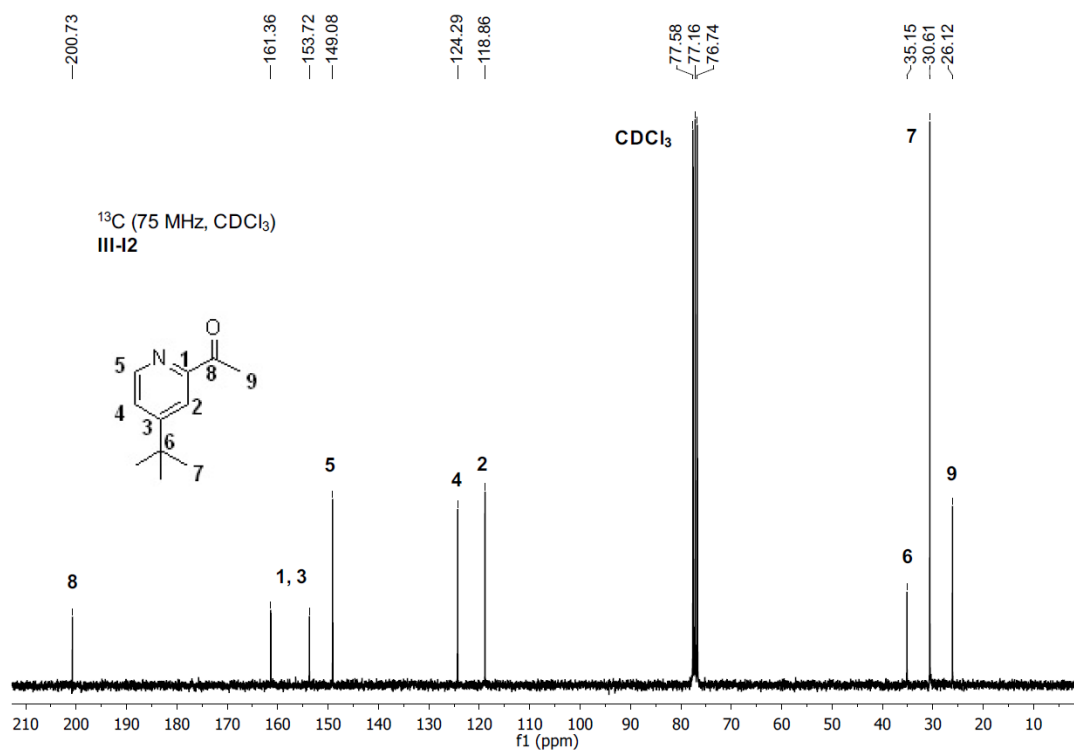
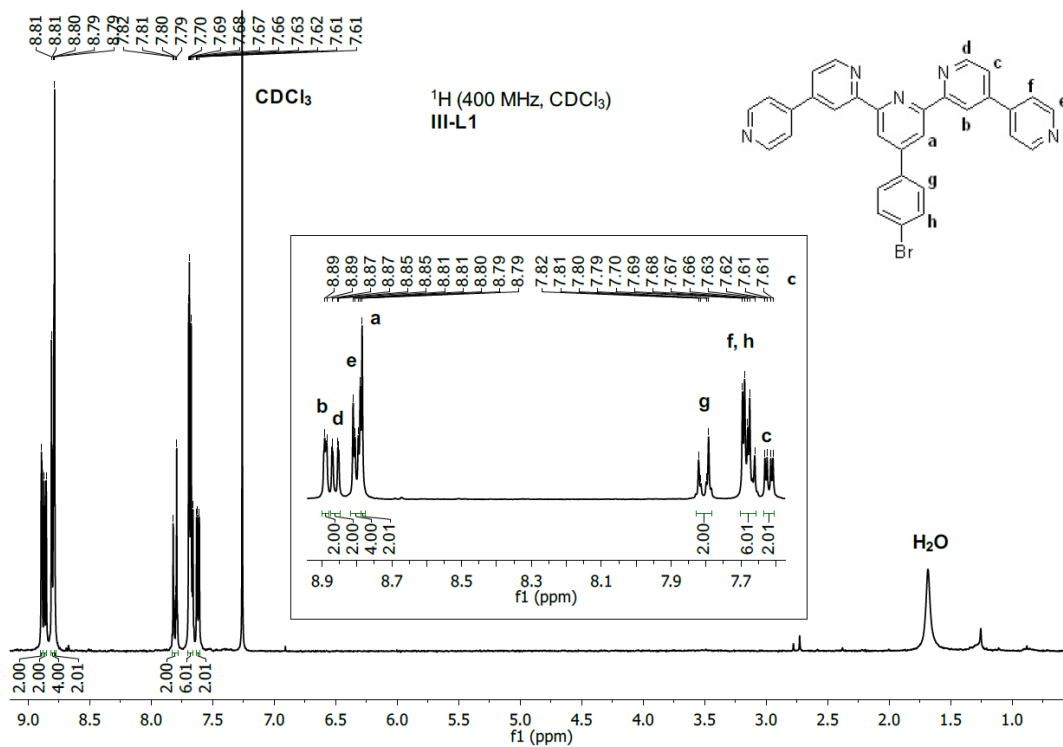
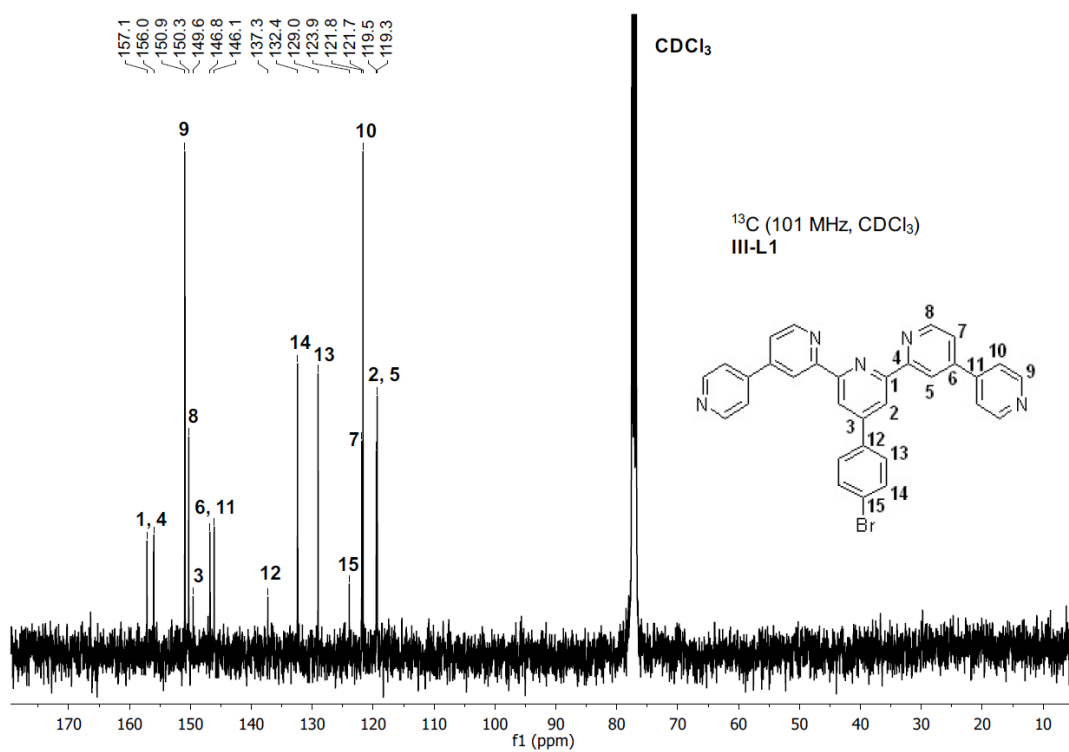
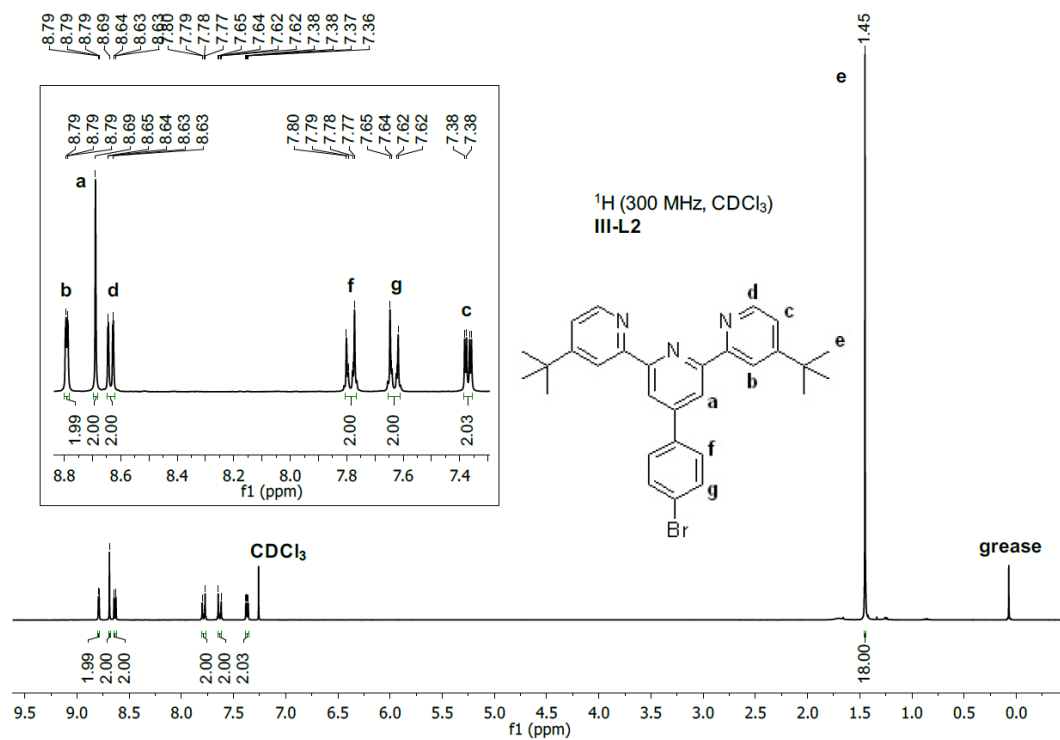
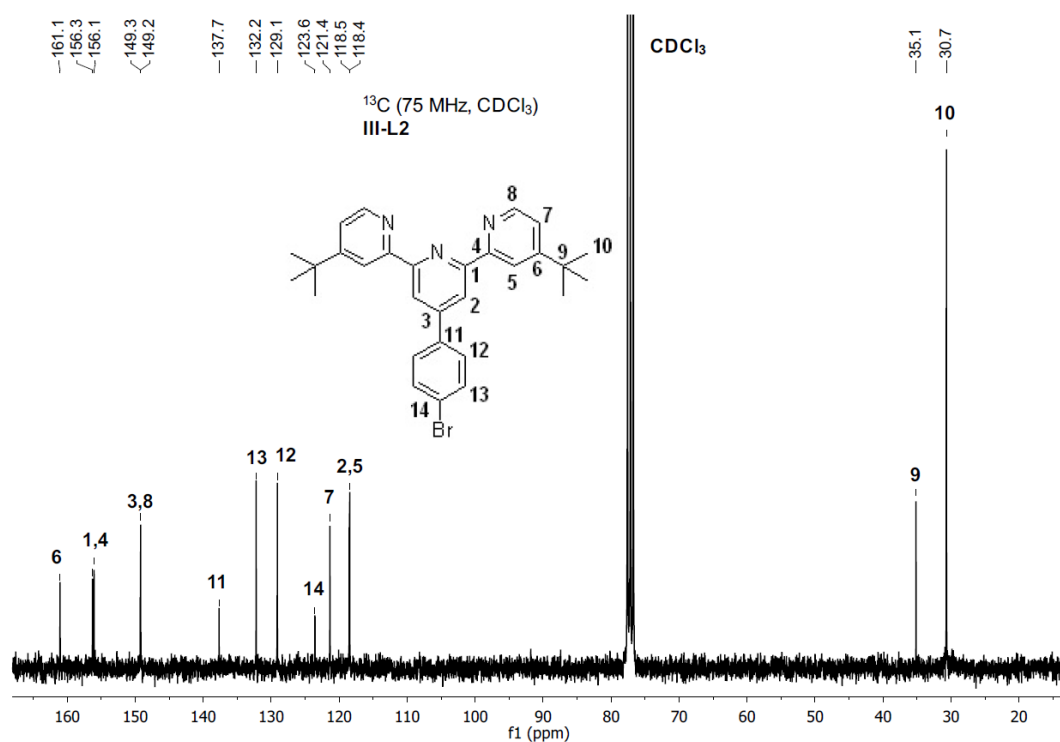
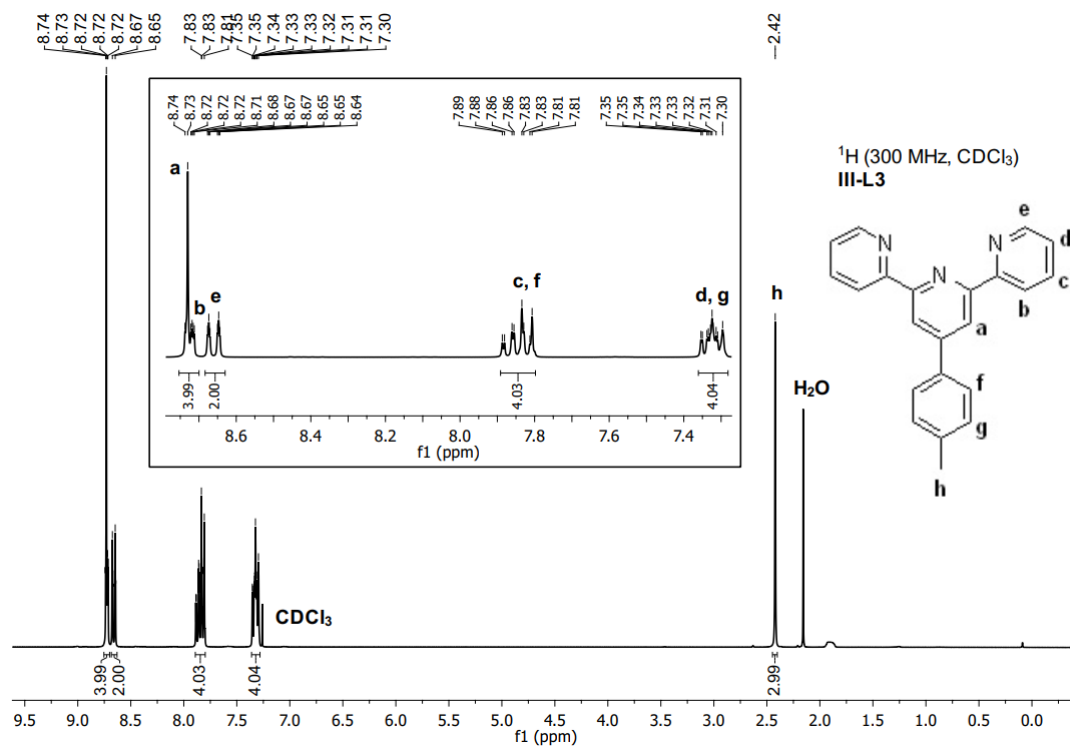
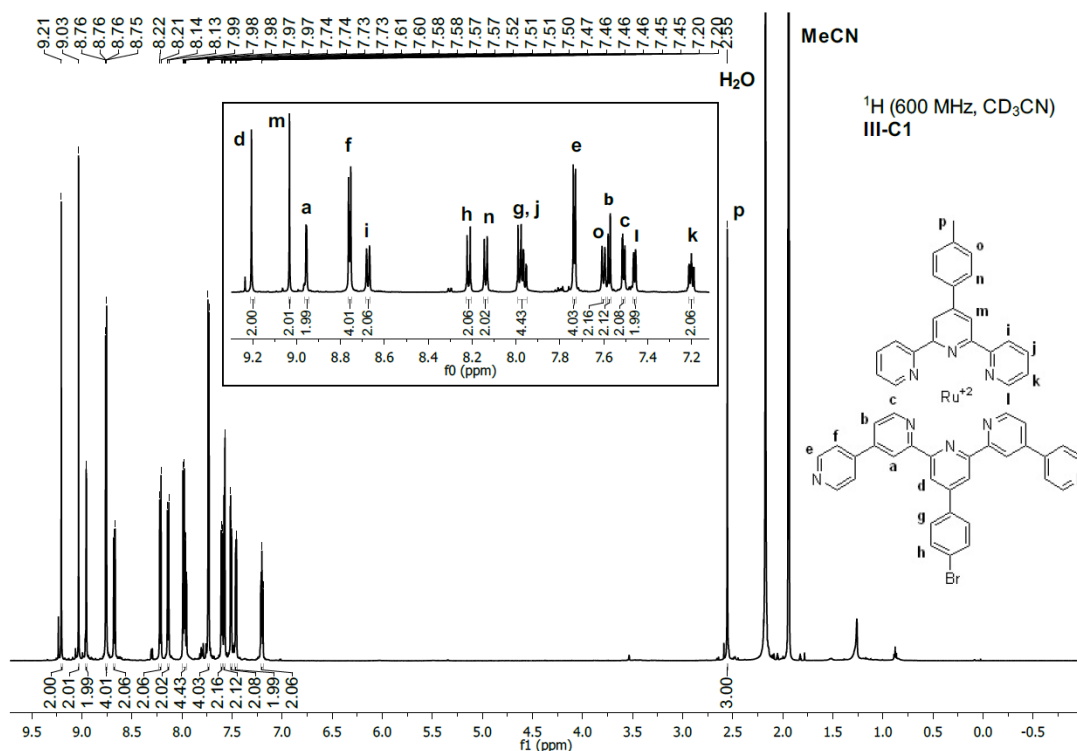


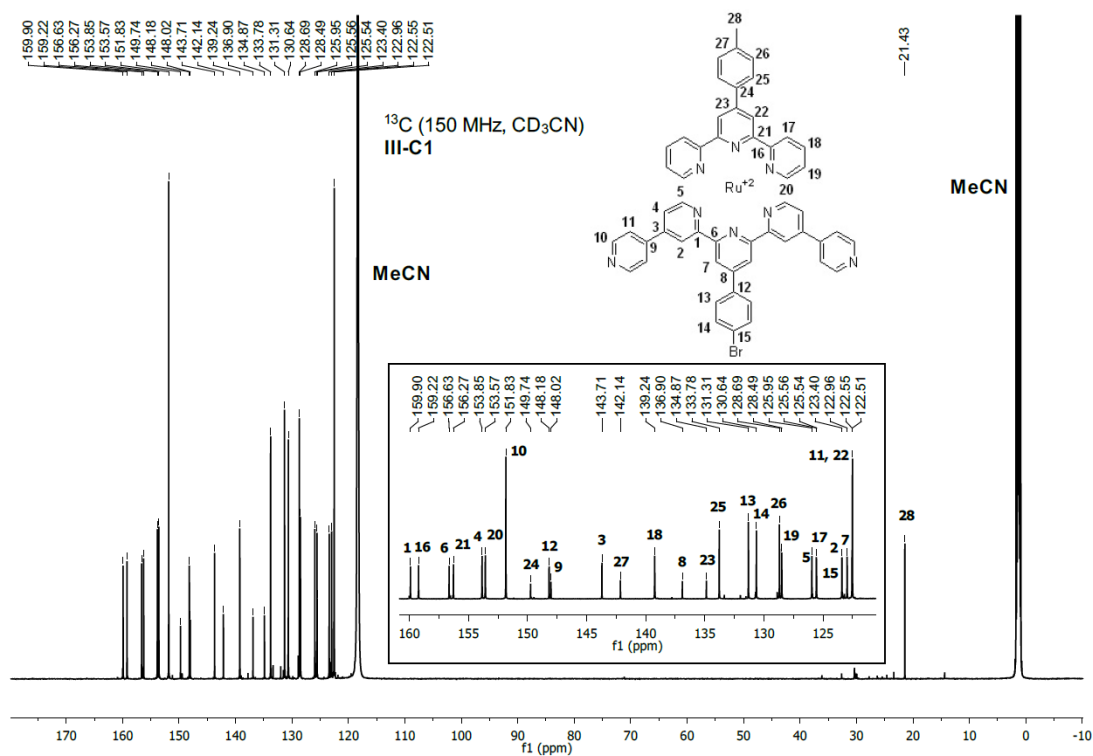
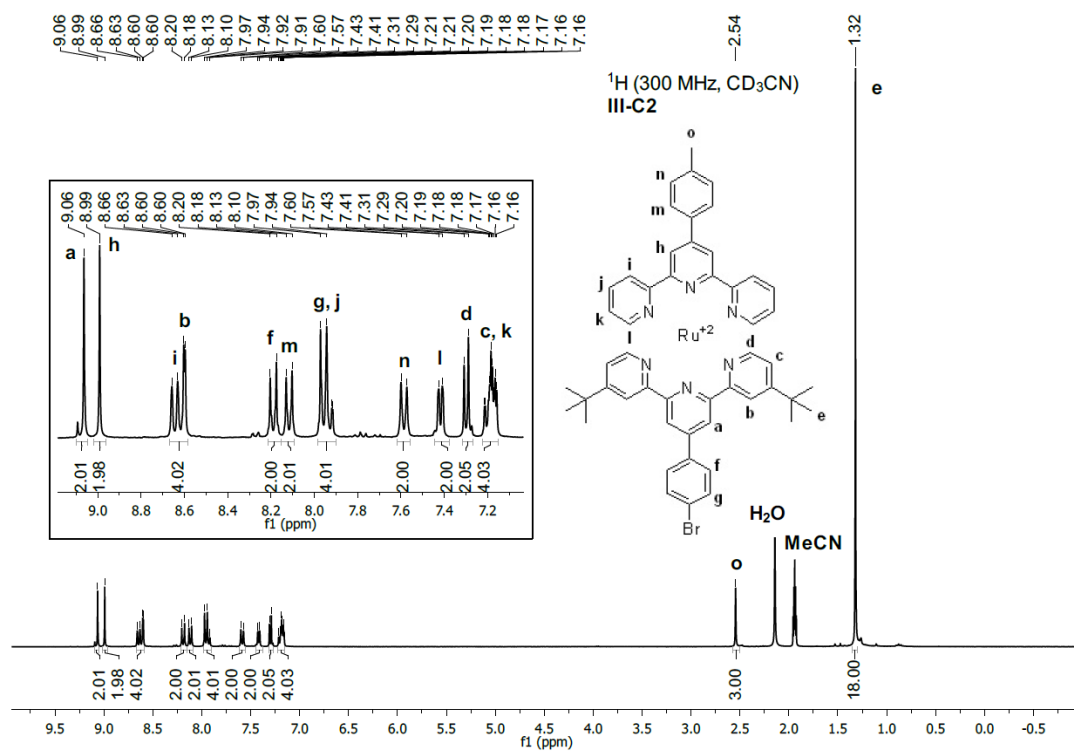
Figure IX-1. ¹H-NMR spectrum (400 MHz, CDCl₃) of III-I1.

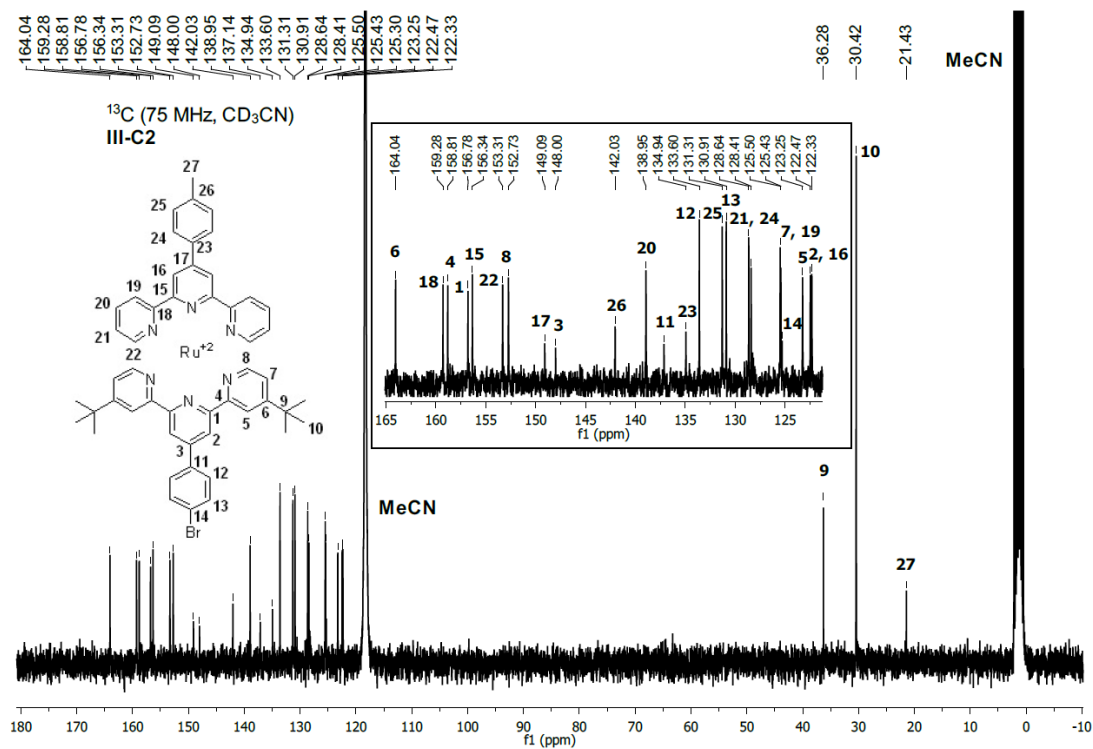
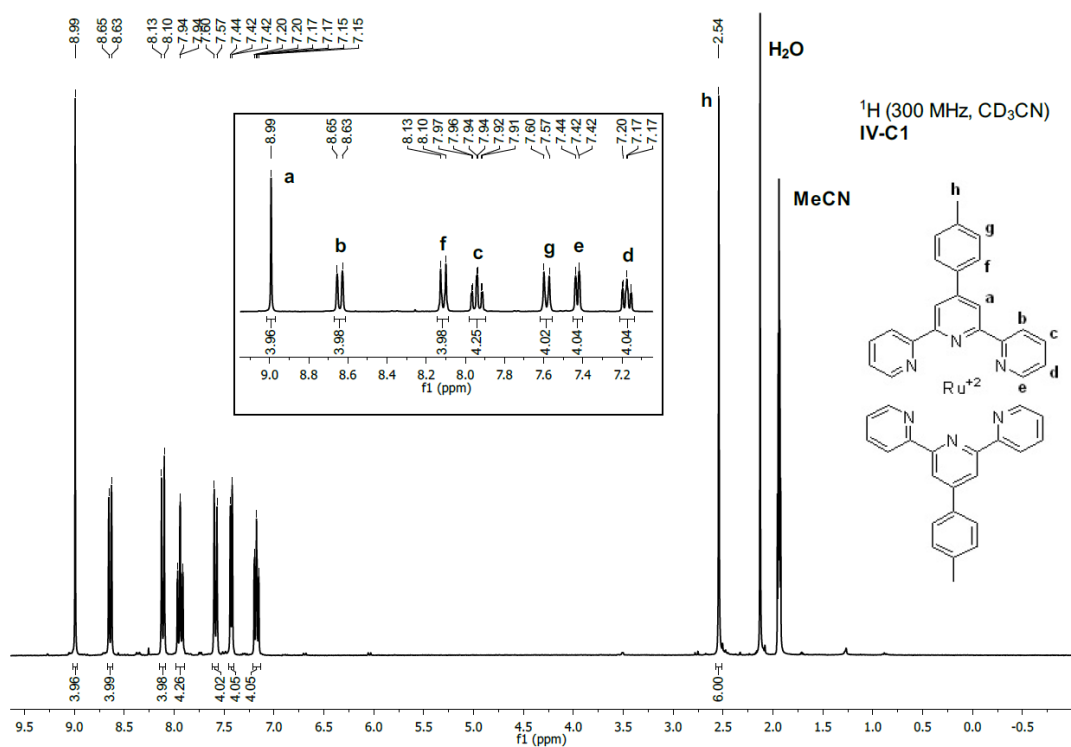
Figure IX-2. ¹H-NMR spectrum (300 MHz, CDCl₃) of III-12.Figure IX-3. ¹³C-NMR spectrum (75 MHz, CDCl₃) of III-12.

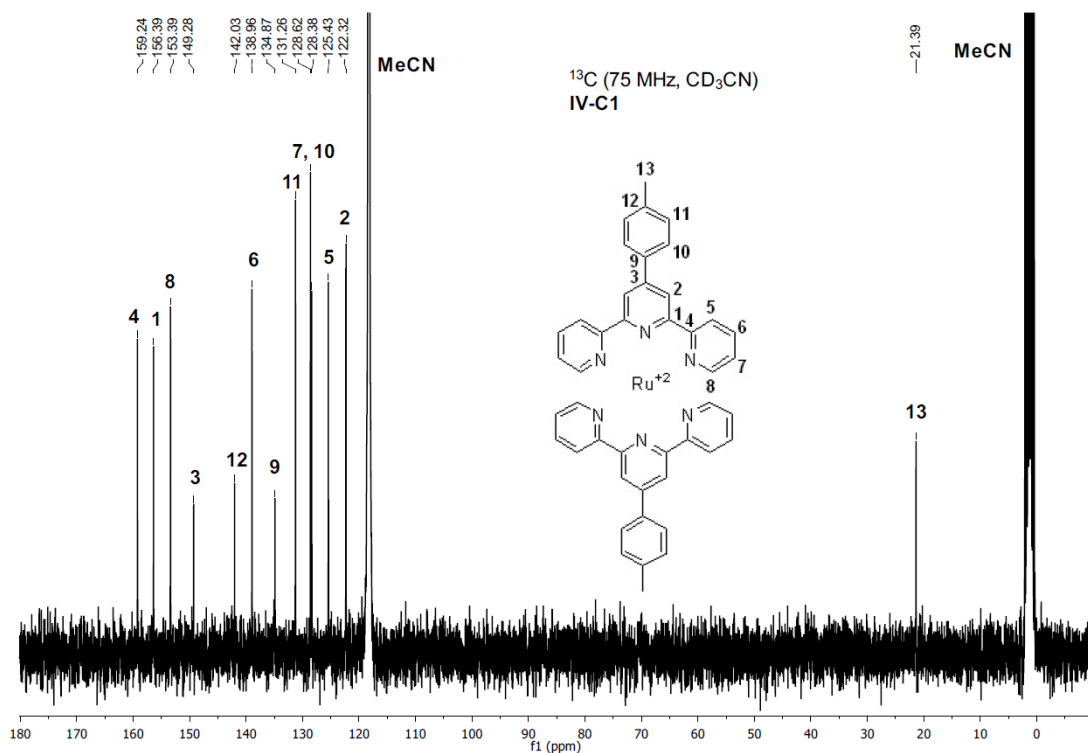
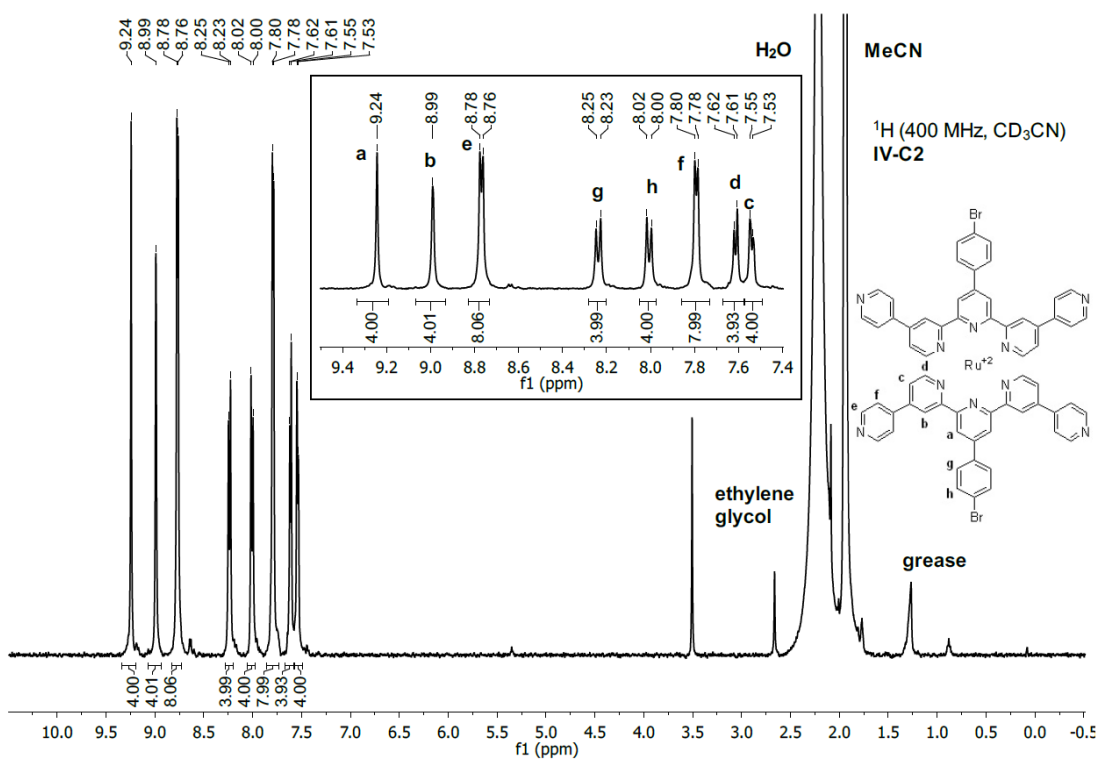
Figure IX-4. ¹H-NMR spectrum (400 MHz, CDCl₃) of III-L1.Figure IX-5. ¹³C-NMR spectrum (101 MHz, CDCl₃) of III-L1.

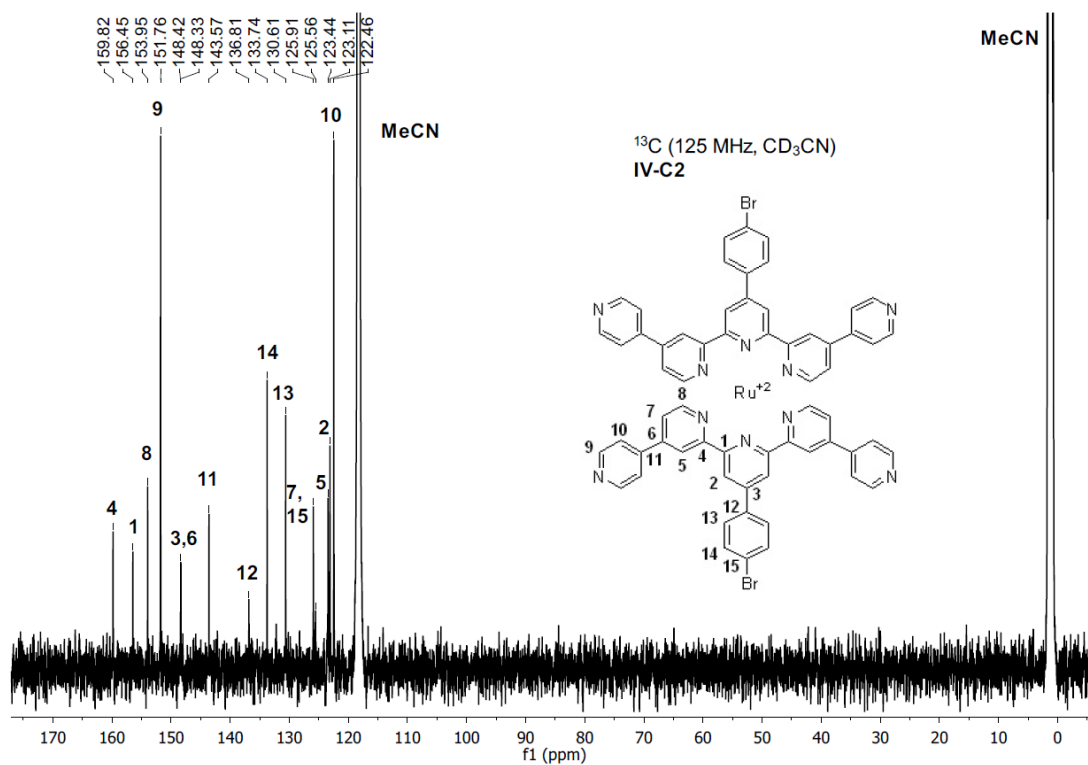
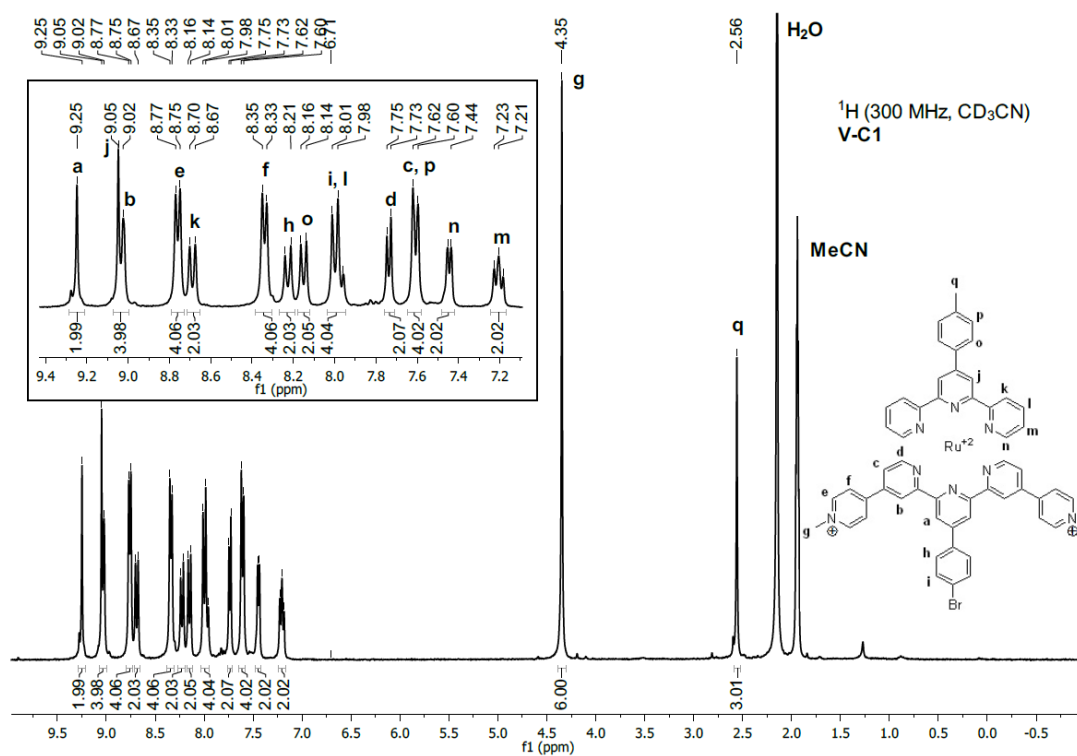
Figure IX-6. ¹H-NMR spectrum (300 MHz, CDCl₃) of III-L2.Figure IX-7. ¹³C-NMR spectrum (75 MHz, CDCl₃) of III-L2.

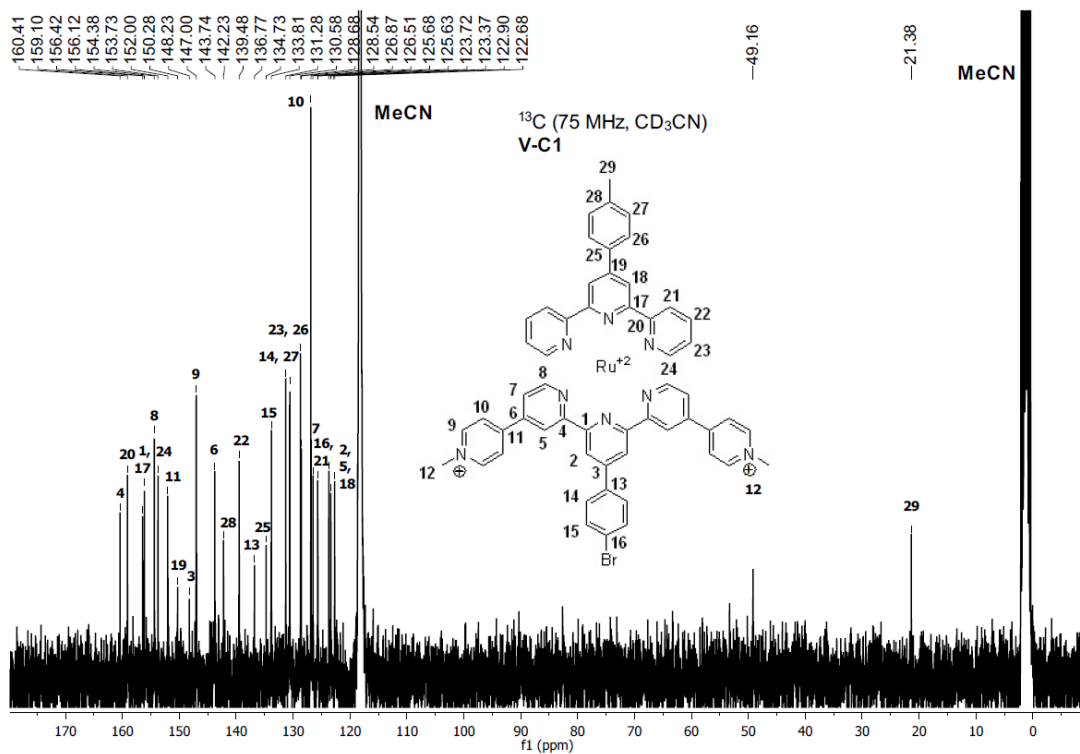
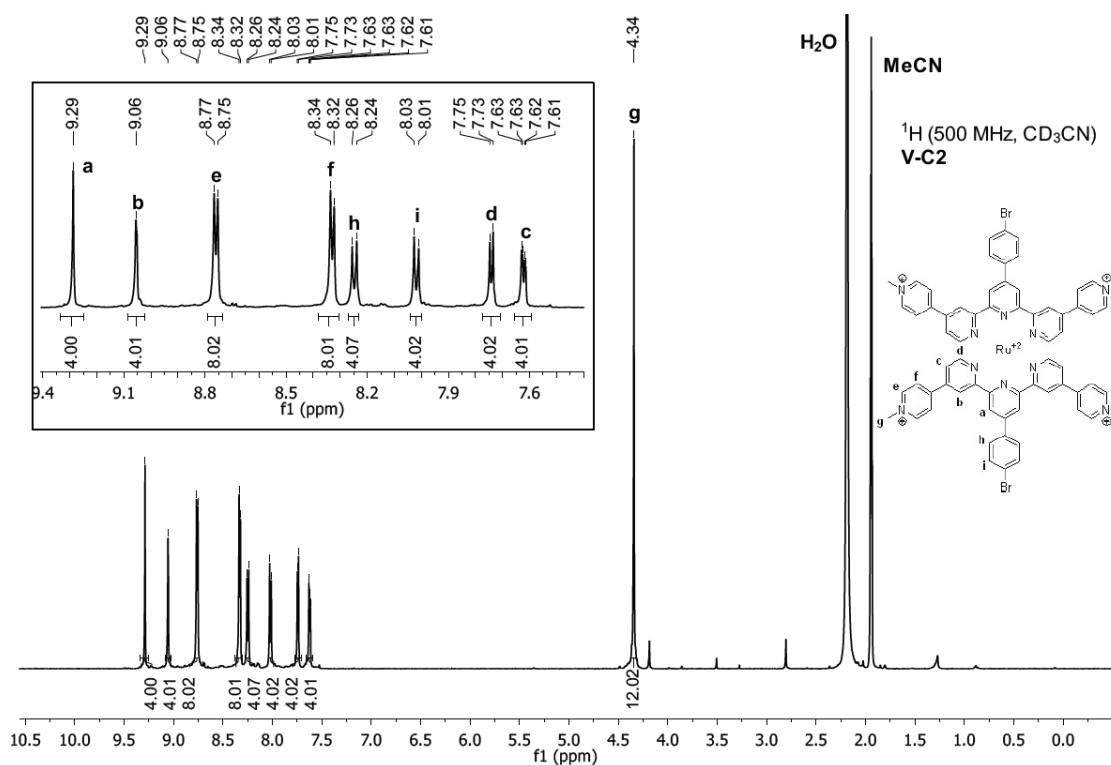
Figure IX-8. ¹H-NMR spectrum (300 MHz, CDCl₃) of III-L3.Figure IX-9. ¹H-NMR spectrum (600 MHz, CD₃CN) of III-C1.

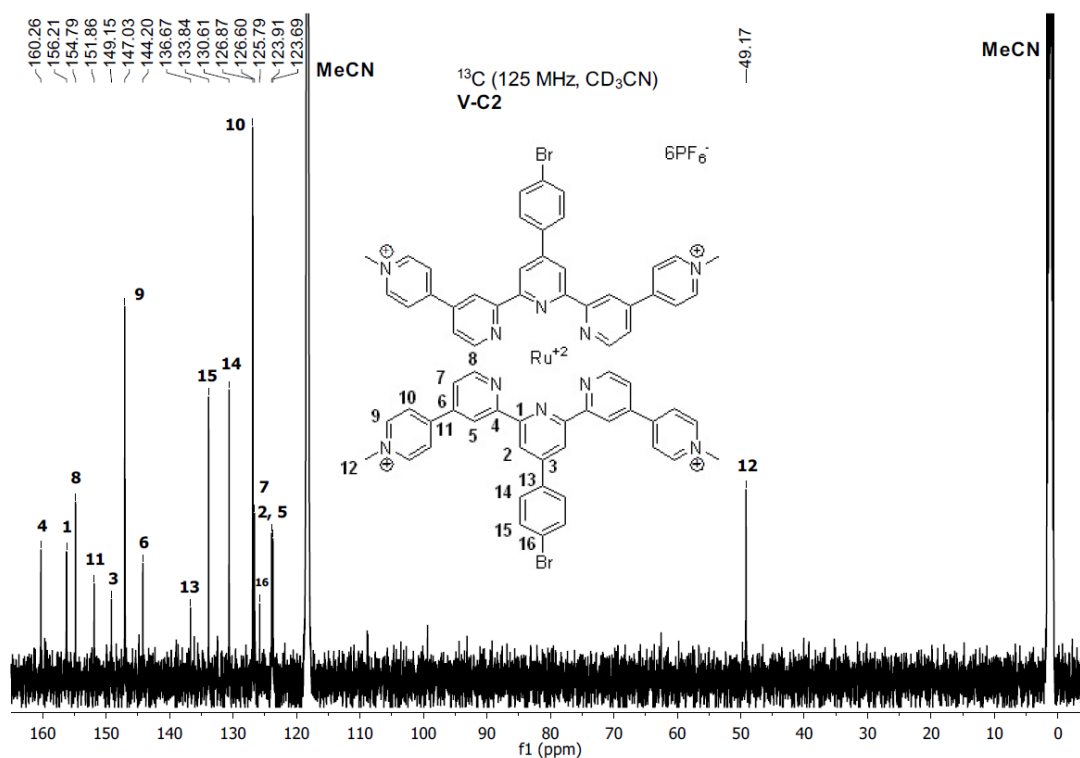
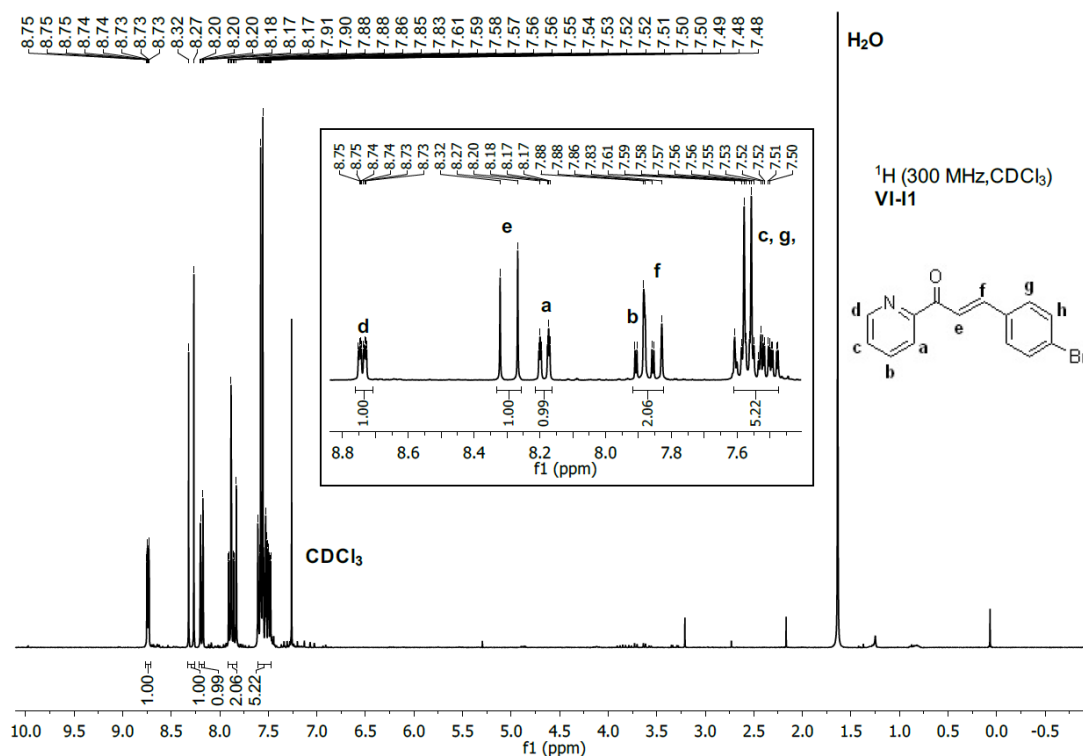
Figure IX-10. ¹³C-NMR spectrum (150 MHz, CD₃CN) of III-C1.Figure IX-11. ¹H-NMR spectrum (300 MHz, CD₃CN) of III-C2.

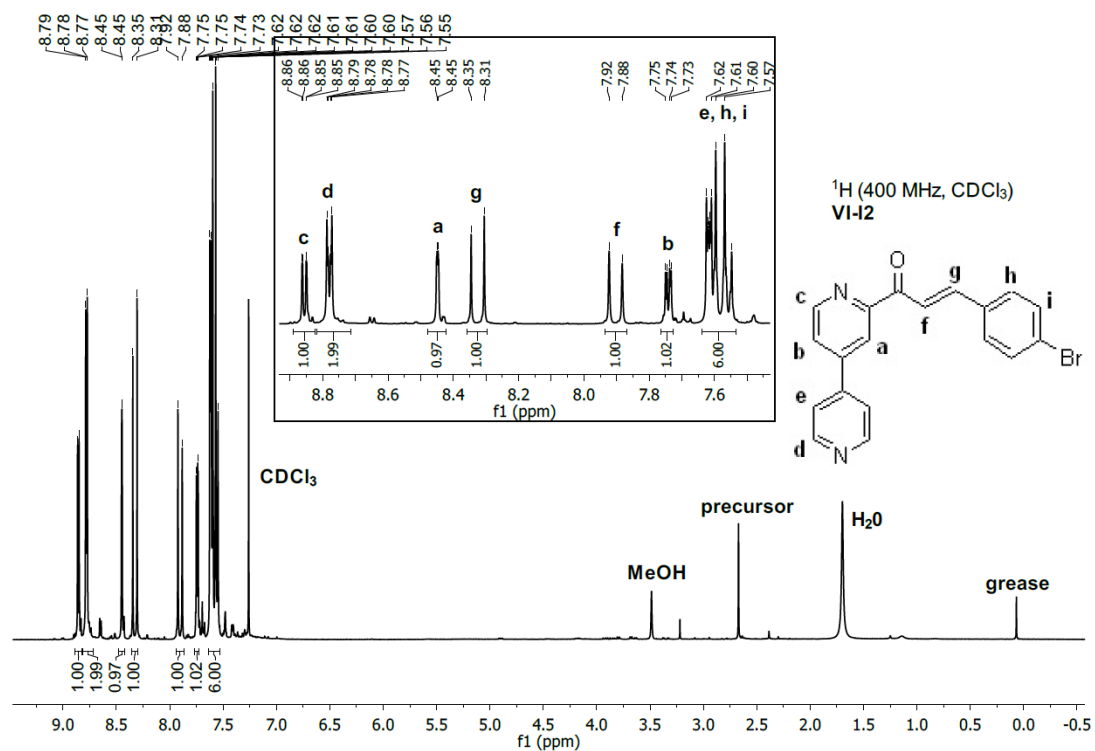
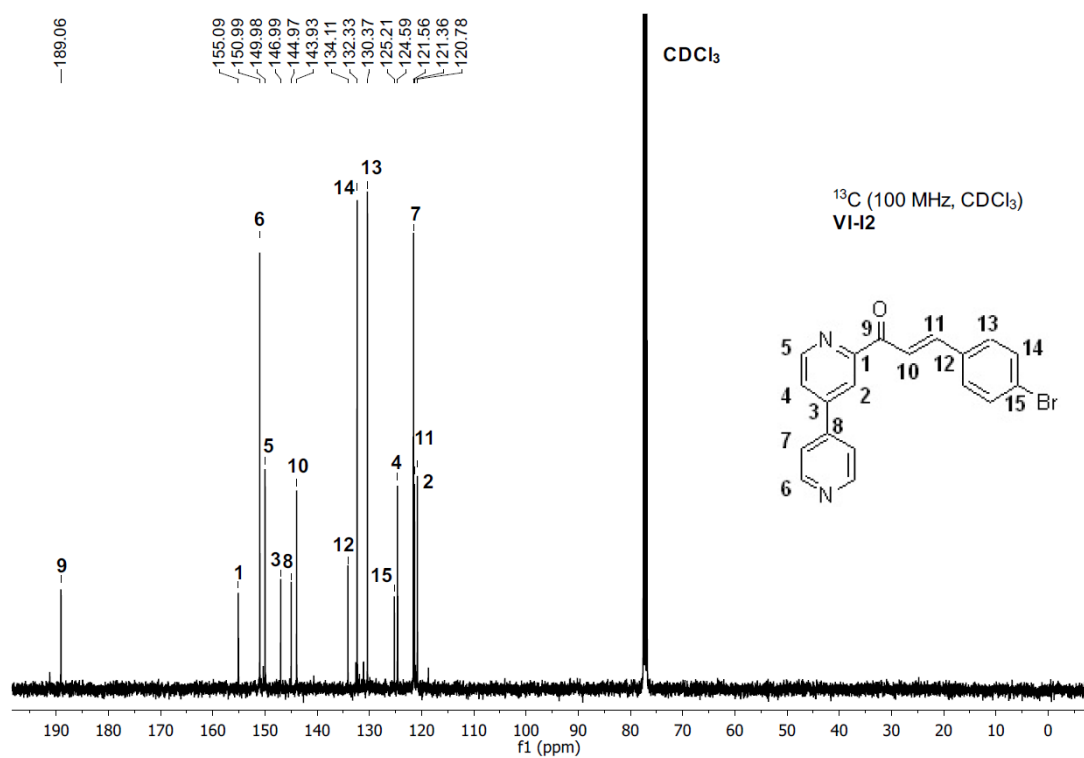
Figure IX-12. ¹³C-NMR spectrum (75 MHz, CD₃CN) of III-C2.Figure IX-13. ¹H-NMR spectrum (300 MHz, CD₃CN) of IV-C1.

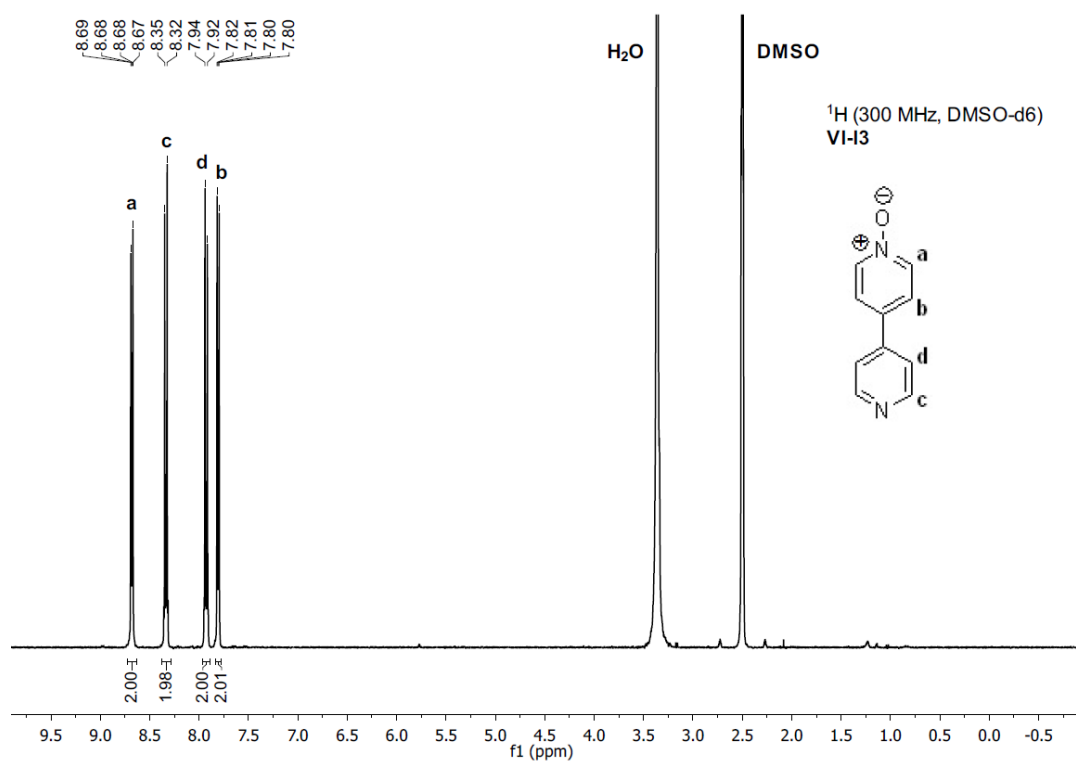
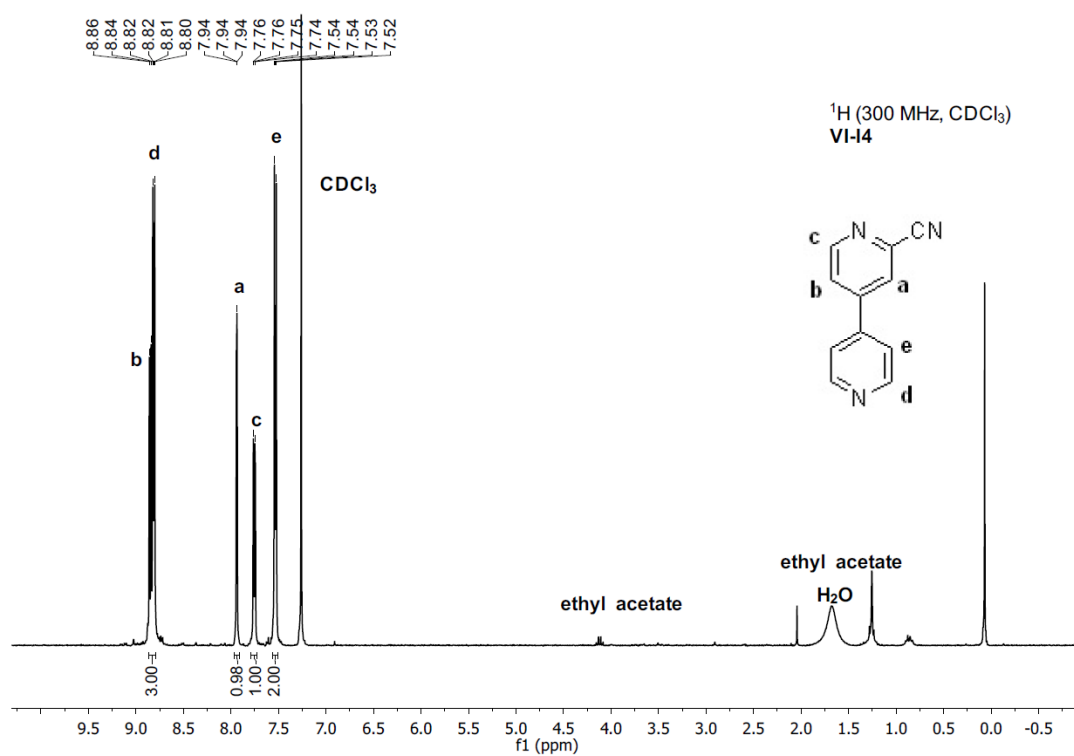
Figure IX-14. ¹³C-NMR spectrum (75 MHz, CD₃CN) of IV-C1.Figure IX-15. ¹H-NMR spectrum (400 MHz, CD₃CN) of IV-C2.

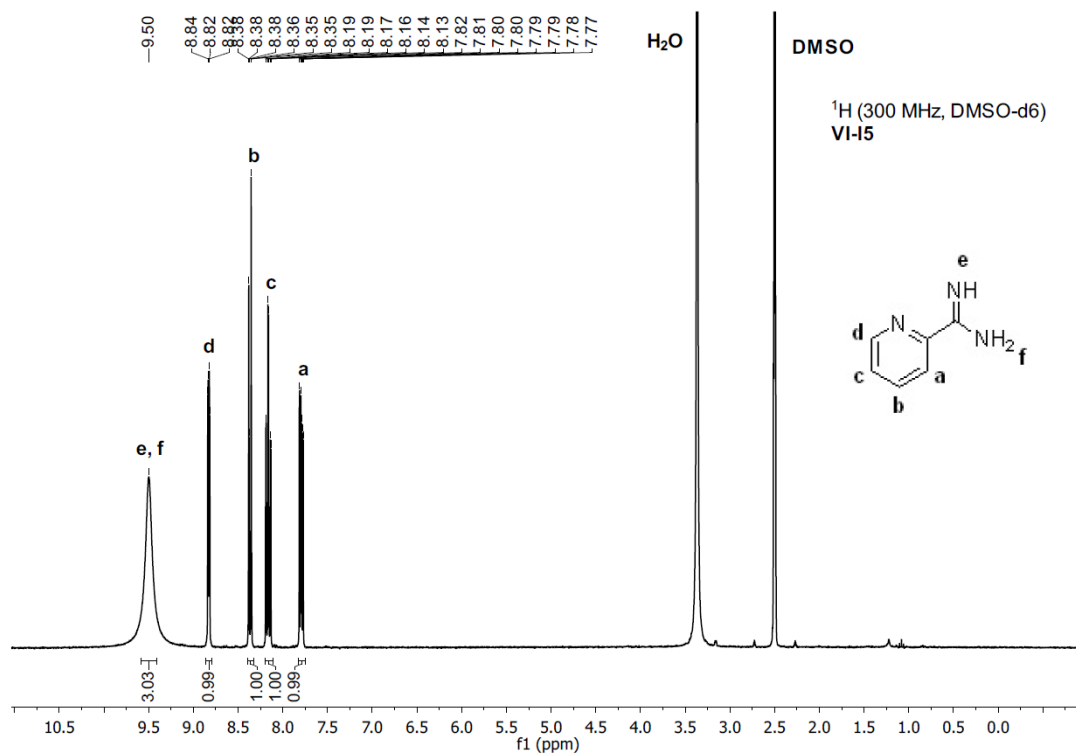
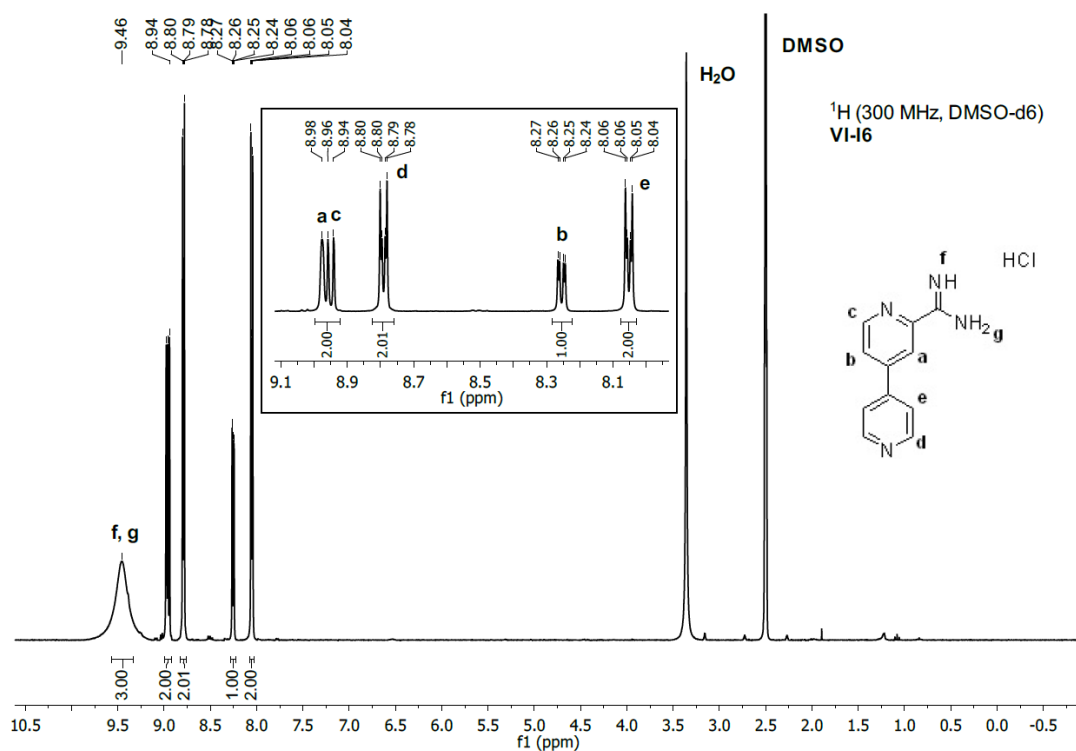
Figure IX-16. ¹³C-NMR spectrum (125 MHz, CD₃CN) of IV-C2.Figure IX-17. ¹H-NMR spectrum (300 MHz, CD₃CN) of V-C1.

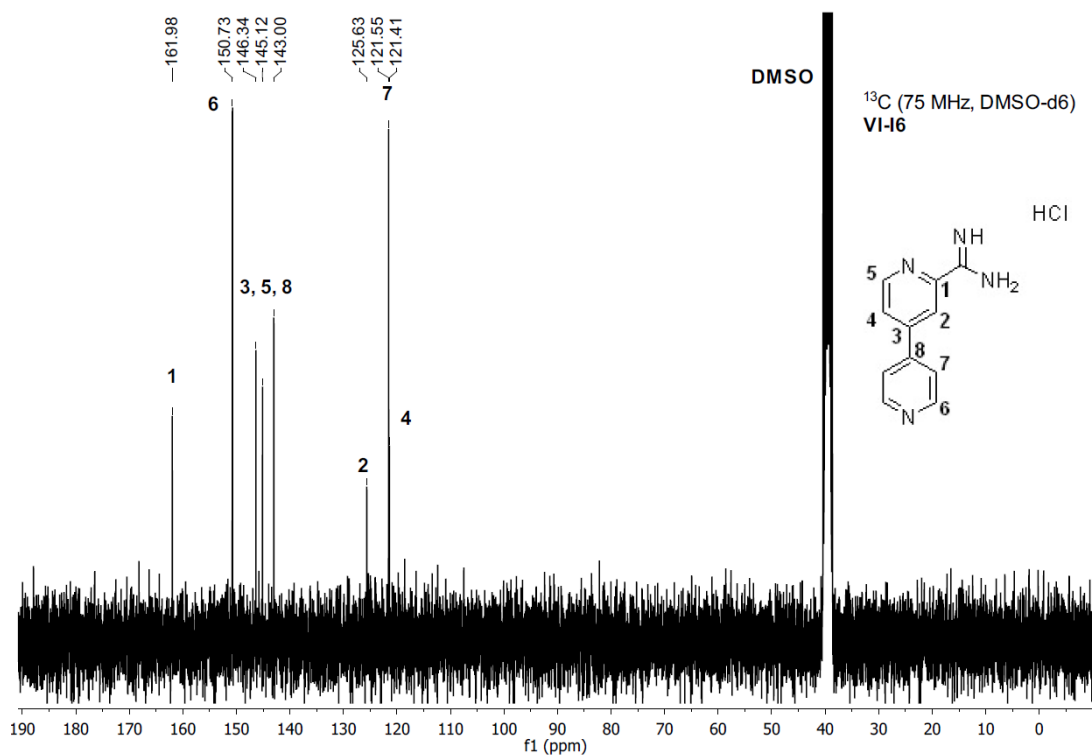
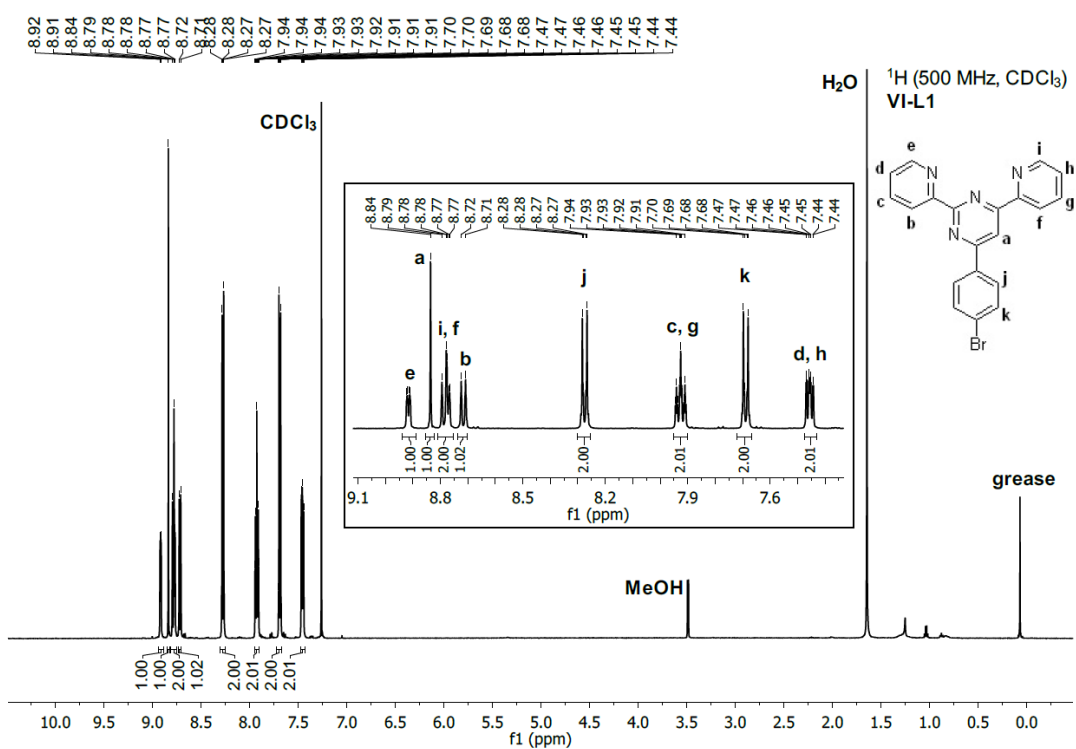
Figure IX-18. ¹³C-NMR spectrum (75 MHz, CD₃CN) of V-C1.Figure IX-19. ¹H-NMR spectrum (500 MHz, CD₃CN) of V-C2.

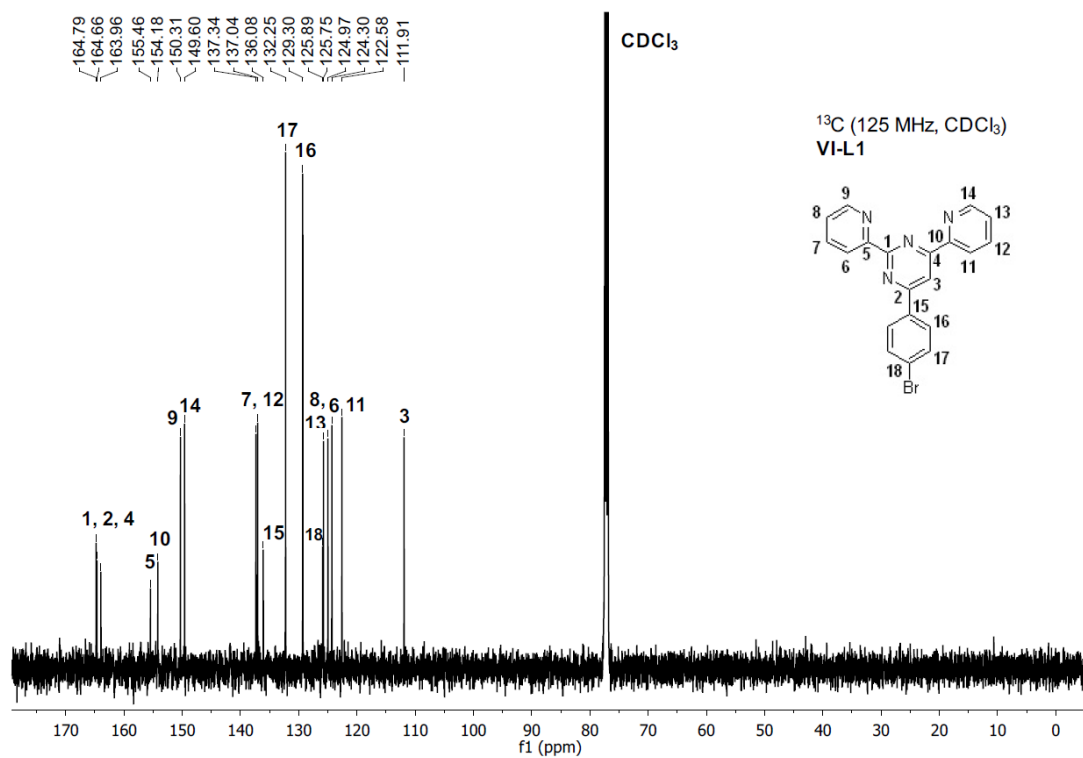
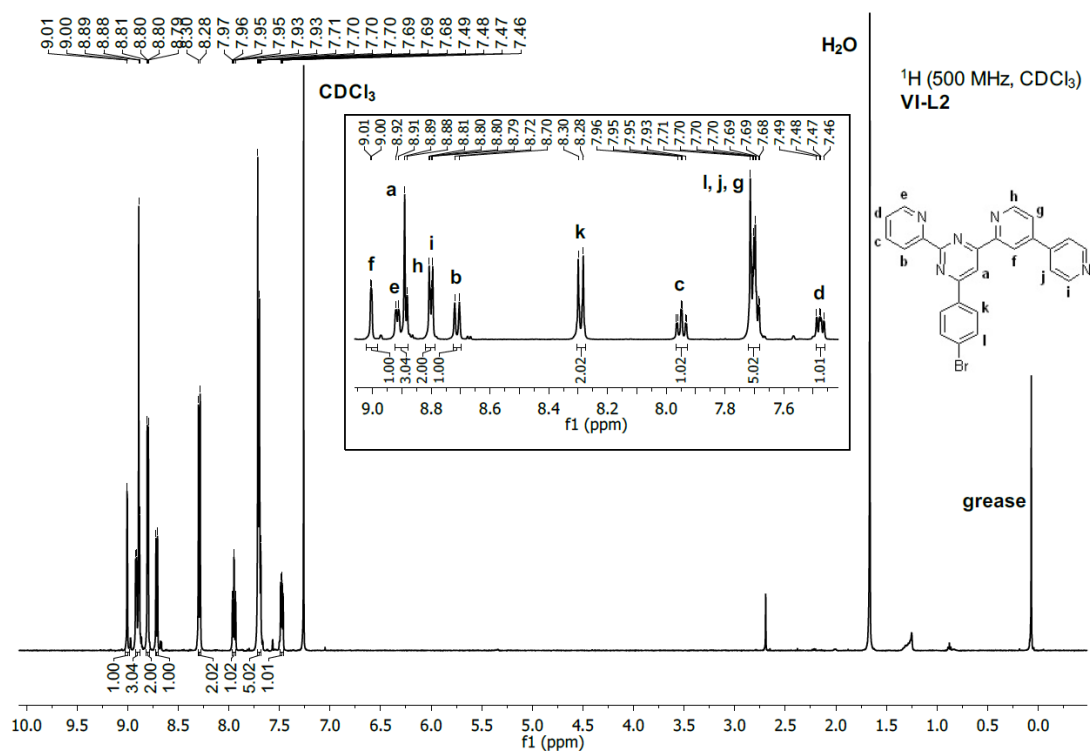
Figure IX-20. ¹³C-NMR spectrum (125 MHz, CD₃CN) of V-C2.Figure IX-21. ¹H-NMR spectrum (300 MHz, CDCl₃) of VI-I1.

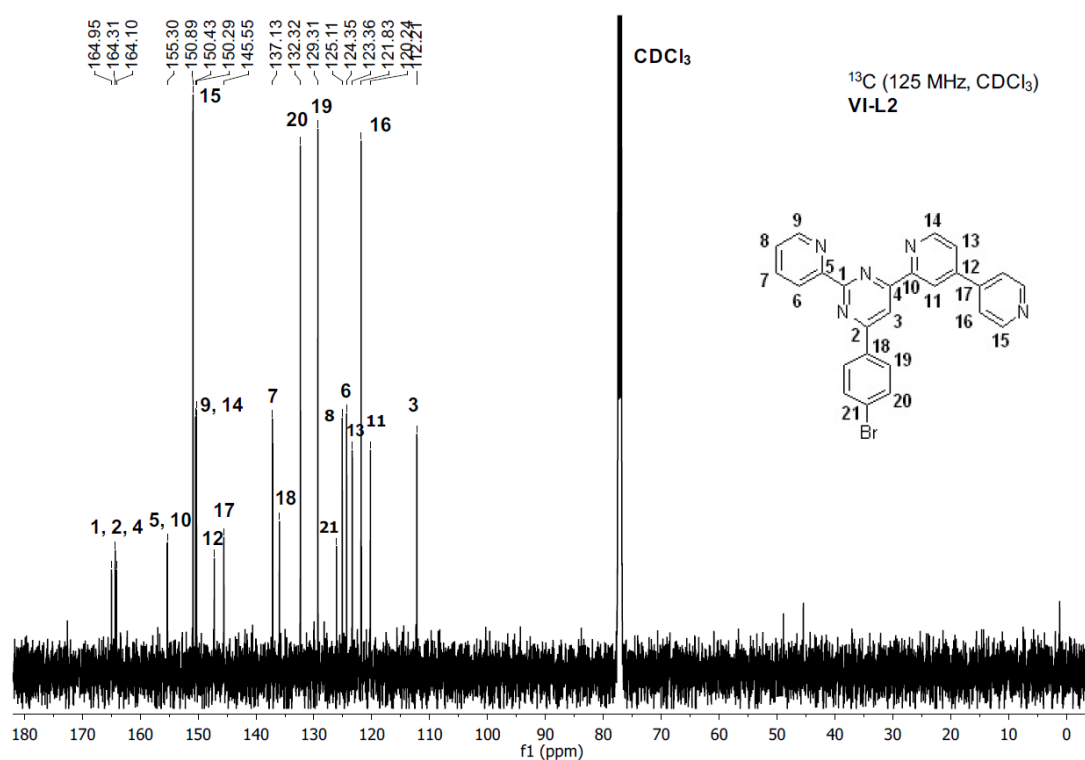
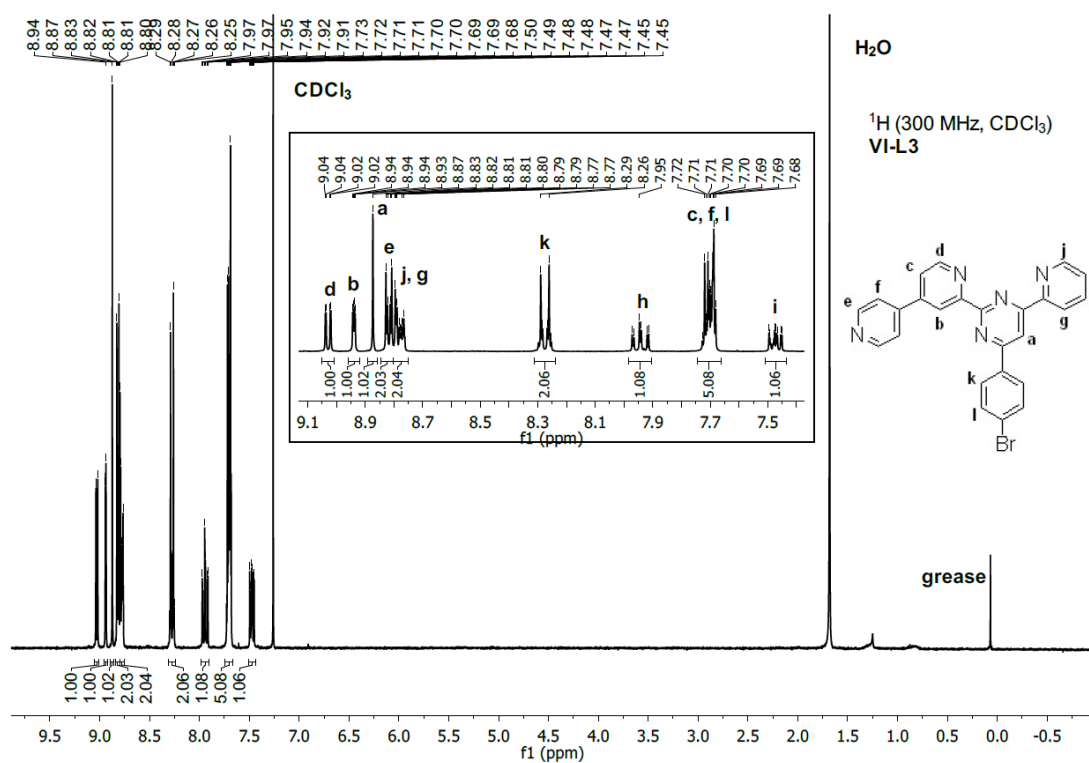
Figure IX-22. ¹H-NMR spectrum (400 MHz, CDCl₃) of VI-2.Figure IX-23. ¹³C-NMR spectrum (100 MHz, CDCl₃) of VI-2.

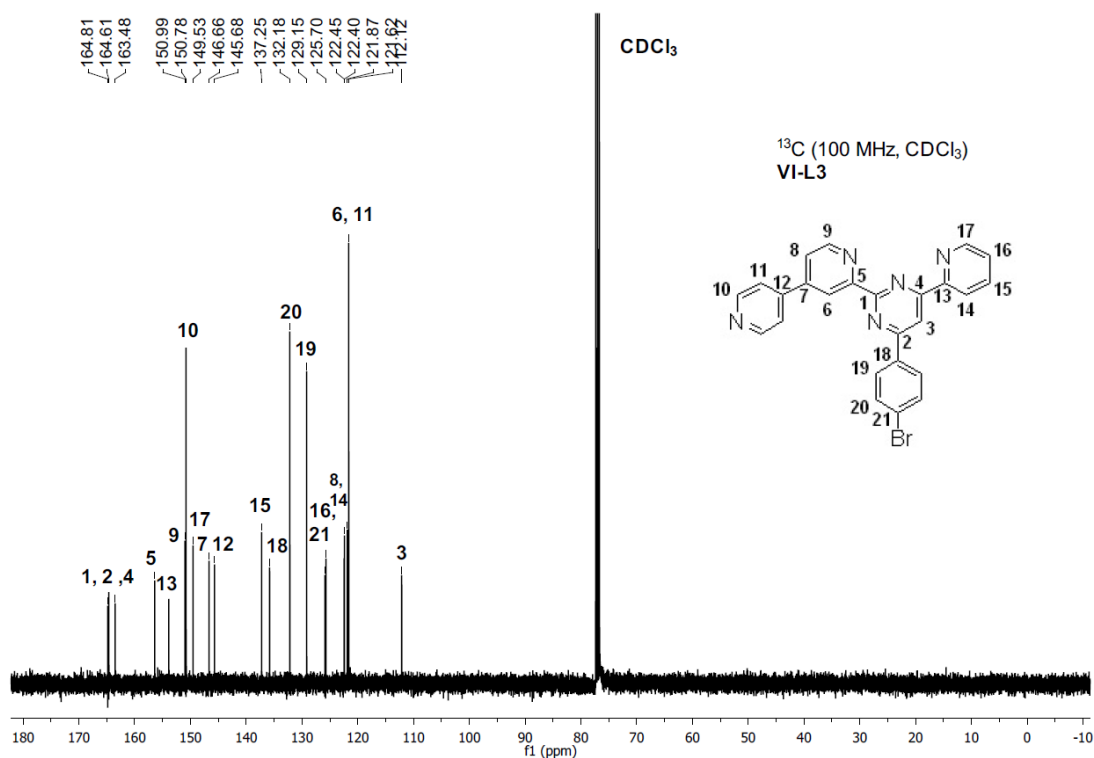
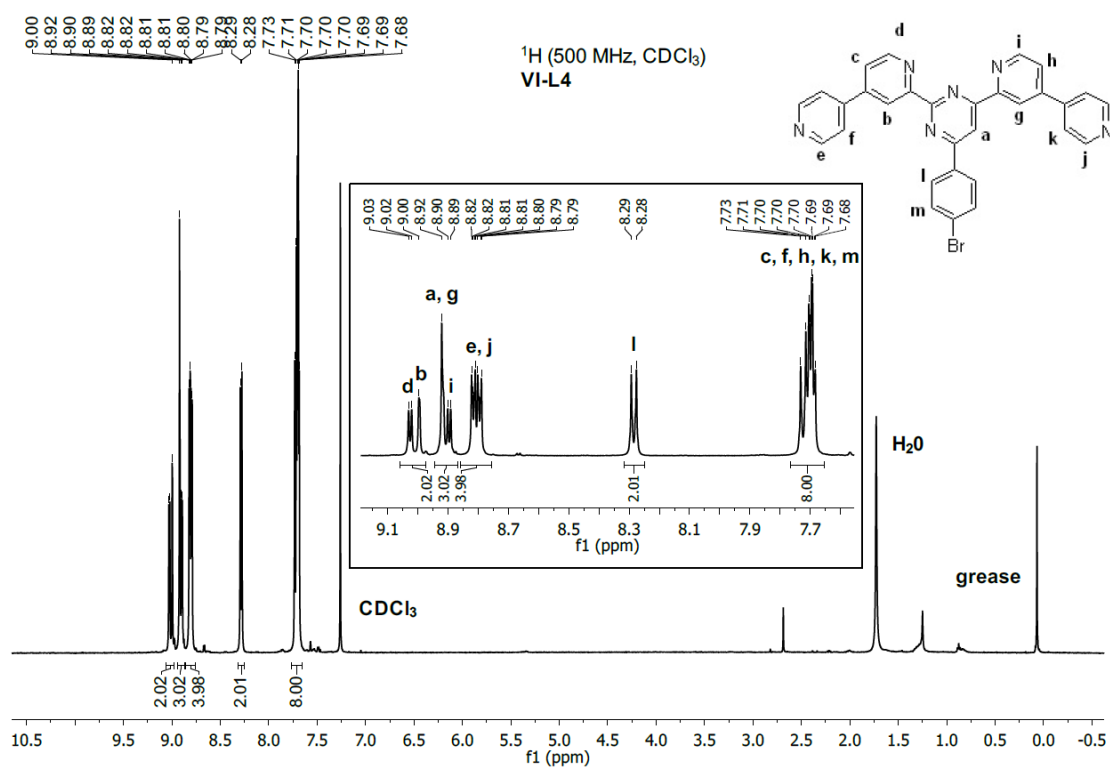
Figure IX-24. ^1H -NMR spectrum (300 MHz, DMSO- d_6) of VI-13.Figure IX-25. ^1H -NMR spectrum (300 MHz, CDCl_3) of VI-14.

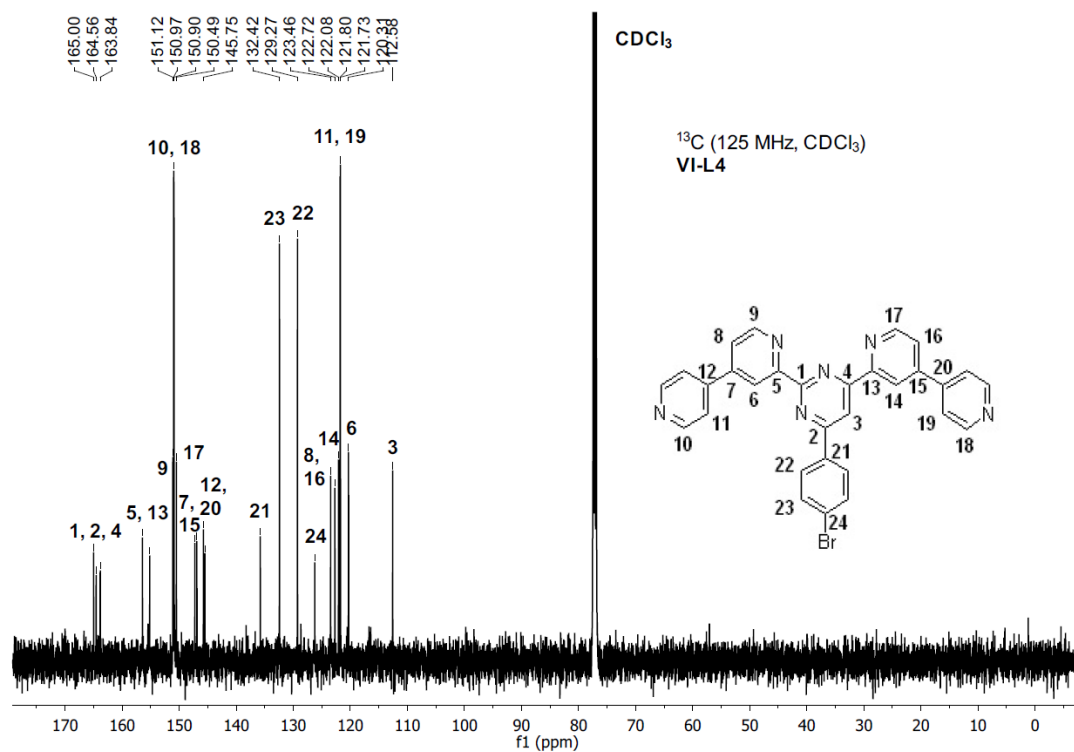
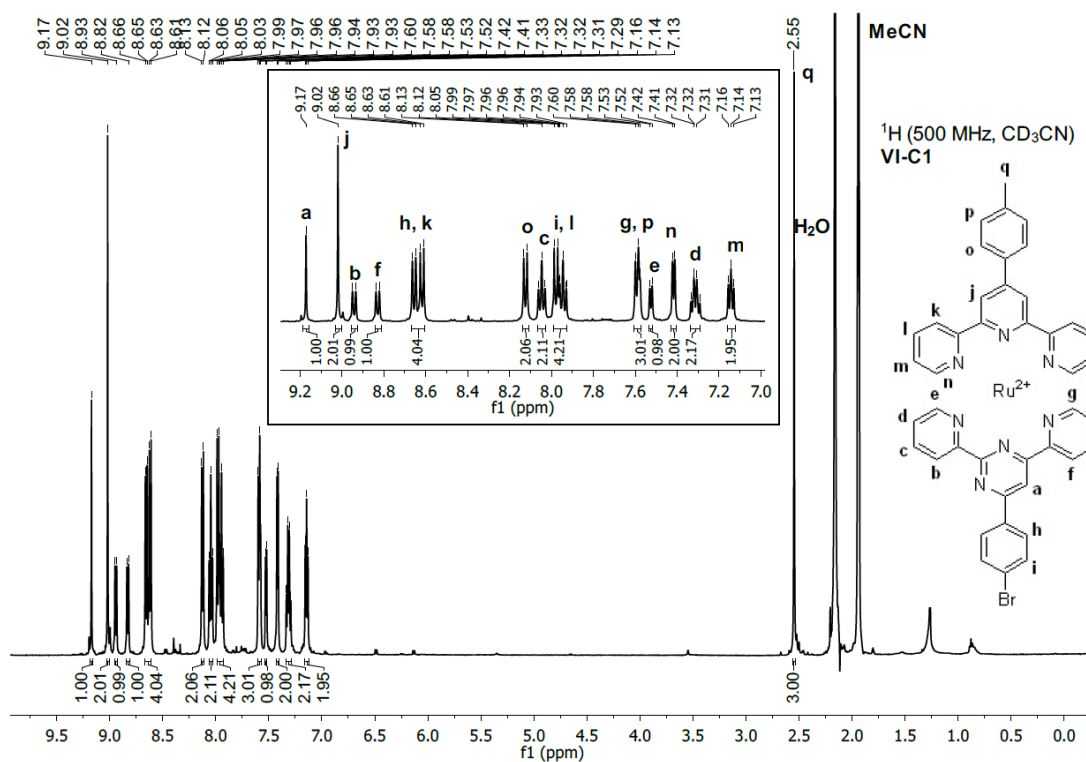
Figure IX-26. ¹H-NMR spectrum (300 MHz, DMSO-d₆) of VI-5.Figure IX-27. ¹H-NMR spectrum (300 MHz, DMSO-d₆) of VI-6.

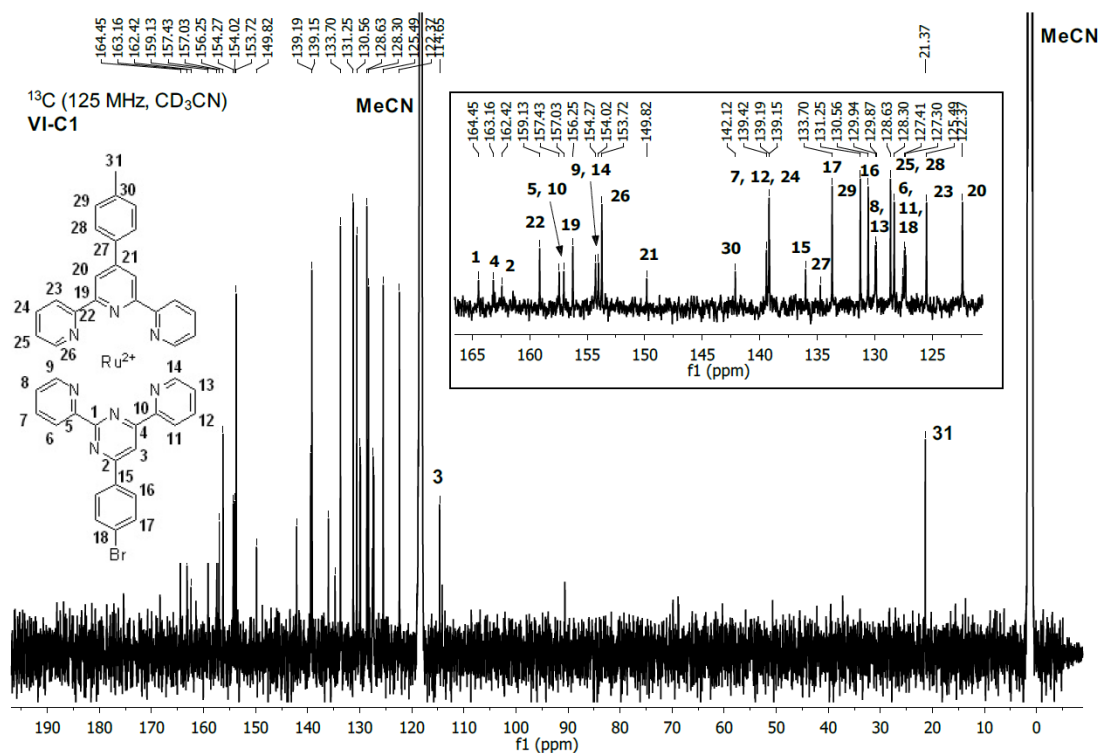
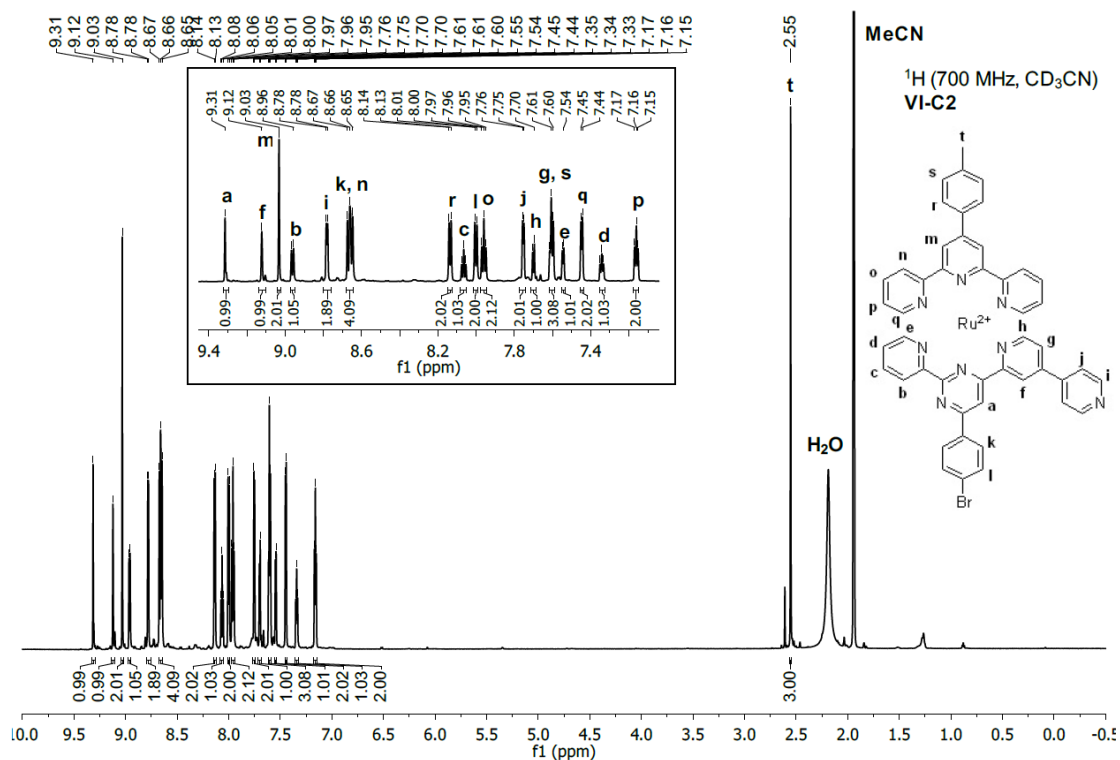
Figure IX-28. ¹³C-NMR spectrum (75 MHz, DMSO-d₆) of VI-I6.Figure IX-29. ¹H-NMR spectrum (500 MHz, CDCl₃) of VI-L1.

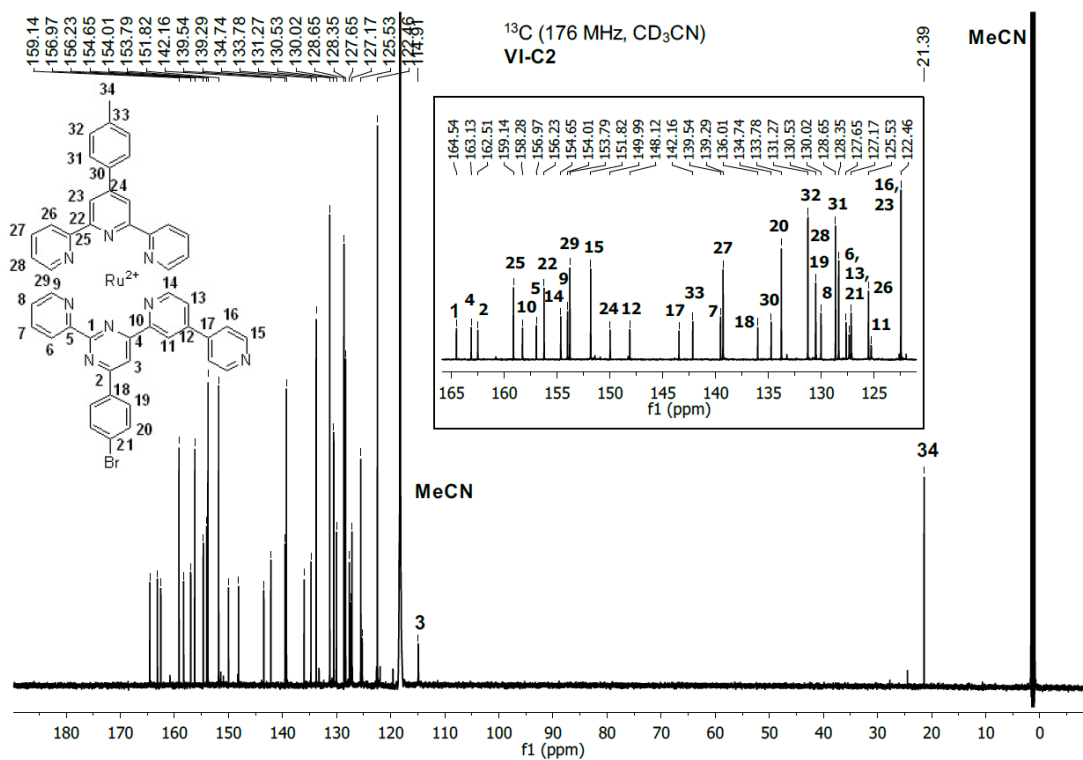
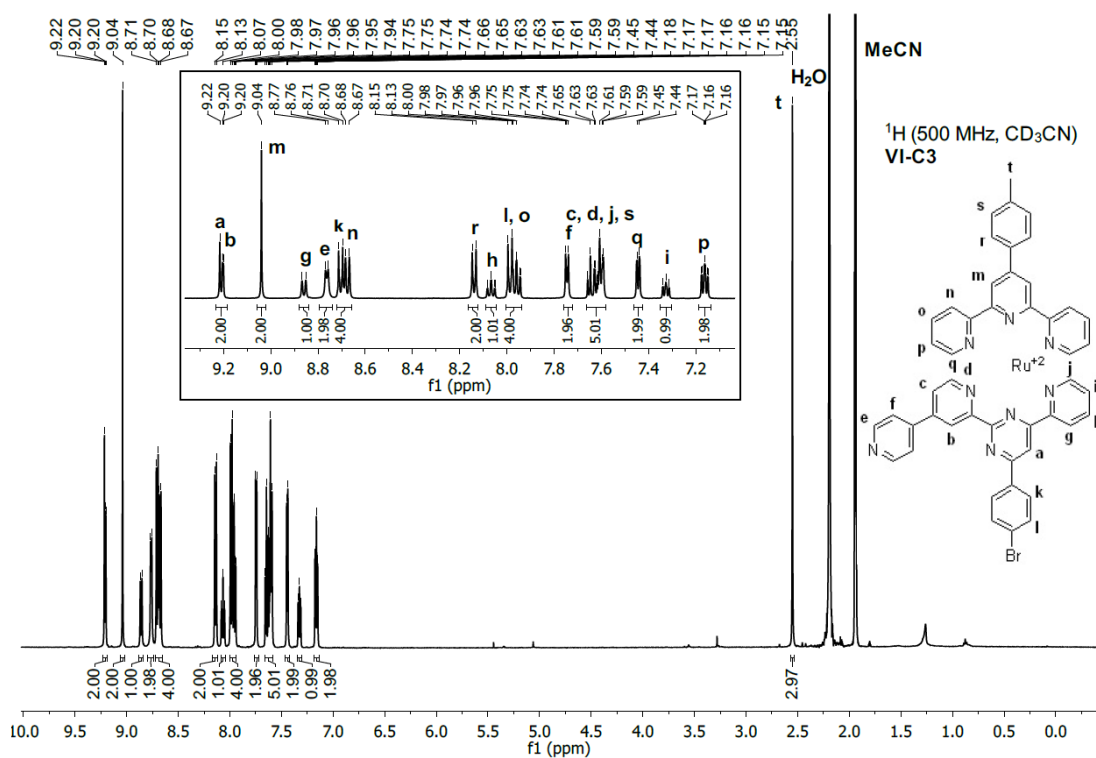
Figure IX-30. ¹³C-NMR spectrum (125 MHz, CDCl₃) of VI-L1.Figure IX-31. ¹H-NMR spectrum (500 MHz, CDCl₃) of VI-L2.

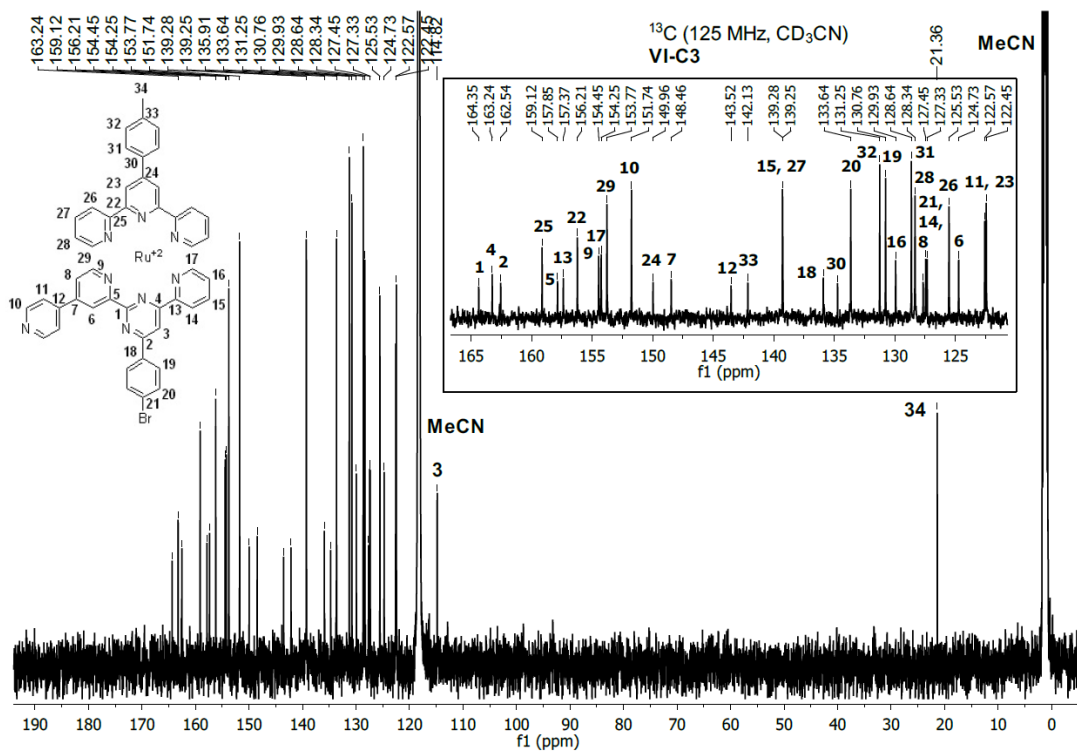
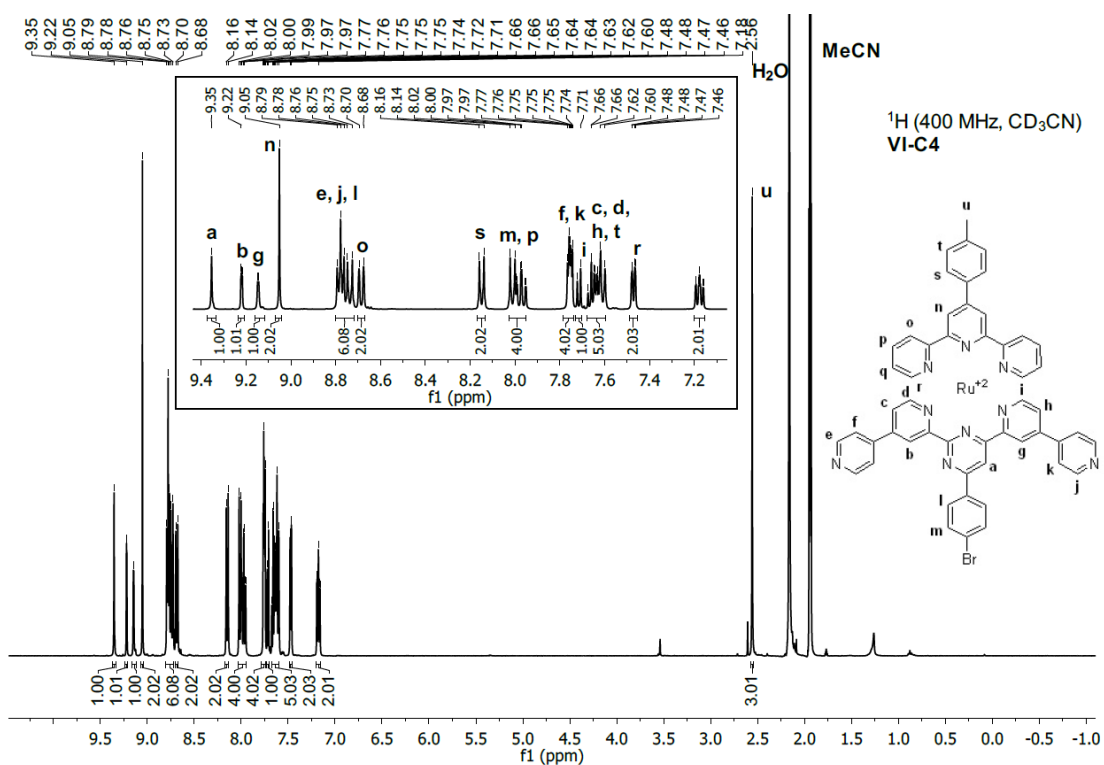
Figure IX-32. ^{13}C -NMR spectrum (125 MHz, CDCl_3) of VI-L2.Figure IX-33. ^1H -NMR spectrum (300 MHz, CDCl_3) of VI-L3.

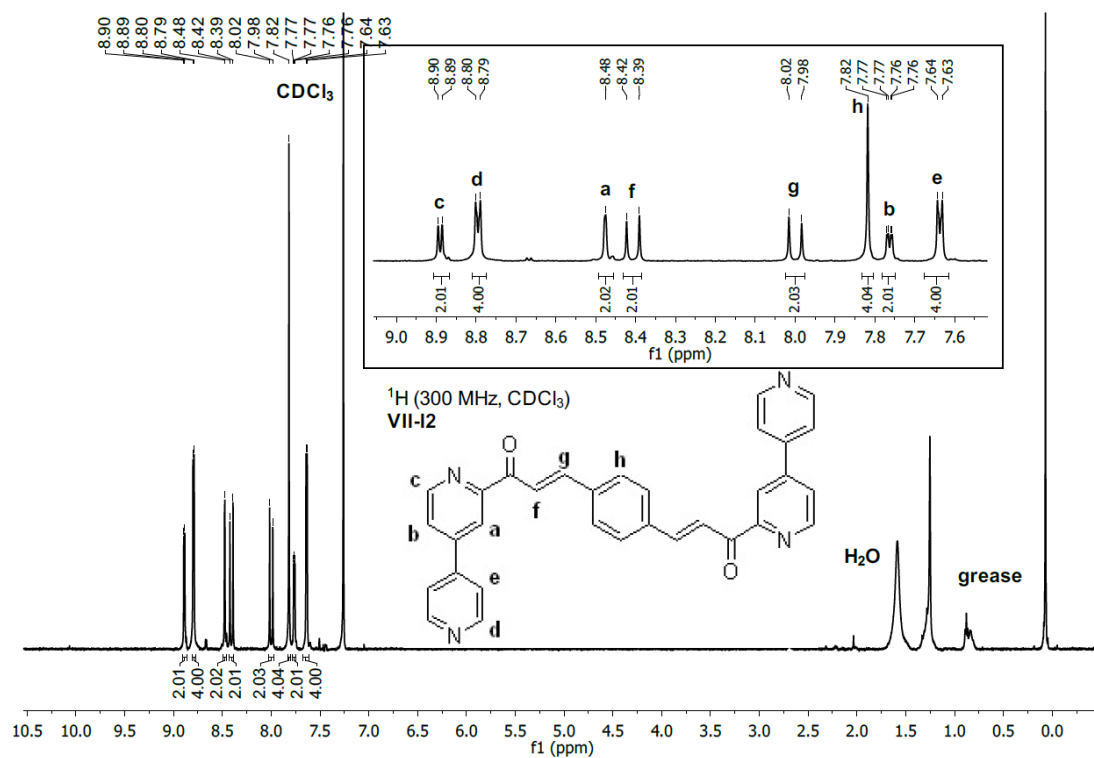
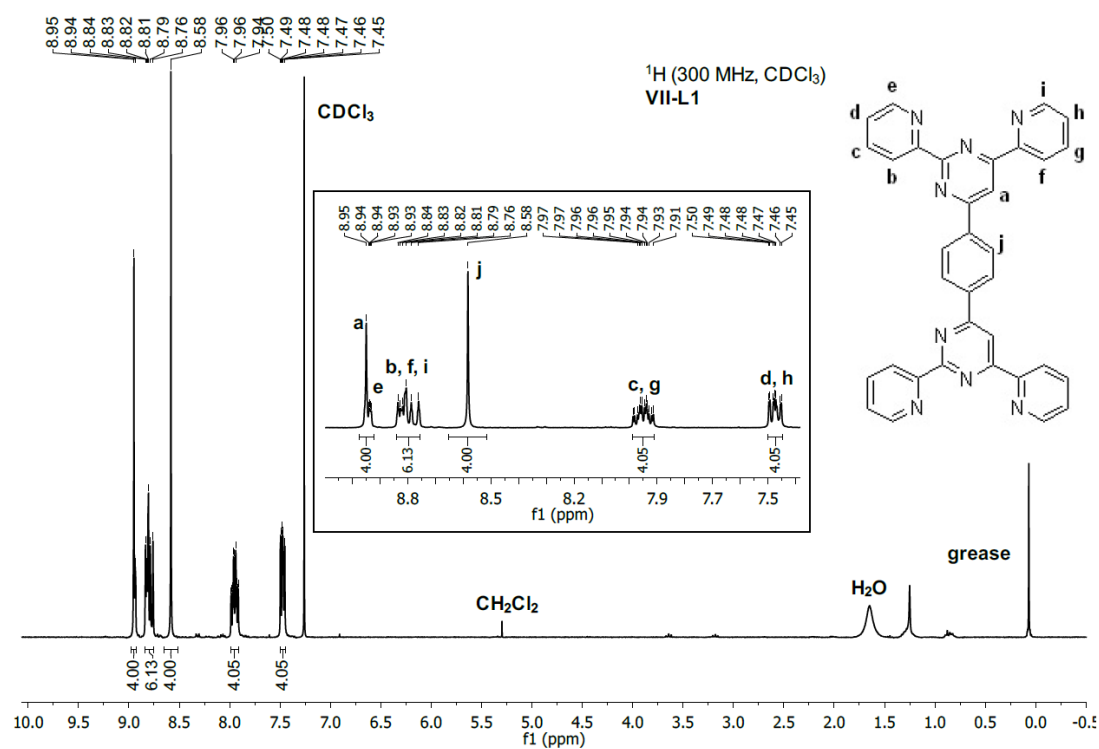
Figure IX-34. ¹³C-NMR spectrum (100 MHz, CDCl₃) of VI-L3.Figure IX-35. ¹H-NMR spectrum (500 MHz, CDCl₃) of VI-L4.

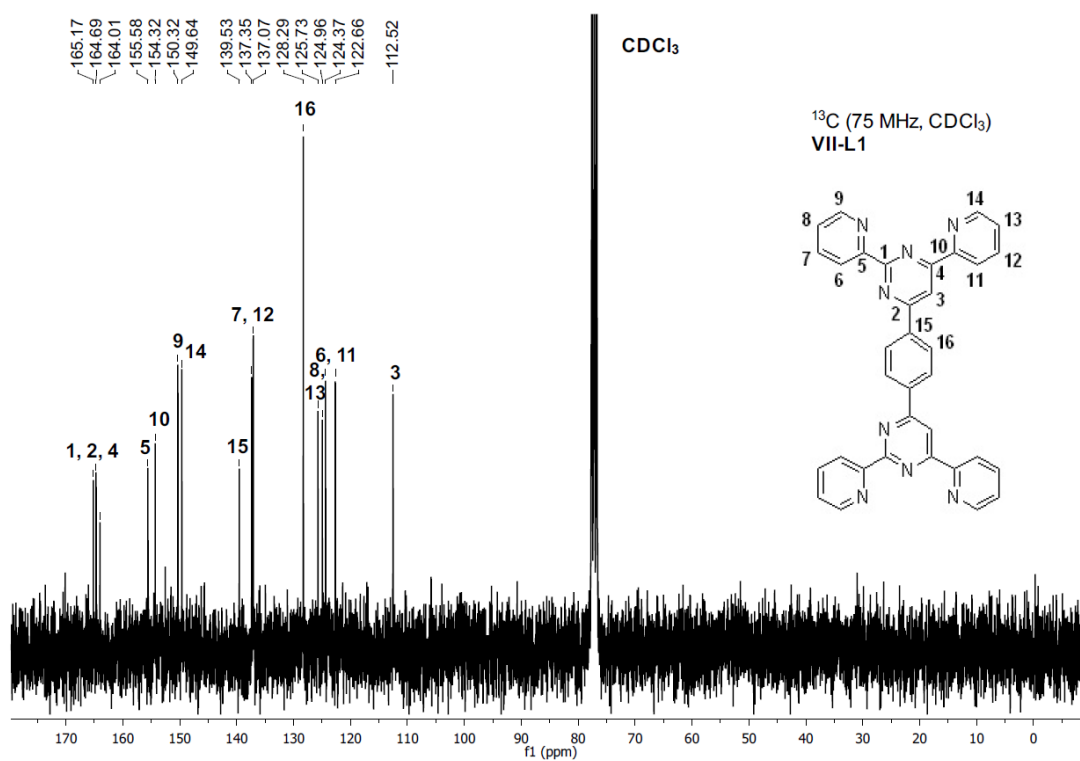
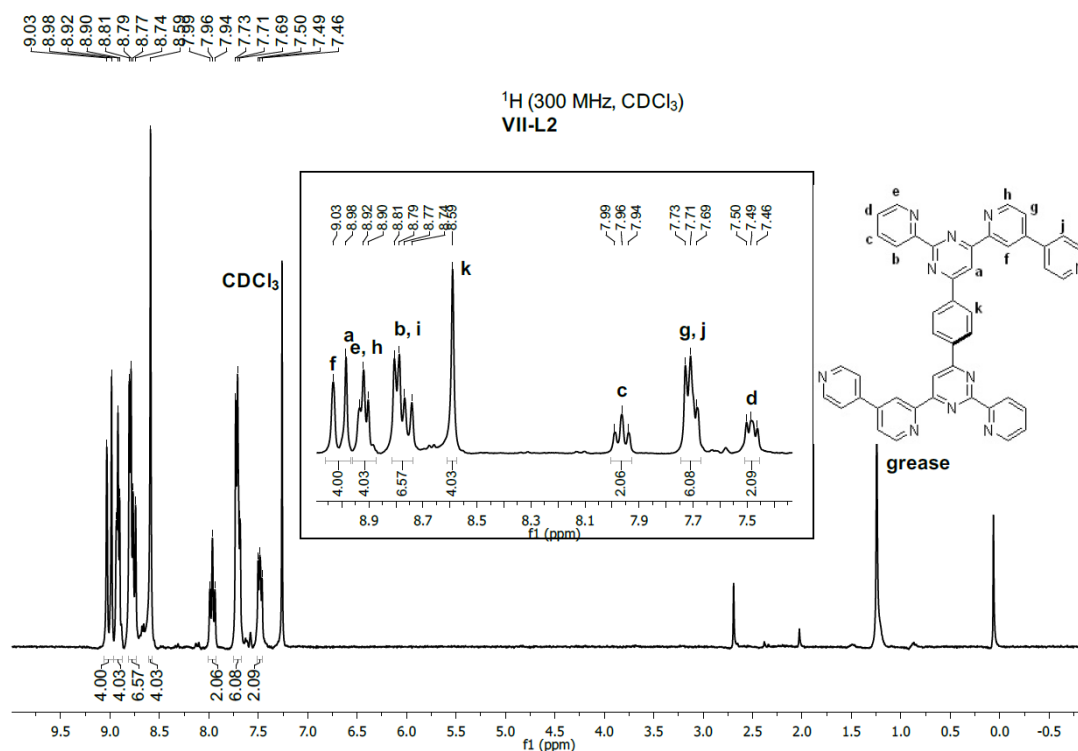
Figure IX-36. ¹³C-NMR spectrum (125 MHz, CDCl₃) of VI-L4.Figure IX-37. ¹H-NMR spectrum (500 MHz, CD₃CN) of VI-C1.

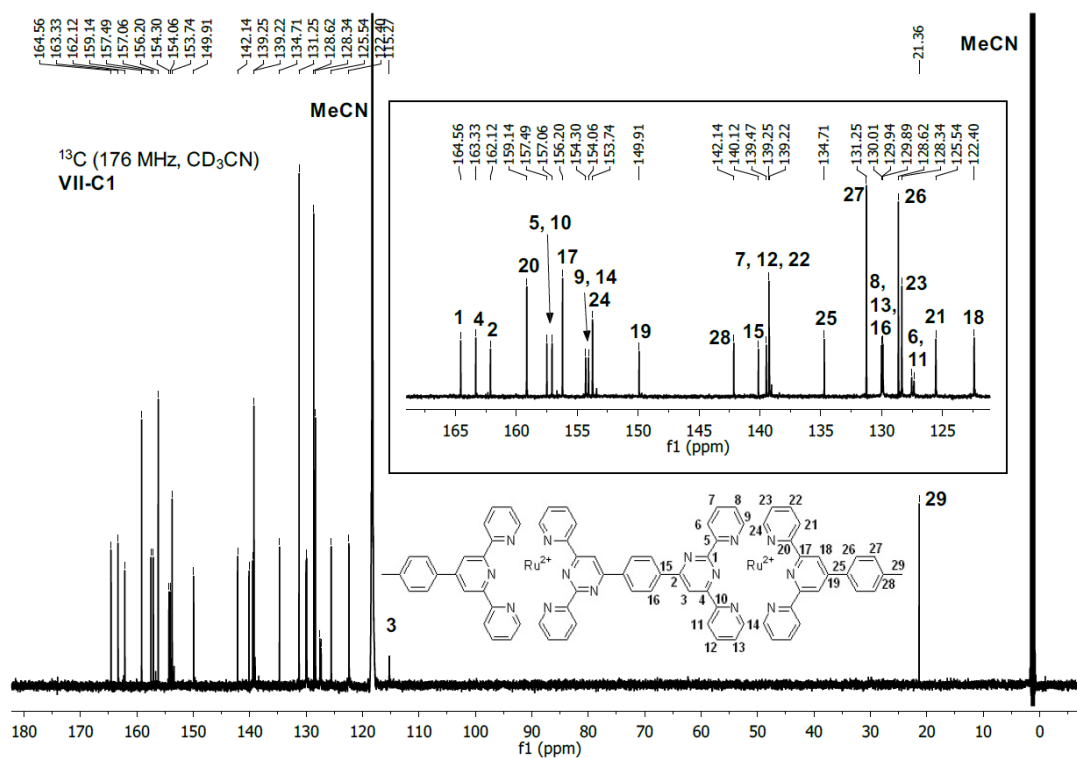
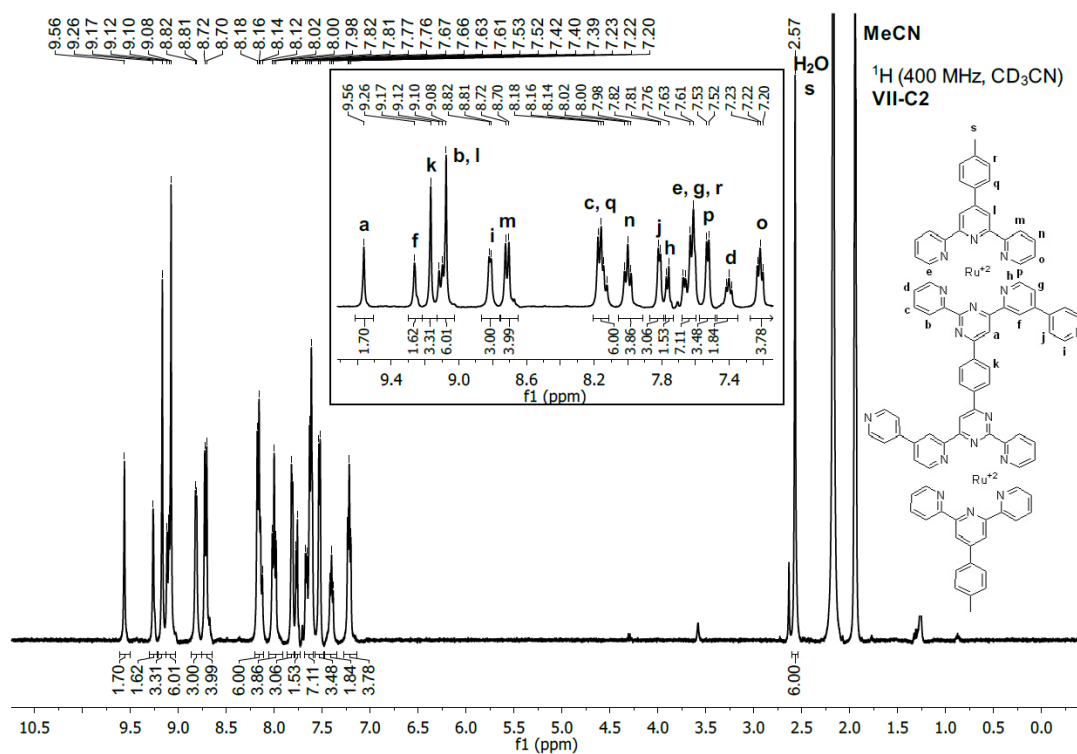
Figure IX-38. ¹³C-NMR spectrum (125 MHz, CD₃CN) of VI-C1.Figure IX-39. ¹H-NMR spectrum (700 MHz, CD₃CN) of VI-C2.

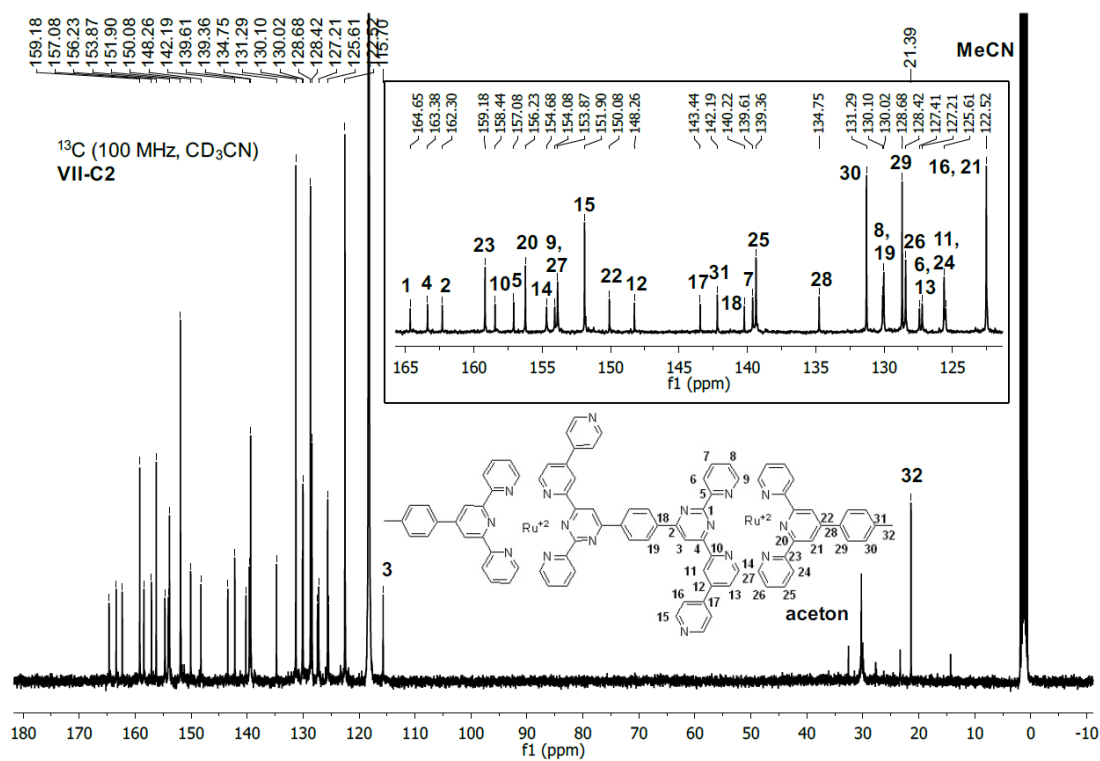
Figure IX-40. ¹³C-NMR spectrum (176 MHz, CD₃CN) of VI-C2.Figure IX-41. ¹H-NMR spectrum (500 MHz, CD₃CN) of VI-C3.

Figure IX-42. ¹³C-NMR spectrum (125 MHz, CD₃CN) of VI-C3.Figure IX-43. ¹H-NMR spectrum (400 MHz, CD₃CN) of VI-C4.

Figure IX-46. ¹H-NMR spectrum (300 MHz, CDCl₃) of VII-12.Figure IX-47. ¹H-NMR spectrum (300 MHz, CDCl₃) of VII-L1.

Figure IX-48. ¹³C-NMR spectrum (75 MHz, CDCl₃) of VII-L1.Figure IX-49. ¹H-NMR spectrum (300 MHz, CDCl₃) of VII-L2.

Figure IX-52. ¹³C-NMR spectrum (176 MHz, CD₃CN) of VII-C1.Figure IX-53. ¹H-NMR spectrum (400 MHz, CD₃CN) of VII-C2.

Figure IX-54. ¹³C-NMR spectrum (100 MHz, CD₃CN) of VII-C2.

IX.4. Crystallography

Suitable crystals were obtained either by slow diffusion of diethyl ether into the concentrated acetonitrile solution of the sample or by slow evaporation of an acetonitrile/water mix containing the sample. A red block was taken out of the mother liquor and mounted on a glass fiber loop. The data collection was carried out either on a Bruker Venture Metaljet diffractometer using Ga-K α radiation ($\lambda = 1.34139 \text{ \AA}$) at 150 K or 120 K, or on a Bruker microstar X8 diffractometer using Cu-K α radiation ($\lambda = 1.54178 \text{ \AA}$) at 100 K. The cell parameters were determined from reflections taken from three sets of omega scans (104 or 110 frames, 1° per frame) using APEX3 software package. Data reduction was performed with SAINT, adsorption correction with SADABS.^[238] The structure was solved via SHELXT^[239] in Olex2^[240]. The non-H atoms were refined anisotropically with SHELXL^[241], using weighted full-matrix least-squares on F^2 , the H-atoms were included in calculated positions and treated as riding atoms. Mercury CSD 2.0^[242] was used to prepare the reported figures.

CIF files of the reported structures can be found in the **Digital Appendix**.

IX.4.1.III-C1

A suitable crystal of **III-C1** was obtained by slow diffusion of diethyl ether into a concentrated acetonitrile solution of **III-C1**.

An initial model led to the complex with one PF₆⁻ counter-anion and a co-crystallized acetonitrile molecule. The PF₆⁻ anion appeared to be disordered and was modeled with two parts (67-33 ratio refined through a free variable) as well as RIGU and SADI restraints. This model, albeit incorrect regarding the electroneutrality, could not be further completed, despite many unassigned densities (max Q peak = 2.4), suggesting a disordered diethyl ether molecule, but none matching the expected second PF₆⁻. Thus, the solvent mask imbedded in Olex2 was used, removing a total of 160.5 electrons in a volume of 527.7 \AA^3 matching the expected count for the missing PF₆⁻ and at least one co-crystallized diethyl ether molecule (111 electrons).

Table IX-1. Refinement parameters for complex III-C1 (CCDC 1872343).

Empirical formula	C ₅₅ H ₄₀ BrF ₆ N ₉ PRu
Formula weight	1152.91
Temperature/K	150
Crystal system	Triclinic
Space group	P-1
<i>a</i> /Å	9.0475(3)
<i>b</i> /Å	16.2790(6)
<i>c</i> /Å	19.8838(7)
<i>α</i> /°	101.823(2)
<i>β</i> /°	92.792(2)
<i>γ</i> /°	103.294(2)
Volume/Å ³	2775.48(17)
<i>Z</i>	2
ρ_{calc} /g/cm ³	1.380
μ /mm ⁻¹	2.635
F(000)	1162.0
Crystal size/mm ³	0.16 × 0.12 × 0.09
Radiation	Ga K α (λ = 1.34139 Å)
2 θ range for data collection/°	4.978 to 121.708
Index ranges	-11 ≤ <i>h</i> ≤ 11, -21 ≤ <i>k</i> ≤ 21, -25 ≤ <i>l</i> ≤ 25
Reflections collected	68449
Independent reflections	12764 [<i>R</i> _{int} = 0.0453, <i>R</i> _{sigma} = 0.0294]
Data/restraints/parameters	12764/192/715
Goodness-of-fit on F ²	1.064
Final <i>R</i> indexes [<i>I</i> ≥ 2 σ (<i>I</i>)]	<i>R</i> ₁ = 0.0676, <i>wR</i> ₂ = 0.2093
Final <i>R</i> indexes [all data]	<i>R</i> ₁ = 0.0801, <i>wR</i> ₂ = 0.2235
Largest diff. peak/hole / e Å ⁻³	1.04/-0.81

IX.4.2.III-C2

A suitable crystal of **III-C2** was obtained by slow diffusion of diethyl ether into a concentrated acetonitrile solution of **III-C2**.

The initial model showed both PF_6^- counter ions. Yet, one of them was disordered on two positions with one position being on a symmetry element. SIMU and SADI restraints were used on one of the modelled PF_6^- counter ions. While several of the fluoride atoms still appeared to be further disordered, modelling this disorder only added more restraints without improving the model. Furthermore, the structure contained channels filled with solvent molecules (acetonitrile and diethyl ether), which were too disordered to be modelled properly. Hence, unassigned densities (max Q peak = 5.3) were accounted for using a SQUEEZE^[243] solvent mask. The solvent mask was calculated, and 284 electrons were found in a volume of 1182 Å³ in two voids per unit cell. This is consistent with the presence of a total of one and a half acetonitrile molecules and one diethyl ether molecule per asymmetric unit, which account for 300 electrons per unit cell. By implementing the SQUEEZE solvent mask, the R_1 value was improved from 10.73 to 5.70. The C-C bond precision changed from 0.0095 Å to 0.0061 Å. All reflections where $|\text{Error/esd}| > 9$ were omitted for the final model.

Table IX-2. Refinement parameters for complex III-C2 (CCDC 2090569).

Empirical formula	C ₅₁ H ₄₇ BrF ₁₂ N ₆ P ₂ Ru
Formula weight	1214.86
Temperature/K	150
Crystal system	Monoclinic
Space group	P2/c
<i>a</i> /Å	22.9599(18)
<i>b</i> /Å	9.2613(8)
<i>c</i> /Å	29.691(2)
<i>α</i> /°	90
<i>β</i> /°	110.303(3)
<i>γ</i> /°	90
Volume/Å ³	5921.2(8)
<i>Z</i>	4
$\rho_{\text{calc}}/\text{g/cm}^3$	1.363
μ/mm^{-1}	2.73
F(000)	2448.0
Crystal size/mm ³	0.37 × 0.24 × 0.04
Radiation	Ga K α ($\lambda = 1.34139 \text{ \AA}$)
2 θ range for data collection/°	4.376 to 55.989
Index ranges	-28 ≤ <i>h</i> ≤ 27, -11 ≤ <i>k</i> ≤ 11, -36 ≤ <i>l</i> ≤ 36
Reflections collected	48137
Independent reflections	11691 [<i>R</i> _{int} = 0.0565, <i>R</i> _{sigma} = 0.0492]
Data/restraints/parameters	11691/120/698
Goodness-of-fit on F ²	1.064
Final <i>R</i> indexes [<i>I</i> ≥ 2 σ (<i>I</i>)]	<i>R</i> ₁ = 0.0570, <i>wR</i> ₂ = 0.1646
Final <i>R</i> indexes [all data]	<i>R</i> ₁ = 0.0625, <i>wR</i> ₂ = 0.1700
Largest diff. peak/hole / e Å ⁻³	1.06/-0.60

IX.4.3.IV-C2

Suitable crystals of **IV-C2** were obtained by slow evaporation of a solution of **IV-C2** in an acetonitrile/water mix.

The initial model of **IV-C2** only showed one of the expected two PF₆⁻ counter ions. Furthermore, two co-crystallized water molecules were modelled and treated as rigid groups. Despite unassigned densities (max Q peak = 3.4), which suggested another disordered PF₆⁻ counter ion and water molecule, and the model being incorrect regarding the electroneutrality, it could not be further refined. Thus, the solvent mask SQUEEZE was used to account for the missing PF₆⁻ counter ion as well as co-crystallized solvent molecules. The calculated solvent mask found 350 electrons in a volume of 1000 Å³ in 3 voids per unit cell, which is consistent with the presence of one PF₆⁻ counter ion and two water molecules per asymmetric unit. By implementing the SQUEEZE solvent mask, the R₁ value was improved from 11.6 to 7.2. The C-C bond precision changed from 0.0097 Å to 0.0068 Å. All reflections where |Error/esd| > 9 were omitted for the final model.

Table IX-3. Refinement parameters for complex **IV-C2** (CCDC 2034792).

Empirical formula	C ₆₂ H ₄₀ Br ₂ N ₁₀ RuPF ₆ (H ₂ O) ₂
Formula weight	1366.93
Temperature/ K	120
Crystal system	Monoclinic
Space group	P21/n
<i>a</i> / Å	12.7078(4)
<i>b</i> / Å	12.2776(3)
<i>c</i> / Å	40.6906(11)
α / °	90
β / °	92.154(2)
γ / °	90
Volume/ Å ³	6344.1(3)
<i>Z</i>	4
ρ_{calc} / g/cm ³	1.431
μ / mm ⁻¹	2.854
F(000)	2740
Crystal size/ mm ³	0.06 × 0.095 × 0.185
Radiation	Ga K α (λ = 1.34139 Å)
2 θ range for data collection/ °	1.890 to 72.121
Index ranges	-16 ≤ <i>h</i> ≤ 17, -12 ≤ <i>k</i> ≤ 16, -46 ≤ <i>l</i> ≤ 54
Reflections collected	75320
Independent reflections	17675 [<i>R</i> _{int} = 0.0613, <i>R</i> _{sigma} = 0.0452]
Data/ restraints/ parameters	17675/0/763
Goodness-of-fit on F ²	1.104
Final <i>R</i> indexes [<i>I</i> ≥ 2 σ (<i>I</i>)]	<i>R</i> ₁ = 0.0722, <i>wR</i> ₂ = 0.2508
Final <i>R</i> indexes [all data]	<i>R</i> ₁ = 0.0958, <i>wR</i> ₂ = 0.2303
Largest diff. peak/hole / e Å ⁻³	1.439/-1.051

IX.4.4.V-C1

Suitable crystals of **V-C1** were obtained by slow diffusion of diethyl ether into the concentrated acetonitrile solution of **V-C1**.

The initial model of **V-C1** suggested that the four PF_6^- anions were disordered on a total of five positions. The occupancy of the anion sites was left to refine as free variables using the SUMP restraint. The occupancies were then fixed to the nearest rational number. Furthermore, one of the PF_6^- anions appeared to be disordered in two orientations. Two sets of fluorides were modeled, and their relative occupancy refined as a free variable. SADI and SIMU restraints were used to obtain a suitable model for the anions. Other anions also appeared to be split. However, modeling the disorder only added more restraints without improving the model. Those anions were thus not further modified. Unassigned densities (max Q peak = 2.8) were accounted for using a SQUEEZE solvent mask. The solvent mask was calculated, and 484 electrons were found in a volume of 2508 Å^3 in four voids per unit cell. This is consistent with the presence of a total of three acetonitrile molecules per asymmetric unit, which account for 528 electrons per unit cell. By implementing the SQUEEZE solvent mask, the R_1 value was improved from 12.9 to 9.4. The C-C bond precision changed from 0.0168 Å to 0.0127 Å . All reflections where $|\text{Error/esd}| > 10$ were omitted for the final model.

Table IX-4. Refinement parameters for complex **V-C1** (CCDC 2034795).

Empirical formula	C ₅₅ H ₄₃ BrN ₈ Ru(PF ₆) ₄
Formula weight	1576.83
Temperature/ K	100
Crystal system	Monoclinic
Space group	C2/c
<i>a</i> / Å	15.1457(14)
<i>b</i> / Å	26.046(2)
<i>c</i> / Å	35.203(3)
α / °	90
β / °	92.684(4)
γ / °	90
Volume/ Å ³	13872(2)
<i>Z</i>	8
ρ_{calc} / g/cm ³	1.510
μ / mm ⁻¹	4.333
F(000)	6272.0
Crystal size/ mm ³	0.38 × 0.22 × 0.09
Radiation	Cu K α (λ = 1.54178 Å)
2 θ range for data collection/ °	2.513 to 70.365
Index ranges	-18 ≤ <i>h</i> ≤ 18, -31 ≤ <i>k</i> ≤ 31, -42 ≤ <i>l</i> ≤ 40
Reflections collected	55217
Independent reflections	13013 [<i>R</i> _{int} = 0.0838, <i>R</i> _{sigma} = 0.0773]
Data/ restraints/ parameters	13013/307/910
Goodness-of-fit on F ²	1.018
Final <i>R</i> indexes [<i>I</i> ≥ 2 σ (<i>I</i>)]	<i>R</i> ₁ = 0.0935, <i>wR</i> ₂ = 0.3111
Final <i>R</i> indexes [all data]	<i>R</i> ₁ = 0.1502, <i>wR</i> ₂ = 0.2602
Largest diff. peak/hole / e Å ⁻³	1.911/-0.895

IX.4.5.VI-C1

Suitable crystals of **VI-C1** were obtained by slow evaporation of an acetonitrile/water solution of **VI-C1**.

The initial model of **VI-1** suggested that the PF₆⁻ anions were disordered on two positions. Therefore, two sets of fluorides were modeled for each anion, and their relative occupancy was refined as free variables. SADI and SIMU restraints were used to obtain a suitable model for the anions. Furthermore, the complex seemed to be disordered in two orientations. The nitrogen atom of the central pyrimidine ring and a carbon atom were modelled to share the same sites using EXYZ and EADP restraints. The methyl group as well as the bromine were modelled in different positions and SADI and SIMU restraints were used to obtain a suitable model. The co-crystallized acetonitrile and water molecule were left to freely refine and the occupancy was fixed to the nearest rational number. The disordered methyl groups as well as the co-crystallized solvent molecules were modelled using DFIX and ISOR restraints to obtain a suitable model. All reflections where |Error/esd| > than 10 were omitted for the final model.

Table IX-5. Refinement parameters for complex **VI-C1** (CCDC 1997105).

Empirical formula	C ₄₂ H ₃₀ BrN ₇ Ru(PF ₆) ₂ ·0.5 CH ₃ CN·0.125 H ₂ O
Formula weight	1126.43
Temperature/ K	100
Crystal system	Triclinic
Space group	P-1
<i>a</i> / Å	9.0673(1)
<i>b</i> / Å	12.7615(2)
<i>c</i> / Å	18.9979(3)
<i>α</i> / °	84.951(1)
<i>β</i> / °	79.029(1)
<i>γ</i> / °	89.968(1)
Volume/ Å ³	2149.45(5)
<i>Z</i>	2
ρ_{calc} / g/cm ³	1.740
μ / mm ⁻¹	5.607
F(000)	1120.0
Crystal size/ mm ³	0.11 × 0.06 × 0.05
Radiation	Cu K α (λ = 1.54178 Å)
2 θ range for data collection/ °	2.378 to 71.824
Index ranges	-11 ≤ <i>h</i> ≤ 11, -15 ≤ <i>k</i> ≤ 15, -22 ≤ <i>l</i> ≤ 23
Reflections collected	57175
Independent reflections	8125 [<i>R</i> _{int} = 0.0270, <i>R</i> _{sigma} = 0.0152]
Data/ restraints/ parameters	8125/629/793
Goodness-of-fit on F ²	1.078
Final <i>R</i> indexes [<i>I</i> ≥ 2 σ (<i>I</i>)]	<i>R</i> ₁ = 0.0342, <i>wR</i> ₂ = 0.0818
Final <i>R</i> indexes [all data]	<i>R</i> ₁ = 0.0371, <i>wR</i> ₂ = 0.0894
Largest diff. peak/hole / e Å ⁻³	0.591/-0.595

IX.4.6.VI-C4

Suitable crystals of **VI-C4** were obtained by slow diffusion of diethyl ether into a concentrated acetonitrile solution of **VI-C4**.

The initial model of **VI-C4** showed that the PF_6^- anions were disordered on two positions. Two sets of fluorides were modeled for each disordered anion, and their relative occupancy refined as free variables. DFIX and SIMU restraints were used to obtain a suitable model for the anions. Furthermore, the bromophenyl ring seemed to be disordered and SADI, SIMU and FLAT restraints were used to obtain a suitable model. In addition, the co-crystallized diethyl ether appeared to be disordered and was modelled using SADI restraints. The occupancy of the disordered atoms was left to refine as free variable.

Table IX-6. Refinement parameters for complex VI-4 (CCDC 1997099).

Empirical formula	C ₅₂ H ₃₆ BrN ₉ Ru(PF ₆) ₂ ·C ₄ H ₁₀ O·2CH ₃ CN
Formula weight	1414.04
Temperature/K	100
Crystal system	Monoclinic
Space group	I2/a
<i>a</i> / Å	16.2651(4)
<i>b</i> / Å	36.7892(10)
<i>c</i> / Å	19.7290(6)
<i>α</i> / °	90
<i>β</i> / °	92.150(2)
<i>γ</i> / °	90
Volume/ Å ³	11797.1(6)
<i>Z</i>	8
ρ_{calc} / g/cm ³	1.592
μ / mm ⁻¹	4.250
F(000)	5712.0
Crystal size/ mm ³	0.40 × 0.06 × 0.02
Radiation	Cu K α (λ = 1.54178 Å)
2 θ range for data collection/°	2.402 to 72.196
Index ranges	-20 ≤ <i>h</i> ≤ 19, -45 ≤ <i>k</i> ≤ 45, -24 ≤ <i>l</i> ≤ 24
Reflections collected	82116
Independent reflections	11594 [<i>R</i> _{int} = 0.0340, <i>R</i> _{sigma} = 0.0201]
Data/restraints/parameters	11594/328/1000
Goodness-of-fit on F ²	1.072
Final <i>R</i> indexes [<i>I</i> > 2 σ (<i>I</i>)]	<i>R</i> ₁ = 0.0398, <i>wR</i> ₂ = 0.1114
Final <i>R</i> indexes [all data]	<i>R</i> ₁ = 0.0417, <i>wR</i> ₂ = 0.1097
Largest diff. peak/hole / e Å ⁻³	0.884/-0.717

IX.5. Computational Details

Tables including the atomic coordinates of the optimized geometries of the investigated structures and a comparison of the experimental absorption spectra with the predicted transitions can be found in the **Digital Appendix**.

The calculations were made with Gaussian16 rev.B.01^[244], using the PBE0 hybrid functional^[245] with LanL2DZ^[246-249] as basis set. The optimizations were conducted without symmetry constraints, followed by frequency calculations to confirm that energy minima have been reached in all cases. The energy, oscillator strength, and related MO contributions for the 100 lowest singlet–singlet and 10 lowest singlet–triplet excitations were obtained from the TD-DFT/singlets and the TD-DFT/triplets output files, respectively, for the S_0 -optimized geometry. GaussView6, GaussSum3.3^[250] and Chemission4.53^[251] were used for data analysis, visualization and surface plots. All calculations were conducted for acetonitrile solvated complexes using a conductor like polarized continuum (CPCM) solvation model.^[252]

IX.5.1. Natural Transition Analysis

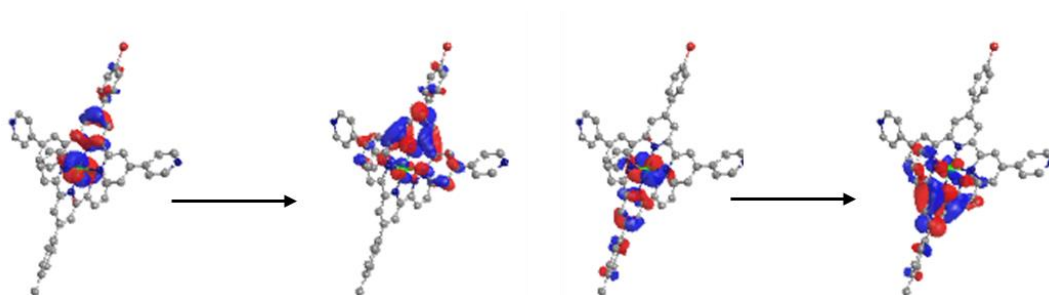


Figure IX-55. Natural transition analysis of the lowest singlet (left of arrow) to triplet (right of arrow) transition for complex **III-C1**; contributions of left transition 90%, contributions of right transition 6%.

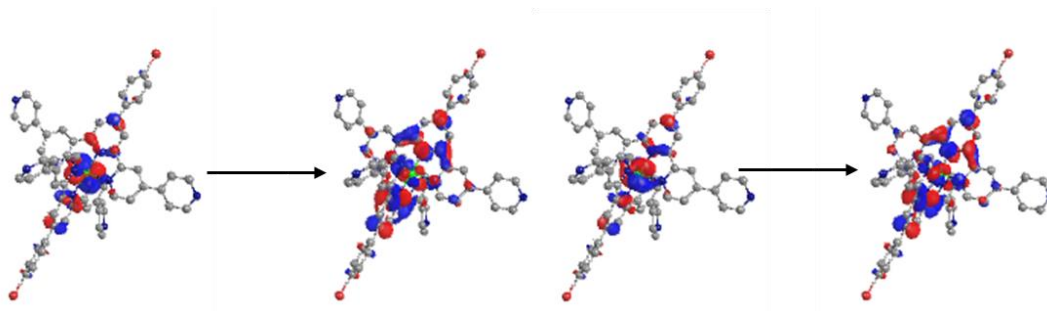


Figure IX-56. Natural transition analysis of the lowest singlet (left of arrow) to triplet (right of arrow) transition for complex **IV-C2**; contributions of left transition 48%, contributions of right transition 47%.

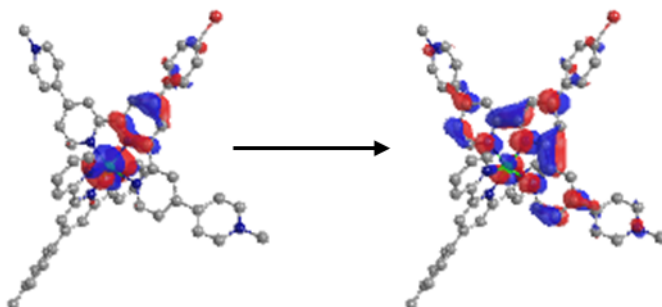


Figure IX-57. Natural transition analysis of the lowest singlet (left of arrow) to triplet (right of arrow) transition for complex **V-C1**.

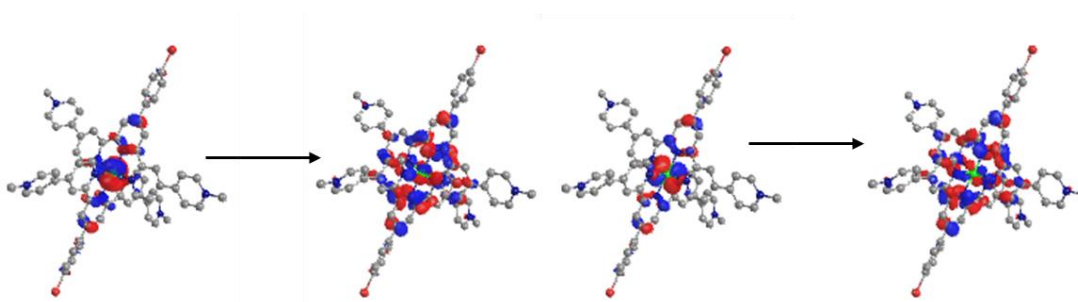


Figure IX-58. Natural transition analysis of the lowest singlet (left of arrow) to triplet (right of arrow) transition for complex **V-C2**; contributions of left transition 48%, contributions of right transition 48%.

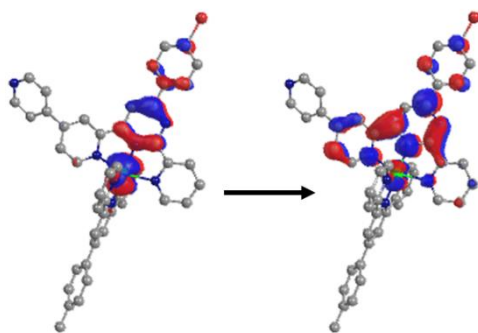


Figure IX-59. Natural transition analysis of the lowest singlet (left of arrow) to triplet (right of arrow) transition for complex **VI-C2**.

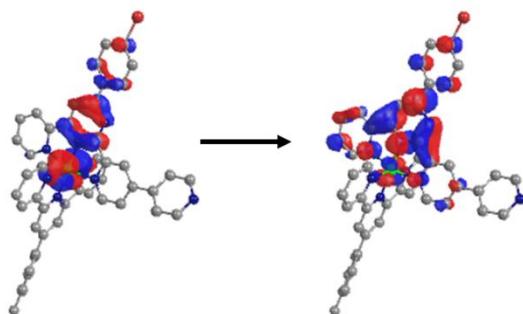


Figure IX-60. Natural transition analysis of the lowest singlet (left of arrow) to triplet (right of arrow) transition for complex **VI-C3**.

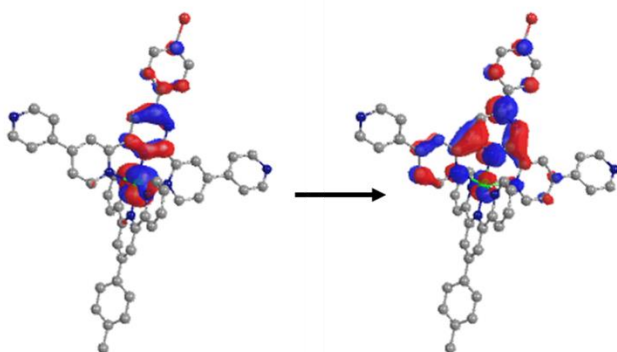


Figure IX-61. Natural transition analysis of the lowest singlet (left of arrow) to triplet (right of arrow) transition for complex **VI-C4**.

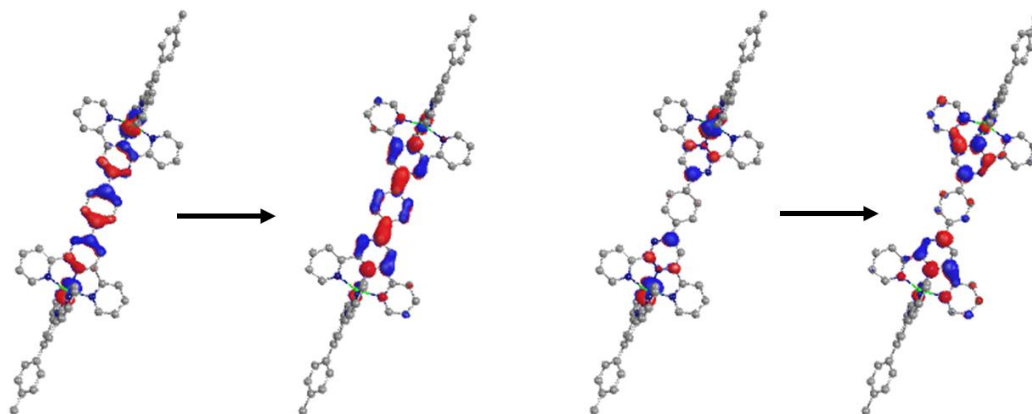


Figure IX-62. Natural transition analysis of the lowest singlet (left of arrow) to triplet (right of arrow) transition for complex **VII-C1**; contributions of left transition 76%, contributions of right transition 20%.

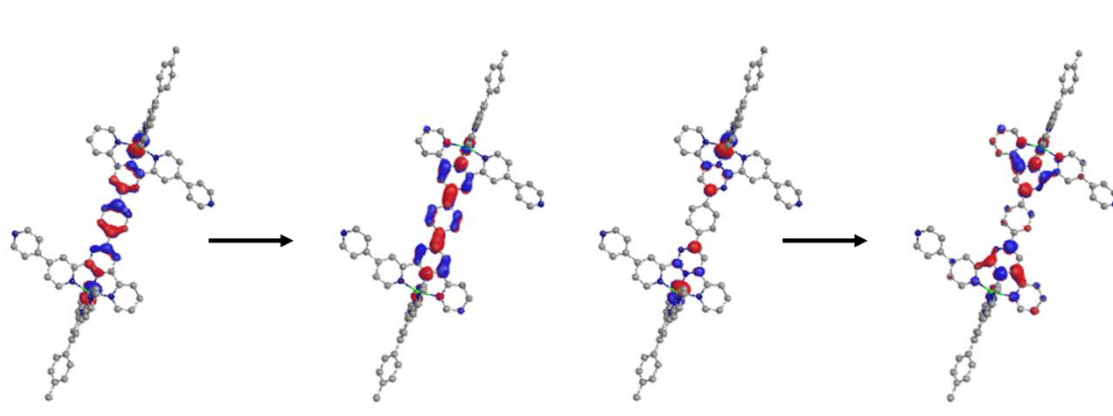
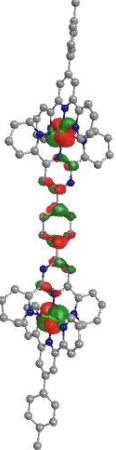
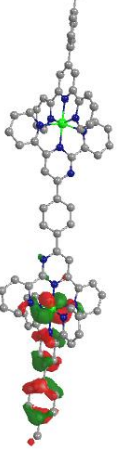
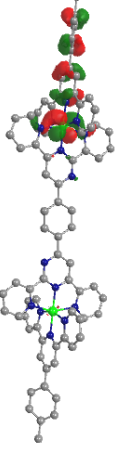
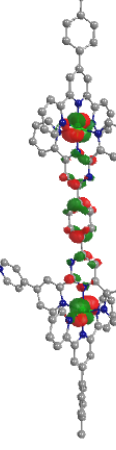
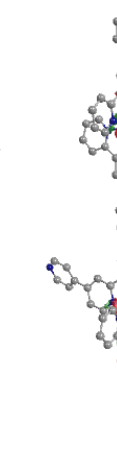

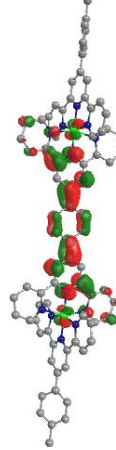
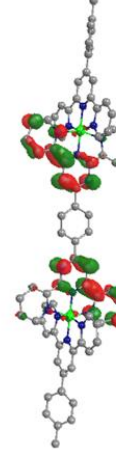
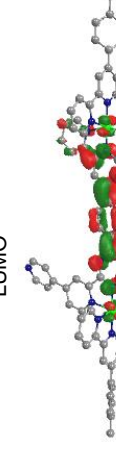
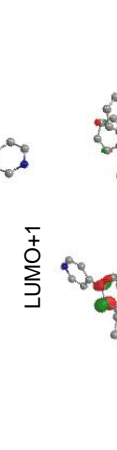
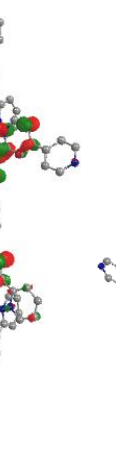
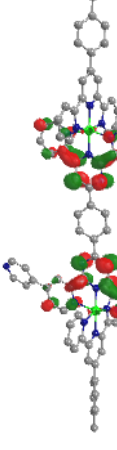


Figure IX-63. Natural transition analysis of the lowest singlet (left of arrow) to triplet (right of arrow) transition for complex **VII-C2**; contributions of left transition 77%, contributions of right transition 20%.

IX.5.2. Contributions to Molecular Orbitals

Table IX-7. Contributions to molecular orbitals for complexes VII-C1 and VII-C2.

	C1			C2		
HOMO						
	-6.61 eV Ru: 61% III-L3: 8% VI-L1: 31%	-6.63 eV Ru: 56% III-L3: 36% VI-L1: 8%	-6.63 eV Ru: 56% III-L3: 36% VI-L1: 8%	-6.64 eV Ru: 60% III-L3: 9% VI-L2: 31%	-6.65 eV Ru: 55% III-L3: 37% VI-L2: 8%	-6.65 eV Ru: 55% III-L3: 37% VI-L2: 8%
LUMO						
	-3.42 eV Ru: 9% III-L3: 1% VI-L1: 90%	-3.04 eV Ru: 2% III-L3: 2% VI-L1: 96%	-3.44 eV Ru: 9% III-L3: 1% VI-L2: 90%	-3.09 eV Ru: 2% III-L3: 2% VI-L2: 96%	-3.08 eV Ru: 2% III-L3: 2% VI-L2: 96%	-3.08 eV Ru: 2% III-L3: 2% VI-L2: 96%

IX.6. Hydrogen Production Experiments

Hydrogen evolution was monitored using a Perkin Elmer Clarus-480 gas chromatograph (GC) with a thermal conductivity detector, argon as carrier and eluent gas, a 7 ft. HayeSep N 60/80 pre-column, a 9 ft. molecular sieve 13 x 45/60 column and a 2 mL injection loop. Three distinct solutions for the sacrificial electron donor and proton source, the photosensitizer and the catalyst were prepared and mixed to obtain 5 mL of solutions in standard 20 mL headspace vials. Using DMF as a solvent, the resulting molar concentration of photocatalytic medium were: 1 M for triethanolamine (TEOA), 0.1 M for HBF₄, 0.56 M for water ($pH_{\text{apparent}} = 8.9$). The concentrations of active species were: 0.1 mM for the photosensitizer, 1 mM of cobalt pre-catalyst ([Co(H₂O)₆](BF₄)₂) or cobalt catalyst [Co(dmgH)₂(py)Cl] and 6 mM of dimethylglyoxime, or 0.05 mM of K₂[PtCl₄] as colloid precursor.

The vials were placed on top of a 450 nm (blue light irradiation), or a 630 nm (red light irradiation) centered LED set to an approximate 62 mW (blue light) or 45 mW (red light) output, in an aluminum cast connected to a thermostatic bath set at 20 °C. They were sealed with a rubber septum pierced with two stainless steel tubes. The first tube carried an argon flow pre-bubbled in DMF. The flow was set between 5 mL/min (adjusted with calibrated mass flow MCseries from Alicat) and referenced with a digital flowmeter (Perkin Elmer FlowMark) depending on the sample. The second tube led the flow to the GC sample loop through a 2 mL overflow protection vial, then through an 8-port stream select valve (VICCI) and finally to GC sample loop. A microprocessor (Arduino Uno) coupled with a custom PC interface allowed for timed injections. For calibration of the H₂ production rate at a specific argon flow, a syringe pump (New Era Pump) equipped with a gas-tight syringe (SGE) and a 26s gauge needle (Hamilton) was used to bubble different rates of pure hydrogen gas into the sample, to a minimum of 0.5 $\mu\text{L}/\text{minute}$. This gave a linear fit for the peak area of H₂ vs. the flow rates of H₂. For calibration testing, stock cylinders of known concentration of H₂ in argon replaced the argon flow (inserted at the pre-bubbler, to keep the same vapor matrix). The measured results, independent of flow rate (under same pressure) could be easily converted into a rate of hydrogen production following Equation IX-2. The errors associated to the *TON* (turn-over number) and *TOF* (turn-over frequency) were estimated to be within 10%.^[253]

$$\text{H}_2 \text{ rate } (\mu\text{L}/\text{min}) = [\text{H}_2 \text{ standard}] (\text{ppm}) \times \text{Ar flow rate } (\text{mL}/\text{min}) \quad \text{Equation IX-2}$$

$$\text{H}_2 \text{ rate } (\text{nmol}/\text{min}) = \text{H}_2 \text{ rate } (\mu\text{L}/\text{min}) / 24.45 \times 1000 \quad \text{Equation IX-3}$$

$$\text{TOF } (\text{mmol}_{\text{H}_2} \cdot \text{mol}_{\text{PS}} \cdot \text{min}^{-1}) = \text{H}_2 \text{ rate } (\text{nmol}/\text{min}) / n_{\text{PS}} (\text{mol}) / 10^6 \quad \text{Equation IX-4}$$

The amount of hydrogen produced between two injections was calculated using the average rate over that period of time $[t_i ; t_j]$, multiplied by the time between two injections $(t_j - t_i)$.

$$n_{\text{H}_2 \text{ total}} (\text{nmol}) = \sum_{t_0}^{t_f} n_{\text{H}_2} [t_i ; t_j] = \sum_{t_0}^{t_f} (\text{H}_2 \text{ rate } (t_i) + \text{H}_2 \text{ rate } (t_j)) / 2 \times (t_j - t_i) \quad \text{Equation IX-5}$$

For a chosen length of experiment (t_f) :

$$\text{TON}(t_f) = n_{\text{H}_2(t_f)} / n_{\text{PS}} \quad \text{Equation IX-6}$$

A Savitzky-Golay smoothing with software Origin was applied for the data of TOFs.

X. Literature

- [1] IEA, 2021, Global Energy Review: CO2 Emissions in 2020, <https://www.iea.org/articles/global-energy-review-co2-emissions-in-2020>, All rights reserved.
- [2] <https://www.esrl.noaa.gov/gmd/ccgg/trends/>, NOAA Global Monitoring Laboratory, (last accessed: 31.05.2021)
- [3] H. Dau, I. Zaharieva, *Acc. Chem. Res.* **2009**, *42*, 1861-1870.
- [4] <https://www.space.com/18175-moon-temperature.html>, What is the Temperature on the Moon?, (last accessed: 02.06.2021)
- [5] https://data.giss.nasa.gov/gistemp/graphs_v4/#, GISS Surface Temperature Analysis, (last accessed: 19.05.2020)
- [6] <https://data.giss.nasa.gov/gistemp/>, GISS Surface Temperature Analysis (GISTEMP), version 4, (last accessed: 31.05.2021)
- [7] N. Lenssen, G. Schmidt, J. Hansen, M. Menne, A. Persin, R. Ruedy, D. Zyss, *J. Geophys. Res. Atmos.* **2019**, *124*, 6307-6326.
- [8] <https://climate.nasa.gov/>, Global Climate Change - Vital Signs of the Planet, (last accessed: 19.05.2020)
- [9] IPCC, **2014**, Climate Change 2014: Synthesis Report. Contribution of Working Groups I, II and III to the Fifth Assessment Report of the Intergovernmental Panel on Climate Change (Geneva, Switzerland)
- [10] IEA, 2019, Global Energy & CO2 Status Report 2018 - The latest trends in energy and emissions in 2018, All rights reserved.
- [11] IEA, 2020, Global Energy Review 2020, <https://www.iea.org/reports/global-energy-review-2020>, All rights reserved.
- [12] <https://energy-charts.info/index.html?l=en&c=DE>, Net public electricity generation in Germany in 2020, (last accessed: 31.05.2021)
- [13] Canada Energy Regulator, **2019**, Canada's Energy Future 2019: Energy Supply and Demand Projections to 2040
- [14] <https://www.consilium.europa.eu/en/5-facts-eu-climate-neutrality/#navigation>, 5 facts about the EU's goal of climate neutrality, (last accessed: 02.06.2021)
- [15] C. Philibert, *Solar Energy Perspectives*, OECD/IEA, Paris, **2011**.
- [16] C. Bozal-Ginesta, J. R. Durrant, *Faraday Discuss.* **2019**, *215*, 439-451.
- [17] IEA, 2019, The Future of Hydrogen, <https://www.iea.org/reports/the-future-of-hydrogen>, All rights reserved.
- [18] H. Kobayashi, A. Hayakawa, K. D. Kunkuma A. Somarathne, Ekenechukwu C. Okafor, *Proceedings of the Combustion Institute* **2019**, *37*, 109-133.
- [19] S. Berardi, S. Drouet, L. Francas, C. Gimbert-Surinach, M. Guttentag, C. Richmond, T. Stoll, A. Llobet, *Chem. Soc. Rev.* **2014**, *43*, 7501-7519.
- [20] D. Voet, J. G. Voet, in *Biochemistry*, 4 ed., John Wiley & Sons, INC., **2010**.
- [21] R. E. Blankenship, D. M. Tiede, J. Barber, G. W. Brudvig, G. Fleming, M. Ghirardi, M. R. Gunner, W. Junge, D. M. Kramer, A. Melis, T. A. Moore, C. C. Moser, D. G. Nocera, A. J. Nozik, D. R. Ort, W. W. Parson, R. C. Prince, R. T. Sayre, *Science* **2011**, *332*, 805-809.
- [22] D. C. I. Yao, D. C. Brune, W. F. J. Vermaas, *FEBS Lett.* **2012**, *586*, 169-173.
- [23] P. M. Vignais, B. Billoud, J. Meyer, *FEMS Microbiology Reviews* **2001**, *25*, 455-501.
- [24] W. Lubitz, H. Ogata, O. Rüdiger, E. Reijerse, *Chem. Rev.* **2014**, *114*, 4081-4148.
- [25] M. Đokić, H. S. Soo, *Chem. Commun.* **2018**, *54*, 6554-6572.

- [26] J. L. White, M. F. Baruch, J. E. Pander, Y. Hu, I. C. Fortmeyer, J. E. Park, T. Zhang, K. Liao, J. Gu, Y. Yan, T. W. Shaw, E. Abelev, A. B. Bocarsly, *Chem. Rev.* **2015**, *115*, 12888-12935.
- [27] T. Inoue, A. Fujishima, S. Konishi, K. Honda, *Nature* **1979**, *277*, 637-638.
- [28] B. Zhang, L. Sun, *Chem. Soc. Rev.* **2019**, *48*, 2216-2264.
- [29] D. Gust, T. A. Moore, A. L. Moore, *Acc. Chem. Res.* **2009**, *42*, 1890-1898.
- [30] J.-M. Lehn, R. Ziessel, *Proceedings of the National Academy of Sciences* **1982**, *79*, 701-704.
- [31] C. J. Seel, T. Gulder, *Chembiochem* **2019**, *20*, 1871-1897.
- [32] I. N. Mills, J. A. Porras, S. Bernhard, *Acc. Chem. Res.* **2018**, *51*, 352-364.
- [33] A. Fujishima, K. Honda, *Nature* **1972**, *238*, 37-38.
- [34] J. Schneider, M. Matsuoka, M. Takeuchi, J. Zhang, Y. Horiuchi, M. Anpo, D. W. Bahnemann, *Chem. Rev.* **2014**, *114*, 9919-9986.
- [35] J. M. Lehn, J. P. Sauvage, *Nouveau journal de chimie* **1977**, *1*, 449-451.
- [36] M. Kirch, J.-M. Lehn, J.-P. Sauvage, *Helv. Chim. Acta* **1979**, *62*, 1345-1384.
- [37] J. Kiwi, M. Grätzel, *Nature* **1979**, *281*, 657-658.
- [38] E. Borgarello, J. Kiwi, E. Pelizzetti, M. Visca, M. Grätzel, *Nature* **1981**, *289*, 158-160.
- [39] E. Borgarello, J. Kiwi, E. Pelizzetti, M. Visca, M. Grätzel, *Journal of the American Chemical Society* **1981**, *103*, 6324-6329.
- [40] B. O'Regan, M. Grätzel, *Nature* **1991**, *353*, 737-740.
- [41] M. Grätzel, *Journal of Photochemistry and Photobiology C: Photochemistry Reviews* **2003**, *4*, 145-153.
- [42] M. Grätzel, *Nature* **2001**, *414*, 338-344.
- [43] A. Hagfeldt, G. Boschloo, L. Sun, L. Kloo, H. Pettersson, *Chem. Rev.* **2010**, *110*, 6595-6663.
- [44] M. R. E. da Silva, T. Auvray, G. S. Hanan, *Inorg. Chim. Acta* **2020**, *499*, 119194.
- [45] P. Semalti, S. N. Sharma, *Journal of Nanoscience and Nanotechnology* **2020**, *20*, 3647-3658.
- [46] M. Ahmed, I. Dincer, *Int. J. Hydrogen Energy* **2019**, *44*, 2474-2507.
- [47] C. S. Ponseca, P. Chabera, J. Uhlig, P. Persson, V. Sundstrom, *Chem. Rev.* **2017**, *117*, 10940-11024.
- [48] Z. Wang, C. Li, K. Domen, *Chem. Soc. Rev.* **2019**, *48*, 2109-2125.
- [49] A. Juris, V. Balzani, F. Barigelletti, S. Campagna, P. Belser, A. von Zelewsky, *Coord. Chem. Rev.* **1988**, *84*, 85-277.
- [50] S. Campagna, F. Puntoriero, F. Nastasi, G. Bergamini, V. Balzani, in *Photochemistry and Photophysics of Coordination Compounds I, Vol. 280* (Eds.: V. Balzani, S. Campagna), Springer-Verlag Berlin, Berlin, **2007**, pp. 117-214.
- [51] X.-y. Wang, A. Del Guerso, R. H. Schmehl, *Journal of Photochemistry and Photobiology C: Photochemistry Reviews* **2004**, *5*, 55-77.
- [52] A. K. Pal, G. S. Hanan, *Chem. Soc. Rev.* **2014**, *43*, 6184-6197.
- [53] P. Atkins, J. de Paula, *Atkins' Physical Chemistry*, 8th ed., Oxford University Press, Great Britain.
- [54] T. Förster, *Annalen der Physik* **1948**, *437*, 55-75.
- [55] T. Förster, *Discussions of the Faraday Society* **1959**, *27*, 7-17.
- [56] D. L. Dexter, *The Journal of Chemical Physics* **1953**, *21*, 836-850.
- [57] P. D. Laible, R. S. Knox, T. G. Owens, *The Journal of Physical Chemistry B* **1998**, *102*, 1641-1648.
- [58] H. Taube, H. Myers, R. L. Rich, *Journal of the American Chemical Society* **1953**, *75*, 4118-4119.
- [59] D. E. Richardson, H. Taube, *Coord. Chem. Rev.* **1984**, *60*, 107-129.
- [60] <https://www.nobelprize.org/prizes/chemistry/1983/press-release/>, Press release. NobelPrize.org. Nobel Media AB 2020, (last accessed: 11.05.2020)

- [61] M. Kuss-Petermann, O. S. Wenger, *Angew. Chem. Int. Ed.* **2016**, *55*, 815-819.
- [62] G. A. Parada, Z. K. Goldsmith, S. Kolmar, B. Pettersson Rimgard, B. Q. Mercado, L. Hammarström, S. Hammes-Schiffer, J. M. Mayer, *Science* **2019**, *364*, 471-475.
- [63] U. S. Schubert, A. Winter, G. R. Newkome, *Terpyridine-based materials*, Wiley-VCH, Weinheim, Germany, **2011**.
- [64] F. Puntoriero, A. Arrigo, A. Santoro, G. L. Ganga, F. Tuyèras, S. Campagna, G. Dupeyre, P. P. Lainé, *Inorg. Chem.* **2019**, *58*, 5807-5817.
- [65] J. Fortage, G. Dupeyre, F. Tuyèras, V. Marvaud, P. Ochsenbein, I. Ciofini, M. Hromadová, L. Pospíšil, A. Arrigo, E. Trovato, F. Puntoriero, P. P. Lainé, S. Campagna, *Inorg. Chem.* **2013**, *52*, 11944-11955.
- [66] S. E. Braslavsky, **2007**, *79*, 293.
- [67] K. Suzuki, A. Kobayashi, S. Kaneko, K. Takehira, T. Yoshihara, H. Ishida, Y. Shiina, S. Oishi, S. Tobita, *Physical Chemistry Chemical Physics* **2009**, *11*, 9850-9860.
- [68] P. G. Potvin, P. U. Luyen, F. Al-Mutlaq, *New J. Chem.* **2001**, *25*, 839-846.
- [69] A. Pöpcke, A. Friedrich, S. Lochbrunner, *J. Phys.: Condens. Matter* **2020**, *32*, 153001.
- [70] B. Durham, J. L. Walsh, C. L. Carter, T. J. Meyer, *Inorg. Chem.* **1980**, *19*, 860-865.
- [71] B. Durham, J. V. Caspar, J. K. Nagle, T. J. Meyer, *Journal of the American Chemical Society* **1982**, *104*, 4803-4810.
- [72] Z.-J. Yu, W.-Y. Lou, H. Junge, A. Pöpcke, H. Chen, L.-M. Xia, B. Xu, M.-M. Wang, X.-J. Wang, Q.-A. Wu, B.-Y. Lou, S. Lochbrunner, M. Beller, S.-P. Luo, *Catal. Commun.* **2019**, *119*, 11-15.
- [73] Z.-L. Xie, W.-X. Jiang, N.-S. Wang, S.-Z. Zhan, *Appl. Organomet. Chem.* **2020**, *34*, e5390.
- [74] E. Deponti, M. Natali, *Dalton Trans.* **2016**, *45*, 9136-9147.
- [75] S. Guo, K.-K. Chen, R. Dong, Z.-M. Zhang, J. Zhao, T.-B. Lu, *ACS Catalysis* **2018**, *8*, 8659-8670.
- [76] E. Rousset, D. Chartrand, I. Ciofini, V. Marvaud, G. S. Hanan, *Chem. Commun.* **2015**, *51*, 9261-9264.
- [77] Y. Tsuji, K. Yamamoto, K. Yamauchi, K. Sakai, *Angew. Chem. Int. Ed.* **2018**, *57*, 208-212.
- [78] G. La Ganga, F. Nastasi, S. Campagna, F. Puntoriero, *Dalton Trans.* **2009**, 9997-9999.
- [79] J. P. Sauvage, J. P. Collin, J. C. Chambron, S. Guillerez, C. Coudret, V. Balzani, F. Barigelletti, L. De Cola, L. Flamigni, *Chem. Rev.* **1994**, *94*, 993-1019.
- [80] J. Wang, G. S. Hanan, F. Loiseau, S. Campagna, *Chem Commun (Camb)* **2004**, 2068-2069.
- [81] R. Passalacqua, F. Loiseau, S. Campagna, Y. Q. Fang, G. S. Hanan, *Angewandte Chemie-International Edition* **2003**, *42*, 1608-1611.
- [82] S. Vaduvescu, P. G. Potvin, *Inorg. Chem.* **2002**, *41*, 4081-4083.
- [83] S. Vaduvescu, Pierre G. Potvin, *Eur. J. Inorg. Chem.* **2004**, *2004*, 1763-1769.
- [84] S. Cerfontaine, L. Marcélis, B. Laramee-Milette, G. S. Hanan, F. Loiseau, J. De Winter, P. Gerbaux, B. Elias, *Inorg. Chem.* **2018**, *57*, 2639-2653.
- [85] B. Bozic-Weber, E. C. Constable, E. Figgemeier, C. E. Housecroft, W. Kylberg, *Energy & Environmental Science* **2009**, *2*, 299-305.
- [86] H. Lv, J. A. Rudd, P. F. Zhuk, J. Y. Lee, E. C. Constable, C. E. Housecroft, C. L. Hill, D. G. Musaev, Y. V. Geletii, *RSC Adv.* **2013**, *3*, 20647-20654.
- [87] E. C. Constable, M. Devereux, E. L. Dunphy, C. E. Housecroft, J. A. Rudd, J. A. Zampese, *Dalton Trans.* **2011**, *40*, 5505-5515.
- [88] A. Call, F. Franco, N. Kandoth, S. Fernández, M. González-Béjar, J. Pérez-Prieto, J. M. Luis, J. Lloret-Fillol, *Chem. Sci.* **2018**, *9*, 2609-2619.

- [89] P. Wang, S. Guo, H.-J. Wang, K.-K. Chen, N. Zhang, Z.-M. Zhang, T.-B. Lu, *Nature Communications* **2019**, *10*, 3155.
- [90] Y.-J. Yuan, Z.-T. Yu, D.-Q. Chen, Z.-G. Zou, *Chem. Soc. Rev.* **2017**, *46*, 603-631.
- [91] C. Ulbricht, B. Beyer, C. Friebe, A. Winter, U. S. Schubert, *Adv. Mater.* **2009**, *21*, 4418-4441.
- [92] B. F. DiSalle, S. Bernhard, *Journal of the American Chemical Society* **2011**, *133*, 11819-11821.
- [93] L.-X. Yang, W.-F. Yang, Y.-J. Yuan, Y.-B. Su, M.-M. Zhou, X.-L. Liu, G.-H. Chen, X. Chen, Z.-T. Yu, Z.-G. Zou, *Chemistry – An Asian Journal* **2018**, *13*, 1699-1709.
- [94] J. I. Goldsmith, W. R. Hudson, M. S. Lowry, T. H. Anderson, S. Bernhard, *Journal of the American Chemical Society* **2005**, *127*, 7502-7510.
- [95] A. Zarkadoulas, E. Koutsouri, C. Kefalidi, C. A. Mitsopoulou, *Coord. Chem. Rev.* **2015**, *304-305*, 55-72.
- [96] P. Zimmer, L. Burkhardt, R. Schepper, K. B. Zheng, D. Gosztola, A. Neuba, U. Florke, C. Wolper, R. Schoch, W. Gawelda, S. E. Canton, M. Bauer, *Eur. J. Inorg. Chem.* **2018**, 5203-5214.
- [97] M. Pápai, M. Abedi, G. Levi, E. Biasin, M. M. Nielsen, K. B. Møller, *The Journal of Physical Chemistry C* **2019**, *123*, 2056-2065.
- [98] M. Natali, F. Nastasi, F. Puntoriero, A. Sartorel, *Eur. J. Inorg. Chem.* **2019**, *2019*, 2027-2039.
- [99] A. Mazzeo, S. Santalla, C. Gaviglio, F. Doctorovich, J. Pellegrino, *Inorg. Chim. Acta* **2020**, 119950.
- [100] Y. Pellegrin, F. Odobel, *Comptes Rendus Chimie* **2017**, *20*, 283-295.
- [101] P. J. DeLaive, T. K. Foreman, C. Giannotti, D. G. Whitten, *Journal of the American Chemical Society* **1980**, *102*, 5627-5631.
- [102] P. J. Smith, C. K. Mann, *The Journal of Organic Chemistry* **1969**, *34*, 1821-1826.
- [103] D. G. Whitten, *Acc. Chem. Res.* **1980**, *13*, 83-90.
- [104] Q. G. Mulazzani, M. Venturi, M. Z. Hoffman, *The Journal of Physical Chemistry* **1985**, *89*, 722-728.
- [105] N. V. Rees, O. V. Klymenko, R. G. Compton, M. Oyama, *J. Electroanal. Chem.* **2002**, *531*, 33-42.
- [106] S. Fukuzumi, S. Koumitsu, K. Hironaka, T. Tanaka, *Journal of the American Chemical Society* **1987**, *109*, 305-316.
- [107] S. Fukuzumi, *Eur. J. Inorg. Chem.* **2008**, *2008*, 1351-1362.
- [108] A. Kobayashi, H. Konno, K. Sakamoto, A. Sekine, Y. Ohashi, M. Iida, O. Ishitani, *Chem. - Eur. J.* **2005**, *11*, 4219-4226.
- [109] Y. Tamaki, K. Koike, T. Morimoto, O. Ishitani, *J. Catal.* **2013**, *304*, 22-28.
- [110] J. Schneider, D. W. Bahnemann, *The Journal of Physical Chemistry Letters* **2013**, *4*, 3479-3483.
- [111] Q. Yin, J. M. Tan, C. Besson, Y. V. Geletii, D. G. Musaev, A. E. Kuznetsov, Z. Luo, K. I. Hardcastle, C. L. Hill, *Science* **2010**, *328*, 342-345.
- [112] Q. Zhang, J. Guan, *ChemSusChem* **2019**, *12*, 3209-3235.
- [113] L. C. Sun, L. Hammarstrom, B. Akermark, S. Styring, *Chem. Soc. Rev.* **2001**, *30*, 36-49.
- [114] J. L. Fillol, Z. Codolà, I. Garcia-Bosch, L. Gómez, J. J. Pla, M. Costas, *Nature Chemistry* **2011**, *3*, 807-813.
- [115] Q. Zhang, Z. Duan, M. Li, J. Guan, *Chem. Commun.* **2020**, *56*, 794-797.
- [116] S. W. Gersten, G. J. Samuels, T. J. Meyer, *Journal of the American Chemical Society* **1982**, *104*, 4029-4030.
- [117] J. J. Concepcion, J. W. Jurss, M. R. Norris, Z. F. Chen, J. L. Templeton, T. J. Meyer, *Inorg. Chem.* **2010**, *49*, 1277-1279.

- [118] D. J. Wasylenko, C. Ganesamoorthy, B. D. Koivisto, M. A. Henderson, C. P. Berlinguette, *Inorg. Chem.* **2010**, *49*, 2202-2209.
- [119] T. Wada, K. Tsuge, K. Tanaka, *Inorg. Chem.* **2001**, *40*, 329-337.
- [120] R. Brimblecombe, G. C. Dismukes, G. F. Swiegers, L. Spiccia, *Dalton Trans.* **2009**, 9374-9384.
- [121] R. Matheu, M. Z. Ertem, C. Gimbert-Surinach, X. Sala, A. Llobet, *Chem. Rev.* **2019**, *119*, 3453-3471.
- [122] S. E. Bettis, K. Hanson, L. Wang, M. K. Gish, J. J. Concepcion, Z. Fang, T. J. Meyer, J. M. Papanikolas, *J. Phys. Chem. A* **2014**, *118*, 10301-10308.
- [123] R. Lomoth, S. Ott, *Dalton Trans.* **2009**, 9952-9959.
- [124] S. Fukuzumi, Y.-M. Lee, W. Nam, *Coord. Chem. Rev.* **2018**, *355*, 54-73.
- [125] M. L. Helm, M. P. Stewart, R. M. Bullock, M. R. DuBois, D. L. DuBois, *Science* **2011**, *333*, 863-866.
- [126] W. T. Eckenhoff, *Coord. Chem. Rev.* **2017**, *373*, 295-316.
- [127] N. Elgrishi, B. D. McCarthy, E. S. Rountree, J. L. Dempsey, *ACS Catalysis* **2016**, *6*, 3644-3659.
- [128] J. Hawecker, J. M. Lehn, R. Ziessel, *Nouv J Chim* **1983**, *7*, 271-277.
- [129] M. Razavet, V. Artero, M. Fontecave, *Inorg. Chem.* **2005**, *44*, 4786-4795.
- [130] R. W. Hogue, O. Schott, G. S. Hanan, S. Brooker, *Chemistry-a European Journal* **2018**, *24*, 9820-9832.
- [131] N. Queyriaux, R. T. Jane, J. Massin, V. Artero, M. Chavarot-Kerlidou, *Coord. Chem. Rev.* **2015**, *304-305*, 3-19.
- [132] J. L. Dempsey, B. S. Brunschwig, J. R. Winkler, H. B. Gray, *Acc. Chem. Res.* **2009**, *42*, 1995-2004.
- [133] X. Hu, B. M. Cossairt, B. S. Brunschwig, N. S. Lewis, J. C. Peters, *Chem. Commun.* **2005**, 4723-4725.
- [134] P. A. Jacques, V. Artero, J. Pecaut, M. Fontecave, *Proceedings of the National Academy of Sciences of the United States of America* **2009**, *106*, 20627-20632.
- [135] B. D. Stubbert, J. C. Peters, H. B. Gray, *Journal of the American Chemical Society* **2011**, *133*, 18070-18073.
- [136] S. Rajak, O. Schott, P. Kaur, T. Maris, G. S. Hanan, A. Duong, *Polyhedron* **2020**, *180*, 114412.
- [137] B. B. Beyene, C.-H. Hung, *Coord. Chem. Rev.* **2020**, *410*, 213234.
- [138] S. R. Soltau, P. D. Dahlberg, J. Niklas, O. G. Poluektov, K. L. Mulfort, L. M. Utschig, *Chem. Sci.* **2016**, *7*, 7068-7078.
- [139] S. C. Marguet, M. J. Stevenson, H. S. Shafaat, *The Journal of Physical Chemistry B* **2019**, *123*, 9792-9800.
- [140] L. M. Utschig, S. C. Silver, K. L. Mulfort, D. M. Tiede, *Journal of the American Chemical Society* **2011**, *133*, 16334-16337.
- [141] L. M. Utschig, S. R. Soltau, D. M. Tiede, *Curr. Opin. Chem. Biol.* **2015**, *25*, 1-8.
- [142] A. Fihri, V. Artero, M. Razavet, C. Baffert, W. Leibl, M. Fontecave, *Angewandte Chemie-International Edition* **2008**, *47*, 564-567.
- [143] K. L. Mulfort, D. M. Tiede, *The Journal of Physical Chemistry B* **2010**, *114*, 14572-14581.
- [144] C. Li, M. Wang, J. Pan, P. Zhang, R. Zhang, L. Sun, *J. Organomet. Chem.* **2009**, *694*, 2814-2819.
- [145] P. Lei, M. Hedlund, R. Lomoth, H. Rensmo, O. Johansson, L. Hammarstrom, *Journal of the American Chemical Society* **2008**, *130*, 26-27.
- [146] S. Rau, B. Schafer, D. Gleich, E. Anders, M. Rudolph, M. Friedrich, H. Gorts, W. Henry, J. G. Vos, *Angewandte Chemie-International Edition* **2006**, *45*, 6215-6218.
- [147] P. Lang, J. Habermehl, S. I. Troyanov, S. Rau, M. Schwalbe, *Chem. - Eur. J.* **2018**, *24*, 3225-3233.

- [148] S. Ott, M. Borgstrom, M. Kritikos, R. Lomoth, J. Bergquist, B. Akermark, L. Hammarstrom, L. C. Sun, *Inorg. Chem.* **2004**, *43*, 4683-4692.
- [149] S. Pyo, E. Pérez-Cordero, S. G. Bott, L. Echevoyen, *Inorg. Chem.* **1999**, *38*, 3337-3343.
- [150] L. Hammarström, O. Johansson, *Coord. Chem. Rev.* **2010**, *254*, 2546-2559.
- [151] A. Breivogel, C. Kreitner, K. Heinze, *Eur. J. Inorg. Chem.* **2014**, 5468-5490.
- [152] E. C. Constable, *Chem. Soc. Rev.* **2007**, *36*, 246-253.
- [153] A. Wild, A. Winter, F. Schlutter, U. S. Schubert, *Chem. Soc. Rev.* **2011**, *40*, 1459-1511.
- [154] E. A. Medlycott, G. S. Hanan, *Chem. Soc. Rev.* **2005**, *34*, 133-142.
- [155] J. V. Caspar, T. J. Meyer, *The Journal of Physical Chemistry* **1983**, *87*, 952-957.
- [156] P. Pal, T. Ganguly, D. Maity, S. Baitalik, *Journal of Photochemistry and Photobiology A: Chemistry* **2020**, *392*, 112409.
- [157] P. Pal, S. Mukherjee, D. Maity, S. Baitalik, *Acs Omega* **2018**, *3*, 14526-14537.
- [158] P. Pal, T. Ganguly, S. Das, S. Baitalik, *Dalton Trans.* **2021**, *50*, 186-196.
- [159] P. Singh, P. J. S. Rana, P. Kar, *Journal of Photochemistry and Photobiology a-Chemistry* **2017**, *346*, 416-430.
- [160] T. Auvray, R. Sahoo, D. Deschenes, G. S. Hanan, *Dalton Trans.* **2019**, *48*, 15136-15143.
- [161] M. W. Cooke, M.-P. Santoni, F. Loiseau, B. Hasenknopf, G. S. Hanan, *Inorg. Chim. Acta* **2017**, *454*, 208-215.
- [162] M. Rupp, T. Auvray, E. Rousset, G. M. Mercier, V. Marvaud, D. G. Kurth, G. S. Hanan, *Inorg. Chem.* **2019**, *58*, 9127-9134.
- [163] J. Eberhard, K. Peuntinger, R. Frohlich, D. M. Guldi, J. Mattay, *Eur. J. Org. Chem.* **2018**, 2682-2700.
- [164] K. Barthelmes, M. Sittig, A. Winter, U. S. Schubert, *Eur. J. Inorg. Chem.* **2017**, 3698-3706.
- [165] P. Pal, S. Mukherjee, D. Maity, S. Baitalik, *Inorg. Chem.* **2018**, *57*, 5743-5753.
- [166] A. K. Pal, S. Serroni, N. Zaccheroni, S. Campagna, G. S. Hanan, *Chem. Sci.* **2014**, *5*, 4800-4811.
- [167] A. K. Pal, A. Duong, J. D. Wuest, G. S. Hanan, *Polyhedron* **2016**, *108*, 100-103.
- [168] M. T. Rupp, T. Auvray, N. Shevchenko, L. Swoboda, G. S. Hanan, D. G. Kurth, *Inorg. Chem.* **2021**, *60*, 292-302.
- [169] M. T. Rupp, T. Auvray, G. S. Hanan, D. G. Kurth, *Eur. J. Inorg. Chem.* **2021**, *2021*, 2822-2829.
- [170] S. Sinn, B. Schulze, C. Friebe, D. G. Brown, M. Jager, E. Altuntas, J. Kubel, O. Guntner, C. P. Berlinguette, B. Dietzek, U. S. Schubert, *Inorg. Chem.* **2014**, *53*, 2083-2095.
- [171] J. Torres, M. C. Carrión, J. Leal, G. Castañeda, B. R. Manzano, F. A. Jalón, *J. Organomet. Chem.* **2019**, *898*, 120880.
- [172] M. Abrahamsson, H. C. Becker, L. Hammarstrom, *Dalton Trans.* **2017**, *46*, 13314-13321.
- [173] A. K. Pal, N. Zaccheroni, S. Campagna, G. S. Hanan, *Chem. Commun.* **2014**, *50*, 6846-6849.
- [174] B. Laramée-Milette, G. S. Hanan, *Dalton Trans.* **2016**, *45*, 12507-12517.
- [175] C. M. Brown, N. E. Arsenault, T. N. K. Cross, D. Hean, Z. Xu, M. O. Wolf, *Inorganic Chemistry Frontiers* **2020**, *7*, 117-127.
- [176] F. Schramm, V. Meded, H. Fliegl, K. Fink, O. Fuhr, Z. Qu, W. Klopffer, S. Finn, T. E. Keyes, M. Ruben, *Inorg. Chem.* **2009**, *48*, 5677-5684.
- [177] J. Moll, C. Wang, A. Pöpcke, C. Förster, U. Resch-Genger, S. Lochbrunner, K. Heinze, *Chem. - Eur. J.* **2020**, *26*, 6820-6832.

- [178] A. R. Naziruddin, C. L. Kuo, W. J. Lin, W. H. Lo, C. S. Lee, B. J. Sun, A. H. H. Chang, W. S. Hwang, *Organometallics* **2014**, *33*, 2575-2582.
- [179] D. Mondal, M. Bar, S. Mukherjee, S. Baitalik, *Inorg. Chem.* **2016**, *55*, 9707-9724.
- [180] J. Otsuki, *Journal of Materials Chemistry A* **2018**, *6*, 6710-6753.
- [181] S. Vitale, B. Laramée-Milette, M. E. Amato, G. S. Hanan, N. Tuccitto, A. Licciardello, *Nanoscale* **2019**, *11*, 4788-4793.
- [182] M. Bar, D. Maity, S. Deb, S. Das, S. Baitalik, *Dalton Trans.* **2017**, *46*, 12950-12963.
- [183] D. Maity, C. Bhaumik, D. Mondal, S. Baitalik, *Dalton Trans.* **2014**, *43*, 1829-1845.
- [184] S. A. Senthana, V. Alexander, *Dalton Trans.* **2015**, *44*, 14813-14822.
- [185] C. Kreitner, M. Grabolle, U. Resch-Genger, K. Heinze, *Inorg. Chem.* **2014**, *53*, 12947-12961.
- [186] A. A. Viveke, V. Alexander, *RSC Adv.* **2014**, *4*, 44269-44273.
- [187] A. Paul, M. Bar, S. Deb, S. Baitalik, *Inorg. Chem.* **2019**, *58*, 10065-10077.
- [188] S. Cerfontaine, Q. Duez, L. Troian-Gautier, G. Barozzino-Consiglio, F. Loiseau, J. Cornil, J. De Winter, P. Gerbault, B. Elias, *Inorg. Chem.* **2020**, *59*, 14536-14543.
- [189] A. Paul, T. Ganguly, M. Bar, S. Baitalik, *Inorg. Chem.* **2021**, *60*, 412-422.
- [190] Z. N. Liu, C. X. He, H. J. Yin, S. W. Yu, J. B. Xu, J. W. Dong, Y. Liu, S. B. Xia, F. X. Cheng, *Eur. J. Inorg. Chem.* **2021**, *2021*, 482-491.
- [191] B. Laramée-Milette, G. S. Hanan, *Chem. Commun.* **2017**, *53*, 10496-10499.
- [192] M. Wachtler, J. Kubel, K. Barthelmes, A. Winter, A. Schmiedel, T. Pascher, C. Lambert, U. S. Schubert, B. Dietzek, *Physical Chemistry Chemical Physics* **2016**, *18*, 2350-2360.
- [193] A. J. Maria Xavier, N. A. Samy, M. W. B. Paul, B. Brainard, M. Letticia, V. Alexander, *New J. Chem.* **2015**, *39*, 4284-4294.
- [194] E. G. Moore, M. Benaglia, G. Bergamini, P. Ceroni, *Eur. J. Inorg. Chem.* **2015**, *2015*, 414-420.
- [195] J. J. Yang, M. Bhadbhade, W. A. Donald, H. Iranmanesh, E. G. Moore, H. Yan, J. E. Beves, *Chem. Commun.* **2015**, *51*, 4465-4468.
- [196] D. Luo, T. Zuo, J. Zheng, Z.-H. Long, X.-Z. Wang, Y.-L. Huang, X.-P. Zhou, D. Li, *Materials Chemistry Frontiers* **2021**, *5*, 2777-2782.
- [197] S. Pai, M. Schott, L. Niklaus, U. Posset, D. G. Kurth, *J. Mater. Chem. C* **2018**, *6*, 3310-3321.
- [198] S. Cao, C.-J. Wang, G.-Q. Wang, Y. Chen, X.-J. Lv, W.-F. Fu, *RSC Adv.* **2020**, *10*, 5930-5937.
- [199] R. T. Ryan, K. C. Stevens, R. Calabro, S. Parkin, J. Mahmoud, D. Y. Kim, D. K. Heidary, E. C. Glazer, J. P. Selegue, *Inorg. Chem.* **2020**, *59*, 8882-8892.
- [200] M. W. Cooke, A. Botti, D. Zok, G. Steinhauser, K. R. Ungar, *Proceedings of the National Academy of Sciences* **2020**, *117*, 14703-14711.
- [201] J. Wang, G. S. Hanan, *Synlett* **2005**, 1251-1254.
- [202] S. Perera, X. P. Li, M. M. Guo, C. Wesdemiotis, C. N. Moorefield, G. R. Newkome, *Chem. Commun.* **2011**, *47*, 4658-4660.
- [203] B. Laramée-Milette, T. Auvray, S. Nguyen, S. Tremblay, C. Lachance-Brais, M. Donguy, V. Taylor, D. Deschenes, G. S. Hanan, *Synthesis-Stuttgart* **2015**, *47*, 3849-3858.
- [204] R.-A. Fallahpour, M. Neuburger, M. Zehnder, *New J. Chem.* **1999**, *23*, 53-61.
- [205] H. Iranmanesh, K. S. A. Arachchige, W. A. Donald, N. Kyriacou, C. Shen, J. R. Price, J. E. Beves, *Aust. J. Chem.* **2017**, *70*, 529-537.
- [206] M. Maestri, N. Armaroli, V. Balzani, E. C. Constable, A. Thompson, *Inorg. Chem.* **1995**, *34*, 2759-2767.
- [207] J. i. Sone, S. Tsuji, *Intelligent Nanosystems for Energy, Information and Biological Technologies*, Springer, Tokyo, **2016**.

- [208] A. Manke, K. Geisel, A. Fetzer, P. Kurz, *Physical chemistry chemical physics : PCCP* **2014**, 16 24, 12029-12042.
- [209] A. Srinivasulu, B. Shantharjun, D. Vani, K. C. Ashalu, A. Mohd, J. Wencel-Delord, F. Colobert, K. R. Reddy, *Eur. J. Org. Chem.* **2019**, 2019, 1815-1819.
- [210] B. P. Sullivan, J. M. Calvert, T. J. Meyer, *Inorg. Chem.* **1980**, 19, 1404-1407.
- [211] M. Kasha, *Discussions of the Faraday Society* **1950**, 9, 14-19.
- [212] K. E. Spettel, N. H. Damrauer, *J. Phys. Chem. A* **2014**, 118, 10649-10662.
- [213] G. R. Newkome, T. J. Cho, C. N. Moorefield, G. R. Baker, R. Cush, P. S. Russo, *Angew. Chem. Int. Ed.* **1999**, 38, 3717-3721.
- [214] E. C. Constable, A. M. W. C. Thompson, *J. Chem. Soc., Dalton Trans.* **1992**, 3467-3475.
- [215] E. C. Constable, A. M. W. C. Thompson, *J. Chem. Soc., Dalton Trans.* **1994**, 1409-1418.
- [216] E. C. Constable, C. E. Housecroft, M. Neuburger, D. Phillips, P. R. Raithby, E. Schofield, E. Sparr, D. A. Tocher, M. Zehnder, Y. Zimmermann, *J. Chem. Soc., Dalton Trans.* **2000**, 2219-2228.
- [217] J. E. Beves, E. L. Dunphy, E. C. Constable, C. E. Housecroft, C. J. Kepert, M. Neuburger, D. J. Price, S. Schaffner, *Dalton Trans.* **2008**, 386-396.
- [218] E. C. Constable, C. E. Housecroft, A. C. Thompson, P. Passaniti, S. Silvi, M. Maestri, A. Credi, *Inorg. Chim. Acta* **2007**, 360, 1102-1110.
- [219] S. Silvi, E. C. Constable, C. E. Housecroft, J. E. Beves, E. L. Dunphy, M. Tomasulo, F. M. Raymo, A. Credi, *Chem. Commun.* **2009**, 1484-1486.
- [220] S. Silvi, E. C. Constable, C. E. Housecroft, J. E. Beves, E. L. Dunphy, M. Tomasulo, F. M. Raymo, A. Credi, *Chem. - Eur. J.* **2009**, 15, 178-185.
- [221] E. C. Constable, E. L. Dunphy, C. E. Housecroft, W. Kylberg, M. Neuburger, S. Schaffner, E. R. Schofield, C. B. Smith, *Chem. - Eur. J.* **2006**, 12, 4600-4610.
- [222] A. L. Kaledin, Z. Huang, Q. Yin, E. L. Dunphy, E. C. Constable, C. E. Housecroft, Y. V. Geletii, T. Lian, C. L. Hill, D. G. Musaev, *J. Phys. Chem. A* **2010**, 114, 6284-6297.
- [223] Y.-Q. Fang, N. J. Taylor, G. S. Hanan, F. Loiseau, R. Passalacqua, S. Campagna, H. Nierengarten, A. V. Dorsselaer, *Journal of the American Chemical Society* **2002**, 124, 7912-7913.
- [224] Y.-Q. Fang, N. J. Taylor, F. Laverdière, G. S. Hanan, F. Loiseau, F. Nastasi, S. Campagna, H. Nierengarten, E. Leize-Wagner, A. Van Dorsselaer, *Inorg. Chem.* **2007**, 46, 2854-2863.
- [225] S. Pai, M. Moos, M. H. Schreck, C. Lambert, D. G. Kurth, *Inorg. Chem.* **2017**, 56, 1418-1432.
- [226] H. Brunner, R. Störiko, F. Rominger, *Eur. J. Inorg. Chem.* **1998**, 1998, 771-781.
- [227] P. Sun, K. Wang, B. Zhao, T. Yang, H. Xu, Y. Miao, H. Wang, B. Xu, *Tetrahedron* **2016**, 72, 8335-8341.
- [228] M. I. J. Polson, E. A. Medlycott, G. S. Hanan, L. Mikelsons, N. J. Taylor, M. Watanabe, Y. Tanaka, F. Loiseau, R. Passalacqua, S. Campagna, *Chem. - Eur. J.* **2004**, 10, 3640-3648.
- [229] S. C. Fu, X. L. Zhong, Y. Zhang, T. W. Lai, K. C. Chan, K. Y. Lee, C. Y. H. Chao, *Energy and Buildings* **2020**, 225, 110313.
- [230] M. Higuchi, Y. Otsuka, R. Shomura, D. G. Kurth, *Thin Solid Films* **2008**, 516, 2416-2420.
- [231] N. Nickita, G. Gasser, P. Pearson, M. J. Belousoff, L. Y. Goh, A. M. Bond, G. B. Deacon, L. Spiccia, *Inorg. Chem.* **2009**, 48, 68-81.
- [232] L. Hammarström, F. Barigelletti, L. Flamigni, M. T. Indelli, N. Armaroli, G. Calogero, M. Guardigli, A. Sour, J.-P. Collin, J.-P. Sauvage, *J. Phys. Chem. A* **1997**, 101, 9061-9069.

-
- [233] A. Jacques, O. Schott, K. Robeyns, G. S. Hanan, B. Elias, *Eur. J. Inorg. Chem.* **2016**, 1779-1783.
- [234] C. Lentz, O. Schott, T. Auvray, G. Hanan, B. Elias, *Inorg. Chem.* **2017**, *56*, 10875-10881.
- [235] A. Duerrbeck, S. Gorelik, J. Hobley, A. M. Yong, G. S. Subramanian, A. Hor, N. Long, *J. Mater. Chem. C* **2015**, *3*, 8992-9002.
- [236] J. N. Demas, G. A. Crosby, *J. Phys. Chem.* **1971**, *75*, 991-1024.
- [237] K. E. Spettel, N. H. Damrauer, *J. Phys. Chem. A* **2014**, *118*, 10649-10662.
- [238] Bruker AXS Inc. APEX3, SAINT, SADABS **2016**, Madison, Wisconsin USA.
- [239] G. Sheldrick, *Acta Crystallogr. A* **2015**, *71*, 3-8.
- [240] O. V. Dolomanov, L. J. Bourhis, R. J. Gildea, J. A. K. Howard, H. Puschmann, *J. Appl. Crystallogr.* **2009**, *42*, 339-341.
- [241] G. Sheldrick, *Acta Crystallogr. C* **2015**, *71*, 3-8.
- [242] C. F. Macrae, I. J. Bruno, J. A. Chisholm, P. R. Edgington, P. McCabe, E. Pidcock, L. Rodriguez-Monge, R. Taylor, J. van de Streek, P. A. Wood, *J. Appl. Crystallogr.* **2008**, *41*, 466-470.
- [243] A. Spek, *Acta Crystallographica Section C* **2015**, *71*, 9-18.
- [244] M. J. Frisch, G. W. Trucks, H. B. Schlegel, G. E. Scuseria, M. A. Robb, J. R. Cheeseman, G. Scalmani, V. Barone, G. A. Petersson, H. Nakatsuji, X. Li, M. Caricato, A. V. Marenich, J. Bloino, B. G. Janesko, R. Gomperts, B. Mennucci, H. P. Hratchian, J. V. Ortiz, A. F. Izmaylov, J. L. Sonnenberg, Williams, F. Ding, F. Lipparini, F. Egidi, J. Goings, B. Peng, A. Petrone, T. Henderson, D. Ranasinghe, V. G. Zakrzewski, J. Gao, N. Rega, G. Zheng, W. Liang, M. Hada, M. Ehara, K. Toyota, R. Fukuda, J. Hasegawa, M. Ishida, T. Nakajima, Y. Honda, O. Kitao, H. Nakai, T. Vreven, K. Throssell, J. A. Montgomery Jr., J. E. Peralta, F. Ogliaro, M. J. Bearpark, J. J. Heyd, E. N. Brothers, K. N. Kudin, V. N. Staroverov, T. A. Keith, R. Kobayashi, J. Normand, K. Raghavachari, A. P. Rendell, J. C. Burant, S. S. Iyengar, J. Tomasi, M. Cossi, J. M. Millam, M. Klene, C. Adamo, R. Cammi, J. W. Ochterski, R. L. Martin, K. Morokuma, O. Farkas, J. B. Foresman, D. J. Fox, Wallingford, CT, **2016**.
- [245] C. Adamo, V. Barone, *J. Chem. Phys.* **1999**, *110*, 6158-6170.
- [246] T. H. D. Jr, P. J. Hay, *Modern Theoretical Chemistry III ed., Vol. 3*, Plenum, New York, **1977**.
- [247] P. J. Hay, W. R. Wadt, *J. Chem. Phys.* **1985**, *82*, 270-283.
- [248] P. J. Hay, W. R. Wadt, *J. Chem. Phys.* **1985**, *82*, 299-310.
- [249] W. R. Wadt, P. J. Hay, *J. Chem. Phys.* **1985**, *82*, 284-298.
- [250] N. M. O'Boyle, A. L. Tenderholt, K. M. Kangner, *J. Comput. Chem.* **2008**, *29*, 839-845.
- [251] S. Leonid, V 4.53 **2005-2017**, www.chemissian.com.
- [252] M. Cossi, N. Rega, G. Scalmani, V. Barone, *J. Comput. Chem.* **2003**, *24*, 669-681.
- [253] C. Lentz, O. Schott, T. Auvray, G. Hanan, B. Elias, *Inorg. Chem.* **2017**, *56*, 10875-10881.
-

Author Contributions

The co-authors of the manuscripts used in this dissertation are aware of and agree to both the use and the stated royalties.

1. *Photocatalytic Hydrogen Evolution Driven by a Heteroleptic Ruthenium(II) Bis(terpyridine) Complex*, Mira Rupp, Thomas Auvray, Elodie Rousset, Gabriel Mercier, Valérie Marvaud, Dirk G. Kurth, Garry S. Hanan, *Inorganic Chemistry*, **2019**, 58, 9127–9134. DOI: <https://doi.org/10.1021/acs.inorgchem.9b00698>

Mira Rupp (MR), Thomas Auvray (TA), Elodie Rousset (ER), Gabriel Mercier (GM), Valérie Marvaud (VM), Dirk G. Kurth (DGK), Garry S. Hanan (GSH)								
Author	MR	TA	ER	GM	VM	DGK	GSH	∑ in percent
Idea and conception						5%	5%	10%
Synthesis of the investigated compounds	20%							20%
Analysis of the investigated compounds	5%							5%
Photophysical and electrochemical analysis	20%							20%
Hydrogen production experiments	1%	8%						9%
Crystal structure determination		3%						3%
DFT calculations		4%						4%
Development of precursor synthesis			3%	3%	1%			7%
Writing of publication	6%	3%						9%
Correction and coordination of publication	1%	2%				5%	5%	13%
Sum	53%	20%	3%	3%	1%	10%	10%	100%

2. *Substituted 2,4-Di(pyridin-2-yl)pyrimidine-Based Ruthenium Photosensitizers for Hydrogen Photoevolution under Red Light*, Mira Rupp, Thomas Auvray, Natali Shevchenko, Lukas Swoboda, Dirk G. Kurth, Garry S. Hanan, *Inorganic Chemistry*, **2020**, 60 (1), 292-302. DOI: <https://doi.org/10.1021/acs.inorgchem.0c02955>

Mira Rupp (MR), Thomas Auvray (TA), Natali Shevchenko (NS), Lukas Swoboda (LS), Dirk G. Kurth (DGK), Garry S. Hanan (GSH)							
Author	MR	TA	NS	LS	DGK	GSH	Σ in percent
Idea and conception					5%	5%	10%
Synthesis of the investigated compounds	20%		5%	5%			30%
Analysis of the investigated compounds	5%						5%
Photophysical and electrochemical analysis	15%						15%
Hydrogen production experiments	5%						5%
Crystal structure determination	4%						4%
DFT calculations		5%					5%
Writing of publication	6%						6%
Correction and coordination of publication	5%	5%			5%	5%	20%
Sum	60%	10%	5%	5%	10%	10%	100%

3. *Electrochemical and photophysical study of homoleptic and heteroleptic methylated Ru(II) bis-terpyridine complexes*, Mira T. Rupp, Thomas Auvray, Garry S. Hanan, Dirk G. Kurth, *European Journal of Inorganic Chemistry*, **2021**, 2021 (28), 2822-2829. DOI: <https://doi.org/10.1002/ejic.202100092>

Mira T. Rupp (MTR), Thomas Auvray (TA), Dirk G. Kurth (DGK), Garry S. Hanan (GSH)					
Author	MTR	TA	DGK	GSH	Σ in percent
Idea and conception			5%	5%	10%
Synthesis of the investigated compounds	20%				20%
Analysis of the investigated compounds	5%				5%
Photophysical and electrochemical analysis	25%				25%
Hydrogen production experiments	5%				5%
Crystal structure determination	4%				4%
DFT calculations		5%			5%
Writing of publication	6%				6%
Correction and coordination of publication	5%	5%	5%	5%	20%
Sum	70%	10%	10%	10%	100%

4. CCDC 2090569: *Experimental Crystal Structure Determination*, Mira T. Rupp, Daniel Chartrand, Garry S. Hanan, Dirk G. Kurth, *CSD Communication*, 2021. DOI: <https://dx.doi.org/10.5517/ccdc.csd.cc285dql>

Mira T. Rupp (MTR), Daniel Chartrand (DC), Dirk G. Kurth (DGK), Garry S. Hanan (GSH)					
Author	MTR	DC	DGK	GSH	Σ in percent
Idea and conception			5%	5%	10%
Crystal growth	10%				10%
X-ray diffraction data collection+integration		40%			40%
X-ray crystal structure refinement	40%				40%
Sum	50%	40%	5%	5%	100%

5. *Dinuclear 2,4-di(pyridin-2-yl)-pyrimidine based ruthenium photosensitizers for hydrogen photo-evolution under red light*, Mira T. Rupp, Thomas Auvray, Garry S. Hanan, Dirk G. Kurth (revised and submitted to *Dalton Transactions*).

Mira T. Rupp (MTR), Thomas Auvray (TA), Dirk G. Kurth (DGK), Garry S. Hanan (GSH)					
Author	MTR	TA	DGK	GSH	Σ in percent
Idea and conception			5%	5%	10%
Synthesis of the investigated compounds	15%				20%
Analysis of the investigated compounds	5%				5%
Photophysical and electrochemical analysis	30%				25%
Hydrogen production experiments	9%				9%
DFT calculations		5%			5%
Writing of publication	6%				6%
Correction and coordination of publication	5%	5%	5%	5%	20%
Sum	70%	10%	10%	10%	100%

6. *Enhancing the photophysical properties of Ru(II) complexes by specific design of tridentate ligands*, Mira T. Rupp, Natali Shevchenko, Garry S. Hanan, Dirk G. Kurth, *Coordination Chemistry Reviews* **2021**, *446*, 214127. DOI: <https://doi.org/10.1016/j.ccr.2021.214127>

Mira T. Rupp (MTR), Natali Shevchenko (NS), Dirk G. Kurth (DGK), Garry S. Hanan (GSH)					
Author	MTR	NS	DGK	GSH	Σ in percent
Idea and conception			5%	5%	10%
Literature research and analysis	10%	20%			30%
Writing of publication	30%	10%			40%
Correction and coordination of publication	10%		5%	5%	20%
Sum	50%	30%	10%	10%	100%